

DISS. ETH Nr. 30443

Modeling and Control of Nanosecond Repetitively Pulsed Discharge for Plasma-Assisted Ignition

A thesis submitted to attain the degree of
DOCTOR OF SCIENCES
(Dr. sc. ETH Zurich)

presented by
Michelangelo Giorgio Balmelli
M.Sc. ETH Zurich
born on 30.04.1992

accepted on the recommendation of
Prof. Dr. Jürgen Biela, examiner
Dr. Patrik Soltic, co-examiner
Prof. Dr. Christian M. Franck, co-examiner
PD Dr. Davide Bleiner, co-examiner
Prof. Dr. Lorenzo Sforza, co-examiner

2024

Acknowledgement

I would like to thank those who have supported me on this journey of personal and intellectual growth.

The first mention goes to the members of my doctoral jury. I am extremely grateful to Dr. Patrick Soltic, who has believed in this project from the start and has been an attentive and supportive mentor, guiding me through the ups and downs of the doctorate. I would also like to acknowledge Prof. Jürgen Biela for his generous supervision. Without Jürgen's encouraging and stimulating feedback, many of the multidisciplinary facets explored in this dissertation would have remained unaddressed. Thanks also to Prof. Christian M. Frank for the illuminating discussions on high-voltage gas insulation. Although in this dissertation the breakdown is the desired outcome, and does not represent a failure of the insulation system, I am glad that we have found many fruitful synergies. I am especially grateful to PD Dr. Davide Bleiner, who has always provided sharp and constructive comments during our frequent conversations on optical emission spectroscopy. Finally, many thanks to Asst. Prof. Dr. Lorenzo Sforza for his time and for agreeing to be the external supervisor on my doctoral committee.

My gratitude extends to Dr. Laura Merotto for our longstanding cooperation and the valuable time she has dedicated to my project. A special thanks goes to Dr. Raphael Färber, whose own enthusiasm and knowledge of the underlying physical process has been a great source of inspiration.

I feel lucky to have been part of the the Chemical Energy Carriers and Vehicle Systems Laboratory at Empa. I am grateful for the first-class infrastructure I had access to in the lab and for all the brilliant colleagues who made many motivating and thought-provoking discussions possible. For providing every single piece of equipment I ever needed on this project, and for his invaluable strategic guidance, I would like to thank Christian Bach. A big thanks goes to Thomas Hilfiker, who has

helped me during the entire experimental campaign on the engine. I enjoyed all the fruitful discussions we had during the long measurement sessions. I am also grateful to Dr. Severin Häggi for setting up the engine control unit, and to PD Dr. Yuri M. Wright for the interesting discussions and for kindly introducing me to many relevant people in the combustion research community. I would also like to give a shout-out to Roland Spüler and to Hugo Ehrensperger for their precious help in setting up the experimental test bench. Finally, a special thanks goes to Norbert Zsiga. Starting a Ph.D. was not one of my goals during my master's degree, but Norbert's great supervision and the nice atmosphere found in this lab during my master's thesis motivated me to take this path.

Over the past four years, I have had the privilege of (co-)supervising many students: Yang Lu, Andreas Hugentobler, Alexander Mah, Larasati Vollenweider, Lapo Carnevali, and Yannick Lätsch. I feel grateful to Prof. Nicolas Noiray for trusting me to supervise these brilliant students: they all made valuable contributions to this project and to my own intellectual development. I would also like to acknowledge the help of three interns from the Swiss Civilian Service: Cornel Dillinger, Sandro Giacomuzzi, and Lukas Meyer.

For their help in recommissioning the RCEM test-rig, I am thankful to Dr. Bruno Schneider, Dr. Walter Vera-Tudela, and Prof. Kai Herrmann from FHNW. Thanks also to Dr. Stephan Caruso for lending me the optical equipment. I also wish to thank a fellow doctoral student, Ms. Anne Beyer for the insightful conversations on jet-guided hydrogen combustion. A big thanks is due to the KIT colleagues, Tobias Michler, Moritz Grüninger, and Olaf Toedler, for their help in calibrating the optical spectroscopy setup. For the useful exchanges about pre-chamber combustion and for providing data for the combustion model validation, I wish to acknowledge Dr. Carlo Beatrice and Dr. Dario Di Maio from STEMS-CNR. I would also like to thank Alexander Lyublinsky from Megaimpulse Ltd, who produced and modified the four-channel pulse generator used in this research project. Alexander and I had very fascinating discussions about measurement techniques and I am convinced that, in more peaceful times, this collaboration could have been even more fruitful.

My research benefited from the results of two projects funded by the

Swiss Federal Office of Energy: the REAL project (Research on alternative combustion concepts for efficient gas engines, contract number SI/501755-01) and the DI Hydrogen Combustion Process (contract number SI/502205-01), which was conducted as part of an international CORNET research project co-funded by FVV e.V. (Frankfurt, Germany, contract number 6014462). I would like to thank both institutions for their generous financial support. My work also benefited from a joint R&D project between Empa and Kistler. I am grateful to Kistler Instrumente AG for financially supporting this joint project and for providing me with their high-end pressure sensors. Within the framework of this collaboration, I am particularly thankful to Dr. David Rogers for sharing with me his unsurpassed knowledge of pressure indication. I would also like to thank Volkswagen AG Konzernforschung for providing the engine hardware.

Finally, I would like to thank my brother Yannick, my uncle Tiziano (who will always be the first “Dr.” in our family), and all my family and friends for their love and support. I am forever grateful to my parents, Aline and Raffaele, for teaching me by example the most important things in life. They are and will always be my role models. My greatest appreciation goes to Chiara Valsangiacomo, the love of my life, for her support, love, and encouragement. In every moment of this journey, she provided me with everything I needed, including relaxing vacations, supportive words, and advice; she even proofread pretty much everything I wrote in this thesis (except for these few sentences). I will always be very grateful for everything you did, and I am looking forward to the next chapters in our life.

Abstract

Robust ignition of hard-to-ignite fuels is essential for future spark ignited internal combustion engines, particularly for introducing efficiency-enhancing diesel-like process parameters like air excess or high amounts of exhaust gas recirculation (EGR). Adopting novel plasma-based ignition systems like Nanaosecond Repetitively Pulsed Discharge (NRPD) is promising in extending the ignition limits and the early flame development speed.

The aim of this thesis is to propose a characterization and modeling of the relevant aspects necessary for the application of NRPD ignition in engines and to investigate the effect of NRPD on ignition and combustion. This thesis is divided into two parts: the first where the fundamental aspects of single Nanosecond Pulse Discharge (NPD) are discussed and analyzed, and the second where the effects of multiple NPD at high repetition frequencies (NRPD) on ignition and combustion are investigated on various setups. Three main research topics are discussed in the fundamental part. First, the electrical characterization of NPD, which includes the modeling of the electrical circuit active during the discharge and the development of a measurement technique for voltage and current measurements. Second, the investigation of the mechanism that leads to an electrical breakdown in sub-mm gas gaps under nanosecond rising voltages, and third, the development of a 0D multiphysics discharge model. The second part incorporates four investigations dealing with plasma-assisted ignition and combustion. The first investigation is performed in a constant volume setup where the plasma to early flame transition under NRPD is analyzed. Two investigations are performed on a Rapid Compression Expansion Machine, one dealing with an ignition detection technique and another investigating hydrogen jet-guided combustion. The fourth investigation is on a 4-cylinder full metal engine setup, where NRPD ignition is investigated both in terms of efficiency and emission.

Nanosecond pulses similar to high-frequency signals are transmitted

from the pulse generator at high repetition frequencies (≥ 10 kHz) to the load (a spark plug) through a high-frequency transmission line. The electrical characterization is crucial for the characterization of NRPD ignition. The voltage and current during the nanosecond discharges are measured using a shunt measurement in the middle of the coaxial cable that connects the pulse generator to the spark plug. The used pulse generators deliver between 8 and 80 mJ in dependence on the pulse generator's specific pulse duration and on the variable amplitude. Ideally, the pulse energy could be completely absorbed by the load in the case of ideal impedance matching between the coaxial cable and the load. In reality, the load impedance varies from high to low values during the discharge, resulting in partial reflection of the pulse energy. When energies in the order of some mJ are delivered to the load, a breakdown followed by the establishment of a well-developed spark channel is always formed, which is recognizable from the high currents at low voltages measured. The ratio of pulse energy to delivered energy is an important optimization factor that is affected by the electrode geometry, the stray capacitance and inductance of the load, the pulse shape, and the initial conditions of the gas.

The breakdown of the gas gaps is of great importance for NRPD ignition; in fact, the breakdown voltage and time affect the energy deposited during the discharge. Under pulsed conditions, the breakdown voltage is always higher than the static breakdown voltage (DC). The breakdown voltage depends on the static breakdown voltage value and the voltage rise rate. The delay between the static breakdown voltage and the breakdown voltage decreases with increasing overvoltage. This delay is composed of a formative and a statistical time lag; interestingly, both the formative and statistical times decrease with overvoltage, contrary to the established expectation that the statistical time would remain somehow constant. The breakdown voltage is therefore investigated in a well-defined geometry offering a quasi-uniform electric field where evidence of a field-assisted emission of seed electrons with a pressure-dependent offset is detected, explaining the statistical time-lag reduction with overvoltages.

To understand the electrical measurements, a 0D multiphysics model that incorporates the high-frequency transmission line, a lumped circuit of the load, a two-temperature model for the electrons and the heavy particles, and an ionization scheme is introduced. The compar-

ison of the experimental results with the simulations shows that the plasma electrical resistance rapidly drops after the breakdown. The resistance decrease is present due to the formation (within a few ns) of a micrometric-sized fully ionized spark in thermal equilibrium with temperatures above $\sim 30\,000$ K. Optical emission spectroscopy measurements support this conclusion.

Plasma to early flame kernel transition under NRPD is investigated and compared against a state-of-the-art inductive ignition system using Schlieren imaging in the pre-chamber of an optical constant volume setup. The evolution of the flame position shows two different phases. The first one is where the expansion is not affected by the initial conditions (Air to fuel ratio (AFR), turbulence level), which lasts approximately 1,5 ms. In this first phase, the expansion rate with NRPD is much higher. The second phase is the region where the AFR and turbulence impact the propagation speed. In this region, the influence of NRPD ignition and increased number of pulses is only apparent when the flame speed is low (low AFR and low turbulence) and has the positive effect of increasing the flame velocity.

Today's high efficiency internal combustion engines are developed in an increasingly narrower range between stable operation, misfire, and knocking. A method for detecting successful ignition under NRPD discharges is therefore investigated. After a nanosecond discharge, the heat loss from the particles (plasma-gas) between the electrodes and the surrounding gas is different if a robust flame kernel is established or not. If a flame kernel is present, the heat losses are lower, resulting in a lower local density of the gas between the electrodes. The breakdown voltage value of a nanosecond pulse depends on the local density. A control pulse is applied after the main ignition sequence to detect successful ignition. The results show that lower breakdown voltages of the control pulse are indeed present if a robust early flame kernel has developed. The control pulse is applied before the pressure rises due to the presence of fast combustion, allowing ignition to be detected during the inflammation phase, thus allowing the possibility to react, if necessary.

Combustion researchers, facing increasingly stringent regulations on efficiency and emissions along with the introduction of novel renewable fuels, are investigating a multitude of innovative combustion concepts. Two of these concepts, where NRPD ignition could be beneficial, are

analyzed and summarized in the following paragraphs.

Hydrogen combustion in engines usually relies on the Otto cycle. This usually results in poor power density and non-ideal efficiencies due to the lean premixed operation and low compression ratio required to avoid preignition and knocking. Alternatively, hydrogen can be directly injected at high pressures into the combustion chamber, and spark ignited at the periphery of the jet, with fuel conversion taking place in jet-guided mode while injection remains active. The high-pressure jet carries significant momentum and exhibits high velocities. Considerable turbulence is produced in the shear layer. Using NRPD ignition, the delay between the spark and ignition is shorter, and the completeness of combustion is higher, highlighting the positive impact of a fast ignition when high turbulence is present. NRPD ignition also results in a lower scatter of the initial combustion phase (premixed phase) that is expected to be the main driver of cycle-to-cycle variations for this combustion concept.

Lastly, the combination of NRPD ignition and Turbulent Jet Ignition (TJI) is investigated using a full engine setup. The aim is to use a technology for a robust early flame phase (NRPD) in combination with a technology for a fast combustion of the bulk charge (TJI). The engine can be fitted with a classical open chamber spark plug or with pre-chambers. NRPD ignition is compared against an inductive discharge ignition system. Despite the faster inflammation present with NRPD ignition, similar peak efficiencies, and emissions are reached in open chamber configuration using the inductive discharge and NRPD ignition systems, which are achieved by varying AFR and EGR rates. Above dilution levels for peak efficiency, the efficiency using NRPD ignition decreases at a slower pace and tolerates higher AFR and EGR rates, thanks to a more complete and shorter combustion. For the pre-chamber experiments using NRPD ignition, an efficiency increase and a reduction of emissions compared to inductive discharge ignition are present. The efficiency increases are present due to a stronger pre-chamber discharge and thanks to a faster end phase of combustion.

Overall, this thesis has outlined that NRPD generates a series of powerful sparks where the plasma is in thermal equilibrium, rapidly expanding to establish a fast and reproducible early flame kernel. This capability allows engines to run at much higher dilutions without misfires. NRPD is particularly interesting for new combustion concepts where a power-

ful ignition source is beneficial, such as in pre-chambers or for jet-guided combustion.

NRPD ignition is still in the early phase of development, and many optimizations remain possible; two of those are developing a tailored igniter for NRPD ignition and a detailed investigation into the effect of pulse duration on ignition and combustion.

Kurzfassung

Eine zuverlässige Zündung schwer entflammbarer Kraftstoffe ist für künftige Ottomotoren von grosser Bedeutung, insbesondere für die Umsetzung von effizienzsteigernden Diesel-ähnlichen Verfahrensparametern wie Luftüberschuss oder hohen Mengen an Abgasrückführung (AGR). Die Anwendung innovativer, plasmabasierter Zündsysteme wie Nanosecond Repetitively Pulsed Discharge (NRPD) ist eine vielversprechende Möglichkeit, die Zündgrenzen zu erweitern und die Geschwindigkeit der frühen Flammenentwicklung zu vergrössern.

Ziel dieser Arbeit ist, die relevanten Aspekte für die Anwendung von NRPD-Zündungen in Motoren zu modellieren und zu charakterisieren sowie die Effekte von NRPD auf Zündung und Verbrennung zu untersuchen. Die Arbeit ist in zwei Teile geteilt: Im ersten Teil werden die grundlegenden Aspekte einer einzelnen Nanosekunden-Pulsentladung (Nanosecond Pulse Discharge - NPD) diskutiert und analysiert und im zweiten Teil werden, an verschiedenen Versuchsträgern, die Auswirkungen von Mehrfach-NPD bei hohen Wiederhol frequenzen (Nanosecond Repetitive Pulsed Discharge - NRPD) auf Zündung und Verbrennung untersucht. Im ersten Teil werden drei Hauptforschungsthemen behandelt. Erstens die elektrische Charakterisierung von NPD, welche die Modellierung des während der Entladung aktiven elektrischen Stromkreises sowie die Entwicklung einer Technik für die Messung von Spannung und Strom umfasst. Zweitens die Untersuchung des Mechanismus, welcher zu einem elektrischen Durchschlag in Sub-mm-Gasspalten während im Nanosekundenbereich steil ansteigenden Spannungen führt und drittens die Entwicklung eines 0D-Multiphysik-Entladungsmodells, welches das NPD Plasma beschreibt. Der zweite Teil besteht aus vier Untersuchungen. Die erste Untersuchung wird in einem Versuchsträger mit konstantem Volumen durchgeführt, wo der Übergang vom Plasma zur frühen Flammenkern unter NRPD analysiert wird. Zwei Untersuchungen werden an einem optisch zugänglichen Einhubtriebwerk durchgeführt. Eine davon befasst sich mit einem Ansatz zur Erkennung der erfolgreichen

Zündung, die andere befasst sich mit strahlgeführter Wasserstoffverbrennung. Die vierte Untersuchung findet an einem mit NRPD Zündung ausgestatteten 4-Zylinder-Motor statt.

In den untersuchten Aufbauten werden Nanosekundenpulse, welche sich wie Hochfrequenzsignale verhalten, vom Pulsgenerator mit hohen Wiederholfrequenzen (≥ 10 kHz) über eine Hochfrequenz Übertragungsleitung an die Last, eine Zündkerze, übertragen. Die elektrische Charakterisierung ist für das detaillierte Verständnis der NRPD Zündung sehr wichtig. Die Spannung und der Strom während der Nanosekunden-Entladungen werden mit einer Shunt-Messung in der Mitte des Koaxialkabels, welches den Nanosekunden-Pulsgenerator mit der Zündkerze verbindet, gemessen. Die verwendeten Pulsgeneratoren liefern zwischen 8 und 80 mJ Energie pro Puls in Abhängigkeit von der spezifischen Pulsdauer sowie der Amplitude. Im Idealfall könnte die Pulsenergie bei gleicher Impedanz von Koaxialkabel und Last vollständig von der Last absorbiert werden. In der Realität hingegen schwankt die Lastimpedanz während der Entladung von sehr hohen zu niedrigen Werten, was zu einer teilweisen Reflexion der Impulsenergie an der Last führt. Wenn Energien in der Größenordnung von einigen mJ an die Last abgegeben werden, kommt es immer zu einem Durchschlag, gefolgt von der Entstehung eines gut entwickelten Funkenkanals, was an den hohen gemessenen Strömen bei niedrigen Spannungen zu erkennen ist. Das Verhältnis von Pulsenergie zu abgegebener Energie ist ein wichtiger Optimierungsparameter, welcher von der Elektrodengeometrie, der Streukapazität und Streuinduktivität der Last, der Pulsform sowie von den Anfangsbedingungen des Gases beeinflusst wird.

Unter gepulsten Spannungen ist die Durchbruchspannung immer höher als die statische Durchbruchspannung. Die effektive Durchbruchspannung hängt vom Wert der statischen Durchbruchspannung und von der Spannungsanstiegsrate ab. Die Zeitspanne zwischen der statischen Durchbruchspannung und der effektiven Durchbruchspannung nimmt mit zunehmender Überspannung ab. Diese Zeitspanne setzt sich aus einer formativen und einer statistischen Zeit zusammen; interessanterweise nehmen sowohl die formative als auch die statistische Zeit mit der Überspannung ab, entgegen der üblichen Erwartung, dass die statistische Zeit etwa konstant bleiben würde. Die Durchbruchspannung wird daher in einer kanonischen (wohldefinierten) Geometrie untersucht, welche ein quasi-gleichförmiges elektrisches Feld erzeugt. Dabei

werden Hinweise für eine feldunterstützte Emission von Startelektronen mit einem druckabhängigen Offset gefunden, was die Reduzierung der statistischen Zeit bei steigender Überspannung erklärt.

Der Durchbruch im Gasspalt ist für die NRPD Zündung von grosser Bedeutung, denn Durchbruchspannung und -zeit beeinflussen die während der Entladung deponierte Energie. Um die elektrischen Messungen korrekt zu interpretieren, wird ein 0D-Multiphysikmodell vorgeschlagen, welches die Hochfrequenzleitung, einen kompakten Stromkreis zur Repräsentation der Last, ein Zwei-Temperatur-Modell für die Elektronen und die schweren Partikel im Gasspalt sowie ein Ionisierungsschema umfasst. Der Vergleich der experimentellen Ergebnisse mit den Simulationen zeigt, dass der elektrische Widerstand des Plasmas nach dem Durchbruch schnell abfällt, weil sich (innerhalb weniger ns) ein mikrometergrosser, vollständig ionisierter Funke im thermischen Gleichgewicht mit Temperaturen über $\sim 30'000$ K bildet. Optischen Emissionsspektroskopie-Messungen bestätigen diese Ergebnisse.

Der Übergang vom Plasma zum frühen Flammenkern unter NRPD wird untersucht und mit einem induktiven Zündsystem unter Verwendung von Schlierenbildern eines optisch zugänglichen Konstantvolumenaufbaus mit Vorkammer verglichen. Die Flamfrontentwicklung zeigt zwei verschiedene Phasen. Die erste Phase, in welcher die Expansion nicht von den Anfangsbedingungen (Luft-Kraftstoff-Verhältnis, Turbulenzniveau) beeinflusst wird, dauert etwa 1,5 ms. In dieser ersten Phase ist die Expansionsrate mit NRPD viel höher als mit dem induktiven System. Die zweite Phase ist der Bereich, in dem das Luft-Kraftstoff-Verhältnis und die Turbulenz die Flammengeschwindigkeit beeinflussen. In diesem Bereich ist der Einfluss der NRPD-Zündung und der erhöhten Anzahl von Pulsen nur bei niedriger Flammengeschwindigkeit (mageres Gemisch und niedrige Turbulenz) erkennbar und hat den positiven Effekt, dass die Flammengeschwindigkeit erhöht wird.

Die heutigen hocheffizienten Verbrennungsmotoren werden in einem immer engeren Bereich zwischen stabilem Betrieb, Aussetzern und Klopfen entwickelt. Mit der Adaption effizienterer Verbrennungsprozesse wird die Grenze einer robusten Zündung erreicht. Daher wird eine Methode zur Detektion einer erfolgreichen Zündung untersucht. Nach einer Nanosekundenentladung ist der Wärmeverlust der Partikel (Plasma-Gas) zwischen den Elektroden und dem umgebenden Gas unterschiedlich, je

nachdem ob sich ein robuster Flammenkern gebildet hat oder nicht. Wenn ein Flammenkern vorhanden ist, sind die Wärmeverluste geringer, was zu einer geringeren lokalen Dichte des Gases zwischen den Elektroden führt. Der Wert der Durchbruchspannung hängt von der lokalen Dichte ab. Der Ansatz ist, nach der Hauptzündsequenz einen Kontrollpuls zu erzeugen welcher ermöglicht, die erfolgreiche Zündung zu erkennen. Die Ergebnisse bestätigen, dass niedrigere Durchbruchsspannungen des Kontrollpulses tatsächlich detektierbar sind, wenn sich ein robuster Flammenkern entwickelt hat. Der Kontrollpuls wird angelegt, bevor der Druck aufgrund einer schnellen Verbrennung ansteigt, so dass ein Verbrennungsaussetzer während der Entzündungsphase erkannt werden kann und somit die Möglichkeit besteht, gegebenenfalls im gleichen Verbrennungszyklus mit weiteren Zündpulsen zu reagieren.

Verbrennungsforscher, die mit immer strengeren Effizienz- und Emissionsvorschriften sowie der Einführung neuartiger erneuerbarer Brennstoffe rechnen müssen, untersuchen eine Vielzahl von innovativen Verbrennungskonzepten. Zwei dieser Konzepte, bei denen die NRPD Zündung von Vorteil sein könnte, werden in den folgenden Abschnitten analysiert und zusammengefasst.

Die Verbrennung von Wasserstoff in Motoren läuft normalerweise nach dem Otto-Zyklus ab. Dies führt in der Regel zu einer schlechten Leistungsdichte und einem vergleichsweise tiefen Wirkungsgrad, da ein magerer Vormischbetrieb und ein niedriges Verdichtungsverhältnis nötig sind um Vorzündungen und Klopfen zu vermeiden. Alternativ kann Wasserstoff mit hohem Druck direkt in den Brennraum eingespritzt und am Rande des Strahls gezündet werden, wobei die Kraftstoffverbrennung im strahlgeführten Modus erfolgt, während die Einspritzung aktiv bleibt. Damit besteht die Möglichkeit, Wasserstoff mit dieselähnlichem hohen Wirkungsgrad umzusetzen. Ein Hochdruckstrahl induziert hohe Geschwindigkeitsgradienten, welche zu starken Turbulenzen führt. Die Ergebnisse am Einhubtriebwerk zeigen, dass mit NRPD-Zündung die Verzögerung zwischen dem Funken und der Zündung kürzer und die Vollständigkeit der Verbrennung höher ist als mit konventioneller Zündung, was die positiven Auswirkungen einer NRPD Zündung bei Brennverfahren mit hohem Turbulenzniveau zum Zündzeitpunkt demonstriert. Die NRPD-Zündung führt auch zu einer geringeren zyklischen Variation während der anfänglichen Verbrennungsphase (Vormischphase), die bei diesem Verbrennungskonzept der Hauptfaktor für

die Schwankungen von Zyklus zu Zyklus sein dürfte.

Schliesslich wird die Kombination von NRPD-Zündung und Vorkammerzündung an einem Vollmotor untersucht. Ziel ist es, die Technologien für eine robuste frühe Flammenphase (NRPD) mit einer Technologie für eine schnelle Verbrennung im Hauptbrennraum (Vorkammerzündung) zu kombinieren. Der Versuchsträger kann mit einer klassischen Zündkerze im Brennraum oder mit auswechselbaren Vorkammern ausgestattet werden. Die NRPD-Zündung wird mit einem induktiven Zündsystem verglichen. Trotz der schnelleren Entzündung bei der NRPD-Zündung werden in der offenen Brennkammer mit dem induktiven Zündsystem und dem NRPD-Zündsystem ähnliche Spitzenwirkungsgrade und Emissionen erreicht, die durch Variation der Luft-Kraftstoff Gemisch und AGR-Raten erzielt werden. Oberhalb der Verdünnungswerte für den Spitzenwirkungsgrad nimmt der Wirkungsgrad mit NRPD-Zündung langsamer ab die NRPD Zündung im offenen Brennraum ist toleranter bezüglich magerer Gemische und höherer AGR-Raten, was sich in vollständigeren und kürzeren Verbrennungen manifestiert. Bei den Vorkammer-Experimenten mit NRPD-Zündung gibt es eine Effizienzsteigerung und eine Verringerung der Emissionen im Vergleich zur induktiven Entladungszündung. Die Effizienzsteigerungen sind auf eine intensivere Vorkammerzündung und auf eine schnellere Endphase der Verbrennung zurückzuführen.

Diese Arbeit hat gezeigt, dass NRPD eine Serie starker Funken erzeugt, bei welchen sich das Plasma im thermischen Gleichgewicht befindet und sich schnell ausdehnt, um einen schnellen und reproduzierbaren frühen Flammenkern zu bilden. Diese Fähigkeit ermöglicht es Motoren bei viel höheren Verdünnungen ohne Aussetzer zu laufen. NRPD ist besonders interessant für neue Verbrennungskonzepte, bei welchen eine leistungsstarke Zündquelle von Vorteil ist, wie z. B. in Vorkammern oder bei strahlgeführter Verbrennung.

Abbreviations

AFRAir to Fuel Ratio
BDCBottom Dead Center
BMEPBrake Mean Effective Pressure
CICompression Ignition
COCarbon Monoxide
COCCenter of Combustion
COVCoefficient of Variation
CRCompression Ratio
DIDirect Injection
DSRDDrift Step Recovery Diodes
EGRExhaust Gas Recirculation
EMIElectromagnetic Interference
EOCEnd of Combustion
EOIEnd of Injection
FOSPFiber-Optics equipped Spark Plug
FWHAFull Width Half Area
FWHMFull Width Half Maximum
GDIGasoline Direct Injection
GNDGround

ABBREVIATIONS

HCCIHomogenous Charge Compression Ignition
HPDIHigh Pressure Direct Injection
HRRHeat Release Rate
HVHigh Voltage
ICEInternal Combustion Engine
IMEPIndicated Mean Effective Pressure
MCMain Chamber
MFBMass Fraction Burned
NPDNanosecond Pulsed Discharge
NRPDNanosecond Repetitively Pulsed Discharge
OCOpen Chamber
OESOptical Emission Spectroscopy
OPCOptical Pre-Chamber
OTFOptical Transfer Function
PCPre-Chamber
PFIPort Fuel Injection
PRFPulse Repetition Frequency
RCEMRapid Compression Expansion Machine
SISpark Ignition
SIBSSpark-Induced Breakdown Spectroscopy
SOCStart of Combustion
SOIStart of Injection
TDCTop Dead Center
THCTotal HydroCarbon

TJITurbulent Jet Ignition

UVUltraViolet

Table of Contents

Acknowledgement	iii
Abstract	vii
Kurzfassung	xiii
Abbreviations	xix
1 Introduction	1
1.1 Background and Motivation	1
1.2 Objectives and Contributions	4
1.3 List of own Publications	7
2 Experimental Setups	11
2.1 Spark Plug	11
2.1.1 Spark Plug Electrode Geometry	13
2.1.2 Quasi-Uniform Electric Field Spark Plug	15
2.1.3 Fiber-Optics Equipped Spark Plug (FOSP)	16
2.2 Ignition Cell	16
2.3 Optical Pre-Chamber	18
2.4 Rapid Compression Expansion Machine	21
2.5 4-Cylinder Engine	27
3 Electrical Analysis of Nanosecond Pulsed Discharge	33
3.1 Solid State Pulse Generators	33
3.2 Electrical Measurement Technique	35
3.2.1 Shunt Measurement Principle	35
3.2.2 Current Shunt Measurement	38
3.2.3 Resistive Coupler	39
3.3 Discharge Analysis	41
3.3.1 Single Pulse Discharge	44
3.3.2 Multiple Pulse Discharges	46

3.3.3	Effect of Electrode Geometry	49
3.3.4	Summary and Discussion	53
3.4	Load Impedance	55
4	Breakdown Analysis	59
4.1	Breakdown Mechanism	60
4.2	Breakdown Analysis Using Spark Plugs	65
4.2.1	Static Breakdown Voltage	66
4.2.2	Breakdown Voltage under Nanosecond Pulsed Discharges	68
4.2.3	Summary and Discussion	74
4.3	Analysis of Breakdown in Quasi Uniform Electric Fields	78
4.3.1	Experimental Setup	79
4.3.2	Static Breakdown Voltage	81
4.3.3	Pulsed Breakdown Voltages and Breakdown Times	85
4.3.4	Seed Electron Generation Rate	90
4.3.5	Summary and Discussion	93
5	Discharge Model	99
5.1	Spark-Induced Breakdown Spectroscopy	101
5.1.1	Qualitative Spectra Analysis	103
5.1.2	SIBS for Concentration Measurement	104
5.2	Discharge Modeling	107
5.2.1	Methods	110
5.2.2	Results	115
5.2.3	Summary and Discussion	126
6	Ignition and Combustion	133
6.1	Investigation of Ignition and Combustion in an Optically Accessible Pre-Chamber Setup	135
6.1.1	Plasma to Early Flame Kernel Transition in the Pre-Chamber	138
6.1.2	Turbulent Jet Ignition and Combustion in the Main chamber	148
6.1.3	Summary and Discussion	154
6.2	Ignition Detection	155
6.2.1	Theory Behind the Ignition Detection Technique	157
6.2.2	Experiments in the Ignition Cell	159
6.2.3	Experiments in the Rapid Compression and Expansion Machine	162

6.2.4	Summary and Discussion	176
6.3	Jet-Guided Hydrogen Combustion	180
6.3.1	Experimental Conditions in the Rapid Compression Expansion Machine	184
6.3.2	Evaluation of Injection Conditions and Non-Reacting Tests	184
6.3.3	Jet-Guided Ignition and Combustion	188
6.3.4	Summary and Discussion	207
6.4	Full Engine Experiments	214
6.4.1	Materials and Methods	214
6.4.2	Results	217
6.4.3	Summary and Discussion	244
7	Summary and Outlook	253
7.1	Summary and Conclusions	253
7.2	Outlook	257
A	Appendix A	261
A.1	Pressure Trace Based Thermodynamic Analysis of Pre-Chamber Combustion	261
A.1.1	Thermodynamic Pegging	263
A.1.2	Determining Pre-Chamber Thermodynamic Conditions	264
A.1.3	Computing Combustion Progresses in Pre-Chamber and Main Chamber	268
A.2	Loss Analysis	269
A.2.1	Ideal Engine, Ideal Load	271
A.2.2	Ideal Engine Real Load	272
A.2.3	Ideal Engine Incomplete Combustion	272
A.2.4	Real Combustion	274
A.2.5	Blowby Losses	275
A.2.6	High and Low-Pressure Loop	276
A.2.7	Expansion Losses	277
A.2.8	Wall Heat Losses (the Rest)	278
A.2.9	Friction Losses	278
A.2.10	Exemplary Result	279
B	Appendix B	281
B.1	Optical Emission Spectroscopy	281

TABLE OF CONTENTS

C Appendix C	283
Bibliography	307

1

Introduction

1.1 Background and Motivation

Robustly igniting air-fuel mixtures is a very important requirement in many applications. Examples are Spark Ignition (SI) Internal Combustion Engine (ICE) and starting combustors for heating purposes or in gas turbine systems. Ignition of hard-to-ignite fuels is particularly important for future ICE applications, especially as renewable, stable fuels like methane of biogenic or synthetic origin and ammonia are adopted for energy security purposes or in hard-to-electrify sectors such as marine, heavy-duty, and co-generation. The development of new ignition technologies for ICE becomes crucial as highly diluted, either stoichiometric with high share of Exhaust Gas Recirculation (EGR), or lean-burn combustion technologies are investigated for efficiency increase and CO₂ emission reduction. [1]

Today's mass-produced ignition systems store electrical energy in a coil or, in some rare cases, in a capacitor and deplete the energy over a spark gap in a rather uncontrolled way. To successfully ignite hard-to-ignite mixtures, such ignition systems are developed by increasing the ignition energies, which usually results in longer electrical discharge times. Classical ignition systems for ICE are characterized by their typical current and voltage waveforms during discharge. Three distinct phases constitute the discharge: breakdown, arc, and glow. The breakdown is defined as the first very short (nanoseconds) phase. In this phase, the current rises to reach its maximal value, which is given by the ratio of

the ignition voltage and near-gap impedance. At the same time, the gap voltage drops to low values [2]. The voltage drop rate depends solely on the inductive (approx. 5 nH) and capacitive (5-15 pF) components of the spark plug. The arc is the second phase, which lasts for approximately 1 μ s. In this phase, the energy stored in the High Voltage (HV) cable's capacitance and in the coil capacitance discharges through the spark resistance in series with the HV cable impedance. The final phase is the glow discharge, which lasts several milliseconds, during which time the main energy storage device (inductor or capacitor) dumps energy into the plasma [3].

During the breakdown phase, the energy stored in the parasitic gap capacitance (spark plug) is transferred, with low heat losses, from the electric field gap to the electrons and subsequently to the heavy particles (molecules and ions). The associated rapid rise in gas temperature results in a rapid increase in pressure, resulting in a shockwave. The plasma initially expands at supersonic speed, which cools down the channel. The energy initially carried away by the blast is transferred to the gas molecules within a small sphere (≈ 2 mm) into which the plasma expands anyhow [3]. The breakdown phase ends when the electron supply mechanism changes from photo or field emission (glow) to thermionic emission, i.e., when cathode hot spots are formed, which turns the discharge into an arc [4]. The electrode erosion that diminishes the spark plug lifetime is most significant once a cathode spot, and therefore, an arc is formed [3].

The objective of ignition is to start a self-sustained chemical reaction. During discharge, the energy transfer process is dominated by plasma expansion. Regardless of the plasma interior condition, there will always be a reaction zone on the plasma surface where temperatures below, 8'000 K offer ideal conditions for very intense chemical reactions leading to self-sustained flame propagation. This layer's thickness is of the same order of magnitude as the flame-front thickness, while the spark discharge determines its energy density. The laminar flame propagation speed is inversely proportional to the laminar flame-front thickness, which is proportional to the temperature difference between the burned and unburned mixtures. High energy densities and temperature gradients in the transition between plasma expansion and flame formation are achieved if spark discharge is accomplished in the shortest possible time interval [3]. Ultrafast, highly powerful discharges should,

therefore, lead to a fast and repeatable transition from ignition to the early flame kernel growth to turbulent flame propagation [2].

With Nanosecond Pulsed Discharge (NPD), the energy input is applied mainly during the breakdown phase, where high-temperature gradients should lead to high flame speeds [5]. Very high pulse amplitudes are needed to supply the energy necessary for ignition with a single nanosecond pulse. High amplitudes result in significant Electromagnetic Interference (EMI) and require careful shielding and complex measurement techniques. Similar advantages of efficient activation of atoms and molecules can be obtained using multiple pulses but with moderate voltage amplitudes at a high repetition rate; this ignition strategy is called Nanosecond Repetitively Pulsed Discharge (NRPD) ignition [6]. Such an approach can be followed by using a solid-state nanosecond pulse generator, which can deliver short electrical pulses with adequate energies at voltage levels sufficient for spark breakdown onset. Moreover, such pulse generator technologies can place multiple discharges at high Pulse Repetition Frequency (PRF). Several investigations [6–8] have shown that using short-duration HV pulses at a high repetition frequency leads to favorable ignition and combustion conditions. Nevertheless, the detailed mechanisms of a short-pulsed discharge in the early stage of gas mixture ignition in engine-relevant conditions are still largely unclear.

The relevance of this thesis is twofold. On the one hand, NRPD is investigated on a fundamental level where there is a lack of knowledge on how nanosecond pulsed plasma forms, and how the electrical energy is transferred to the gas to activate chemical reactions. This lack of knowledge is particularly relevant for (above) atmospheric pressures, which are particularly interesting to various engineering applications, for example, for plasma reforming and air cleaning [9–11]. On the other hand, a detailed, application-oriented investigation of NRPD for ignition in ICE is presented for the first time. Its benefits and challenges are outlined that could serve for the application of this technology for more efficient energy conversion.

1.2 Objectives and Contributions

From the above-sketched framework, this thesis aims at understanding modeling and optimizing the plasma forming process, the electrical discharge, and the impact on ignition and combustion of NRPD ignition.

NRPD has been investigated on a fundamental level in various studies [12–14] and has also been successfully applied to ignition and combustion in numerous investigations [15–17]. Both fundamental and applied research present some limitations: fundamental investigations are typically conducted at atmospheric or sub-atmospheric pressures and focus on specific processes or mechanisms (e.g., the nanosecond heating mechanism presented [14]), while applied research on ignition and combustion often deviates from application-oriented conditions [6, 18] or only reports the advantages achievable with NRPD ignition without delving into the mechanism responsible for the advantage [19].

This thesis aims to bridge the gap between the fundamental and applied investigations of NRPD, particularly in the context of ignition in engines. On the fundamental side, a multidisciplinary approach is employed to provide a novel contribution to the existing literature by simultaneously focusing on application-relevant conditions that are not well studied. On the applied side, NRPD ignition and combustion are analyzed using various optical test rigs and a full metal engine setup. This thesis offers the advantage of investigating NRPD ignition on both a fundamental and applied level under similar conditions, aiming to elucidate the responsible mechanisms and the benefits achievable.

This investigation involves different scientific disciplines, such as combustion science, electrical engineering, and plasma physics. The related topics are:

1. Electrical modeling of the load and the HV line under NPD. Measurement techniques for voltage and current characterization during NPD.
2. Investigation and modeling of breakdown initiation in sub-mm gaps under NPD at high pressure levels.
3. Investigation into the plasma formed with NPD at engine relevant conditions.

4. Ignition and combustion investigations using NRPD in classical open chamber and in pre-chamber setups.

Figure 1.1 graphically depicts the four investigated topics; in the figure, the corresponding Chapter in which each topic is discussed is also reported.

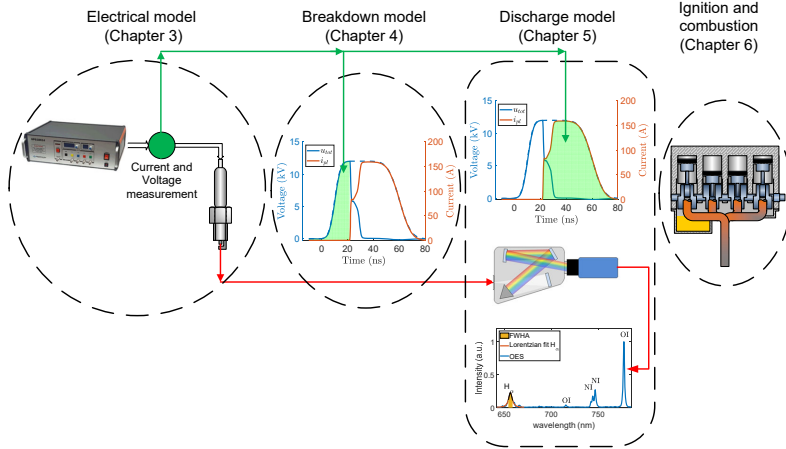


Figure 1.1: Graphical representation of the investigated topics

The thesis structure is presented below, outlining the main objectives, connections between the different chapters, and main scientific contributions.

- ▶ Chapter 2 presents the experimental setups used throughout this thesis.
- ▶ Chapter 3 introduces the method for current voltage and energy measurement and the electrical model of the circuit active during NRPD ignition. The qualitative analysis of the voltage and current variation and the impact of the electrode geometries are discussed as well. The main contributions of this chapter are the development and detailed description of a method for voltage and current measurement based on the shunt measurement principle and the proposal of an equivalent circuit to describe the load im-

pedance.

- ▶ Chapter 4 explains the mechanism leading to an electrical breakdown in "sub"-mm gas gaps under nanosecond rising voltages. The main contribution is the description of the effect of the pulse rise rate and pulse duration on the breakdown under engine-relevant conditions; in spite of these effects being known, they were not studied for sub-mm gaps and high pressures, where breakdown times and voltages are impacted by those conditions. Furthermore, this chapter highlights the important role of seed electron provision for a breakdown under nanosecond transient voltages and shows the evidence for a field-assisted emission of seed electrons from the metallic cathode surface. A parametrization of this emission is proposed and represents a novel contribution that can be used to estimate the breakdown onset under fast voltage transients.
- ▶ Chapter 5 present a 0D model for NPD. The Optical Emission Spectroscopy (OES) analysis of the plasma produced is also described. The main contribution of this chapter is the development of a multiphysics discharge model that effectively describes the discharge under NPD. The comparison of the simulation results with the experimental data shows that the plasma electrical resistance rapidly drops to low values within approximately 1-2 ns after the breakdown. The drop is explained by the formation of a fully ionized micrometer-sized thermal spark. Both the modeling approach and the rapid formation of a thermal spark are novel contributions.
- ▶ Chapter 6 presents the investigations about ignition and combustion under NRPD in different setups, from constant volume test rigs to a full metal engine. The main contributions are threefold: firstly, the analysis of the plasma to early flame transition under NRPD where the evolution of the flame position using NRPD shows that right after the discharge, the expansion rate with NRPD is higher when compared to a conventional ignition system, highlighting the capability of NRPD ignition to form a larger initial flame kernel that leads to a more reliably establishment of a self-sustained flame propagation. Second, NRPD ignition results in a faster inflammation also while investigating a novel com-

bustion concept based on spark-ignited jet-guided combustion of hydrogen. Thirdly, the effect of combining Turbulent Jet Ignition (TJI) and NRPD ignition is investigated in a four-cylinder engine for the first time, where improvements both in efficiency and emissions are measured.

Throughout the thesis, the NRPD and NPD abbreviations are used; it is worth clarifying how and when this two similar terms are used.

- ▶ NRPD is used to define a sequence of nanosecond pulses delivered at a constant repetition frequency that is usual several kHz. Due to the high PRF, the initial condition for subsequent pulses varies during the NRPD.
- ▶ NPD is used to describe a single nanosecond pulse that is not contained in a series of pulses at high PRF. If the plural is used (NPDs), the meaning is that more experiments or simulations with single pulses are performed with known initial conditions.

1.3 List of own Publications

Most of the material presented in this thesis has already been published or is currently under review for publication. This includes figures, equations, and text passages. The publications and the respective authors' contributions are:

1. [20]: M. Balmelli, R. Farber, L. Merotto, P. Soltic, D. Bleiner, C. M. Franck, and J. Biela, "Experimental Analysis of Breakdown With Nanosecond Pulses for Spark-Ignition Engines," *IEEE Access*, vol. 9, pp. 100 050–100 062, 2021.
MB, JB, and RF conceived the project. MB developed the measurement technique, performed the experiments, analyzed the data, and wrote the original draft. All authors discussed the results and the publication structure and proofread the paper.
2. [21]: M. Balmelli, Y. Lu, R. Farber, L. Merotto, P. Soltic, D. Bleiner, J. Biela, and C. M. Franck, "Breakdown of Synthetic Air Under Nanosecond Pulsed Voltages in Quasi-Uniform Electric Fields," *IEEE Access*, vol. 10, pp. 53 454–53 467, 2022.
RF, MB, and CMF conceived the project. YL and MB performed

the experiments. YL, MB, and RF analyzed the data. MB wrote the original draft. All authors discussed the results and the publication structure and proofread the paper.

- [22]: M. Balmelli, L. Merotto, P. Soltic, and J. Biela, “Ignition detection with the breakdown voltage measurement during nanosecond repetitively pulsed discharges,” *Energy Conversion and Management*, vol. 292, p. 117382, Sep. 2023.

MB conceived the project, developed the detection technique, performed the experiments, analyzed the data, and wrote the original draft. MB and LM recommissioned the optical test rig. All authors discussed the results and the publication structure and proofread the paper.

- [23]: M. Balmelli, L. Merotto, Y. Wright, D. Bleiner, J. Biela, and P. Soltic, “Optical and thermodynamic investigation of jet-guided spark ignited hydrogen combustion,” *International Journal of Hydrogen Energy*, vol. 78, pp. 1316–1331, 2024.

PS, LM, and MB conceived and planned the project. LM and MB performed the experiments. MB analyzed and interpreted the data and wrote the manuscript. All authors discussed the results and the publication structure and proofread the paper.

- [24]: M. Balmelli, R. Farber, P. Soltic, D. Bleiner, C. M. Franck, and J. Biela, “Zero-dimensional modeling of a nanosecond pulsed discharge,” In final preparation for submission.

MB, JB, and DB conceived and planned the project. MB developed the model and the validation and wrote the manuscript. RF, CMF, and MB analyzed and interpreted the results. All authors discussed the results and the publication structure and proofread the paper.

- [25]: M. Balmelli, T. Hilfiker, J. Biela, and P. Soltic, “Effects of using Nanosecond Repetitively Pulsed Discharge and Turbulent Jet Ignition on Internal Combustion Engine Performance,” *Energy Conversion and Management*.

PS and MB conceived and planned the project. TH and MB performed all experiments and adapted the experimental setup. MB did the analysis of the experiments and wrote the manuscript. All authors discussed the results and the publication structure and proofread the paper.

7. [26]: M. Balmelli, D. Rogers, T. Hilfiker, Y. Wright, and P. Soltic, “Method for pressure trace based thermodynamic analysis of pre-chamber combustion,” *Energy Conversion and Management*, vol. 312, p. 118561, 2024.

PS, DR, and MB conceived and planned the project. TH and MB performed the experiments. MB developed the analysis technique and wrote the manuscript. All authors discussed the results and the publication structure and proofread the paper.

Furthermore, some of the findings and conclusions which are already published in three further publications are included in this thesis.

8. [27]: L. Merotto, M. Balmelli, W. Vera-Tudela, and P. Soltic, “Comparison of ignition and early flame propagation in methane/air mixtures using nanosecond repetitively pulsed discharge and inductive ignition in a pre-chamber setup under engine relevant conditions,” *Combustion and Flame*, vol. 237, p. 111851, Mar. 2022.

PS, LM, and WVT conceived and planned the project. LM, MB, and WVT analyzed and interpreted the results. WVT controlled and prepared the experimental campaign. LM and MB mostly performed the experiments. LM wrote the manuscript draft. All authors discussed the results and the publication structure and proofread the paper.

9. [28]: W. Vera-Tudela, L. Merotto, M. Balmelli, and P. Soltic, “Experimental study of the ignition of lean methane/air mixtures using inductive and NRPD ignition systems in the pre-chamber and turbulent jet ignition in the main chamber,” *Energy Conversion and Management*, p. 115012, Dec. 2021.

WVT, PS, and LM conceived and planned the project. LM, MB, and WVT analyzed and interpreted the results. WVT controlled and prepared the experimental campaign. LM and MB mostly performed the experiments. WVT wrote the original manuscript’s draft. All authors discussed the results and the publication structure and proofread the paper.

10. [29]: R. Färber, Y. Lu, M. Balmelli, O. Sefl, and C. M. Franck, “Static breakdown threshold modeling of quasi-uniform gas gaps with a focus on the PDIV of contacting enameled wire pairs,” *Journal of Physics D: Applied Physics*, vol. 56, no. 43, p. 435204,

Oct. 2023.

RF conceived and planned the project. RF developed the modeling. RF wrote the manuscript. All authors discussed the results and the publication structure and proofread the paper.

A technical report and a conference contribution constitute part of the used material as well.

11. [30]: R. Färber, Y. Lu, M. Balmelli, O. Seifl, and C. M. Franck, "Dynamic electric breakdown modeling of quasi-uniform, dielectric bounded gas gaps," ETHZ, Tech. Rep., 2024.

RF conceived and planned the project. RF wrote the manuscript. RF, YL, and MB developed the modeling. All authors discussed the results and the publication structure and proofread the paper.

12. [31]: Berlin, 13th September 2022, M. Balmelli, L. Merotto, and P. Soltic, "Plasma to Early Flame Kernel Transition under Nano-second Repetitively Pulsed Discharge in an Optical Accessible Pre-chamber", International Conference on Ignition Systems for Gasoline Engines – International Conference on Knocking in Gasoline Engines. Expert Verlag, 2022

PS and LM conceived and planned the project. MB analyzed the results and wrote the draft. All authors discussed the results and the publication structure and proofread the paper.

For the sake of transparency, the table below (table 1.1) lists which contributions are used in which chapter.

Table 1.1: List of publications

Chapter	Publication
Chapter 3	[20, 22]
Chapter 4	[20, 21, 29]
Chapter 5	[24, 30]
Chapter 6	[23, 25, 27, 28, 31]
Appendix A	[25, 26]

2

Experimental Setups

Four complementary setups are used in this investigation: an optically accessible ignition cell (Section 2.2), an optically accessible Optical Pre-Chamber (OPC) (Section 2.3), an optical accessible Rapid Compression Expansion Machine (RCEM) (Section 2.4), and a full metal 4-cylinder engine mounted on an engine test bench (Section 2.5). The ignition cell is used for investigations dealing with the modeling of the NPD, from the mechanism responsible for the electrical breakdown to the plasma formation and energy deposition. The OPC and RCEM are used to optically and thermodynamically investigate early flame formation and combustion. The overall performance of NRPD ignition is studied in the 4-cylinder full metal engine setup.

Within this chapter, the working principles, design, and instrumentation are described.

2.1 Spark Plug

In SI engines, an air-fuel mixture is ignited using an electrical discharge. For this HV electricity is supplied to a spark plug that generates a spark in the gap between the HV and the ground electrode, providing enough energy to start the self-sustained flame propagation.

Figure 2.1 shows the construction and main components of a typical automotive spark plug (having a similar geometry as the NGK C9E).

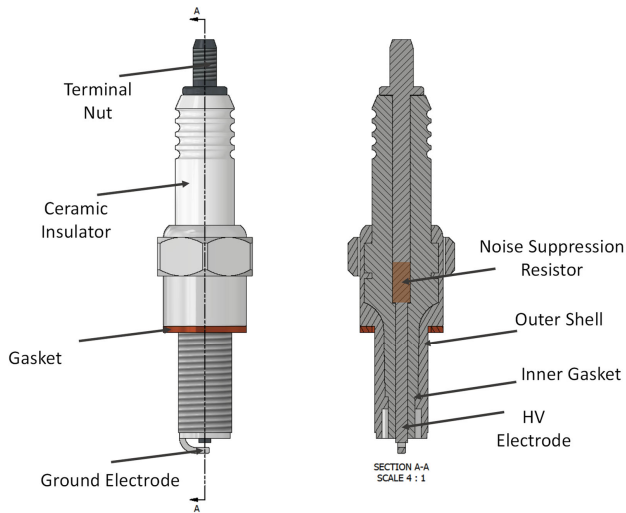


Figure 2.1: spark plug construction and main components

The main components of a spark plug are the center electrode, also called HV electrode, the ground electrode connected to the spark plug's outer shell, and the ceramic insulator that insulates the HV electrode from the spark plug's shell and allows for the discharge to happen between the ground and the HV electrode's tip. The shape of the ceramic insulator's tip also determines how well the tip of the spark plug retains heat and, thus, the spark plug's heat range. Usually, a hotter spark plug is present when a larger free volume (filled with gas) is present between the ceramic and outer shell, diminishing the heat flow from the gas to the outer shell. The noise-suppressing resistor is there to filter out the EMI that rise from the discharge. The noise-suppressing resistor is not necessary and actually unwanted in NRPD ignition systems as it introduces signal reflection.

In the present work, the pulse generator is usually connected to a commercial spark plug via a coaxial cable with an impedance of 75 Ohms. If not otherwise stated, commercial spark plugs (NGK-7471-C8E) are used, modified to have different gap sizes ranging from 0,2 mm to 1 mm

with an accuracy of $^{+0.05}_{-0.00}$ mm. Figure 2.2 (right) depicts the electrode shape. The center electrode is connected to the center core of the coaxial cable, while the ground electrode is connected to the shield of the coaxial cable through the ignition cell (see Figure 2.2 on the left).

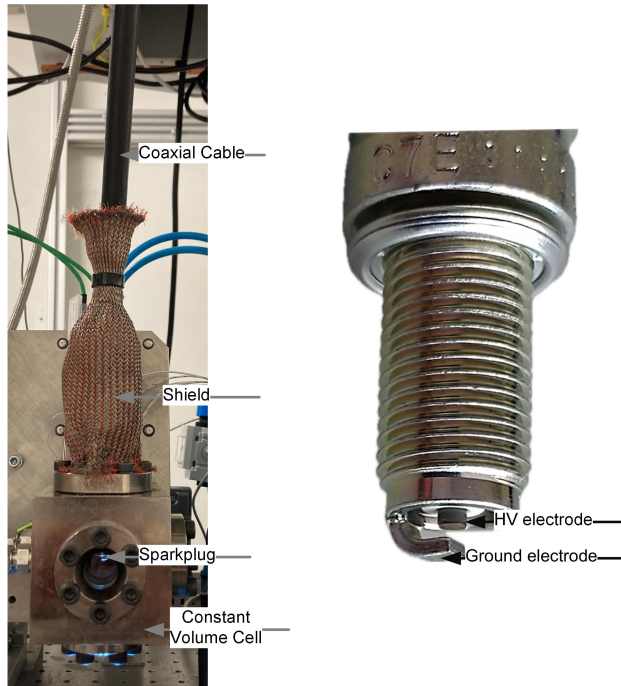


Figure 2.2: Picture of ignition cell (left) and spark plug's electrodes (right)

When a positive polarity pulse is applied to a commercial spark plug, the center electrode is positive (anode), while the ground electrode is negative (cathode). Therefore, the electrons are attracted to the center electrode, and the ions travel toward the ground electrode; the opposite is true when negative pulse polarity is used.

2.1.1 Spark Plug Electrode Geometry

There are many designs of spark plugs, including different geometry electrodes, gap widths, and arrangements. The electrode arrangements

are typically categorized into two main groups: the air gap (standard J-type plug design) and the surface gap (where the discharge occurs on the insulator surface). Hybrid designs are present as well. [32]

Both of these geometries are tested with NRPD. Figure 2.1 shows the construction of a typical air gap (J-type) spark plug while Figure 2.3 shows a rendering of a surface gap spark plug (having a similar geometry as the Champion G54V)

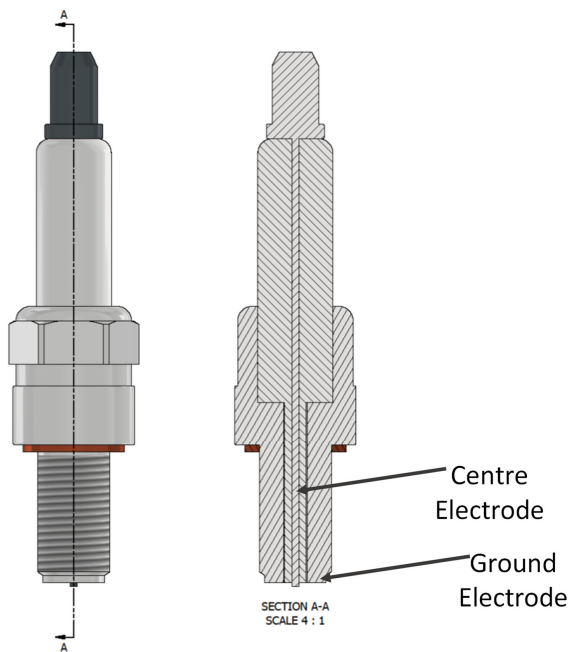


Figure 2.3: Surface gap spark plug construction

For this surface gap spark plug, the ground electrode extends from the outer shell and partially overlaps with the insulator tip, so the discharge occurs along the insulator surface. In contrast, for the J-type spark plug, the ground electrode comes off of the housing and discharges into the center.

2.1.2 Quasi-Uniform Electric Field Spark Plug

For the breakdown investigation in quasi-uniform electric fields (Section 4.3, an automotive spark plug (depicted in Figure 2.4) is modified to obtain a quasi-uniform electric field between the electrodes.

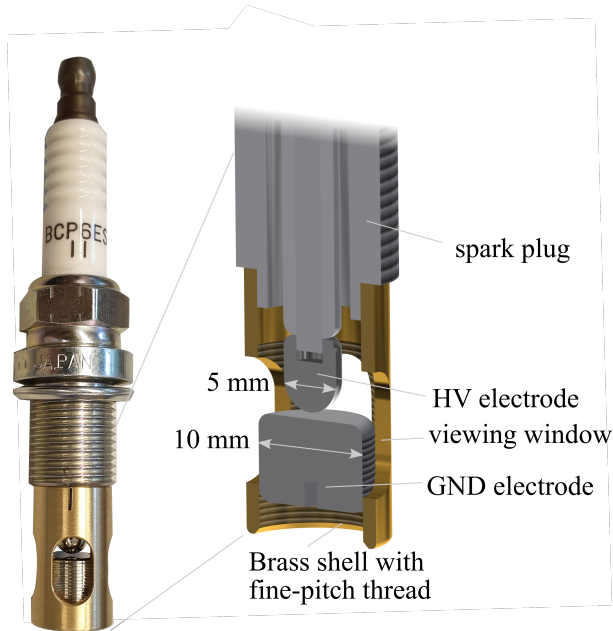


Figure 2.4: Modified spark plug with hemispherical HV electrode and plane-cylindrical GND electrode.

The field efficiency factor [33] decreases with increasing gap size and ranges from 0.98 for the 0,1 mm gap to 0.78 for the 1 mm gap. The cylindrical Ground (GND) electrode is held in place by a brass shell. The HV electrode is a half-sphere with a diameter of 5 mm. The distance between the HV and ground electrodes can be adjusted between 0.1 and 1 mm by means of a fine-pitch thread and precision gauges. From breakdown tests on gaps with the same nominal gap setting, the maximum relative deviation of breakdown voltages due to systematic errors in gap distance is determined to be approximately $\pm 10\%$.

2.1.3 Fiber-Optics Equipped Spark Plug (FOSP)

Kistler Instrumente AG, Winterthur, Switzerland developed a non-resistive Fiber-Optics equipped Spark Plug (FOSP) suited for NRPD ignition and equipped with fiber-optics. This allows for collecting the light emitted by NPD without the need for a lens system. Figure 2.5 shows the schematics used to perform OES in the ignition cell.

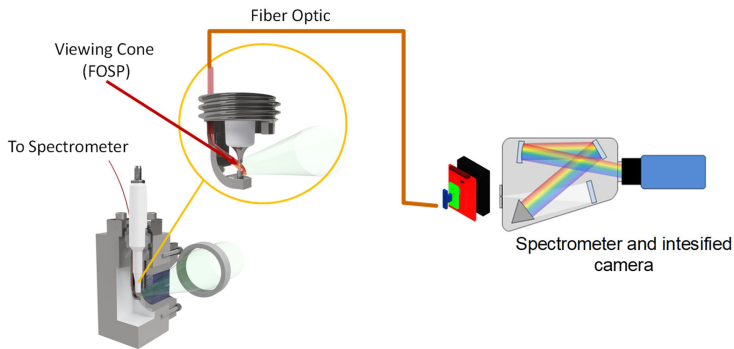


Figure 2.5: Schematics of the spectral acquisition setup using the Fiber-optics equipped spark plug

The spark plug has a 0,4 mm gap size and allocates two fiber optics. Sapphire lenses of 0,7 mm cover the 440 μm diameter fibers and collect the light emitted in the ignition area.

2.2 Ignition Cell

The ignition cell is a 20 cm³ constant volume cell, designed and built at Empa to study ignition phenomena. Its volume represents a situation of an engine cylinder close to Top Dead Center (TDC), where typically ignition takes place. The ignition cell allows for maximum pressures of 60 bar and precise gas supply via four mass flow controllers (Bronkhorst) dedicated to air, methane, hydrogen, and synthetic EGR. On-line mixing allows for precise control of the desired mixture composition. The ignition cell is equipped with pneumatically actuated in- and outlet

valves. The slow filling procedure of the cell is based on the measured pressure which is done using a high-precision absolute pressure sensor (Keller PAA-33X) while the fast combustion pressure is monitored using a high-end piezoelectric pressure sensor (Kistler 6052C). The signals are acquired via a data acquisition card (National Instruments PXI-5105) or via a 1 GHz oscilloscope (LeCroy Wavesurfer 10). [34]

The light emitted by the NPD is collected via a lens system to a spectrograph (Acton IsoPlane SCT 320) and recorded using an intensified CCD camera (PCO DiCam Pro) to perform OES. A mercury neon lamp is used for wavelength calibration, while a Wolfram lamp is used to characterize the spectral sensitivity of the system and get a relative transfer function of the optical path.

Figure 2.6 shows a scheme of the ignition cell setups, when OES is performed via the lens systems.

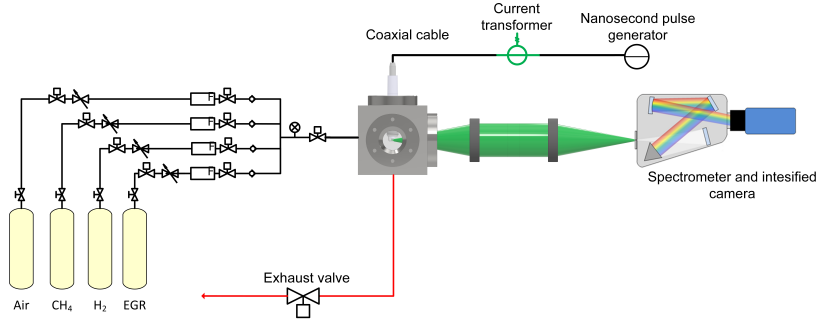


Figure 2.6: Schematic of the ignition cell with the OES setup

Thanks to the possibility of precisely controlling the conditions, the calibration of the OES analysis using the FOSP is performed in the ignition cell. The optical path used is schematically reported in Figure 2.5.

A Berkley Nucleonics 577 delay generator (DEG) with 8 Channels (250 ps Delay and Width Resolution and 50 ps internal channel to channel jitter) ensures precise triggering of the pulse generator and the intensified camera. The DEG sends the triggering signals to the nanosecond pulse generator for sparking and to the camera for image acquisition. The oscilloscope is used to precisely time the delay between spark and

image acquisition. Due to the NPD shortness, even delay in the ns-range needs to be accounted for. The signal propagation time in the BNC cables can, therefore, be significant; for this reason, similar-length cables are used to connect the current monitor and the camera sync-out.

2.3 Optical Pre-Chamber

A constant volume combustion chamber, the OPC, was designed at the LAV lab of ETH to study TJI [35], and is now at the Institute of Thermal and Fluid Engineering of the FHNW. The optically accessible test rig contains two volumes connected through a single interchangeable nozzle. The smaller of the two volumes (the Pre-Chamber (PC)) contains an ignition source, the spark plug, which allows the ignition of the mixture inside the PC. The larger of the volumes (Main Chamber (MC)) is ignited by the turbulent, hot, reactive jet that exits the PC. The orifice connecting the PC to the MC has a cylindrical shape of 2 mm in diameter and 5,2 mm in length. Figure 2.7 shows the OPC setup, the volume of the MC is 187 cm^3 , whereas the PC has a volume of $3,6 \text{ cm}^3$ ($\sim 1.9\%$ of the total volume). The PC is fitted with two opposing windows, which allow optical access through the entire PC volume. The MC also has two opposing windows, allowing optical access from the nozzle exit to the bottom of the chamber.

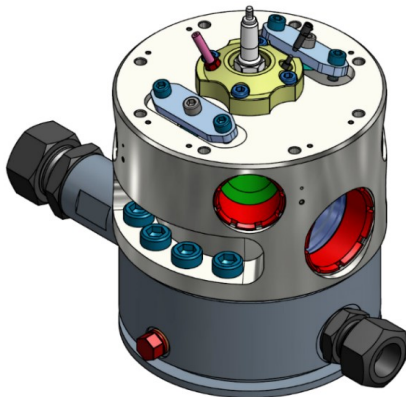


Figure 2.7: Rendering of the OPC

The operation and control sequences of the OPC allow the accurate

setting of conditions in both chambers before ignition (pressure, temperature, Air to Fuel Ratio (AFR) and turbulence). Figure 2.8 shows the graphical sequence of the control sequence.

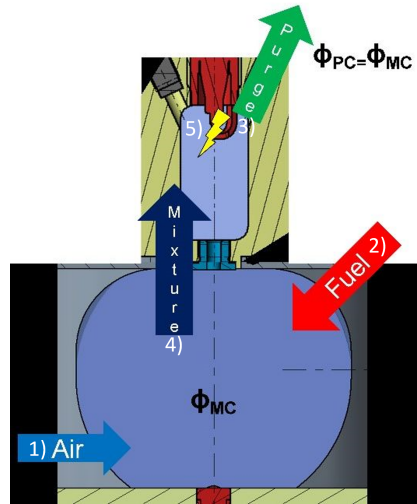


Figure 2.8: OPC, control sequence and operation

First, the fuel is injected into the MC, and the AFR is calculated using the ideal gas law based on the measured pressure and temperature. Then a purge valve is opened to allow the PC air out while allowing the air-fuel mixture from the MC to flow through the nozzle into the PC. The flow through the purge valve creates a dynamic (turbulent) air movement. The dwell time between the closing of the purge valve and the ignition event affects how much turbulence is dissipated. Dwell time variations are used as an indicator of laminar or turbulent conditions in the chamber [27, 28].

In this setup, three simultaneous Schlieren high-speed videos are recorded to monitor ignition and early flame propagation in the PC and TJI in the MC (Figure 2.9).

A single-pass Schlieren arrangement is used in the PC. A Xenon light source is focused on a plano-convex lens ($f = 250$ mm) to generate collimated light beams that enter the combustion chamber. A second

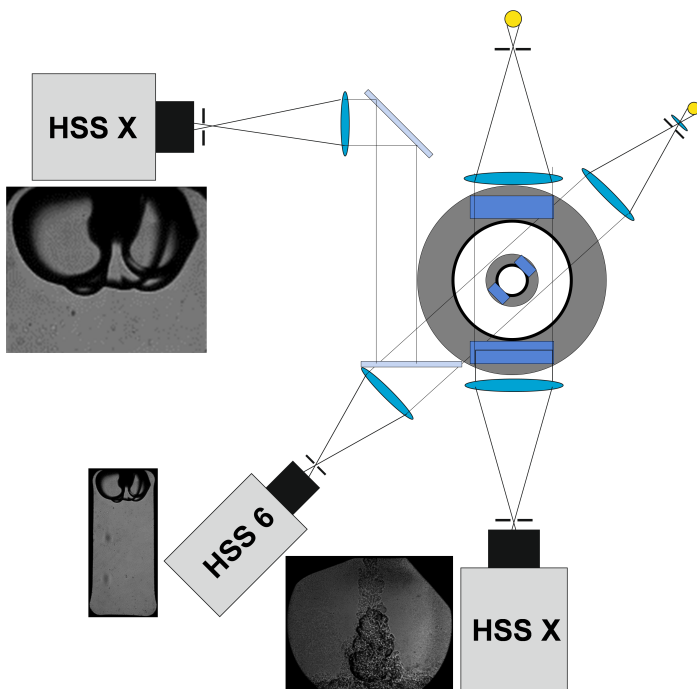


Figure 2.9: simultaneous schlieren setup for PC and MC

plano-convex lens ($f = 250$ mm) refocuses the collimated light. A diaphragm at the focal point filters the light beams that have been diverted from their original parallel direction due to density gradients. The resulting Schlieren high-speed video is recorded using an HSS6 high-speed camera from LaVision with an exposure time of $2 \mu\text{s}$, a resolution of 128×256 px, and recording at 10 kFPS. An additional parallel setup (using a beam splitter) is used to observe the phenomena occurring near the spark plug's electrodes. For this, a second Schlieren setup is implemented in the PC with a resolution of 128×128 px and a frame rate of 100kFPS using an HSSX high-speed camera. This setup uses the same light source with a second identical plano-convex lens ($f = 250$ mm) and an additional diaphragm. A second light source, a diaphragm, and a couple of plano-convex lenses ($f = 250$ mm) are used in the MC. An HSSX high-speed camera from LaVision is used in the MC with an exposure time of $1 \mu\text{s}$ and a resolution of 640×512 px. Figure 2.9

shows a schematic of the setup, near each camera an exemplary frame of the video recorded is present.

2.4 Rapid Compression Expansion Machine

The RCEM is a mass-balanced piston test rig that is used to achieve a single compression expansion stroke while ensuring optical access through the piston as well as through the combustion chamber. Experiments can be performed at varying thermodynamic conditions similar to engine operations. Its advantage is that thermodynamic conditions can be reproduced, such as those in ICE or the second stages of turbine combustors. The RCEM has been successfully used for investigations of hydrogen-air and hydrogen-enriched methane-air mixture combustion [2, 36], PC ignition [37], diesel-pilot ignited methane mixtures [37], and Homogenous Charge Compression Ignition (HCCI) combustion [38]. The working principle and the specification in the current configuration are detailed below. The machine consists of two main sections, the driving and experimental parts, connected by a rod. Figure 2.10 depicts a schematic of the RCEM where the names of the components are shown.

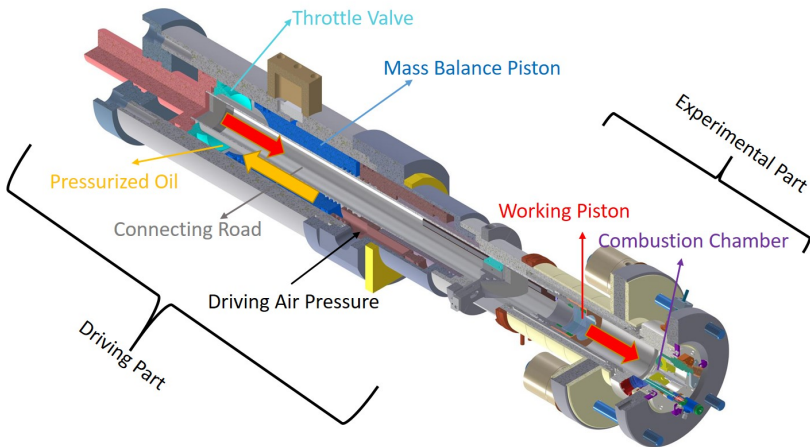


Figure 2.10: Schematic of the RCEM, component names, and working principle.

The red arrows represent the motion of the pistons during fast compression. A mass balance piston that allows for nearly vibration-free operations divides the two parts and moves in the opposite direction of the working piston. After the combustion chamber's scavenging procedure, the experiment starts by pushing the piston to Bottom Dead Center (BDC) and setting the driving air pressure to the desired value. Afterward, the combustion chamber is filled with air to the desired filling pressure. The connecting rod at the BDC is inside a sealed cavity that prevents the pressurized oil from acting on the connecting rod (starting position). The compression stroke begins by opening a valve that connects the pressurized oil to the back of the piston rod and slowly pushes the piston out of the starting position. When the connecting rod exits the throttle valve, the pneumatic force of the air is transmitted to the oil via the mass balance piston that now acts on the full area of the rod. The pressure difference between the driving volume and the combustion chamber now determines the acceleration of the moving parts. The compression increases the pressure inside the combustion chamber, slowing the piston. The combustion (if present) further increases the pressure in the combustion chamber, pushing the piston back. The movement of the piston is determined by the kinetics of the process and not by kinematics, as is the case with conventional reciprocating engines. For this reason, besides the pressure difference between the driving and working parts, the friction of the piston on the cylinder walls and the hydraulic oil viscosity (that transmits the energy between the driving and working part) also affect, to some extent, the piston motion.

The piston position is measured at 100 kHz sampling frequency with an inductive position measurement system having a 0,01 mm resolution. The pressure in the cylinder is measured using two pressure sensors: a piezoelectric Kistler 7061B to measure the transient pressure during combustion and a piezoresistive Kistler 4075A10 mounted in a fast-switching adapter that closes at approx. 5 bar to measure the absolute pressure.

The fuel injector used in the RCEM experiments is a Bosch HDEV1 inward-opening solenoid injector developed for gasoline. The injector has a single hole with a non-axial orifice of 0,60 mm diameter. The cone is estimated to have an inclination of 20° by injecting a colored liquid into atmospheric air and photographing the jet. Gaseous fuels

(CH₄ and H₂) are injected, the feed pressure is regulated with pressure regulators, and the injector's voltage and current profile is controlled with a Skynam DMS06 driver.

Table 2.1 lists the RCEM specifications, and setup used.

Table 2.1: RCEM setup.

Component	Specification
Bore	84 mm
Max. Stroke	120-250 mm
Cylinder head	Flat, two valves
Piston window	$d = 52$ mm, 4 mm depth
Side windows' optical access	$d = 36$ mm
In-cyl pressure measurement 1	Piezoelectric Kistler 7061B ($\pm 0.5\%$, 0–250 bar)
In-cyl pressure measurement 2	Kistler 4075A10 ($\pm 1\%$, 0 – 10 bar), inserted in a fast switching adapter, Kistler 741A
Heating	Cylinder head and liner
Fuel injection system	Skynam DMS06 driver, Bosch HDEV 1 injector
Spark plug	NGK 5096
Ignition system	NRPD, FID 15-10NK Inductive, BERU
High-speed camera	LaVision HS6
Light source (Xenon)	Ankin Xenon Nova 300
Plano-convex lens	PCX 75 \times 250 vis 0 (Diameter \times focal distance mm)

The spark plug is located in the center of the cylinder head axial to the piston, while the injector is placed tangentially 5 mm below the cylinder head. Figure 2.11 shows a rendering of the setup.

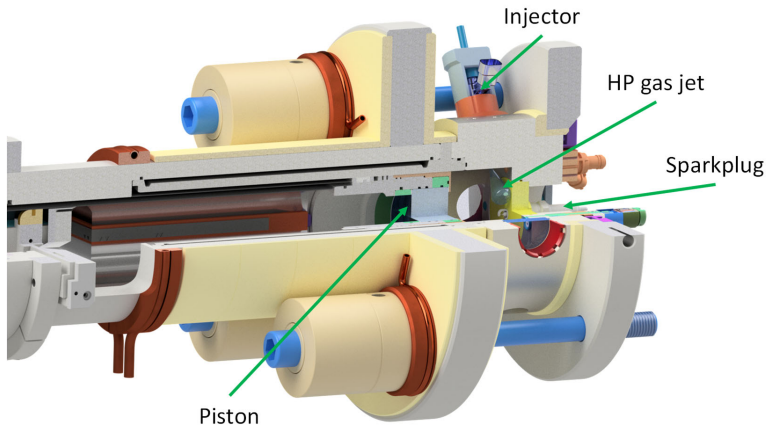


Figure 2.11: RCEM, combustion chamber rendering with HDEV1 injector and spark plug

Combustion Heat Release Rate Analysis

The combustion Heat Release Rate (HRR) inside the RCEM is calculated using a thermodynamic approach that divides the gas into two zones (fresh and burned gas) with equal pressure but different temperatures [32]. This allows for more precise caloric properties estimation assuming the chemical equilibrium of 18 species. The wall heat losses are modeled using Woschni's approach [39], the wall temperatures are calculated using Bargende's approach [40], and the blowby is accounted for using a labyrinth-seal approach [41].

The calculation uses the working piston position and the measured cylinder pressure value. The data from both pressure sensors, the piezoelectric as well as the piezoresistive, are acquired at a 100 kHz sampling rate. The pressure trace is derived from the piezoelectric sensor pegged during the compression stroke using the piezoresistive sensor. The piston position is acquired with a 100 kHz sampling rate, and the sensor has a 0,02 mm resolution with an error below 0.1 %.

Optical Diagnostics: Schlieren Visualization, OH* Chemiluminescence and Spark Induced Breakdown Spectroscopy

The RCEM provides two optical accesses to the combustion chamber: the first, located through the piston, is utilized to capture OH* chemiluminescence during combustion, while the second comprises two windows (side window) aligned tangentially to the piston's motion, used for Schlieren imaging. Schlieren imaging is employed for visualizing changes in density within a transparent medium by detecting variations in refractive index. The setup involves a xenon lamp and a diaphragm to focus light onto a planoconvex lens, generating collimated light. This collimated light is then directed into the combustion chamber through a side window and exits from the opposite side. Subsequently, the collimated light is refocused through another plano-convex lens onto an HSS6 high-speed camera. A diaphragm is positioned at the focal point of the convex lens to eliminate diverging beams and enhance the sensitivity gradients of the setup. The OH* chemiluminescence setup includes a High-Speed La Vision IRO intensifier, coupled with an HSS6 highspeed camera and a Halle 100 mm UV lens. Additionally, it incorporates a 310 nm passband filter with a Full Width Half Maximum (FWHM) of 10 nm. This configuration allows for capturing spontaneously emitted light at the reaction front during the combustion process by detecting the transition of the hydroxyl (OH*) radical back to its ground state. During the ignition process, the FOSP is employed in conjunction with a spectrometer (Acton IsoPlane SCT 320) and an intensified CCD camera (PCO DiCam Pro) to capture the spectral emission during ignition. This method, known as Spark-Induced Breakdown Spectroscopy (SIBS), relies on the analysis of spectral features observed during the breakdown process. It is employed to estimate the local AFR in the proximity of the spark plug during ignition, as outlined in [42]. Figure 2.12 shows a schematic of the optical setup along with a representative post-processed image acquired during an experiment.

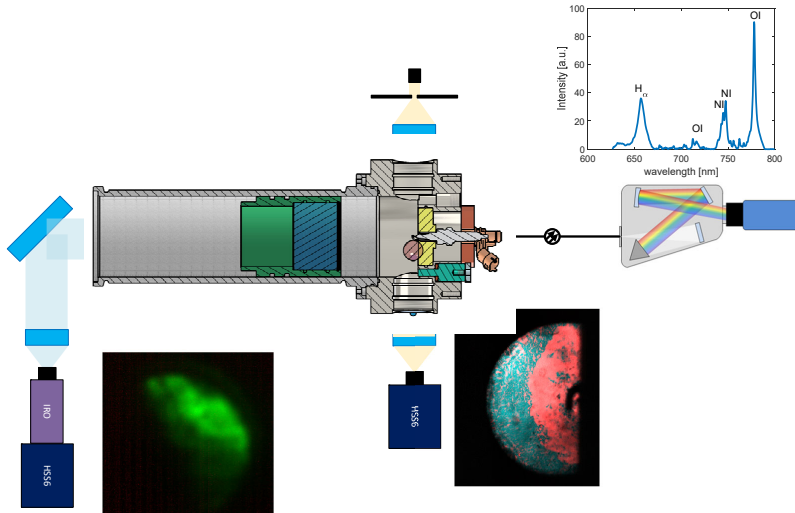


Figure 2.12: Optical setup schematics with representative post-processed images

Figure 2.13 shows the expected visualization during reactive experiments for the OH^* chemiluminescence on the left and for the Schlieren experiments on the right.

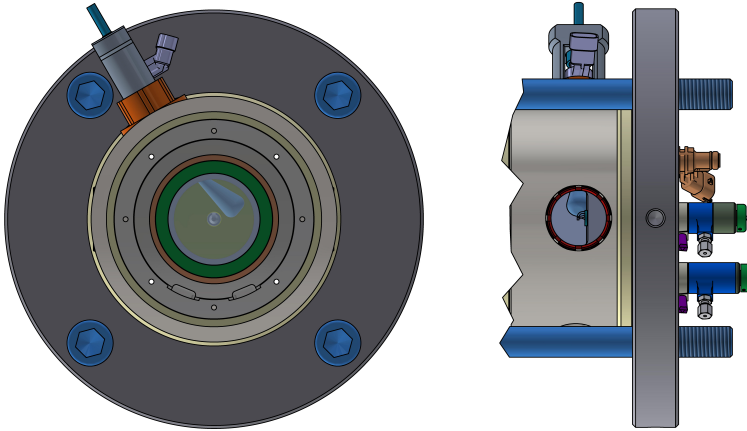


Figure 2.13: Visualization of the views through the piston (left) and from the side (right)

When non-reactive optical experiments are performed, Schlieren high-speed videos are recorded through the piston view, in order to profit from the larger window. In fact, the visualization diameter through the piston is 52 mm while through the side is only 36 mm, with the additional disadvantage that the head occupies 13 mm of the side window. For non-reactive optical experiments, the spark plug and holder (yellow part in Figure 2.12) are removed and substituted with a glass window. By doing so, two parallel windows are present, thus allowing for moving the Schlieren setup to the larger piston view. During the Schlieren imaging for the non-reactive experiments, the expected visualization, in this case, is the one depicted on the left in Figure 2.13.

2.5 4-Cylinder Engine

NRPD ignition is investigated in a light-duty four-cylinder engine based on a serial-production diesel engine (Volkswagen EA288) with a redesigned cylinder head, redesigned air and exhaust paths, a Variable Turbine Geometry (VTG) as well as low-pressure EGR. Pistons with hemispherical bowls are used, and the geometrical Compression Ratio

(CR) is 14.5. The engine operates on natural gas and is mounted on an engine test bench equipped with an automotive certification-grade emission measurement system. The main engine features are reported in [43, 44], the modifications and important parameters are repeated in Table 2.2.

Table 2.2: Main engine characteristics

Characteristic	Specification
Number of cylinders	4
Bore/stroke (mm)	71.0 / 95.5
Displacement (cm ³)	1968
Geometrical CR	14.5
Piston bowl geometry	hemispherical
Port Fuel Injection (PFI)	4 Bosch NGI2
PC fueling	Bosch NGI2 injectors (throttled) via cannula and check valve
PC volume (cm ³)	1.8
PC nozzles:	
number × diameter horizontal	7×1.5 mm
number × diameter vertical	3×1.4 mm
PC fuel flow measurement	Bronkhorst EL-FLOW Select
Total fuel flow measurement	Rheonik RHM015 Coriolis flow meter
Air flow measurement	ABB Sensyflow P
λ measurement	Bosch LSU 4.9 wide band sensor mounted before the turbine
Cylinder pressure sensor	All four cylinders using water-cooled piezoelectric sensors (Kistler 6041C)
PC pressure sensor	Cylinder1 using an M3.5 uncooled piezoelectric Kistler 6081s
Pressure indication system	Kistler KiBox, evaluation at 0.1 °CA
Rapid prototyping ECU	dSPACE Microautobox

A rapid prototyping engine control unit controls the fueling, ignition,

throttle, the variable turbine geometry as well as EGR. The overall AFR equivalence ratio (λ) is feedback controlled acting on the parameters of the port fuel injectors. The Center of Combustion (COC) is cylinder-individually feedback controlled to a value of 8°CA after the TDC, evaluating the apparent HRR. The pressure in all four cylinders is measured using cooled piezoelectric sensors (Kistler 6041C). The pressure in the PC of cylinder one is monitored using an uncooled piezoelectric sensor (Kistler 6081s). Pressure is measured with a 0.1°CA resolution. Detailed thermodynamic evaluations are made by averaging 300 consecutive cycles.

The cylinder head can accommodate removable active PCs. This investigation uses PCs with a $1,8\text{ cm}^3$ volume and 10 holes. This results in a volume ratio between PC and MC at TDC of 5%. PCs with different volumes and numbers of holes (and locations) were tested on the engine in another research project [43]. The used PCs offer the best performance with the hemispherical piston. Figure 2.14 shows on the left a scheme of the combustion chamber with the adapter to mount the spark plug directly in the combustion chamber, we call this the Open Chamber (OC) setup. The scheme with the active PC is reported on the right.

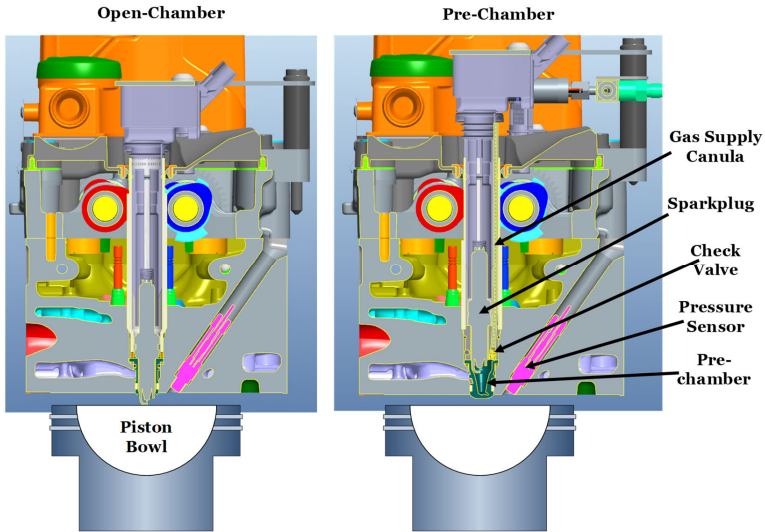


Figure 2.14: Scheme of the combustion chamber layout, Open-chamber (left), PC (right)

Two spark plugs are used with NRPD ignition: a J-gap spark plug (NGK C9E), with a 0,4mm gap size, and a surface discharge spark plug (Champion G54V). NRPD ignition is compared against inductive discharge ignition using a state-of-the-art Borgwarner inductive coil storing up to 60mJ energy in the coil and having a spark duration of 1,5ms. The inductive discharge experiments use a J-gap spark plug with a noise-dampening resistor (NGK CR8E) with a 0,6mm gap size. This spark plug is similar to the NGK C9E, but with a 5kOhm resistor.

Figure 2.15 shows a schematic of the experimental setup.

The experimental setup in Figure 2.15 shows the low-pressure EGR path as well. The exhaust gas is taken after the turbocharger is cooled and fed in the fresh air before the compressor, resulting in good charge mixing and distribution over the cylinders.

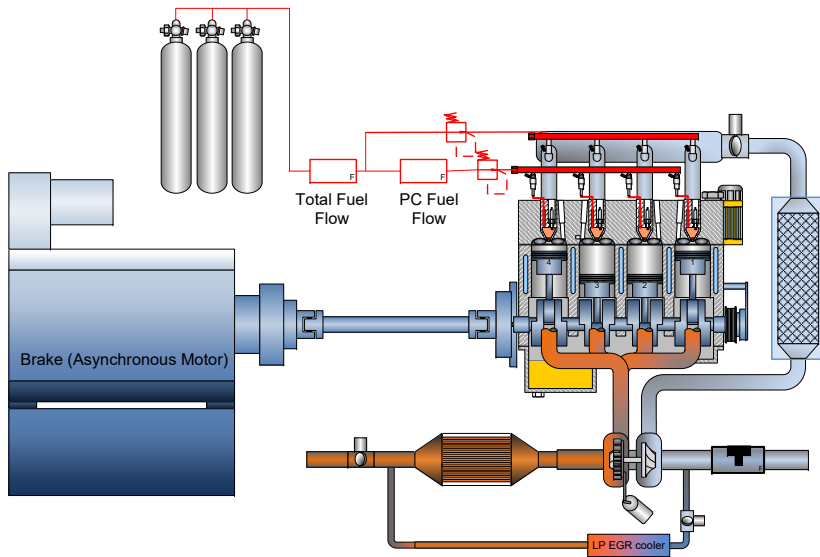


Figure 2.15: Scheme of the experimental setup

3

Electrical Analysis of Nanosecond Pulsed Discharge

Determining the electrical characteristics during discharge is crucial for understanding and analyzing the mechanism responsible for the breakdown, the plasma formation, and the energy deposition during NRPD. In fact, the electrical circuit active during NPD affects the current and voltage to the plasma, and thus the plasma state. Furthermore, due to the voltage and current transients in the order of some nanoseconds, even small parasitic capacitances and inductances of the load can have an important impact on the discharge.

Section 3.1 presents the used pulse generators. Section 3.2 presents the active circuit during the discharge and discusses the technique used to measure voltage and current. Section 3.3 presents the qualitative analysis of the discharge in different conditions, finally section 3.4 presents the equivalent circuit of the load that will be used in 5 for the modeling of the discharge.

3.1 Solid State Pulse Generators

An option to generate ns-long pulses is to use transmission line-based pulse generators where the line length dictates the pulse duration and the switch the minimum possible rise time. Drift Step Recovery Diodes (DSRD) are often used as fast-switches for ns pulse generators because

they allow a current interruption within hundreds of picoseconds with jitter in the order of tens of picoseconds [45, 46].

DSRD is a $p^+p'Nn^+$ silicon diode featuring a deep diffusion $p'N$ that allows to store and rapidly discharge carriers (electrons and holes). During the forward pulse current, the energy is stored in the electron-hole plasma of the $p'N$ layer. During the reverse pulse current, the stored plasma is pulled off from the p' and N layer, and if these fronts collide at the junction, ns-current interruption is achieved. The diode resistance rapidly increases, switching the current to the load connected in parallel [45, 47].

Nanosecond pulses, similar to high-frequency signals, are transmitted from the generator to the load through high-frequency transmission lines, such as coaxial cables to prevent pulse distortion. The three used nanosecond pulse generators have a 75-Ohm output coaxial connector and consequently, HV coaxial cables with a 75-Ohm impedance are used. Table 3.1 lists the pulse generators' main specifications.

	FID FPG 30-100NM	FID FID 15-10NK	Megaimpulse NPG18N14
Pulse generator	A	B	C
Pulse amplitude	13 kV	10 kV	18 kV
HV channels	1	1	4
Pulse polarity	positive	positive	negative
Pulse rise time	6-10 ns	2-3 ns	4 ns
Pulse duration	50 ns	10 ns	10 ns
Pulse energy	80 mJ	8-9 mJ	30 mJ
max PRF	10 kHz	100 kHz	100 kHz

Table 3.1: Specifications of the pulse generators used for NRPD ignition

Since for these pulse generators, the transmission line dictates the pulse duration and the DSRD the switch time, the pulse shape of this device presents a fixed rise and fall time and duration, nevertheless, the capacitor or inductor feeding the DSRD can be charged to different voltages which results in different maximal pulse's amplitudes. The possibility of varying the pulse's maximal amplitude is used for the investigation in Chapter 4. The right subplot in Figure 4.5 reports typical pulses'

shape for different maximal amplitudes.

3.2 Electrical Measurement Technique

When a pulse produced from the pulse generator arrives at the HV cathode, it is reflected and transmitted depending on the ratio between the cable impedance and the load impedance. Equation (3.1) describes the velocity of a pulse (v_p) traveling within a coaxial cable as a function of the relative permittivity (ϵ_r) and the speed of light (c) [48].

$$v_p = \frac{1}{\sqrt{\epsilon_r \epsilon_0 \mu_0}} = c \frac{1}{\sqrt{\epsilon_r}} \quad (3.1)$$

In the investigated setup, the pulse travels one meter in approx. 5 ns, and for cables longer than 10 m, the 50 ns long pulse is completely contained inside the cable; there is no connection between the pulse generator and spark plug. Therefore, it can be assumed that the applied voltage is independent of the pulse generator [49]. This results in an HV transmission line [33] that governs the relation between the voltage and the current over the load. In this configuration, the transmission line wave Equations describe the voltage and current.

The gap voltage (u_g) and total current (i_g) can be reconstructed by measuring the incident (i_i) and reflected (i_r) pulse current, or incident (v_i) and reflected (v_r) pulse voltage and knowing the coaxial cable impedance (Z_0) according to Equation (3.2). Figure 3.1 qualitatively shows u_g and i_g as a function of the i_i and i_r or as a function of v_i and v_r .

$$\begin{aligned} u_g &= v_i + v_r = Z_0(i_i + i_r) \\ i_g &= i_i - i_r = \frac{1}{Z_0}(v_i - v_r) \end{aligned} \quad (3.2)$$

3.2.1 Shunt Measurement Principle

According to basic principles of HF transmission lines [33], the pulse energy can be absorbed by the load completely only in the case of ideal

impedance matching, i.e., if the load impedance is constant in time and equal to the cable impedance. In reality, the gap impedance during electrical breakdown changes from high values before the breakdown (insulating air between the electrodes) to less than one Ohm after it (high conductive plasma). In the investigated setups, part of the pulse energy reflects from the load and travels back to the generator. The shunt measurement is a technique for measuring the incident and reflected pulse waveforms, which allows the calculation of the energy of both pulses and, therefore, determines the discharge's energy efficiency. In addition, evaluating the pulse voltage on the load and pulse current is possible.

The reflection coefficient Γ is calculated according to Equation (3.3) and describes the ratio between incident and reflected voltage waveform as a function of the load impedance (Z_1).

$$\Gamma = \frac{v_r}{v_i} = \frac{Z_1 - Z_0}{Z_1 + Z_0} \quad (3.3)$$

According to equation (3.3), if the load impedance (Z_1) is larger than (Z_0), then Γ is within 0 and 1, and the reflected pulse has the same polarity as the incident one. If the load impedance is lower than (Z_0), then Γ is within -1 and 0, and the reflected pulse has the opposite polarity with respect to the incident pulse. Figure 3.1 qualitatively shows current and voltage over the gap for the high load impedance ($Z_1 > Z_0$) on top and the current and voltage over the gap for the low load impedance ($Z_1 < Z_0$) on the bottom.

Combining Equations (3.2) and (3.3), the voltage and current over the gap can be described solely as a function of v_i , Z_0 and Z_1 according to Equation (3.4).

$$\begin{aligned} v_g &= v_i \frac{2Z_1}{Z_0 + Z_1} \\ i_g &= \frac{v_i}{Z_0} \frac{2Z_0}{Z_0 + Z_1} \end{aligned} \quad (3.4)$$

When Γ is equal to zero, no reflection is present $Z_1 = Z_0$, and the load absorbs the pulse power completely. $\Gamma = 1$ and $\Gamma = -1$ are the two

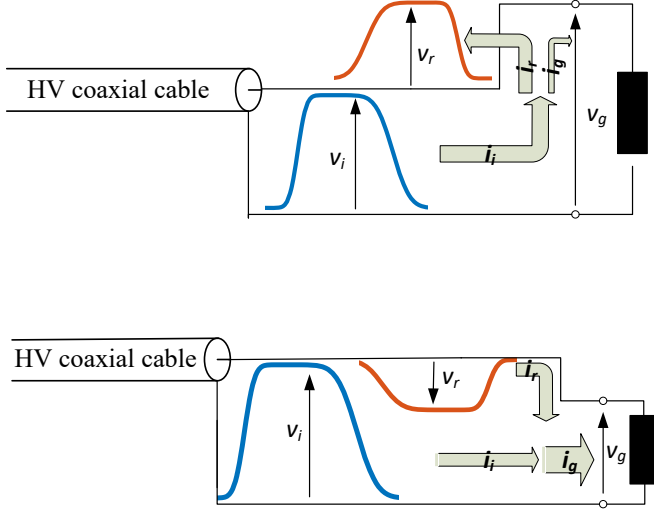


Figure 3.1: Voltage and current at the load high impedance case (top) and low impedance case (bottom)

extreme cases that represent open and short load, and the reflected pulse amplitude is equal to the incident one.

The pulse energy ($E_{i,r}$) can be calculated according to Equation (3.5), and varies with the square of the pulse's amplitude. Where t_0 is the instant right before the fast-rise of the pulse and Δt_p is the total pulse duration.

$$E_{i,r} = \int_{t_0}^{t_0 + \Delta t_p} \frac{v_{i,r}^2(t)}{Z_0} dt \quad (3.5)$$

Due to the fast transients present, even small capacitance and inductance of the load can result in distortion of the reflected pulse, resulting in a difficult accurate shift of the incident and reflected signal. Calculating the energy deposited at the load as a function of current and voltage measurement (3.2) can result in some errors. To mitigate this problem, the energy absorbed by the load (E_1) can be calculated as the difference between the incident and the reflected pulse, and by taking

into account the energy loss (E_{loss}) in the coaxial cable, according to Equation (3.6).

$$E_{\text{load}} = E_i - E_r - E_{\text{loss}} = \int \frac{v_i^2(t)}{Z_0} dt - \int \frac{v_r^2(t)}{Z_0} dt - E_{\text{loss}} \quad (3.6)$$

3.2.2 Current Shunt Measurement

To measure the incident and reflected waveforms of the pulses (generated with the FID pulse generators) without superposition, a 30 m long cable is used. Section 3.2.3 describes the shunt measurement using the Megaimpulse's pulse generator. The shielding is removed from a small section in the middle of the cable. A shielded current monitor (Pearson current monitor model 6585 with a rise time of 1.5 ns) is placed around the exposed cable section to measure the current. Figure 3.2 shows the measurement setup in the ignition cell.

In this way, at the measurement location (C in Figure 3.2), the incident and reflected pulses are divided by 30 m of cable (approx. 150ns). Any further reflection at the pulse generator will also have a similar delay w.r.t. the reflection. The cable shielding is reconstructed around the current monitor. Negligible reflections at the current probe location are detected. Pulses sent at the open circuit result in signal attenuation between the incident and reflected pulses of approximately 2%. To validate the measurement technique, a pulse is sent to a 470 Ohm non inductive resistance. Two measurements are performed: the current measurement in the middle of the cable and a voltage measurement using a HV probe (Tektronix p6015a) placed directly across the resistance. Subplot (a) in Figure 3.3 depicts the current and the equivalent voltage measurement in the middle of the coaxial cable. Since the current monitor returns positive or negative values depending on the current direction, i_r measurements needs to be multiplied by -1. Subplot (b) shows the measured voltage in blue and the reconstructed voltage from the current measurement in red (subplot (a)) according to Equations (3.2).

The gap voltage can be accurately reconstructed with the current measurement. The theoretical propagation delay for the chosen cable length matches the measured delay time (Δt). Due to the difficulty of placing

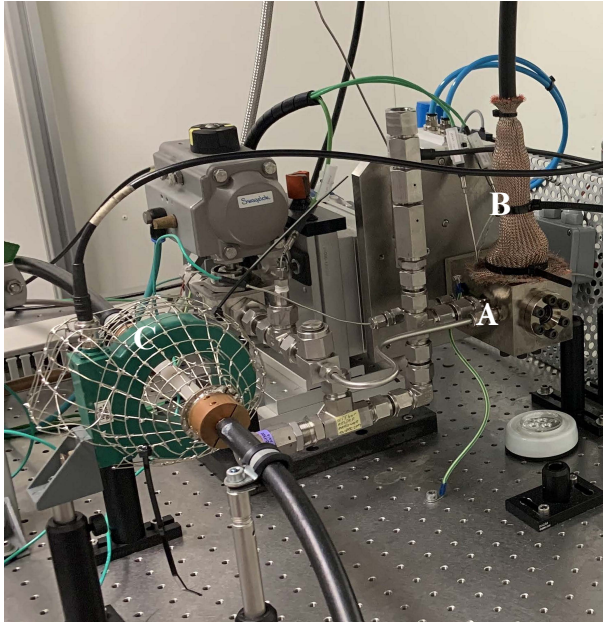


Figure 3.2: Experimental setup: A: constant volume cell, B: coaxial cable shielding, C: current monitor.

the voltage probe in the immediate vicinity of the HV electrode, the current and voltage at the gap are reconstructed using the measured current waveforms in the middle of the cable. Therefore, the voltage probe is not used in actual experiments.

The error in the current and voltage measurement depends, therefore, solely on the current probe that has a precision of 1 % and a sensitivity of 1 V/A, which is attenuated four times to display on an oscilloscope with a DC gain accuracy of full scale (40 V) of 1.5 %. Assuming the worst-case scenario of linear error propagation, the error on a typically measured breakdown voltage of 10 kV is 5 %.

3.2.3 Resistive Coupler

The megaimpulse pulse generator has a resistive coupler that operates on a principle similar to the current shunt. Since the pulse duration is

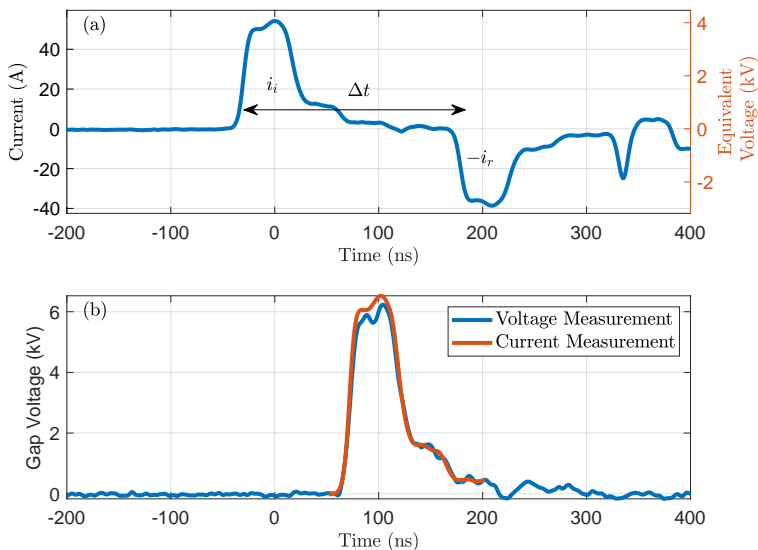


Figure 3.3: Measurement technique validation.

only 20 ns long, the HV cables connected to the resistive coupler are only 5 m in length. The resistive coupler features a voltage divider of approximately 1:50 and is operated with one additional 6 dB and one 20 dB N-type attenuator and an SMA 20 dB attenuator, which results in an additional attenuation of 1:200 for a total of 1:10000. Therefore, the 20 kV pulse in the HV cable is divided in, 10000 times results in a 2V signal in 50 Ohm that can be measured with an oscilloscope.

The Megaimpulse's HV cables experience a more significant energy loss during the pulse transfer than the cable used with the FID pulse generators (also due to the faster pulse). By measuring the signal attenuation between incident and reflected pulse in open load experiments. The loss in this case is 1.23% per meter of cable, so the energy loss between the incident and reflected is 13%.

3.3 Discharge Analysis

In the analyzed setup, the plasma and electrode configuration form a loop. Therefore, the impedance of the load is composed of resistance in series with an inductance. As shown in [49], for a small loop radius (tens of mm), the inductance of the electrode configuration is rather small (5-10 nH). Therefore, the assumption of a purely resistive plasma impedance is a valid approximation. Nevertheless, the impedance could be much higher due to the 10-20 cm where the coaxial shield is enlarged and the cable's HV core is connected to the spark plug, as shown in Figure 2.2.

The plasma impedance is treated as a resistance (R_{pl}) in parallel with a stray capacitance (C_{stray}). In this case, the measured current (i_g) is the sum of the displacement current (i_d), which corresponds to the current that charges the capacitance of the HV electrode, and the conduction current flowing through the plasma (i_{pl}) [14]. The displacement current is related to the derivation of the gap voltage by the spark plug capacitance according to Equation (3.7)

$$i_g = i_{pl} + i_d$$

$$i_d = C_{stray} \frac{dv_g}{dt} \quad (3.7)$$

The value of the capacitance is affected by the electrode geometry. The spark plug capacitance is measured using low amplitude pulses where the entire measured current is the capacitive current (no breakdown). The stray capacitance C_{stray} for the used spark plugs ranges from 5,1 pF to 5,7 pF depending on the bending of the ground electrode. One would expect a higher capacitance for a smaller gap distance, but since the ground electrode bend shape affects the capacitance, this is not always the case. The displacement current is directly proportional to the capacitance, and a maximal displacement current of up to 30 A is measured. These values are considerably smaller in comparison with the plasma current (~ 200 A). The average value (5,5 pF) for the measured capacitance between different spark plugs is used, which results in maximal variation of capacitive current below 5%. This uncertainty is even less relevant when compared to the plasma current, which lies below 0.5%

on average. The average value is also used because the spark plug gap is typically frequently adjusted during experiments, and the capacitance slightly varies (due to different bend radii of the ground electrode).

The plasma current is the difference between the total gap current and the capacitive current necessary to charge and discharge the spark plug stray capacitance. Only the displacement current is measured when the gas resistance is high (insulating air between the electrodes). This applies to the situation before the electric field in the gap leads to significant gas ionization, thus increasing its electrical conductivity. The pulse is reflected with the same polarity. At a certain moment, the streamer bridges the gap, the gap resistance decreases, and the current increases accordingly. When the gap resistance is equal to the cable impedance, the pulse power is entirely absorbed by the plasma, and nothing is reflected. After the breakdown, the streamer develops into a strongly ionized, highly conducting spark (transient discharge) channel, and if the discharge is long enough, a spark-to-arc transition occurs. A defining feature of arc discharge is the high temperature of the neutral gas particles. The gas particles receive energy via collision with energetic electrons, and these collisions occur with an average frequency f_{en} . The associated timescale for the equilibration of temperature is calculated according to Equation (3.8) [50]:

$$\tau \sim \frac{m_{\text{n}}}{2f_{\text{en}}m_{\text{e}}} \quad (3.8)$$

The mass ratio between air molecules and electrons is approx. $5 \cdot 10^4$. The effective frequency for momentum transfer is extracted from the Boltzmann equation solver BOLSIG+ [51] using the cross-sectional data sets reported in [52–54]. The total collision frequency ranges between $5 \cdot 10^{12}$ and $4 \cdot 10^{13} \text{ s}^{-1}$. The calculated characteristic time for energy equilibration ranges between 0.5 ns and 5 ns. However, this estimation can only represent a lower bound estimate for the arc formation time. The breakdown to arc transition is a complex multistage process that also involves a transient glow discharge phase and cathode spot formation [55]. Nonetheless, the derived range of values agrees well with typical spark arc transition times for discharges using spark plugs under the investigated conditions [56]. When the spark channel is established, the spark gap acts as a low-impedance termination for the cable, reflecting most of the source's pulse power. The pulse is reflected

with opposite polarity. Two discharge regimes are recognizable during this type of discharge. First is the low (displacement) current regime, where a low-conductivity medium (non or weakly ionized gas) is present between the electrodes, and the voltage across the gap is twice as high as the pulse voltage. The second regime is the high current regime, in which only the cable impedance limits the maximal current.

Equations (3.9) describe the voltage (v_g) across and the current (i_g) through the spark gap by assuming a load composed only by a varying air-plasma electrical resistance (R_{pl}) and a stray capacitance C_{stray} in parallel.

$$\begin{aligned} v_g &= v_i \frac{2R_{pl}(t)}{Z_0 + R_{pl}(t)} \\ i_g &= \frac{v_i}{Z_0} \frac{2Z_0}{Z_0 + 2R_{pl}(t)} + C_{\text{stray}} \frac{dv_g}{dt} \end{aligned} \quad (3.9)$$

The two different regimes can be recognized as well from Equations (3.9). Before breakdown, the air between the electrodes provides a very high resistance (>1 MOhm), preventing electrical charge flow in the gas. Therefore, the cable impedance of 75 Ohm is negligible with respect to the very high R_{pl} , resulting in a negligible current flowing through the gap and a doubling of the gap voltage with respect to the pulse voltage. Experimentally, the measured current before breakdown is tens of amperes. The measured current is not a conduction current but a pure displacement current that charges the spark plug capacitance.

After the breakdown, when the plasma is formed, the resistance is much lower than the cable impedance. In this case, v_g drops to low values. This setup offers the advantage of doubling the pulse generator voltage to initiate breakdown at high electric fields and limited current injection after breakdown, which should prevent or slow the transition to a thermal plasma [6].

By assuming a purely resistive load ($C_{\text{stray}} = 0$) when air is present between the electrodes (Air, $R_{pl} \gg Z_0$), the setup is similar to an open circuit. When there is a well-developed spark ($R_{pl} \ll Z_0$), a short circuit is present. An intermediate regime (matching impedance) can be recognized where the power to the plasma is the highest, no

reflection occurs, the total power is absorbed from the gas/plasma, and the R_{pl} is equal to the cable impedance. The features of these three regimes for an ideal load are summarized in Table 3.2.

Table 3.2: Regimes occurring during a NPD.

	Gas/Plasma resistance	Voltage reflected	Gap voltage	Gap current	Input power
Low current discharge (open-load)	$R_{pl} \gg Z$	$v_r = v_i$	$v_g = 2v_i$	$i_g = 0$	$p_g = 0$
Matched impedance (matched-load)	$R_{pl} = Z$	$v_r = 0$	$v_g = v_i$	$i_g = \frac{v_i}{Z}$	$p_g = \frac{v_i^2}{Z}$
High current discharge (short-load)	$R_{pl} \ll Z$	$v_r = -v_i$	$v_g = 0$	$i_g = \frac{2v_i}{Z}$	$p_g = 0$

3.3.1 Single Pulse Discharge

Figure 3.4 shows the discharge electrical measurements (measured in the ignition cell with the current shunt) for a 50 ns pulse at ambient temperature and a pressure of 1,5 bar with a gap distance of 0,8 mm. Subplot (a) shows the incident (blue) and reflected (red) pulse current. The equivalent voltage axis (right) shows the corresponding voltage amplitudes inside the coaxial cable for the same waveforms. Subplot (b) shows the plasma current (red) and the voltage (blue) across the gap (calculated using Equations (3.2) with input the incident and reflected pulse current from subplot (a)). The dashed red line shows the displacement current at the spark plug magnified ten times. Subplot (c) depicts the plasma resistance calculated as the ratio between the gap voltage and plasma current. The blue line in subplot (b) of Figure 3.4 in relation to the blue line in subplot (a) outlines the voltage doubling before breakdown. The high current (~ 100 A) and discharge time (tens of nanoseconds) after the breakdown outline the probable transition to an arc. As expected, the plasma's resistance transitions from high to

low values. The breakdown is the point where the maximal voltage is reached, in this case, at seven ns and 6,4 kV.

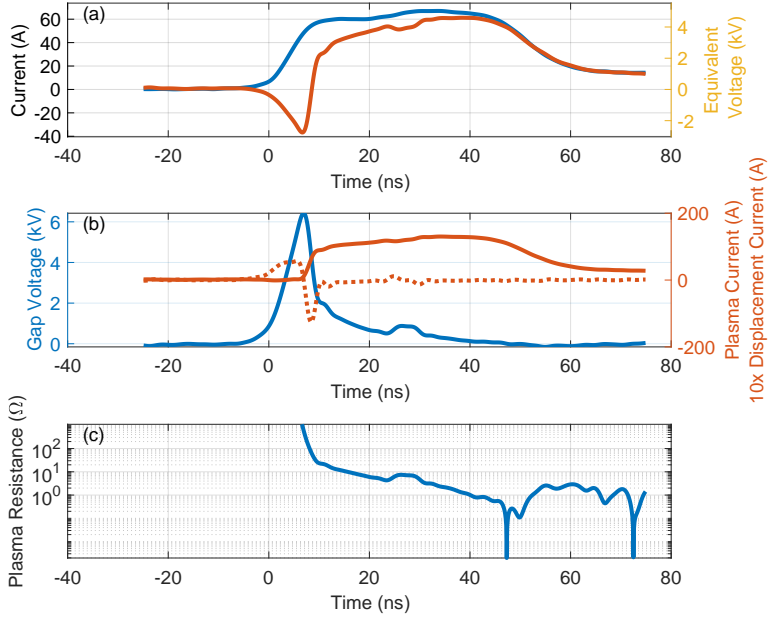


Figure 3.4: Discharge analysis, air, 1,5 bar, 0,8 mm

Figure 3.5 shows the voltage across the gap (full blue line) and the plasma current multiplied by the coaxial cable impedance (dotted blue line). The dashed blue line is twice the incident pulse voltage (i.e., the voltage that would develop in the absence of breakdown and without any displacement current (v_{\max}), which is calculated according to Equation (3.10).

$$v_{\max} = \max(2v_i) = \max(2Z_0 i_i) \quad (3.10)$$

The red line depicts the cumulative energy injected into the plasma as a function of time, which is calculated according to Equation (3.11):

$$e_{cum}(t) = \int_0^t i_{pl}(t)v_g(t)dt \quad (3.11)$$

With the current setup, the sum of the total current multiplied by the cable impedance and the gap voltage is always double the supplied pulse voltage. This relation is due to the electrical circuit being active during discharge. When no current flows through the gap, the voltage is doubled due to full reflection. When the gap resistance is equal to the cable impedance, the gap voltage is equal to the pulse voltage and equal to the total current multiplied by the cable impedance. At this point, no reflection is present, and the power transferred to the plasma is the highest (matched load). The high power input during the matched regime is also visible in the cumulative energy deposition (highest energy deposition rate); afterward, the voltage decreases, and the current increases, reaching double the pulse current. Figure 3.5 also reports the breakdown voltage (V_{bd}) and the prospective voltage (V_{max}).

3.3.2 Multiple Pulse Discharges

Multiple pulses at high repetition frequencies are used per ignition event in engines to provide the energy necessary for robust ignition. Ten pulses with a duration of 50 ns at a repetition frequency of 10 kHz in synthetic air at 8 bar and ambient temperature are applied to a spark plug having a gap distance of 0,35 mm (in the ignition cell using the current shunt measurement). Figure 3.6 shows the amplitude of the supplied pulse (subplot (a)), the voltage at the gap (subplot (b)), and the total current, namely, the sum of the displacement and plasma currents (subplot (c)). The breakdown is present when the current rises to hundreds of amperes.

This ignition sequence lasts 1 ms, which is shorter than the ignition duration of classical ignition systems [3]. The incident pulse shape and the static breakdown voltage mostly dictate the breakdown voltage (which is discussed in detail in Section 4.2). In Figure 3.6, the pulse amplitude is approximately constant for the individual pulses. Under this condition, the static breakdown voltage is 9 kV, and the maximal voltage present without breakdown is 13 kV, resulting in a discharge probability of approx. 55%, as determined from the data reported in

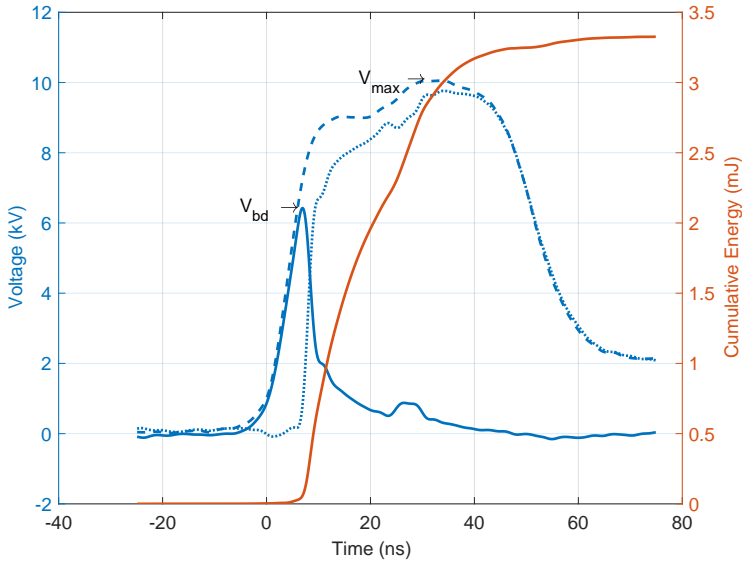


Figure 3.5: Current and voltage relation during nanosecond pulsed discharge, air, 1,5 bar, 0,8 mm

the next chapter and shown in Figure 4.7 (b). In this case, for the first three pulses, no discharge is present. The first breakdown voltage at 11 kV is in line with that for the single-pulse experiments (next chapter, Section 4.2). For the following pulses, breakdown occurs at a lower voltage.

Figure 3.7 depicts the discharge characteristics at 12 bar, a gap size of 0,5 mm, using higher incident pulse amplitudes and also using 10 pulses at 10 kHz.

The static breakdown voltage is 14 kV, and the maximal voltage in the absence of breakdown is 15 kV for the first pulse and 21 kV for the second pulse, respectively. For the first pulse, the maximum voltage is only slightly above the static breakdown voltage, and breakdown is, therefore, difficult (probability of discharge approx. 30%). For the second pulse, which has a higher maximal impulse factor (often, the

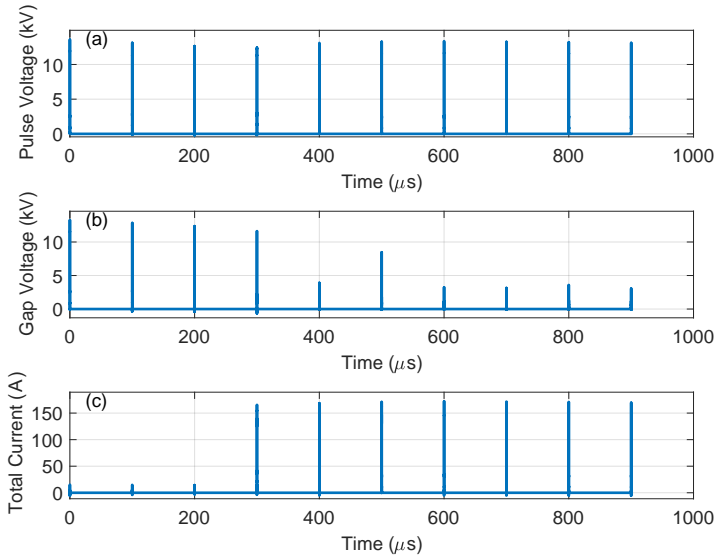


Figure 3.6: Multiple pulse discharge at 8 bar. and gap distance of 0,35 mm

first pulse in multiple pulse mode has a lower amplitude), the discharge probability is higher (60%), and breakdown is achieved at 18 kV. Afterward, the breakdown occurs at lower voltage levels as in the previous experiment (Figure 3.6). The discharge probabilities are interpolated from the data presented in the next chapter (Figure 4.7) using the maximal impulse factor as the interpolation point.

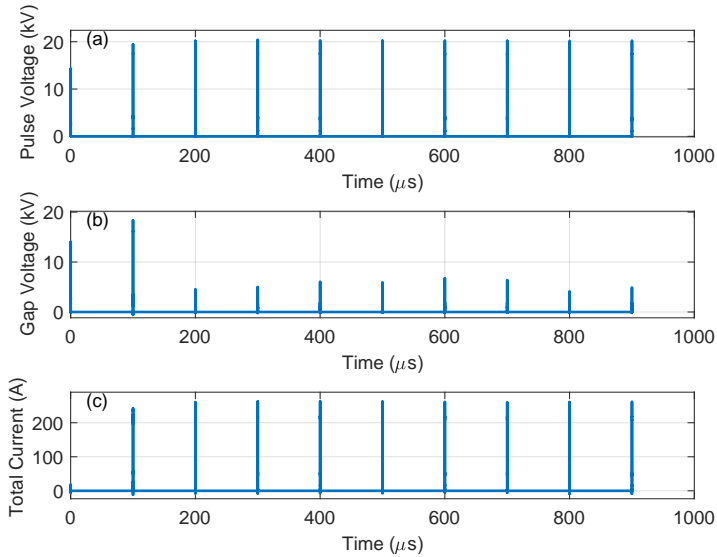


Figure 3.7: Multiple pulse discharge at 12 bar. and gap distance of 0,5 mm

3.3.3 Effect of Electrode Geometry

The effect of the electrode geometry on the current and voltage variation during the discharge is investigated in the ignition cell using the current shunt measurement technique. A J-gap spark plug (NGK 5096) and a surface gap spark plug (NGK 2522), shown respectively to the left and right in Figure 3.8 are used.

This analysis of the differences between different electrode geometries is done assuming an ideal load composed solely by an Ohmic resistance ($R_{pl}(t)$) present due to the time-varying electrical resistance of the gas/plasma present between the electrodes.

The efficiency η_d of the NRPD discharge is defined as the ratio of the plasma to the pulse energy, according to Equation (3.12). The pulse energy is the energy that would be deposited to an ideal load with



Figure 3.8: Images of J gap spark plug (left) and surface gap spark plug (right).

resistance equal to the cable impedance (matched-load). For an ideal load (no stray components) the efficiency is zero for low-current (open-load) and high-current (short-load) cases.

$$\eta_d = \frac{E_{pl}}{\frac{\int v_1^2}{Z}} \stackrel{Z_1 \equiv R_{pl}}{=} \frac{\int v_g i_g}{\frac{\int v_1^2}{Z}} \quad (3.12)$$

During the NPD shown in Section 3.3, the air plasma resistance undergoes the three regimes; therefore, its efficiency is always below unity. Higher efficiencies are reached the longer the plasma resistance is close to the cable impedance.

Figure 3.9 (upper left and right) shows the evolution of the voltage between the spark plug electrodes for the two different spark plugs. Ten pulses at 10 kHz are applied in both experiments at a pressure of 10 bar and ambient temperature, and the pulse generator offering a 50 ns pulse duration is used (Pulse generator A). The cell is filled with air and methane with an AFR equivalence ratio of $\lambda = 1.6$ for the surface gap spark plug and $\lambda = 1.35$ for the J-gap spark plug. The start of each pulse is shifted to zero time to match each pulse with the first pulse on a nanosecond timescale. The gap voltage for the first, second, third, and ninth pulses is depicted in the upper subplots in different colors.

The maximal voltages that would appear across the gap if no discharge were present are shown in black for the same pulses. The cumulative energy deposited to the plasma, calculated according to Equation (3.11) is plotted for the same pulses with the same color scheme in the bottom subplots.

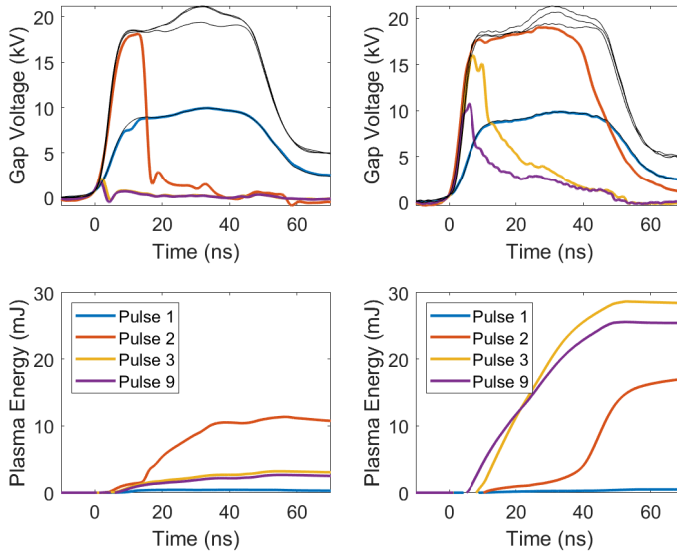


Figure 3.9: Pulse voltage waveform for pulses 1, 2, 3, and 9 in a ten-pulse ignition sequence at 10 kHz PRF and 10 bar, on the right for the surface gap spark plug and on the left for a J-gap spark plug.

The first pulse is of lower amplitude, which frequently occurs due to the internal circuit of the pulse generator. The first breakdown voltages are similar for the two different spark plugs (approx. 18 kV) and at the second pulse. The time at which breakdown occurs varies between the two experiments and is approximately 15 and 30 ns after the start of the pulse.

Similar energy deposition in the two cases is achieved with the first discharge (pulse 2) and amounts to 15 mJ and 11 mJ, respectively. The

energy deposition and maximal gap voltage per pulse decrease rapidly for the J-gap spark plug. After one pulse, the energy per discharge is approximately constant at approx. 3 mJ. For the surface spark plug, the maximal gap voltage decreases (for subsequent pulses) but at a much slower pace. In fact, due to the longer discharge time available (the breakdown happens earlier) and the still relatively high maximal gap voltage of 16 kV, the energy deposit to the plasma increases for the third pulse up to 28 mJ. Afterward, the breakdown voltage decreases, as does the plasma's energy back to approx. 25 mJ.

The energy deposition to the plasma is highest when the cable impedance links the current and gap voltage, (matched impedance in Table 3.2). When this condition is fulfilled, the plasma impedance equals that of the cable; there is no reflection and, therefore, no energy dissipation.

Assuming that the impedance varies linearly from infinity to zero during the transition from streamer to spark, higher plasma energy is achieved with a lower voltage decrease rate. Slower voltage decrease rates after a breakdown are visible for the surface spark plug. The efficiency of discharge for the surface gap spark plug is 39 %, while that for the J-gap spark plug is approximately 7 %.

Similar results are achieved using the pulse generator C (10 ns pulse duration) and two other spark plugs, one having a j-gap electrode configuration (NGK C9E) and the other being a surface gap spark plug (Champion G54V). Figure 3.10 shows the voltage (v_g) and the current (i_g) over the spark plug gap as well as the energy deposition (e_{cum}) to the plasma for an NRPD ignition sequence performed with ten pulses at 50 kHz PRF in an air methane mixture at $\lambda = 1.3$ at ambient temperature and 10 bar. The red line depicts the discharge features using the J-gap spark plug, while the blue one uses the surface discharge spark plug (scale on the left). The black line in the third subplot depicts the cumulative energy delivered by the pulse generator (scale on the right), which is the same for both experiments.

For the engine experiments (Section 6.4), surface and J-gap spark plug are used in combination with the 4-channel pulse generator (pulse generator C). Similar effects, as reported above, are visible despite the different pulse generator, PRF and pulse polarity used, i.e., a higher energy deposition with the surface spark plug thanks to a lower voltage drop rate after the breakdown and a higher breakdown voltage after

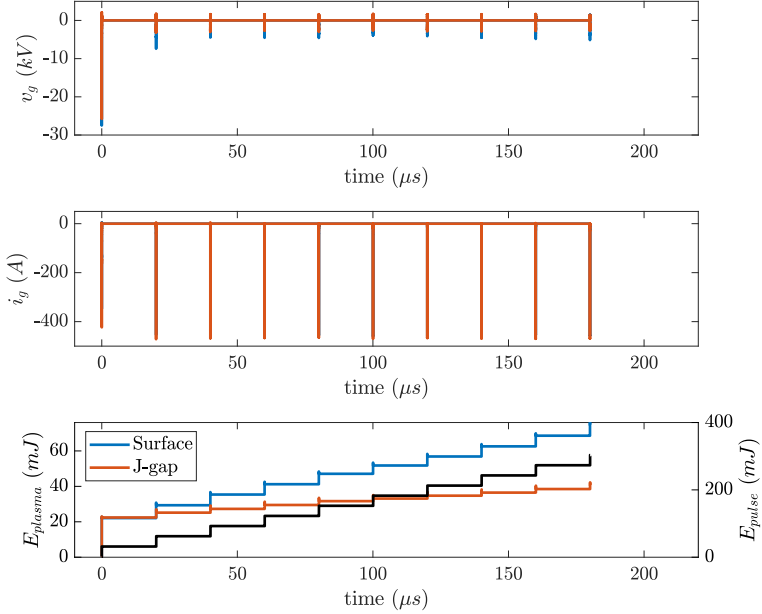


Figure 3.10: Voltage, current and energy deposition with the surface gap (blue) and J-gap (red) spark plugs.

the first pulse. This investigation uses a shorter and faster-rising pulse. Therefore, the effect of the stray capacitance and inductance makes precise measurement of the actual gap current and voltage (especially for the pulses 2-10) difficult; the energy deposition is therefore measured as the difference between incident and reflected pulse energy according to Equation (3.6).

3.3.4 Summary and Discussion

Under the investigated conditions, notable energy deposition (necessary for ignition purposes) to the plasma occurs only when a breakdown occurs. After the breakdown, the gap voltages drop to some kV in a

few nanoseconds. Afterward, the plasma resistance decreases further, and the voltage drops to practically zero while the current rises to its maximal value (only limited by the active electrical circuit).

When high pulse amplitudes are used, the breakdown happens in the fast-rising part of the pulse. The discharge times are thus above the characteristic timescale for temperature equilibration (1-5 ns), suggesting that the plasma has enough time to thermalize. Therefore, a spark-arc transition is likely to occur. If an arc transition occurs, the discharge is sustained by electron emission from the cathode hot spot, diminishing the spark plug life. For the temperature equilibration characteristic time, the field is assumed to be homogenous at the breakdown voltage level, but the electric field during plasma thermalization decreases, and, therefore, the actual characteristic time increases. Field inhomogeneity should lead to different characteristic times, namely, faster plasma heat up in the electric field enhanced regions and slower plasma heat up where the electric field is locally lower.

Once multiple pulses at high PRF are delivered, the breakdown voltage of subsequent pulses is lower and, therefore, also the energy deposited per pulse. After a nanosecond discharge, the temperature between the electrodes is expected to be several tens of thousands of Kelvin [13]. Afterward, the plasma expansion and heat losses cool the region between the electrodes. After 100 μ s, the local density of the gas is still expected to be highly reduced; furthermore, ionized atoms and molecules or, in electronegative gases, such as air, negative ions can still be present between the electrodes, reducing the breakdown strength of the gas between the electrodes.

A much higher breakdown voltage is present for the following pulses for the surface gap spark plug. The reason is threefold. First, the geometry of the surface gap spark plug results in a more homogeneous electric field, which can lead to a larger plasma surface; therefore, the energy is deposited over a broader volume. Second, the surface gap spark plug has a higher heat range (NGK 7 vs. 12). The surface gap spark plug has a better heat dissipation capability between the gap and the spark plug thread. Third is due to the active breakdown mechanism, (discussed in detail in Chapter 4). The breakdown is a stochastic process that (in our case) seems to start with the emission of a seed electron from the cathode surface. The inhomogeneous electric field present using the

J-gap spark plug results in the possibility of the breakdown only from a small area, between the sharp corners of the electrodes, where the field and, therefore, ionization rate is enhanced. Instead, due to the more homogenous electric field present all around the electrode of the surface gap spark plug, the discharge can potentially happen on the entire circumference. Therefore, if the voltage rise rate is fast enough and the seed electron appears in another location, the breakdown can happen in a different region of the spark plug. Since all the pulses deliver ~ 10 mJ of energy, each pulse has enough energy to potentially establish a self-propagating flame. Therefore, it is not necessary for the discharge to always form in the same region within a train of pulses to support flame propagation. Instead, different pulses can generate a larger early flame kernel, which may help to reduce cyclic variation or overcome unfavorable local conditions.

All influences would result in a higher local density between the electrodes for the surface gap spark plug, increasing its breakdown strength for subsequent pulses.

The larger plasma surface could also explain the voltage decrease behavior during the pulse for the surface spark plug, where slower decrease rates are measured. The energy during the pulse is deposited over a larger volume, reducing the temperature increase and, therefore, the ionization frequency and current growth. Different stray parameters are present due to the different geometries and construction of the spark plugs under analysis. A higher stray inductance or lower stray capacitance of the surface spark plug could also explain the slower voltage decrease rate after the breakdown.

3.4 Load Impedance

Due to the fast voltage and current variations that are present during NPDs, even small parasitic capacitances and inductances of the load can significantly modify the voltage over the load and the current through the load. This is particularly important for modeling NPD.

The equivalent circuit for the spark gap that is used for modeling purposes (Section 5.2) is shown in Figure 3.11. The load is composed of a stray inductance (L_{stray}), a stray capacitance (C_{stray}), and a time-varying resistance (R_{pl}). The circuit is similar to other proposed spark

gap equivalent circuits [57, 58]. The only difference is that the inductance is assumed to be constant since the length of the spark channel is also assumed constant. As the load has small mechanical dimensions (propagation time < 1 ns), the load is treated as a lumped element.

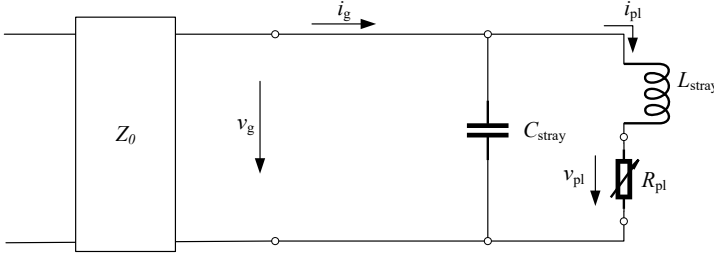


Figure 3.11: Equivalent electrical circuit of the spark gap (load).

Equation (3.13) describes the voltage applied to the plasma as a function of L_{stray} , C_{stray} , and R_{pl} for the presented equivalent circuit.

$$\begin{aligned} v_{pl} &= \frac{R_{pl}(t)}{L_{stray}} \int (v_g - v_{pl}) dt \\ v_g &= \frac{1}{C_{stray}} \int \left(i_g - \frac{v_{pl}}{R_{pl}(t)} \right) dt \end{aligned} \quad (3.13)$$

Equation (3.13) together with Equation (3.2), uniquely describes the current and voltage over the gap as a function of v_i , Z_0 , L_{stray} , C_{stray} , and R_{pl} .

R_{pl} can be modeled using Equation (3.14) [59], where d is the spark gap distance, A is the plasma's cross-sectional area, μ_e the electron mobility, q is the elementary charge, and n_e is the electron number density.

$$R_{pl}(t) = \frac{d}{A\mu_e(t)qn_e(t)} \quad (3.14)$$

For the proposed electrical circuit, Equation (3.15) describes the relation between the gap and plasma voltage.

$$v_{pl} = v_g - L_{\text{stray}} \frac{di_{pl}}{dt} \quad (3.15)$$

The modeling of the NPD based on the here presented load impedance will be discussed in Section 5.2.

4

Breakdown Analysis

The electrical breakdown of gases under nanosecond HV transients is of great interest for various technical applications. In some applications, such as chemical plasma reactors [60], plasma surface treatments [61], or SI systems [3], the creation of plasma is the desired outcome. In other applications, such as insulation systems for inverter-fed motors and transformers, repetitive nanosecond HV transients can occur during the switching process and ignite an undesired plasma in gas gaps bounded by solid insulation materials. Usually of a transient nature, these partial discharges (discharges that do not completely bridge the space between the two conductors) cause chemical and physical erosion of the solid insulation, which is the leading cause of premature insulation failures in inverter-driven systems [62].

In [63], only a minor influence of different AFRs in reacting mixtures on the discharge dynamics and structure up to plasma channel formation are detected. For this reason, the discharge analysis is performed only in dry synthetic air in this chapter. Furthermore, even at a stoichiometric AFR, the fuel percentage (by volume) is only approx. 9%.

This chapter is organized into three sections: Section 4.1 describes the mechanism for the electrical breakdown of gas with a focus on sub-mm gaps. Section 4.2 describes the analysis of the breakdown using commercially available spark plugs and presents the results published in [20]; it discusses the breakdown mechanism active under NPD, discusses the needed voltage levels to achieve the breakdown, and gives advice

for the ideal pulse shape for ignition purposes. Section 4.3, outlines the results published in [21] and discusses the breakdown voltage under a well-defined quasi-uniform electrode configuration, focusing on the effects influencing the statistical time lag under NPD.

4.1 Breakdown Mechanism

The electrical breakdown of a gas gap starts with one or more free electrons – so-called seed electrons – that gain kinetic energy from the applied electric field. Seed electron generation is a stochastic process and leads to a fluctuating breakdown delay known as the statistical time lag [64, 65]. The seed electron can appear in the gas gap via several mechanisms: ionization of the background gas by energetic radiation (cosmic, radioactive, UV), detachment from negative ions in electronegative gases, or emission from the cathode surface. If the field magnitude exceeds the gas' critical field strength, an electron avalanche can result from the impact ionization of neutral gas molecules. According to the streamer mechanism, a direct breakdown can occur if the electron number in an avalanche grows to $10^6 \dots 10^8$ electrons. If so, a direct breakdown without cathode feedback can occur according to the streamer mechanism [33]. Alternatively, breakdown may occur as a result of a growing number of secondary avalanches starting from electrons liberated from the cathode by energetic input (positive ions, photons, metastable atom, etc.) from previous avalanches (Townsend mechanism).

The gas breakdown mechanisms depend on the time-varying electric field and on the seed electron provision. The gas contains relatively few free charged particles and is thus a good electrical insulator. However, if the electrical field is high enough, positive ions, photons, or excited neutral molecules created in an avalanche can reach the cathode surface and release secondary electrons (if they can impart with an energy exceeding the work function of the cathode surface to the electrons). This feedback process is quantified by the secondary feedback emission coefficient (γ), which is defined as the number of secondary electrons released per ionization event in an avalanche. In each avalanche generation, the number of electrons is enhanced by the amplification factor (μ) given by Equation (4.1).

$$\mu = \gamma e^{\int_0^d \alpha_{eff} \cdot dx} = \gamma e^S \quad (4.1)$$

According to Townsend's theory, a breakdown occurs when each avalanche creates, on average, more than one successor avalanche, that is, when $\mu > 1$. The corresponding Townsend criterion thus reads:

$$S = \int_0^d \alpha_{eff} \cdot dx = \int_0^d \alpha - \eta \cdot dx = \ln(\gamma^{-1}) \quad (4.2)$$

The integral S is called the ionization integral and equals the line integral of the effective ionization coefficient (α_{eff}) along a considered field line across the gas gap. The term α_{eff} considers the effects of both ionization (α) and attachment (η) of electrons. If the Townsend criterion is fulfilled, the number of avalanches in subsequent generations will increase exponentially until a certain critical number $E_a \approx 10^6 \dots 10^{10}$ of avalanches is formed, where space charge effects start to dominate the subsequent dynamics of the breakdown [66].

The formative time of Townsend breakdown is estimated as the time it takes for the critical number of avalanches to form, which requires an average number r (Equation (4.3)) of generations [66].

$$r = \frac{\ln[(\mu - 1)E_a]}{\ln \mu} \quad (4.3)$$

The formative time of Townsend breakdown is calculated as the product of the number of generations r and the mean time $\tau_{s.a.}$ between successor avalanches according to Equation (4.4), where v_e is the drift velocity of electrons. Note that only secondary emission due to the photoelectric effect is considered here, as it is the only mechanism fast enough to be of potential relevance for highly transient voltages.

$$t_{f,t} = r \cdot \tau_{s.a.} = \frac{\ln[(\mu - 1)E_a]}{\ln \mu} \cdot \left[\tau_1 + \left(1 - \frac{1}{\alpha_{eff} \cdot d} \right) \cdot \frac{d}{v_e} \right] \quad (4.4)$$

τ_1 is the deexcitation time of the species emitting the feedback photons.

The photons are mostly emitted close to the anode, especially at high electron amplification, which is considered by the factor $1 - \alpha_{eff} \cdot d^{-1}$.

If the electron number in the avalanche becomes so large that its associated space-charge electric field distorts the background electric field, the avalanche-to-streamer transition can occur.

When the electron amplification in the gas is sufficiently large (electron number in an avalanche exceeding $n_{e,crit} = 10^6 \dots 10^8$), the field associated with the space charge of the avalanche can significantly distort the background field; secondary avalanches can grow in the field-enhanced region and lead to the formation of a streamer channel. This channel can further develop into the filamentary breakdown channel known as a spark. Several authors have suggested criteria for streamer inceptions of varying complexity. Raether's ignition condition for streamer breakdown requires the ionization integral S to be larger than the logarithm of a critical number $n_{e,crit}$ of electrons in the avalanche head [67].

$$S = \int_0^d \alpha_{eff} \cdot dx = K_{st} = \ln(n_{e,crit}) \quad (4.5)$$

The streamer constant K_{st} can be derived from first principles. K_{st} varies as a function of gap distance and pressure for submillimeter gaps and synthetic air according to Equation (4.6) [68], where d is the gap distance in mm and p is the pressure in bar. The corresponding range is $K_{st} \approx 14 \dots 17$ for the gap distances and pressures considered here.

$$K_{st} = \ln \left(\max \left(\frac{7.3710^6}{p}, 1.71 \cdot 10^7 d \right) \right) \quad (4.6)$$

After its inception, the streamer can propagate the ionization into regions where the undistorted electric field is below the critical field strength. Secondary avalanches growing from seed electrons provided by UltraViolet (UV) radiation emitted by excited species feed into the streamer head and extend the streamer channel toward the electrodes. Due to UV photon participation, streamer growth is a fast process, occurring at velocities exceeding the electron drift velocity. Once the streamer channel bridges the discharge gap, it can develop

into a strongly ionized, highly conducting spark channel (transient discharge) or even into an arc (thermally ionized plasma channel driven by a low impedance voltage source) [69, 70]. Once the streamer channel is formed, its velocity is generally one order of magnitude greater than the electron drift velocity. The formative time is thus approximated as the time an electron avalanche needs to grow to the critical size (Equation (4.7)) [71].

$$t_{f,s} = \frac{\ln(n_c)}{\alpha \left(\frac{E}{N}\right) v_e \left(\frac{E}{N}\right)} = \frac{K_{st}}{\alpha \left(\frac{E}{N}\right) v_e \left(\frac{E}{N}\right)} \quad (4.7)$$

The formative times of both mechanisms are compared in Figure 4.1 using the modified spark plug that offers a quasi-uniform electric fields between the electrodes (modified spark plug visible in Figure 2.4).

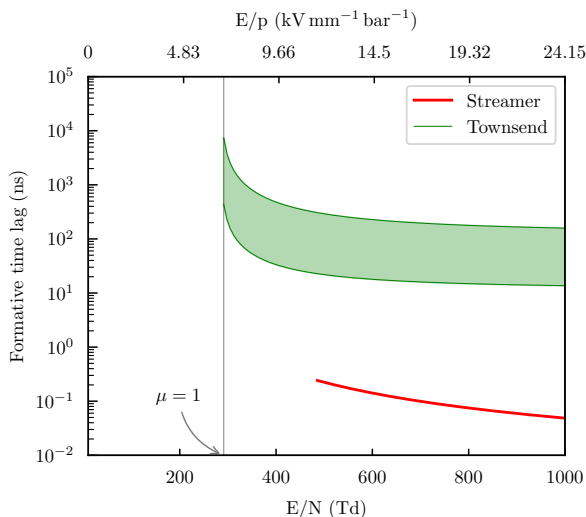


Figure 4.1: Estimated formative times of the streamer and Townsend breakdown mechanisms as a function of the reduced electric field at a 1 mm gap distance

The Townsend formative time area is calculated for the range of the

relaxation time (τ_1) of the excited species emitting photoelectrons (10-100 ns) and the typical avalanche number E_a of $10^6 \dots 10^{10}$ required to transition into the glow discharge [72]. From criteria (4.4) and (4.5), it follows that if $\gamma > n_{e,\text{crit}}^{-1}$, the voltage threshold for a Townsend breakdown is lower than that for streamer inception, and the static breakdown voltage V_0 is determined by the Townsend criterion. However, if the voltage increases to a sufficiently large overvoltage (see Figure 10 in [68]) during the statistical time lag t_s (i.e., after crossing the Townsend threshold), then the streamer criterion is reached, and a seed electron can induce a streamer breakdown in the first avalanche generation.

Under quasi-static voltage stress, streamers are usually not considered to occur in submillimeter gaps at ambient pressure [33]. The reason for this is that for typical electron feedback emission coefficients for the cathode ($\gamma \gtrsim 10^{-5}$), i.e., the number of secondary electrons per electron in the avalanche [33], Townsend breakdown occurs at voltages where streamers cannot yet be incepted. The Townsend breakdown develops over many generations of electron avalanches, wherein secondary electron emission at the cathode generates new seed electrons. These secondary electrons are generated via photon or ion impact on the electrode surface [70].

Due to the high pressures (1 bar to 12 bar) relevant for this project and the inhomogeneous electrode geometry (Figure 2.2 shows the spark plug electrodes), the streamer mechanism can lead to breakdown at a lower voltage than the Townsend mechanism. The value of the feedback coefficient γ can explain the presence of streamer breakdown instead of Townsend breakdown: the lower the feedback coefficient, the more likely it is that streamer breakdown will occur. Two factors in the current electrode configuration considerably reduce the feedback coefficient. First, the relatively high densities make it more difficult for photons to reach the cathode. Second, the electrode inhomogeneity: the edge provides favorable conditions for generating large avalanches. Nevertheless, it also means that secondary electron feedback must occur in a very narrow area of the cathode. Hence, the probability that a photon hits this area is relatively small. The feedback coefficient values for SF₆ (electrical insulator gas) are shown as a function of pressure and field in [73]. An increase in pressure from 13 mbar to 133 mbar leads to a decrease in γ by a factor of ~ 100 . Two factors are reported to reduce secondary electrons with higher pressure: first, a higher photon ab-

sorption coefficient, and, second, a higher probability for nonradiative deexcitation of excited molecules via collisions with other molecules. Due to relatively slow current growth over many-electron avalanche generations, the Townsend breakdown features a higher formative time than the streamer breakdown. High formative times are the reason why the streamer mechanism becomes the dominant breakdown mechanism above a certain overvoltage: even though Townsend discharge can occur already, it is too slow. Instead, the streamer mechanism kicks in at a certain overvoltage and leads to breakdown before the multiple electron generations have time to build up.

All breakdown mechanisms start with the appearance of a seed electron, which starts the ionization process that ultimately leads to a breakdown. Seed electrons can originate from the background gas or the cathode surface. The required ionization energy (gas) or work function (cathode) can be provided by a multitude of processes, among which cosmic and radioactive background radiation, as well as energetic photons (UV, X-ray, ...), are commonly mentioned [73]. The electric field itself can assist the release of an electron from the cathode in what is called field emission or thermionic emission (combined effect of the cathode electric field and temperature) of electrons [74]. Moreover, in electronegative gases such as synthetic air, unstable negative ions can constitute an important source of seed electrons [65]. The mentioned processes are subject to statistical fluctuations, which gives rise to a statistical time lag, i.e., the time interval between the crossing of the static breakdown threshold and the appearance of the seed electron. The total delay time is the sum of the statistical time lag (t_s) and the formative time lag (t_f).

$$t_{\text{delay}} = t_s + t_f \quad (4.8)$$

4.2 Breakdown Analysis Using Spark Plugs

Although research into ignition using NRPD has gained considerable momentum in recent years [75, 76], the mechanism leading to breakdown under pulsed discharge in strongly inhomogeneous fields at high pressures remains largely unclear. Breakdown at a high overvoltage is advantageous for achieving reliable ignition in challenging conditions

(e.g., lean mixture, stable fuels, high or low turbulence levels). The dynamics of the applied voltage influence the breakdown voltage, but how this occurs is not yet fully understood. Pulse generators available on the market have various rise times, amplitudes, and pulse durations, but their influence on breakdown level and discharge probability is still unclear, especially for the conditions necessary for engine application. This section experimentally investigates the breakdown onset at density conditions relevant to ICE applications (pressures from 1 bar to 12 bar and temperatures of 300 K and 350 K). These conditions correspond to gas densities ranging from 1,2 kg/m³ to 13,9 kg/m³.

4.2.1 Static Breakdown Voltage

When fast-rising voltages are applied to the gap, as with the nano-second pulsed discharge under investigation, the time needed to reach breakdown influences the value of the measured breakdown voltage V_{bd} [33]. To quantify this effect, the breakdown voltage under slowly rising voltage (DC) is experimentally determined for the same electrode configuration and gas densities to relate the breakdown voltages under fast-pulsed voltages to quasi-static conditions. A HV generator module capable of generating up to 20 kV is used. An empirical formula for estimating the static breakdown voltage (V_0) as a function of the gap distance, density, and electrode gap is derived according to Equation (4.9).

$$V_0 = A + B \left(\frac{dp}{T} \right) \eta_{\text{rel}} \quad (4.9)$$

Figure 4.2 outlines the agreement between the experiments and the fitted empirical formulas.

The parameters A and B for the linear regression are 1,9 kV and 838,0 $\frac{\text{kVK}}{\text{mmbar}}$, respectively. The factor (η_{rel}) depends on the electrode geometry, and it decreases with increasing electrode distance. It is set to 1 for the smallest gap size of 0,2 mm and 0.64 for a gap size of 1 mm; η_{rel} varies with the degree of homogeneity.

Photon absorption is expected to increase with higher pressures. The effective absorption coefficient scaled by pressure depends on the product between pressure and distance from the radiation sources [77]. Data

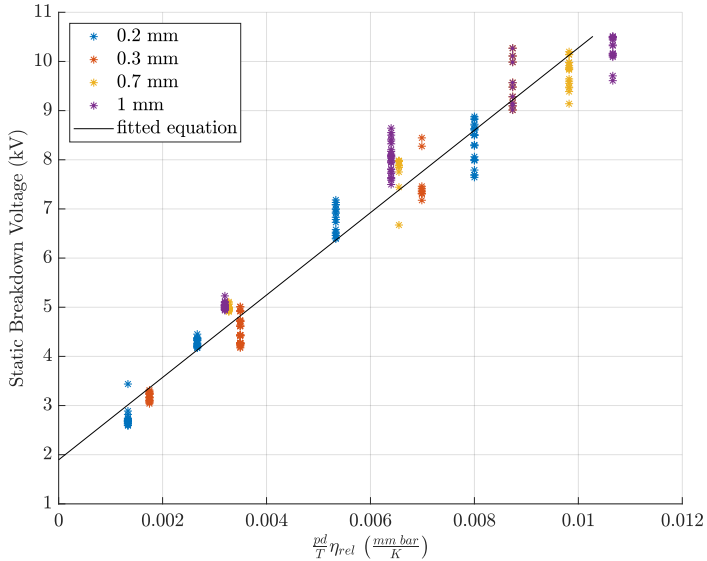


Figure 4.2: Static breakdown voltage

from [78] are used to estimate typical photon absorption lengths for air. Figure 4.3 shows the ratio between the photon absorption length and gap distance on the y-axis and the product of the pressure and gap distance on the x-axis. The distance ratio decreases with increasing product of pressure and distance. For low pressure distance products, the absorption length and the gap distance are similar in value, while for higher values, the gap length is approximately twice the absorption length.

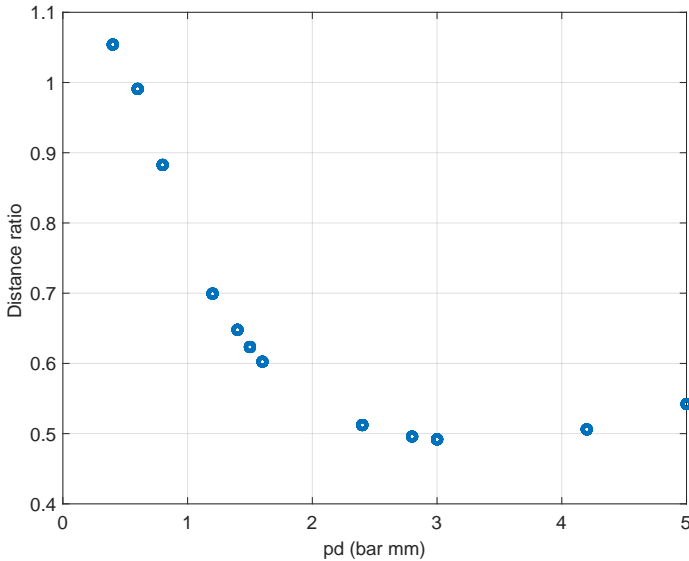


Figure 4.3: Ratio of photon absorption length to pressure gap distance product.

4.2.2 Breakdown Voltage under Nanosecond Pulsed Discharges

By changing the output amplitude of the pulse generator, different breakdown voltages are recorded for air densities ranging from $1,2 \frac{\text{kg}}{\text{m}^3}$ to $11,6 \frac{\text{kg}}{\text{m}^3}$ and for four different gap distances (0,2 mm, 0,3 mm, 0,5 mm, and 0,8 mm). Since the pulse rise time is constant for each pulse generator, different pulse amplitudes result in different pulse rise rates. The cell conditions defined as the multiplication of gas density and gap distance are relevant conditions for ICE operations (where a typical density gap distance of approximately $1 \frac{\text{kg}}{\text{m}^3}\text{mm}$ to $6 \frac{\text{kg}}{\text{m}^3}\text{mm}$ can be expected). The total experimental count is 1754, with breakdown found to occur in 1302 experiments. Figure 4.4 depicts the experimentally measured breakdown voltage under pulsed voltage for all the experiments as a function of the discharge condition (defined as the product of density

and gap distance).

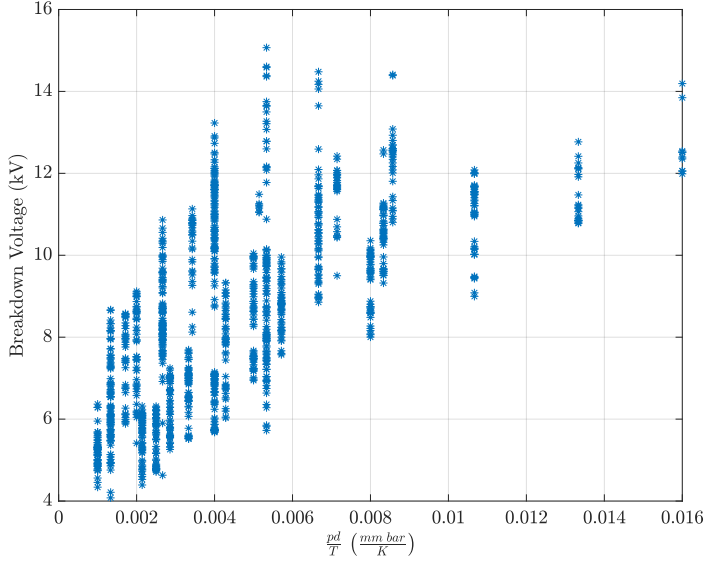


Figure 4.4: Breakdown voltage under pulsed discharge as a function of the density gap distance product for different pulse shapes.

To understand the difference in breakdown voltage, the time needed to achieve breakdown (the time lag) needs to be considered. The ion mobility swarm data (μ_i) are extracted from LXCat [79]. For oxygen and nitrogen, the maximal values are approx. $2 \frac{\text{cm}^2}{\text{Vs}}$ for a density gap distance of $5,5 \frac{\text{kg}}{\text{m}^3}$ mm and applied voltage of 12 kV. The drift time is calculated according to Equation (4.10).

$$\tau = \frac{d}{\mu_i E_{\text{bd}}} \quad (4.10)$$

The corresponding ion drift times range from 20 ns to 400 ns. The electron drift time is approx. two orders of magnitude lower, ranging from

0,5 ns to 7 ns. Equation (4.4) is used to estimate the Townsend formative time: for μ equal to 2 and a fast electron drift time of 1 ns, the deexcitation time dominates the τ_s values ($\tau_s \sim 10$ ns) [66]. The minimum expected formative time for these experiments is approx. 300 ns.

The streamer formative time is estimated using Equation (4.7) without accounting for electric field inhomogeneity with a reduced electric field equal to that at breakdown and neglecting attachment. The average formative time among all experiments is approx. 4 ns with a maximum value of 64 ns and a minimum of 0.1 ns. The formative time estimated from Equation (4.7).

Figure 4.5 subplot (a) shows different gap voltages for the same cell condition (4 bar, ambient temperature, and gap distance of 0,8 mm). Subplot (b) shows the corresponding incident pulse current. The two different pulse generators (FID 30-100NM and FID 15-10NK) are recognizable by the different pulse durations of 10 ns and 50 ns (subplot (b)).

In addition to the pulse duration, the pulse rise rate also plays a role in the breakdown voltage; the higher the rise rate, the higher the average breakdown voltage. Furthermore, very similar pulse shapes can lead to different breakdown voltage levels, and, thus, to successful or failed breakdown: the blue and red traces lead to discharge in one case and no discharge in the other (identical red and blue traces in subplot (b); the blue trace in subplot (a) shows a breakdown, the red trace does not). In all experiments, no breakdown is measured for voltages below the static breakdown voltage (V_0).

The overvoltage at the time of breakdown is given by the difference between the dynamic breakdown voltage $V_{bd} = V(t_s + t_f)$ and the static breakdown voltage V_0 (Equation (4.11)).

$$\Delta V_{bd} = v(t_s + t_f) - V_0 \quad (4.11)$$

The impulse factor is a measure of the overvoltage, and it is obtained by normalizing the overvoltage with the static breakdown voltage, according to Equation (4.12):

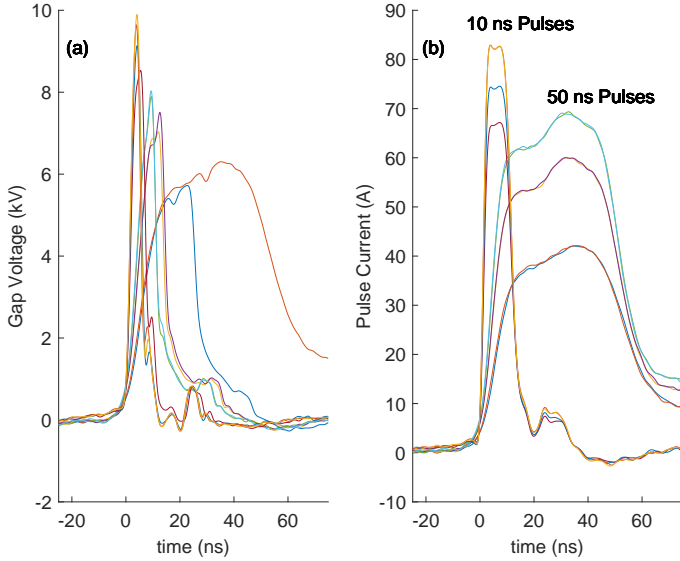


Figure 4.5: Gap voltage (a) and supplied pulse current (i_i) (b), 4 bar, ambient temperature, d : 0,8 mm

$$K = \frac{\Delta V_{\text{bd}}}{V_0} = \frac{V_{\text{bd}}}{V_0} - 1 \quad (4.12)$$

The maximal impulse factor σ is calculated in the same way, but with the breakdown voltage replaced by the maximal voltage that would appear across the gap if no discharge occurs, i.e., the prospective voltage, according to Equation (4.13).

$$\sigma = \frac{V_{\text{max}}}{V_0} - 1 \quad (4.13)$$

$$V_{\text{max}} = 2 \max(v_i)$$

The two parameters K (Equation (4.12)) and σ (Equation (4.13)) quantify the actually achieved and maximal possible overvoltages, respect-

ively. The selected pulse generator amplitude and the cell condition limit the maximal impulse factor value.

If the formative time for a given condition shows minor scatter, an upper limit for the formative time is given by the minimum value for all observed delay times. The higher the number of observations, the closer one gets to the actual values.

Figure 4.6 shows the delay time analysis for all 1754 experiments as a function of the maximal impulse factors. Subplot (a) outlines the minimal observed delay time, which is an upper bound for the formative time, and the lines represent the estimated mean formative time according to Equation (4.7) for the 50 and the 10 ns long pulse (in yellow and purple, respectively). Subplot (b) in Figure 11 shows the mean statistical time for each maximal impulse factor, which is calculated as the mean of the difference between the measured delay and its minimum. The blue and red colors represent the measurements for the 50 ns and 10 ns pulses, respectively.

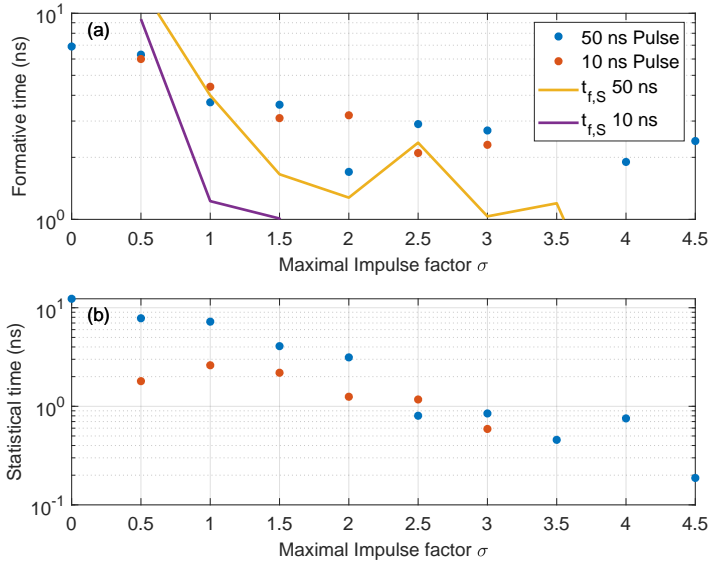


Figure 4.6: Pulsed discharge formative and statistical delay time

Both the formative and the statistical time decrease for higher maximum impulse factors. With the only exception being the peak in statistical time for the 10 ns pulse duration for δ between 0.5 and 1.5. For high impulse factors, the delay time levels off at approximately 3 ns for both pulse generators with a low statistical variation. Figure 4.7 depicts the discharge probability (number of breakdowns divided by number of applied pulses) and the measured impulse factor as a function of the maximal impulse factor in subplots (a) and (b), respectively. For subplot (b), the error bars depict the minimal and maximal measured values. For maximal impulse factors above ~ 1.25 , discharge is always present. When the discharge probability is below 100%, the measured impulse factor is limited by, and closely follows, the maximal possible impulse factor. The trends reported in Figure 4.6 and Figure 4.7 remain invariate by taking into account only experiments having a similar density and gap distance product.

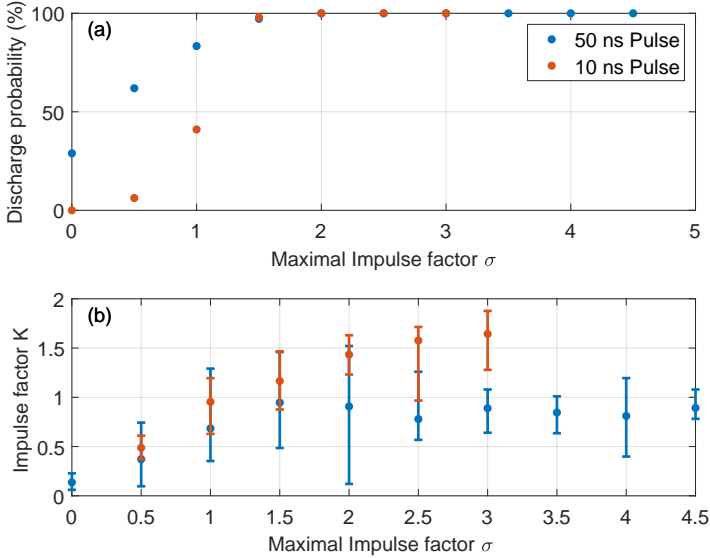


Figure 4.7: Pulsed discharge probability and measured over-voltage

4.2.3 Summary and Discussion

The static breakdown voltage is linearly correlated to the product of the density gap distance and η_{rel} . The decrease in η_{rel} for larger gaps correlates with the expected increase in electric field inhomogeneity. The field inhomogeneity increases with increasing gap size.

The secondary avalanche plays a minor role in the breakdown onset for the analyzed electrode configuration. Two factors contribute to the increase in breakdown voltage sustained by the Townsend mechanism. First, the relatively high densities make it more difficult for photons to reach the cathode. The length ratio between the gap distance and absorption length decreases with increasing pressure gap distance product from approx. 1 to 0.5. At higher pressure, it is increasingly difficult for photons to reach the cathode. Second, it is difficult for secondary electron emission to occur in a strongly inhomogeneous electrode config-

uration. The sharp edges of the electrodes and the corresponding electric field enhancement provide favorable conditions for strong electron multiplication, but secondary electron feedback can then only occur in a relatively small area. Nevertheless, for slowly varying voltages, secondary avalanches may play a role in the discharge process in a narrow range of small overvoltages.

A Townsend breakdown in a pulsed discharge is very unlikely, as there is not sufficient time for its formation even when the breakdown is sustained by photoelectrons from the cathode (minimum formative time of approx. 300 ns). For the pulse durations employed in this work, the Townsend breakdown mechanism is not compatible with the observed delay times.

In pulsed discharge mode, the breakdown voltage is always above the static voltage. Under pulsed discharge, the delay time between reaching the static breakdown voltage and the actual breakdown voltage is affected by the pulse shape. With the current setup for a given condition, the higher the maximal impulse factor, the higher the pulse rise rate. Statistical time variations are present due to the time needed for the appearance of seed electrons. The formative time is the time necessary for an avalanche to grow to the critical size, bridge the gap and form a conductive channel. Differences between practically identical experiments suggest that statistical influences of seed electron generation are present. Thus, statistical time lag variation gives rise to different discharges for similar pulses.

The decreasing trend for the formative time lag for higher impulse factors agrees with Equation (4.7). The formative time lag is inversely proportional to the ionization coefficient and the electron drift velocity, both of which increase with increasing electric field. The streamer formative time, Equation (4.7), is estimated without accounting for field inhomogeneity and temporal electric field variation. These assumptions give the proper order of magnitudes for the time involved. Nevertheless, assuming a homogenous field will probably lead to higher estimates of the formative times when in reality the avalanche to streamer transition occurs near the electrodes where the electric field, and, therefore, the ionization coefficient are enhanced. For avalanche to streamer transition positions far from the electrodes, the difference should be lower [80]. The non-varying electric field assumption will lead to underestim-

ation of the formative time when breakdown occurs on the fast rising pulse flank. In this case, the streamer will develop at a lower reduced electric field than the breakdown electric field. Due to formative time, the breakdown voltage is higher than the average voltage during avalanche formation [81]. The first assumption will probably have more influence at lower overvoltages, where the avalanche will propagate in the more favorable part. The second assumption will likely have a more significant impact at high overvoltage because the static breakdown voltage is crossed during the fast-rising phase of the pulse. The real formative time is perhaps lower for low overvoltage and higher for high overvoltage. This hypothesis agrees well with the discrepancies observed between the estimated and measured values. The formative time is experimentally defined as the minimal measured delay time for a given condition. The statistical time reduction can be explained by the increase in the critical volume, i.e., the volume where a seed electron can lead to breakdown with a high probability ($>50\%$). The possible discharge volume increases, and with that, the probability that one seed electron is present and develops into a streamer also increases.

When a sufficiently high external electric field is applied to a metal surface, the electrons can escape by tunneling from the metal [74]. This mechanism can also reduce the statistical time, increasing the seed electron generation rate at higher overvoltages.

When the discharge probability is below one, the delay times are limited by the pulse duration. The peak of the statistical time lag for the 10 ns pulses can be explained by the limited pulse time; even though the seed electron generation rate is lower for lower overvoltages, the average statistical time is lower, but a seed electron is not present (no breakdown) for all the experiments. The higher the maximal impulse factor for a given pulse generator, the higher the measured impulse factor. This means that breakdown at a higher voltage can be reached by using higher amplitude pulses with a higher rise rate. The discharge probability is influenced by the pulse duration and overvoltage. The higher the maximal impulse factor and the higher the pulse duration, the more likely the breakdown. When the pulse overvoltage is below 1.25, the probability of discharge is below one. For shorter pulses, the breakdown probability is lower. The breakdown voltage under pulsed discharge can be successfully estimated for each pulse generator as a function of the maximal impulse factor and the static breakdown voltage. The

discharge probability and the breakdown voltage depend on the pulse duration, overvoltage, and pulse rise rate. Multiple pulses at a high repetition frequency are used for ignition in engines to give the minimum energy necessary for ignition at moderate amplitudes. Short-duration pulses are advantageous to reduce arc discharge as much as possible, which is believed to be an effective way to reduce electrode wear. Experiments with ten pulses at a repetition frequency of 10 kHz (Section 3.3) show that the discharge probability, breakdown voltage, and formative time in multiple pulse modes can be interpolated from single-pulse experiments up to the first breakdown. Afterward, the breakdown occurs at a lower level. A possible explanation for this is the reduced local density due to the energy deposition in the previous pulse or the presence of ionized molecules, excited species and free electrons (no lack of seed electrons).

Experiments have outlined that in addition to pulse duration, the pulse rise rate is the factor that mostly influences discharge characteristics. The maximal overvoltage dictates the discharge probability, total delay time, and breakdown value. Moreover, these findings can be used in repetitively pulsed discharge up to the first breakdown. Theoretical estimates of the formative times for the Townsend and streamer mechanisms suggest that only the streamer mechanism is compatible with the observed delay times under pulsed voltage conditions. For the investigated configuration, both the statistical and formative time lags can be of the same order of magnitude, and it is, thus, not generally possible to neglect the influence of the formative time on the breakdown voltage. These findings can be successfully used to describe the breakdown voltage as well as the discharge probability. The experimental results indicate that high breakdown voltages of up to 290% of the breakdown voltage with a slowly varying voltage are achievable with high pulse amplitudes with steep voltage rise rate. High breakdown voltages are expected to create a more favorable ignition area (high temperatures with high radical concentrations), leading to a fast and reproducible transition to a self-sustained chemical reaction. The ideal pulse shape for ignition purposes is probably one that gives the maximal amount of energy in the breakdown phase. Therefore, the voltage rise rate should be as high as acceptable (considering electromagnetic interference, cost) because this will lead to a high breakdown voltage. The ideal pulse duration should be short (approx. ten to twenty nanoseconds) to avoid or reduce the transition to an arc. The reduced time,

or, ideally, absence of an arc should extend the lifetime of the spark plug.

4.3 Analysis of Breakdown in Quasi Uniform Electric Fields

The influence of the nanosecond pulse rise rate on the breakdown voltage and breakdown time is discussed in Section 4.2. Two pulse durations of 50 and 10 ns are used, and streamer theory is identified as the breakdown onset mechanism. Due to the fast but finite pulse rise time, significantly different breakdown voltages and times for varying pulse rise rates are present. In Section 4.2, the minimal observed breakdown delay time is used as an upper bound for the formative time. The statistical time lags decrease with increasing overvoltages. Moreover, the seed electron generation rate, which primarily determines the statistical time lag, strongly increase at large fields. Nevertheless, a quantitative analysis of the seed electron rate is difficult with the data discussed in Section 4.2 because the study used automotive spark plugs where the electrode geometry is complex and nonuniform. In such a geometry, estimating the active cathode area, for which an electron appearing near the cathode can induce breakdown, is complex and subject to considerable uncertainties.

This section aims to provide and analyze similar experimental data but for a simplified electrode geometry (sphere-plane, quasi-uniform electric field), for which the seed electron generation rate can be determined more accurately using the calculated active cathode area.

The provided parametrization of the seed electron rate as a function of the gap electric field and pressure is a novel contribution, which can be used to develop models for breakdown or discharges under nanosecond transients.

Breakdown thresholds for DC voltage are also measured under the same conditions of gap distance and pressure to allow for direct comparison and normalization of the transient breakdown voltages. For both the transient and DC voltages, the effect of the electrode material and UV illumination of the cathode are investigated to obtain information about the presence of secondary feedback and the role of seed electron pro-

vision. As the timescale of the voltage application drops to the same order of magnitude as the statistical delay, the seed electron generation rate is expected to have a significant impact on the observed breakdown voltage. A clearer physical picture and a quantitative description of the seed electron generation mechanism in small gaps are thus required.

4.3.1 Experimental Setup

The constant volume cell (see Section 2.2) is used to characterize the breakdown onset for static and nanosecond pulsed voltages using the modified spark plug offering the quasi-uniform electric field. The absolute pressure in the constant volume cell is varied from 1.5 to 8 bar (six pressure values).

The first few breakdowns conditioned the electrodes. After the preliminary tests, the electrodes do not show any further "conditioning effect". The static breakdown voltage is measured for different conditions at the start and end of the measuring campaign and does not show any appreciable difference. This suggests that the impact of field distortions caused by the discharge's micro-asperities remained constant throughout the experiments.

A DC HV module capable of generating up to 12kV is used to perform short-term breakdown tests under slowly increasing voltage. The voltage is monitored with a HV probe (Tektronix p6015a) during the voltage increase (approx. 100 V/s), and the recording is triggered on the breakdown current pulse.

Nanosecond pulses are generated by the commercial nanosecond pulse generator delivering the 50 ns long pulses (FID 30-100NM). Figure 4.8 depicts in red the prospective voltage waveform, i.e. the voltage waveform that would appear across the gap if no breakdown occurred, while in blue the actual gap voltage.

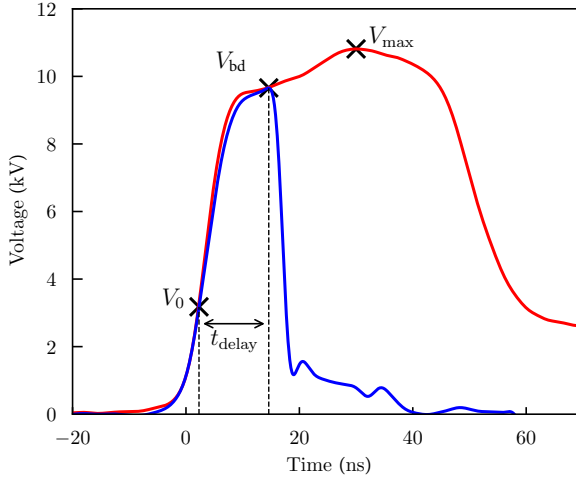


Figure 4.8: Nanosecond voltage pulse prospective voltage (red) and gap voltage (blue) at 1.5 bar and 0.1 mm gap distance with aluminum electrodes.

UV Illumination

In selected experiments, a mercury lamp is mounted onto the fused silica glass window of the constant volume cell to illuminate the cathode with UV light. The impact of UV illumination is tested in both the static and nanosecond pulsed cases.

Material Effect

Electrodes (HV and GND) made of aluminum, copper, and stainless steel are used to investigate the impact of the electrode material on the breakdown voltage in both the static and pulsed voltage cases. The effect on breakdown time lag is also quantified for the pulsed voltage. The materials were chosen because of their difference in the vacuum work functions, which are ~ 4.26 eV (Al), ~ 4.47 eV (Cu), and ~ 5.08 eV (Steel), respectively [82, 83].

Electric Field Data

The electric field is determined with COMSOL Multiphysics software. The electrode system is modeled with rotational symmetry, as shown in Figure 4.9, based on the geometry shown in Figure 2.4. Only the electric field lines ending on the GND electrode are considered in this analysis. The field amplitude is shown for a voltage of 1 V and is scaled accordingly for the actual applied voltages.

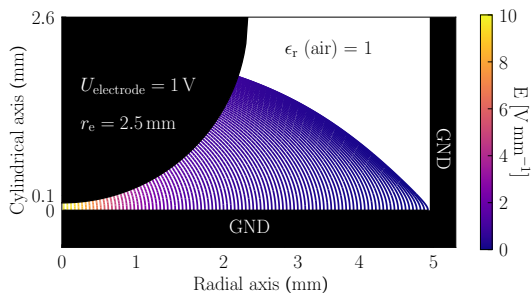


Figure 4.9: Electric field simulation for a gap distance of 0.1 mm.

4.3.2 Static Breakdown Voltage

Figure 4.10 shows the breakdown voltage value under a slowly increasing voltage ($\sim 0,1$ kV/s) for ambient temperature and absolute pressures ranging from 1.5 to 8 bar. The gap size is varied, where possible, from 0,1 mm to 1 mm. The full line for the 3 bar case represents the breakdown values according to Townsend theory for $\gamma = 2.2 \cdot 10^{-4}$. The minimum and maximum measured breakdown values are shown as well for the 3 bar case. The dashed lines represent a linear fit of the calculated mean breakdown value for a given pressure.

A linear fit follows Townsend theory in the investigated pressures and gap sizes. The indicated measured values are averaged over approximately 20 breakdown measurements. The maximal relative deviation of individual readings from the mean value is always below 10% for each experiment, while the average of the maximal deviations for all the investigated conditions is $\sim 3\%$. The relative deviation of the mean

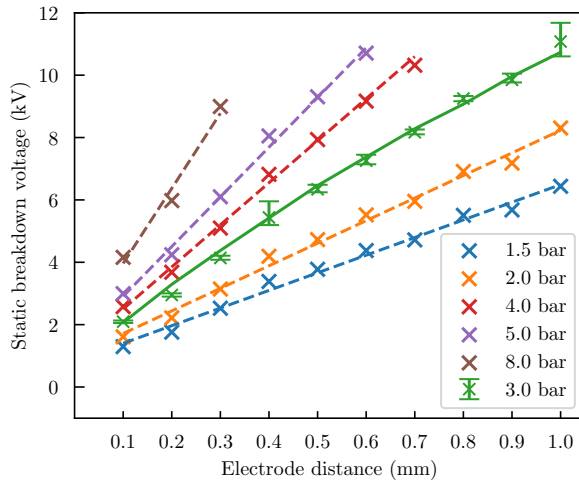


Figure 4.10: Static breakdown voltages as a function of gap distance and synthetic air pressure (for steel electrodes).

value with respect to the fit line remains below $\sim 12\%$, with an average deviation of $\sim 3\%$. Figure 7 shows that the mean breakdown voltage increases approximately linearly with gap distance.

Figure 4.11 illustrates the effect of UV illumination on the static breakdown voltage. The box plot represents, from top to bottom, the maximal measured value, the 75th percentile, the mean value, the 25th percentile, and the minimal value.

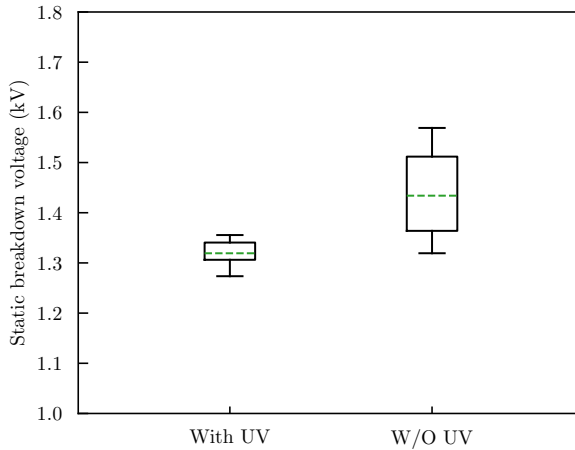


Figure 4.11: Electric field simulation for a gap distance of 0.1 mm.

The mean breakdown voltage under UV illumination is lower in the investigated cases. No relative error in gap distance is present because the electrode distance is not reset between the experiments with and without UV illumination. Generally, the relative lowering of mean breakdown voltages is more significant at lower pressure-gap distances, as is the reduction in scattering around the mean. An overview of the results is given in Table 4.1.

Condition (p,d)	Mean (w/o UV)	Mean (UV)	p value
1.5 bar, 0.1 mm	1.43 kV	1.32 kV	4.6×10^{-7}
3 bar, 0.5 mm	6.11 kV	6.02 kV	2.5×10^{-4}
3 bar, 0.9 mm	9.44 kV	9.35 kV	9.8×10^{-4}

Table 4.1: UV impact on the static breakdown voltage.

Breakdown voltages and times are subject to relatively large scatter even when all macroscopic parameters are held constant. It is thus often not directly obvious from the measured data whether a change in the experimental conditions indeed influences the underlying probability distribution (i.e., the breakdown process). The difference in the col-

lected data may be due to random variations that occur in finite sample sizes. In such cases, statistical tests are required, which determine (under certain assumptions) the probability that the observed difference in, e.g., the mean breakdown voltage, is just due to the finite sample size. In this section, the Mann–Whitney U test [84] is used, whose p value indicates the probability mentioned above that the null hypothesis H_0 "the underlying probability distributions are the same" is true. For example, the probability that the observed differences between the sample with and without UV illumination at 1,5 bar and 0,1 mm is pure chance is less than 10^{-6} . The Mann–Whitney U test is nonparametric and, in particular, does not assume the normality of the underlying distributions. This comes at the cost of lower power, i.e., a larger probability of a Type II error (not rejecting H_0 when it is false).

Table 4.2 lists an example measurement of the static breakdown voltage for the three different materials, a gap size of 0,5 mm and a pressure of 1,5 bar. The p value is the result of the Mann–Whitney U test between the two different sets of results for the two materials in parentheses.

Material	Mean Voltage	Confidence Interval (95%)	p value
Steel	3.73 kV	0.024 kV	0.01 (Steel-Cu)
Copper	3.65 kV	0.044 kV	1.96×10^{-6} (Cu-Al)
Aluminum	3.51 kV	0.048 kV	1.85×10^{-12} (Al-Steel)

Table 4.2: Electrode material impact on the static breakdown voltage.

The measured mean breakdown voltages are on the order of the associated cathode vacuum work functions. To take into account the effect of the gap size error, the breakdown voltages of each material are measured three times consecutively by resetting the electrode distance to the same nominal gap distance. When the associated sample's breakdown voltage means do not show a significant difference ($p > 0.05$), i.e., when the distance setting does not significantly change the observed breakdown values (as is the case reported in Table 4.2), ordering according to the work function values is observed. In some instances, however, the error introduced by the gap setting dominates the order of the mean breakdown values. In these cases, the mean breakdown values of the three repetitions show a significant difference ($p < 0.05$).

4.3.3 Pulsed Breakdown Voltages and Breakdown Times

Figure 4.12 and Figure 4.13 show, respectively, the breakdown voltage and breakdown time of 1093 experiments with pulsed voltages in synthetic air with pressures ranging from 1.5 to 8 bar and for electrode distances between 0.1 and 1 mm in 0,1 mm steps. For clarity reasons, the breakdown voltages and times are slightly offset to the right for increasing pressures.

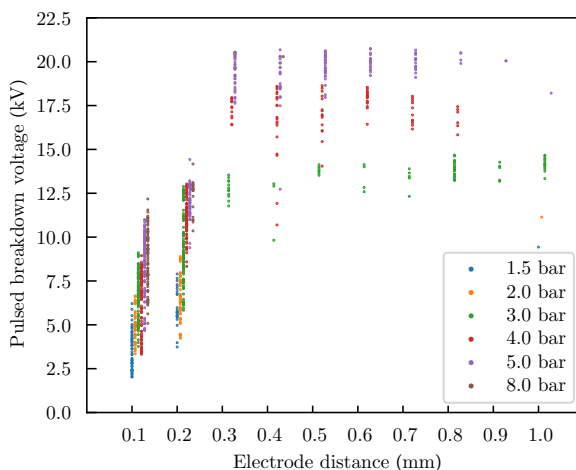


Figure 4.12: Pulsed breakdown voltages as a function of gap distance and synthetic air pressure (for steel electrodes).

As shown in Figure 4.1, the formative time lag is negligible compared to the measured delay times. The statistical time lag t_s causes a breakdown to occur at a certain overvoltage characterized by the impulse factor K (Equation (4.12)). The measured impulse factors ranged from 0.2 to 4.4 for the different conditions and were above the corresponding Townsend-to-streamer transition voltages for $\gamma = 2.2 \cdot 10^{-4}$ (see Section 4.1). Due to the short but non-negligible pulse voltage rise time of approximately 9 ns, breakdown can occur on the rising part of the pulse as well on the nearly flat part of the pulse. The maximal impulse factor σ describes where the breakdown occurs.

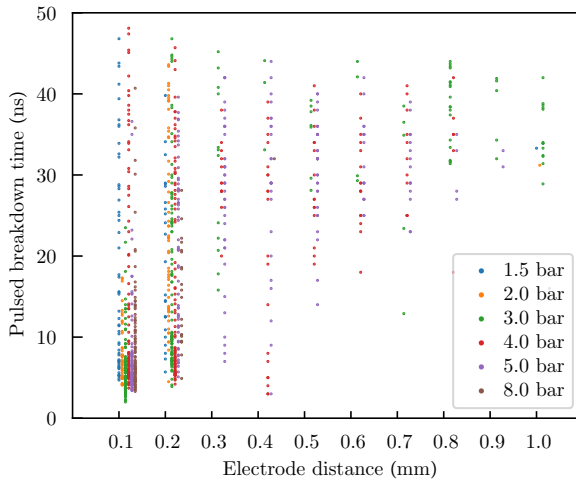


Figure 4.13: Delay time under pulsed breakdown voltages as a function of gap distance and synthetic air pressure (for steel electrodes).

Figure 4.14 and Figure 4.15 provide, an overview of the measured impulse factors and the measured breakdown time for a 0,1 mm gap at 1,5 bar pressure and ambient temperature under 52 voltage pulses of different maximal impulse factors. The box plots in Figure 4.14 and Figure 4.15 represent from top to bottom the maximal measured value, the 75% percentile, the mean value, the 25% percentile, and the minimal value.

The maximal impulse factor σ and the impulse factor K as defined in Equations (4.12) and (4.13) are used in this investigation as well. Breakdown occurs with relatively small scatter near the voltage maximum for maximal impulse factors $\sigma < 2$ (rising line in Figure 4.14). At higher prospective overvoltages, the achieved impulse factors are considerably smaller than the maximal impulse factor, indicating that breakdown occurs in the early rising part of the pulse. In addition, the scatter in the breakdown voltages is significantly larger.

The measured breakdown times follow a specific pattern. As shown in Figure 4.15, they fall off rapidly with increasing maximum overvoltage

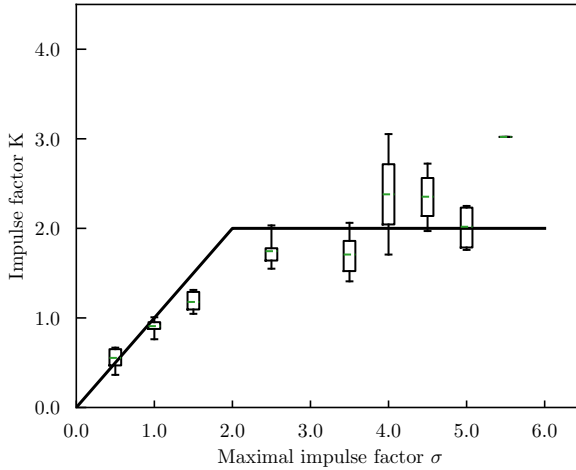


Figure 4.14: Measured impulse factors (relative overvoltage at breakdown) as a function of the maximal impulse factor (maximum relative overvoltage of the applied pulse) at 1,5 bar and 0,1 mm.

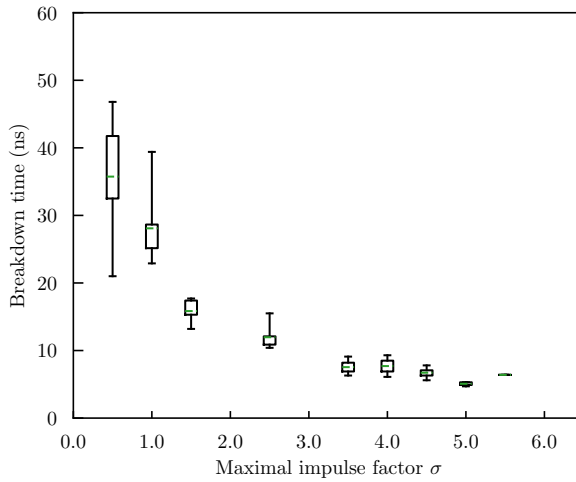


Figure 4.15: Measured breakdown time as a function of the maximal impulse factor at 1,5 bar and 0,1 mm gap distance.

of the applied pulse ($0.5 < \sigma < 2$) but show a saturation for $\sigma > 2$. For the breakdown times, the scatter decreases with increasing overvoltage.

Only one experimental point is present for ($\sigma = 5.5$), represented by the green line, since the calculation of percentiles, minimal, and maximal values is impossible.

These trends of breakdown voltages and times are present at different pressures and gap distances whenever high maximal impulse factors are reachable with the setup used.

Figure 4.16 shows the impact of UV illumination on breakdown times for the 0,1 mm gap size and 8 bar synthetic air pressure. The mean value and the 95% confidence interval of the mean are reported in the plot.

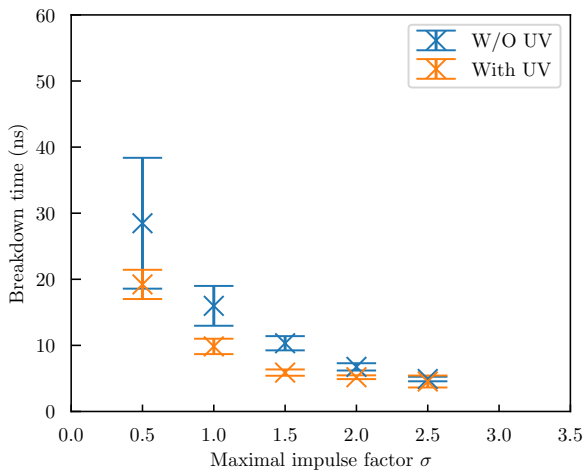


Figure 4.16: Impact of UV illumination on the breakdown time as a function of the maximal impulse factor.

The results are representative of all the investigated conditions where the range of accessible σ is large. The mean breakdown times and their scatter are significantly lower in the presence of UV light, but the effect decreases with increasing overvoltage.

The effect of different materials on the mean breakdown threshold un-

der pulsed voltages is illustrated in Figure 4.17 for a 0,2 mm gap size, synthetic air pressure of 3 bar, and ambient temperature. The mean value and the 95% confidence interval of the mean are reported.

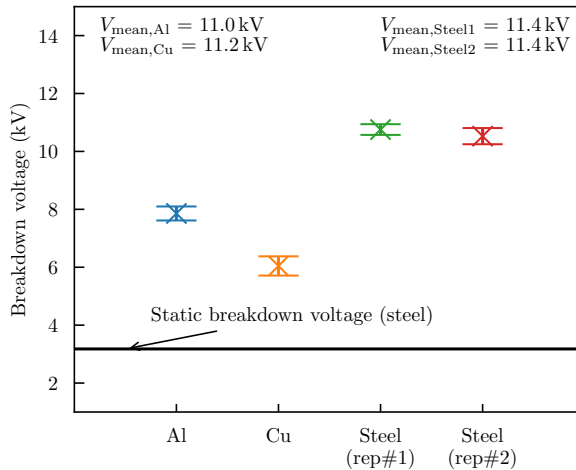


Figure 4.17: Electrode material effect on the breakdown voltage under pulsed voltages at 3 bar and 0,2 mm gap distance.

Interestingly, the steel electrodes show a significantly higher breakdown threshold than the aluminum and copper, and there is even a significant fraction of cases ($\sim 15\%$) where no breakdown occurs with the steel electrodes for the tested range of overvoltages. To check the validity of the experimental results, the measurement series is repeated for the steel electrodes (rep#2), and the previously obtained values (rep#1) are confirmed. Moreover, a possible bias due to fluctuations in the maximum prospective pulse voltage is examined: it turned out that the prospective pulse amplitudes applied to the steel electrodes are even slightly larger (see Figure 4.17, top) and cannot explain the significantly larger breakdown values. The maximum prospective voltage is between 10.5 and 11,5 kV. The horizontal line in Figure 14 represents the static breakdown voltage for the shown condition.

Figure 4.18 depicts the mean breakdown time and the 95% confidence intervals of the experiments where a breakdown is present. The m and

n numbers on the top of Figure 4.18 list the number of experiments with and without breakdown, respectively.

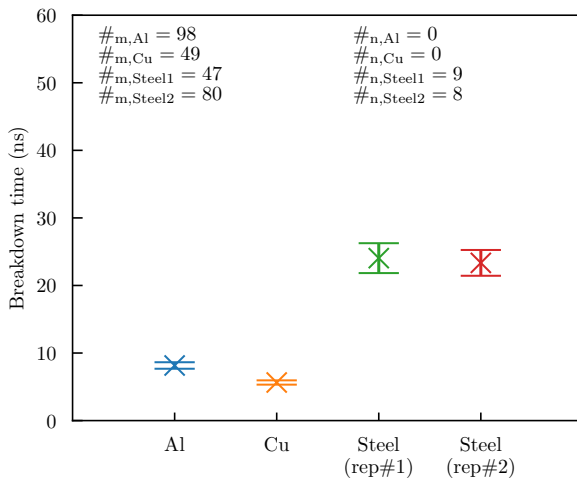


Figure 4.18: Electrode material effect on the breakdown time under pulsed voltages at 3 bar and 0,2 mm gap distance.

4.3.4 Seed Electron Generation Rate

This section aims to derive an expression for the seed electron generation rate as a function of the gap electric field strength. The following analysis is meant to provide an order of magnitude estimation, thus including a number of simplifying steps. For example, due to the quasi-uniform geometry, a mean electric field strength U/d is attributed to the applied voltage U and used to parametrize the derived electric field dependencies. The analysis is carried out for 0,1 mm and 0,2 mm gap distances and pressures of 1.5, 2, 3, 4, 5, and 8 bar, as these conditions fully cover the experimentally accessible range of electric fields up to approximately 120 kV/mm. A total of 960 breakdown measurements are available for the analysis.

An important parameter in the analysis is the active cathode area A_{act} , which is the area on the cathode where the associated field lines satisfy the streamer criterion (Equation (4.5)) for $K_{st} > 16$. Thus, a free electron near the active cathode area is likely to induce a breakdown, while

outside this area, it is likely to become attached and simply drift to the anode. The attachment and ionization coefficients required for this calculation are extracted from the Boltzmann equation solver BOLSIG+ [51] using the cross-sectional datasets reported in [52–54].

First, the dependence of the average time to breakdown on the electric field strength is derived from the measurement data in the following way. A list of voltages with equally spaced bins spanning a range from the calculated streamer onset voltage to the largest measured breakdown voltage is defined for each pressure and gap distance. The voltage list size is chosen so the distance between the values is approx. 500 V. Division by the gap distance generates an associated (mean) electric field list $[E_i]$. Let then Δt_i be the cumulated time (i.e., from all measurements at a given pressure and gap distance), let the applied mean electric field $U(t)/d$ value lie in bin number i , and let O_i be the number of observed breakdown values in this bin. The average time the system gas is “stable” (no breakdown) when exposed to the field E_i is given by Equation (4.14).

$$t_{bd}(E_i) = \frac{\Delta t_i}{O_i} \quad (4.14)$$

This average time to breakdown is shown in Figure 4.19 for gap distances of 0,1 mm and 0,2 mm and all available pressures.

The time to breakdown is determined by the number of electrons generated near the active cathode area per unit time. Thus, if $\dot{n}_e(E)$ is the seed electron generation per unit time and cathode area at the electric field strength E , Equation (4.15) describes the relation between $t_{bd}(E)$ and $\dot{n}_e(E)$.

$$t_{bd}(E) \approx t_s(E) = \frac{1}{A_{act}(E) \cdot \dot{n}_e(E)} \quad (4.15)$$

The only unknown quantity is then $\dot{n}_e(E)$. Note that the formative time is negligible with respect to the measured time to breakdown and can thus be omitted in Equation (4.15). The dotted lines in Figure 4.19 indicate that field-independent seed electron generation does not fit the experimental data adequately. Instead, the full lines are based on a

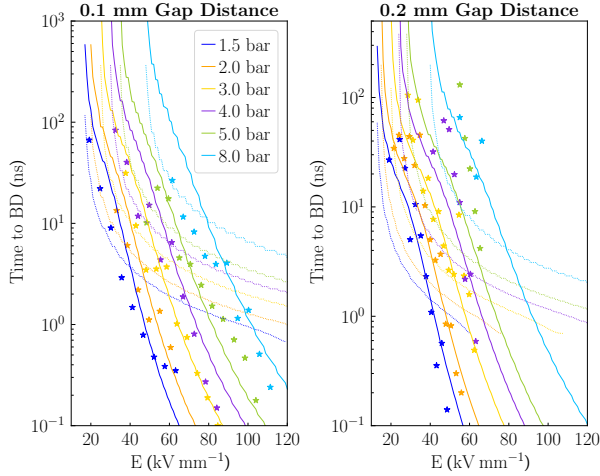


Figure 4.19: Determined mean times to breakdown as a function of the gap electric field. Fit lines are based on seed electron generation rates with (full line) and without (dotted line) activated field emission.

field emission contribution based on the Fowler-Nordheim formula [85] (with empirically derived parameters), which is activated at high fields on top of a constant background rate $\dot{n}_{e,0}$ (Equation (4.16)).

$$t_{bd}(E) = \frac{1}{A_{\text{act}} \cdot \left[\dot{n}_{e,0} + C \cdot E^2 \exp\left(-\frac{Dp^b}{E}\right) \right]} \quad (4.16)$$

A least-square fit over the 112 available data points for 0.1 mm and 0.2 mm gap distances leads to the following parameters: $\dot{n}_{e,0} = 1,1 \text{ ns}^{-1} \text{ cm}^{-2}$, $C = 6.7 \cdot 10^3 \text{ ns}^{-1} \text{ kV}^{-2}$, $D = 178 \text{ kV mm}^{-1}$ and the coefficient $b = 0.53$.

Figure 4.20 shows the resulting seed electron generation as a function of the mean gap electric field.

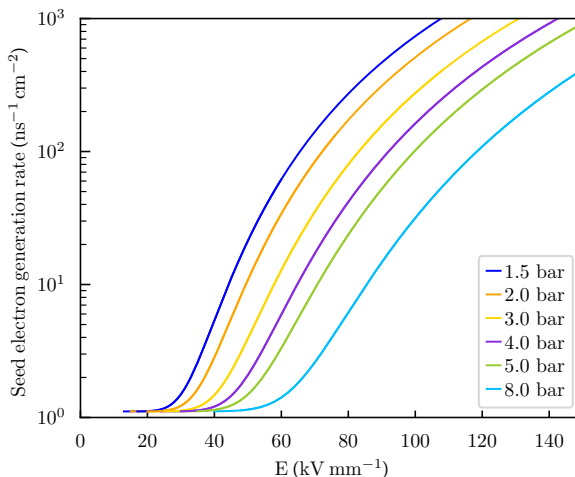


Figure 4.20: Derived seed electron generation rate as a function of the electric field.

4.3.5 Summary and Discussion

The observed quasi-linear increase in the static breakdown voltage with the gap distance is in good agreement with the predictions from Townsend's theory and a secondary feedback emission coefficient of $\gamma = 2.2 \cdot 10^{-4}$, which is a typical value reported for air [86]. Indeed, all the investigated cases are well above the Paschen minimum at $(p \cdot d)_{min} = 7.3 \mu\text{m bar}$ [33], which explains the approximately linear increase with both pressure and gap distance.

The reduction of the statistical spread in the static breakdown voltage under UV illumination might, on a first account, be attributed to the corresponding increase in seed electron generation. UV illumination reduces the statistical time lag and hence the breakdown voltage (dU/dt is small but not zero). However, with a background rate of $\dot{n}_{e,bk} = 1.1 \text{ ns}^{-1}\text{cm}^{-2}$, the voltage slew rate would need to be much larger than the applied $\sim 100 \text{ V/s}$ to see any observable spread in the breakdown voltage. A possible explanation is the following. Just around the onset voltage of Townsend breakdown, the active area is concentrated at a small section at the tip of the half-sphere. The prob-

ability of a seed electron triggering a sequence of avalanches, in which all feedback photons hit the active area, can be tiny. This means that the vast majority of secondary seed electrons will not induce breakdown, and hence, the apparent statistical time lag is much larger than what is expected from the seed electron generation rate. This reasoning assumes that the main secondary feedback mechanism is the photoeffect at the cathode, which is in accordance with the available literature for pressurized air and metallic electrodes [73].

The simultaneously observed lowering of the average static breakdown voltage under UV illumination is also in line with qualitative theoretical reasoning based on the increase in the amplification factor $\mu' > \mu$ in the presence of a constant source of external seed electrons [72].

Finally, the reduction of the static breakdown voltage with the reduced cathode work function values can also be explained within Townsend's theory by an increase in the amplification factor (larger secondary electron emission coefficient). All observations support the conclusion that the discharge under slowly increasing voltages and the investigated range of pd values from 0.1 to 8 mm bar is governed by the Townsend mechanism.

The remainder of the discussion is dedicated to breakdown under nano-second pulsed voltages, for which the DC breakdown voltages serve as a helpful point of reference. Due to the short rise time of the voltage pulse (~ 9 ns), large overvoltages can develop during the time before a seed electron appears. Indeed, breakdown voltages exceeding the static threshold by up to 440% were observed.

Two breakdown regimes are present (see Figure 4.14 and Figure 4.15): at a low maximal impulse factor, the breakdown time has large variability, but the breakdown voltage has low scatter. Conversely, at high maximal impulse factors, the breakdown voltage scatters significantly, whereas the time falls in a relatively narrow interval. Similar breakdown regimes are reported in Section 4.2, where, due to the complex geometry involved, the calculation of the active area is difficult. This behavior can be related to the employed voltage pulse shape. When the maximum overvoltage is small, breakdown is likely to occur in the plateau of the pulse because seed electrons are unlikely to become available in the few nanoseconds it takes to reach the voltage plateau in the small active area that is created by the low overvoltages. The break-

down voltage is equal to the plateau voltage, and breakdown times span the whole duration of the pulse (up to 50 ns). In contrast, when the maximum overvoltage is large, seed electrons are generated at a higher rate over a larger area due to the large fields developing during the rising edge of the pulse or shortly thereafter. With the breakdown occurring in this interval, the breakdown times are small and localized, whereas the breakdown voltages scatter significantly due to the large dU/dt (even minor breakdown time variations result in significant breakdown voltages variation). For a synthetic air gap of 0,1 mm and pressure of 1,5 bar, the breakdown times for impulse factors above 3 vary between 5 and 9 ns, with the latter being equal to the typical pulse rise time.

The sharp transition between the two regimes also supports the conclusion of a field-dependent seed electron generation rate. Without the field emission, the breakdown rate increase should follow the slower increase in the active area.

The quantitative analysis presented in 4.3.4 shows that the time to breakdown is a strongly decreasing function of the electric field. For relatively small field strengths, the increase in the active area can explain the observed decrease in the mean breakdown time. However, this effect alone cannot explain the rate of decrease in breakdown times at higher field strengths, where the seed electron generation rate itself seems to increase significantly above the low field (background) value. The breakdown times are well reproduced by a Fowler-Nordheim-type equation [85], suggesting a field emission of electrons from the cathode. The proposed parameterization of the associated seed electron generation represents a novel contribution. After the field emission activation, electron emissions over the macroscopic surface of $\sim 10^8$ electrons per second and cm^2 are estimated. [87] reports the release of electrons from cold, heavily oxidized steel electrodes in the atmosphere. Up to 10^6 electrons per second are released under an applied field of 1 kV/mm, which matches the proposed prediction based on the Fowler-Nordheim emission equation. In [87], the area from which the electrons are emitted is of $\sim 10^{-14} \text{cm}^2$, suggesting that the electrons might be liberated from groups of negative ions at the cathode surface.

Comparing the experimentally derived field-dependent seed electron emission rate with the quantitative predictions from the Fowler-Nordheim equation allows the determination of the actively emitting surface

fraction and the effective work function of these emitters as a function of pressure [88]. A pressure-independent active surface fraction of $2 \cdot 10^{-15}$ is obtained, and the effective work function is found to increase from 2,25 eV at 1.5 bar to 4 eV at 8 bar. These numbers suggest that field emission occurs over groups of atoms with low effective work functions. Moreover, a higher gas number density seems to hinder electron emission from these sites. The increasingly effective work function of the emission sites at larger pressure may thus be an effect of the adsorption of gaseous constituents onto the emission sites, thereby reducing the electron emission yield.

While the field emission hypothesis paints a consistent picture with the obtained data and has also been previously invoked for the explanation of time lags of electrical breakdown under pressurized gases [89], another a priori plausible explanation (for pulsed breakdown) based on the field-dependent detachment of electrons from unstable negative oxygen ions is argued to be less consistent with the observed data. First, the detachment of electrons occurs on average in a few collisions at fields as low as $3,8 \text{ kVmm}^{-1}$ in air at atmospheric pressure [90]. Hence, a negative ion available in the gap before the voltage pulse arrives would lose its electron in a fraction of a nanosecond and not lead to a field dependent detachment that could explain the observed time delays. Second, if detachment from negative ions dominates, the detected breakdown dependency on the electrode material should be lower. Third, and even more importantly, the equilibrium number density of unstable negative ions (N_i) is low in the considered small gaps, such that the probability of finding a suitably placed negative ion upon arrival of the voltage pulse is negligible for practical purposes. The maximum equilibrium number density in the gap is proportional to the background ionization rate Q ($\sim 10 \text{ cm}^{-3}\text{s}^{-1}$), gap distance d , diffusion coefficient D_i ($5 \cdot 10^{-2} \text{ cm}^2\text{s}^{-1}$ at 1 bar) and pressure [6]:

$$N_i = \frac{Qd^2p}{8 \cdot D_i} \quad (4.17)$$

For $d = 0.2 \text{ mm}$ and a pressure of $p = 8 \text{ bar}$, $N_i \sim 8 \cdot 10^{-2} \text{ cm}^{-3}$, while the active volume is only a fraction of a cm^{-3} . The generation of a seed electron by detachment from negative ions thus seems unlikely in such small gaps, unless the volume ionization rate is increased significantly

(e.g., by exposing the gap to artificial ionizing radiation) or nonequilibrium conditions apply (e.g., in repetitively pulsed discharges). It thus remains unclear what is the source of seed electrons constituting the background rate, and more targeted investigations at lower overvoltages are needed to clarify this point.

UV illumination under pulsed voltages is found to increase the background seed electron generation rate approximately fivefold. As expected, this enhancement becomes negligible above the onset field strength for field emission.

The investigation with different electrode materials and pulsed voltages suggests that the field electron emission is affected by the material of the electrodes. Breakdown is observed to occur at the plateau for the steel electrode. Most notably, not all applied pulses with steel electrodes result in a breakdown. The breakdown occurs during the rising part of the applied voltage for the copper and aluminum electrodes. All the experiments result in a breakdown for the copper and aluminum electrodes. This supports the conclusion that steel has a significantly lower field-enhanced seed electron emission rate than copper and aluminum, which is in accordance with their vacuum work function values. Based on this argument, one would, however, also expect that the seed electron generation rate is the lowest for aluminum electrodes. Nevertheless, the lowest breakdown voltages and times are obtained for the copper electrode. Although the measured prospective voltages are slightly higher in the case of the copper electrodes (see Figure 4.17), the difference cannot explain the measured trend. One plausible conclusion at present is to envisage that tabulated vacuum work functions may not, in all cases, be representative of electrodes in pressurized synthetic air. Another explanation could be hidden in the presence of the microstructure on the surface of the electrodes.

Interestingly, similar differences between the breakdown strength of pressurized synthetic air for aluminum and steel electrodes under DC voltages and quasi-uniform fields above ~ 10 kV/mm have been reported in a previous study [89]. The deviation from Paschen's law at high pressures (above ~ 7 bar) is attributed to the field-assisted electron emission from the cathode surface, which assists the Townsend mechanism, particularly when the macroscopic electric field is on the order of ~ 50 kV/mm [87, 89]. This is in good agreement with the present

results, where strong electric fields are obtained by fast pulse rise times instead of very large pressures. Indeed, depending on the pressure value, a significant reduction in the statistical time lag is observed above ~ 20 to 60 kVmm^{-1} .

The breakdown under slowly increasing and nanosecond pulsed voltages are investigated in pressurized synthetic air (1.5 to 8 bar) in quasi-uniform electric fields with gaps ranging from 0.1 to 1 mm. The main findings are listed below. In the investigated conditions under slowly varied voltages, breakdown occurs according to the Townsend mechanism with a secondary feedback emission coefficient of $\gamma = 2.2 \cdot 10^{-4}$. With different electrode materials, the DC breakdown voltage qualitatively decreases with the value of the cathode's material work functions. UV light reduces the mean breakdown and the scatter around the mean for DC voltages.

Compared to the DC case, higher breakdown voltages (up to 440%) are recorded when nanosecond voltage pulses are used. The breakdown under nanosecond voltage pulses is affected by UV light. For similarly applied nanosecond voltage pulses, the time to breakdown is, on average, shorter and scatters less when the electrodes are illuminated with UV light. The effect vanishes at large overvoltages. The breakdown under nanosecond pulsed voltages is affected by the electrode material. Notable differences in the breakdown time and voltage are measured between aluminum/copper and steel electrodes. An analogical breakdown onset could be expected for metals having similar work functions. For example, nickel, which is a typically used material for spark plugs, has a work function similar to that of steel [91].

The observed characteristics under nanosecond pulsed voltages are supposed to be attributable to an altered seed electron generation mechanism. A constant background emission rate (which can be increased using UV light) is observed at low electric fields. Above a pressure-dependent onset field, most electrons are generated by field emission. An expression for the seed electron generation rate consisting of a constant background term and a field emission contribution based on the Fowler–Nordheim formula is derived from the measured breakdown delays under nanosecond pulsed voltages.

5

Discharge Model

Under NPD, the breakdown happens according to the semi-empirical streamer criterion, where the electrons in an avalanche exceed a threshold such that the distortion of the background electric field changes the ionization dynamics in the gap. The distortion triggers a rapid chain of reaction of secondary avalanches due to photoionization, where the electric field is enhanced (near the streamer head), pushing the low electron density plasma channel towards the electrodes. As the channel extends, the electric field in the gap is concentrated in thin layers in front of the electrodes. At the cathode, the large electric field leads to enhanced secondary emission of electrons into the streamer channel. A cathode spot starts forming and, when active, efficiently supplies the streamer with electrons. This sudden increase in electrons causes the cathode sheath to collapse and sends a fast electric wave, called a "return stroke," back toward the anode. This wave increases the ionization, temperature, and electrical conductivity of the channel, leading to spark formation and a collapse of the gap voltage. If sufficient power is available, the spark discharge transits into an arc. [30]

This chapter discusses the analysis of the plasma produced under NPD using OES and the development of a 0D discharge model to describe the spark formation and state of the plasma under NPD.

A plasma is formed by adding energy to a gas so that the electrons are removed from atoms, producing free, charged particles. The charged particles produce a collective response to electric and magnetic fields.

The plasma is, therefore, regarded as the fourth state of matter. Elevated temperatures are usually present; the electrons usually occupy the excited bound or the free unbound quantum state; these excitations and ionization emit electromagnetic radiation, typically in the infrared to x-ray range. The analysis of the emission of light is an effective non-intrusive method known as plasma spectroscopy to measure plasma conditions, such as density and temperature [92]. In spite of more than 99% of the observable universe being made of plasma, plasma usually exists only in the vacuum. Otherwise, the surroundings will cool the plasma and recombine electrons and ions. The Saha equation (5.1) describes the ratio between ionized (n_i) and neutral atoms (n_n) to be expected in a gas in thermal equilibrium at a temperature (T) [93].

$$\frac{n_i}{n_n} \approx 2.4 \cdot 10^{21} \frac{T^{3/2}}{n_i} e^{-U_i/kT} \quad (5.1)$$

U_i is the ionization energy in J, for atomic nitrogen corresponds to 14.5 eV, and is 13,6 eV for atomic oxygen (29,6 eV and 35,1 eV for the second ionization respectively) [94]. At atmospheric pressure and room temperature, the fractional ionization ($n_i/n_i + n_n$) is very low (10^{-22}). Figure 5.1 shows the fractional ionization of nitrogen at different pressures for the first ionization degree (N^+) and at 1 bar also for the second ionization degree (N^{++}).

As the temperature increases, the ionization degrees remain low till $\sim 10^4$ K and then increase abruptly, and the plasma eventually becomes fully ionized. The higher the pressure, the lower the ionization degree.

When thermal equilibrium is present, particles have different velocities, and the most probable distribution of these velocities is known as the Maxwellian distribution. Interestingly, plasma can have several temperatures. For example, if the collision rate between electrons and electrons and ions and ions is larger than the collision rate between electrons and ions, each species can be at its own thermal equilibrium (T_e, T_i) [93].

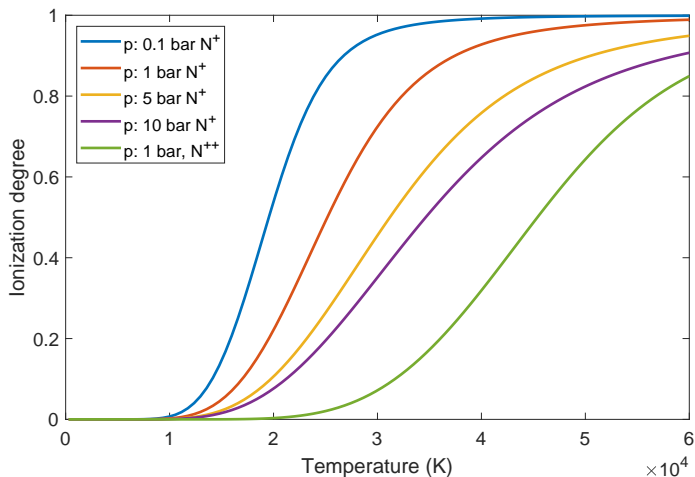


Figure 5.1: Ionization degree expected in a gas (monatomic nitrogen) in thermal equilibrium as a function of temperature.

5.1 Spark-Induced Breakdown Spectroscopy

The plasma generated by an electrical discharge always emits some form of electromagnetic radiation, which is related to the excited species present. SIBS consists in the spectral analysis of the light emitted by the electrical discharge [34].

Spectroscopic investigations of laser-induced sparks show that the optical emission consists of spectral atomic lines and a strong continuum. In the early part of the development of the spark, the continuum is the dominant component of emission in addition to broad lines of ions and neutral atoms. Less broadened lines from neutral atoms are observed when the spark has expanded and cooled.

The energy levels (n) of an atom arise from electrons in quantized states. As the principal quantum number (n) increases, the separation between consecutive energy states decreases until reaching the ionization limit, where the electron is freed and the energy is no longer quantized. The transition of an atom between a pair of discrete states results in a

spectral line, whereas transitions between the continuum and a discrete state, as well as transitions within the continuum, give rise to continuum emission. In optically thin plasmas, where there is no photon reabsorption, the intensity of a spectral line depends on the atomic population of the initial level and the intrinsic probability of transition to the final level. The energy levels of the two discrete quantum states involved in the transition are denoted E_1 and E_2 , with the resulting spectral line's wavelength given by $\lambda = hc/(E_2 - E_1)$. Additionally, various broadening effects influence the spectral lines, including natural, Doppler, Stark, and instrumental broadening. [95]

SIBS uses the spontaneous optical emission that occurs after the electrical discharge when an excited species (atom or molecule) relaxes from a higher to a lower quantum state and emits a photon having energy equal to the difference between the two quantum states [34].

The Boltzman plot method can be used to graphically determine the electron temperature using Equation (5.2) [96].

$$\ln \left(\frac{I_{k,i} \cdot \lambda_{k,i}}{g_k \cdot A_{k,i}} \right) = C - \frac{E_k}{k_B T_e} \quad (5.2)$$

Where $I_{k,i}$ is the emissivity, $\lambda_{k,i}$ is the wavelength, g_k is the statistical weight, $A_{k,i}$ is the Einstein transition probability, E_k/k_B is the normalized energy of the upper electronic level and $C = -\ln(4\pi Z/hcN_0)$. Different values of the logarithm on the right in Equation (5.2) plots on a straight line with slope $-1/kT$. The statistical weights and Einstein transition probabilities are retrieved from the NIST database [94].

Electron densities are usually derived from a line profile's FWHM. However, ion dynamics affects both the line widths and their shapes. This effect is important for the H_α lines [97]. An alternative method to calculate the electron density from the Stark broadening of the H_α line is using the Full Width Half Area (FWHA), since it is much less influenced by ion dynamics [98]. Equation (5.3) returns the electron density as a function of the FWHA [97].

$$FWHA = 10^{23} \left(\frac{FWHA}{1.098} \right)^{1.47135} m^{-3} \quad (5.3)$$

5.1.1 Qualitative Spectra Analysis

Figure 5.2 shows eight spectra taken at various delays after a discharge performed in air at 10 bar using an inductive ignition system (on top) and NRPD discharge. The NRPD is composed of 10 pulses at 10 kHz using the pulse generator A. Time 0 for NRPD is a few $\sim 0.3 \mu\text{s}$ before the last pulse. For each delay, 20 repetitions are performed and averaged. The camera exposure is 100 ns, and the spectrometer's slit opening is $50 \mu\text{m}$.

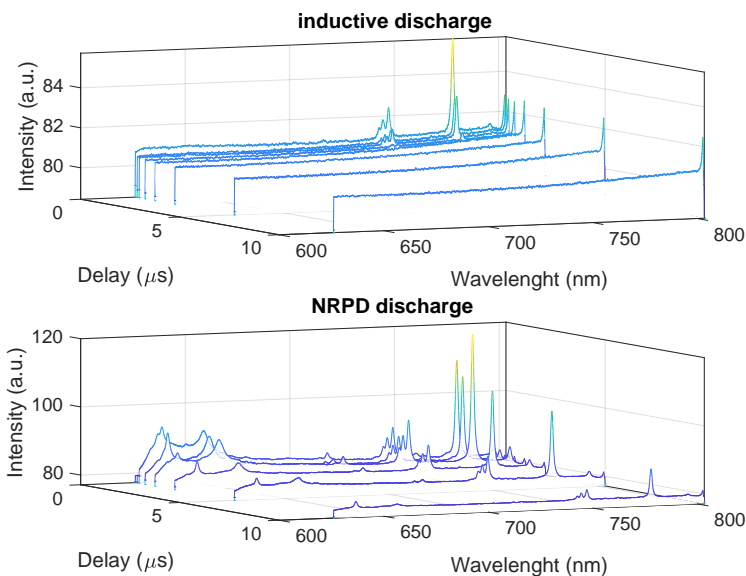


Figure 5.2: SIBS emission in air, 10 bar inductive ignition (top) and NRPD ignition, 10 pulses 10 kHz (bottom)

Using the inductive ignition system, atomic emissions from oxygen at 777 nm and nitrogen at 746 nm are visible. For the NRPD ignition system also the oxygen atomic emission at 715 nm is clearly recognizable. The atomic emissions using the NRPD ignition system last longer and have higher intensity.

Figure 5.3 shows the same experiment as reported in Figure 5.2. The

only difference is that now a mixture of air and methane at an AFR equivalence ratio of 2.5 is present.

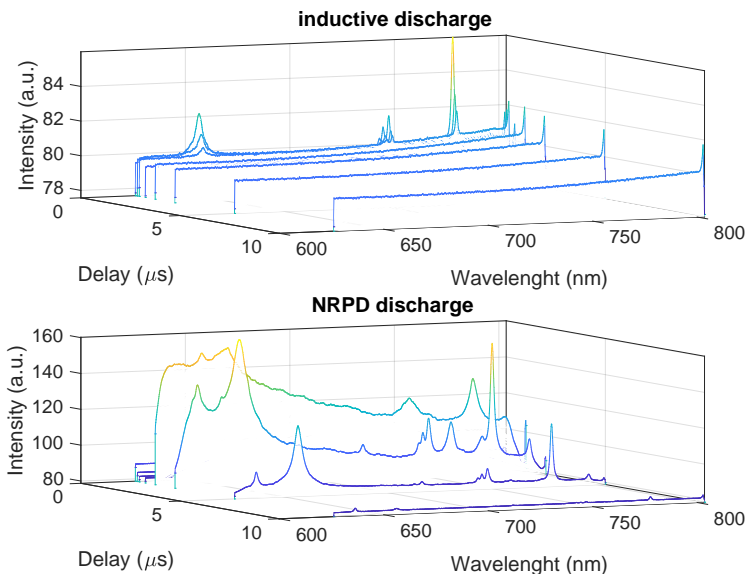


Figure 5.3: SIBS emission in methane-air mixture ($\lambda = 2.5$), 10 bar inductive ignition (top) and NRPD ignition, 10 pulses 10 kHz (bottom)

In addition to the aforementioned atomic lines also the H_{α} line at 656 nm is clearly visible for both ignition systems. The NRPD ignition system presents a much higher continuum.

5.1.2 SIBS for Concentration Measurement

The measurement of the mixture concentration (λ) in engines at the ignition time and location is of significant importance, particularly as combustion concepts where the local AFR is different from the average value over the entire cylinder, making the measurement using the lambda sensor not the value of interest. Some examples are in active PC or as charge stratification is present.

The method developed in [42] is used to estimate the local AFR at ignition time and location, using the FOSP. The SIBS method allows determining the local mixture concentration at the ignition location by examining the gas spectral emission during the electrical discharge, focusing in particular on the H_α (656 nm) line and the atomic oxygen emission at 777 nm. The idea behind this technique is that the electrical discharge results in the formation of plasma. During the breakdown phase, the gas molecules dissociate and ionize. Afterward, ions and electrons recombine, emitting photons at element-specific wavelengths. The spectral analysis of the emitted light can be correlated to the AFR. Nevertheless, tests performed with standard automotive ignition systems have shown very weak spectra, making it challenging to have enough sensitivity for precise AFR estimation due to the high noise-to-signal ratio. NRPD ignition results in much higher sensitivity and, therefore, more precise measurement.

To calibrate the SIBS technique to measure the local AFR for hydrogen jet-guided combustion, which will be discussed in the next chapter in Section 6.3, the ignition cell is utilized under controlled homogeneous AFR conditions, ensuring a comparable density to that of the targeted experiments. The calibration process employs the same camera, spectrometer, and triggering settings for consistency. Eleven AFRs are tested in the cell, from air to a λ of two. For each AFR, the experiments are repeated 20 times for the reactive and 40 times for the non-reactive experiments. The spectra are acquired 400 ns after the breakdown with a 500 ns exposure time. Before calculating the peak ratios, the spectroscopy images are filtered and averaged over the spacial component; afterward, a baseline is subtracted to eliminate the continuum emission, which exhibits a stochastic variation and would result in wrong AFR estimation if not accounted for.

Figure 5.4 shows the sum of all the post-processed spectra having the same AFR starting from air up to $\lambda = 3$. The spectra are normalized by dividing the spectra by the O (777) intensity. The different atomic emissions are reported on top of the relative peak.

The analyzed spectral range shows clear emissions from atomic hydrogen, oxygen, and nitrogen. The ratio between oxygen peaks and oxygen and nitrogen peaks remains constant by varying the AFR (as expected since the ratio of N_2 to O_2 remains constant) while their ratio to hy-

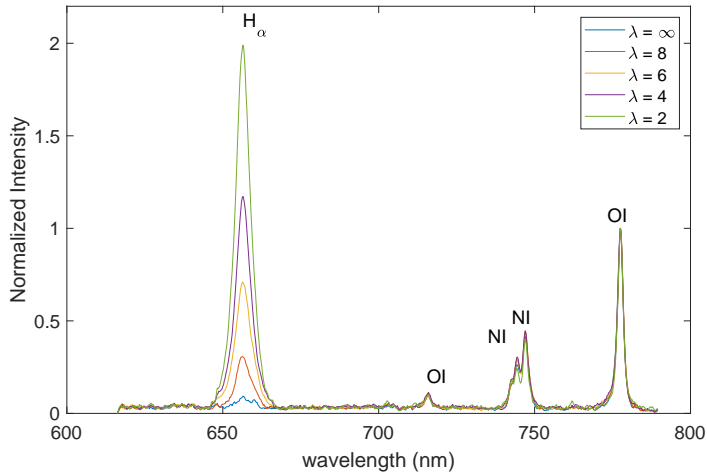


Figure 5.4: Post-processed SIBS spectra for different λ values.

drogen changes. The emission ratio between hydrogen and oxygen or hydrogen and nitrogen can be used to estimate the AFR, since oxygen presents a higher peak, the H/O sensitivity is better, resulting in a more accurate prediction.

Results of the SIBS calibration for hydrogen-air mixtures regarding atomic emission ratios vs. λ are shown in Figure 5.5 for H/O emission ratio.

The H/O ratio (Figure 5.5) decreases with increasing λ . The standard deviation around the H/O emissions ratio for the tested AFR is 13%. A cubic regression is fitted to the H/O atomic emission ratio. A third-grade polynomial is selected because it correctly follows the H/O trend and helps in smoothing out noise and capturing the underlying trend; interpolation between the points in Figure 5.5 does not change appreciably the estimations. Equation (5.4) reports the used polynomial where R is the H/O ratio.

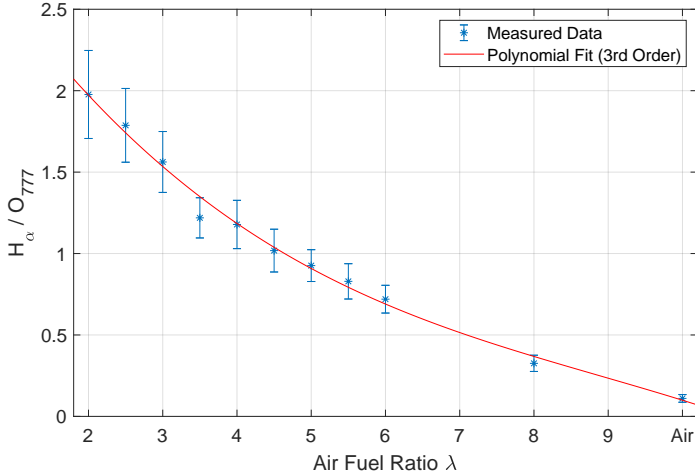


Figure 5.5: Post-processed SIBS spectra for different λ values.

$$\lambda(R) = -0.025R^3 + 0.067R^2 - 0.72R + 3.17 \quad (5.4)$$

The decreasing H/O trend for increasing λ is always expected. Nevertheless, the actual value also depends on the setup used since, for example, intensified cameras have a non-negligible variation in quantum efficiency depending on the wavelength.

In the experiments, a peak ratio of approx. 1 is often measured, which would result in a λ estimation of 4.6 with an uncertainty of approx. ± 0.5 .

5.2 Discharge Modeling

The material presented in this section is extracted from the article titled "Zero-Dimensional Modeling of a Nanosecond Pulsed Discharge".

HV NPDs are gaining interest in many applications, such as plasma

reforming [99] and plasma-assisted ignition and combustion [6, 19].

NRPD ignition typically utilizes pulses with durations in the 10-100 ns range, amplitudes ranging from some kV up to tens of kV, and repetition frequencies up to hundreds of kHz [45].

Electrons can be accelerated to energies high enough to ionize molecules when a strong electric field is applied to a gas gap. Suppose the electric field exceeds the breakdown threshold. In that case, the ionization process can develop into an avalanche that could result in either a single avalanche breakdown (known as streamer breakdown) or an exponential growth of secondary avalanches (Townsend mechanism). After the breakdown, if the current is not limited, the gas' degree of ionization, temperature, and electrical conductivity increases, and a spark is formed. The transition from the breakdown to a well-developed spark channel is still not completely understood [59, 100]. For high-pressure gas discharges (near atmospheric and above), even a small variation in amplitude or repetition frequency of the applied voltage results in plasma instabilities, causing the transition from a diffuse discharge into a more stable filamentary discharge that usually develops in a well-developed spark and a subsequent transition into an electric arc [100]. As reported in the review by Černák et al. [100], the mechanism responsible for plasma instabilities is still rather contradictory despite the large body of research regarding these instabilities.

The analysis of the formative time for the Townsend and streamer mechanism suggests that only the streamer mechanism can explain the spark formation under NPD (Section 4.2). Under NPD, the provision of the initial seed electron at an ideal location (near the cathode) to start the avalanche gives rise to the statistical time lag, which is dependent on the applied electric field (Section 4.3). Due to the currents present during the spark, a cathode spot can form, turning the discharge into an arc [3]. Due to the short current application present in NRPD, non-equilibrium or transient plasma is believed to be present [6, 101].

Three regimes of NRPD discharge are distinguished in [102], called corona, glow, and spark discharges. High electric fields and low conduction currents are present in the corona and glow discharges, which produce low gas heating and low electron number densities (less than 10^{19} m^{-3} in atmospheric air) [103]. A higher current characterizes the spark regime ($>$ tens of A) and higher gas heating at around some

thousand degrees without reaching a thermal spark [102].

More recently, the formation of thermal sparks generated in the air by NRPD is discussed in [13]. The authors noted that the three regimes of non-equilibrium NRPD of nanosecond discharges are not able to explain recent observations of nanosecond discharges where electron densities increase in the same order of magnitude as the molecule number density and temperature increase of several tens of thousands of K in some ns are measured [104]. In [13], the authors propose a 0D kinetic mechanism that includes 100 reactions, 12 species, and 12 excited electronic states to explain the formation of a fully ionized plasma under NPD. The investigation outlined a transition to a fully ionized plasma in less than a ns with a 1 μm diameter, followed by a growth up to 10 μm within 20 ns. A simple NPD model for ICE to be coupled with CFD engine simulations is presented in [101]. The authors modeled the NPD as a low-temperature plasma discharge. In fact, in the reported simulations after the breakdown, the voltage between the electrodes remains above 50% of the value that is present without discharge, despite the plasma current rising to several A. Nevertheless, due to the high currents at low electric fields measured during NRPD ignition experiments in Chapters 3 and 4, it seems that such a model does not correctly capture the energy deposition and the plasma state in conditions relevant for ICE.

In experimental studies dealing with NRPD, the measurement of the voltage and the current during the discharges are applied in various studies [6, 15]. These measurements represent a simple and effective measurement for calculating plasma energy and plasma electrical resistance. The measurement of current and voltage during NPD is described in detail in Section 3.2.

This section proposes a simple 0D model of NPD that can be used to understand the plasma state present after an NPD in dependence on the measured current and voltage waveforms. The model incorporates the high-frequency transmission line (described in detail in Section 3.2), the electrical circuit for the load (described in Section 3.4), the increase in gas-plasma temperature, and the evolution of electron density during a single NPD.

This kind of model is of interest to both experimental plasma researchers and electrical engineers. Plasma research could benefit from a simple model that allows for understanding the plasma regimes using simple

measurements and the parameters affecting it; electrical engineering will have information regarding the load impedance, which is an important parameter to consider during the design of pulse generators. The main limitation of this model is that chemical reactions are neglected; the model does not allow for tracking single species. It only outputs the ionization degree and the plasma temperature (electrons and heavy species). The model represents a valuable tool for understanding the relation between voltage and current over the gap, plasma formation, and plasma properties; it is not suited for tracking the evolution of single species or specific reactions.

This section is structured as follows: first, the governing equations and assumptions implemented in the model are presented. The model is then evaluated across a large set of parameters. The impact of plasma temperature (heavy species) and degree of ionization on current and voltage over the gap is discussed for various combinations of plasma radius and pulse amplitude. Finally, experimentally measured voltages and currents under NPD using automotive spark plugs as electrodes are compared against simulation results to understand the plasma properties that are typically present when NRPD ignition is used in engines.

5.2.1 Methods

The 0D model incorporates three interconnected physical sub-models: a model of the electrical circuit (described in Section 3.4), which drives the plasma, a model of the ionization dynamics in the plasma, and a model of the energy exchange between the driving circuit and the plasma, as well as between the electrons and heavy particles in the plasma.

Plasma Ionization

The plasma electrical resistance is calculated according to Equation (3.14). The electron density (n_e) is calculated according to Equation (5.5), where N is the particle density, E_{pl} is the electric field applied to the plasma by assuming a uniform electric field between the electrodes, and f_i is the effective ionization frequency.

$$n_e = \int f_i(N - N_e) \cdot n_e dt = \int \frac{\alpha - \eta}{N} \mu_e E_{pl} (N - n_e) \cdot n_e dt \quad (5.5)$$

Ionization (α) and attachment (η) coefficients, as well as the electron mobility μ_e , are calculated using the Boltzmann equation solver BOLSIG+ [51] using the cross-sectional datasets reported in [52–54], at different initial gas temperatures from 300 up to 40'000 K. The basic model with ionization and attachment proposed in [105] is used. The model accounts for the impact ionization of nitrogen and oxygen molecules and two- and three-body attachment to oxygen molecules.

Figure 5.6 shows the effective ionization frequency as a function of the reduced electric field for different initial temperatures.

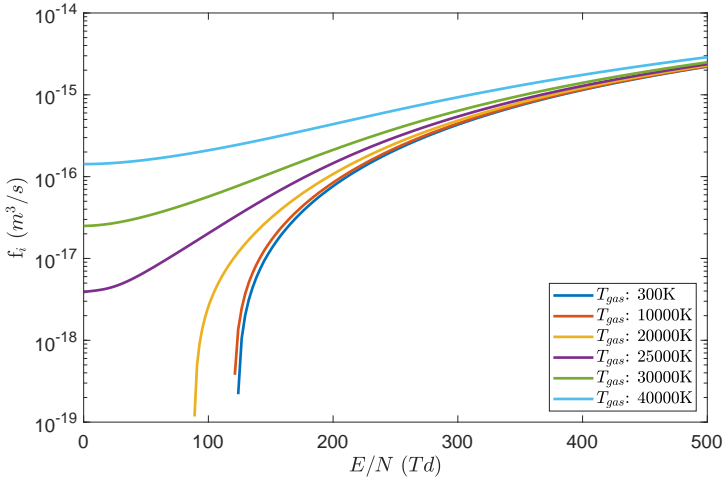


Figure 5.6: Effective ionization frequency as a function of the reduced electric field for different initial gas temperatures.

Thermodynamics

During an NPD, the power from the electrical circuit increases the internal energy of the air-plasma channel either by molecular ionization, dissociation, and excitation (potential energy), or by temperature increase (kinetic-thermal energy).

The gas's kinetic-thermal energy increases as a function of temperature. During the ns-long voltage application, the volume of the gas plasma

is assumed to be constant, which agrees well with the measurements reported in [13]. Therefore, the heating is assumed to be isochoric. Figure 5.7 shows the estimated internal energy of the gas channel as a function of temperature in blue (fitted line). The yellow line shows the plasma kinetic energy calculated according to Equation (5.6), assuming that the entire plasma is dissociated and all the atoms are ionized to the first degree, resulting in a four times higher particle density when compared to the neutral, nondissociated gas. As shown in [106], for a constant volume process at equilibrium, the second degree ionization of N and O plays a role only for temperatures above 40'000 K. The red line represents the internal energy increase of air at constant volume as a function of temperature retrieved from NASA polynomials [107] of the heat capacity at constant volume.

$$E_{plasma} = \frac{3}{2}k_B T \cdot 4N \quad (5.6)$$

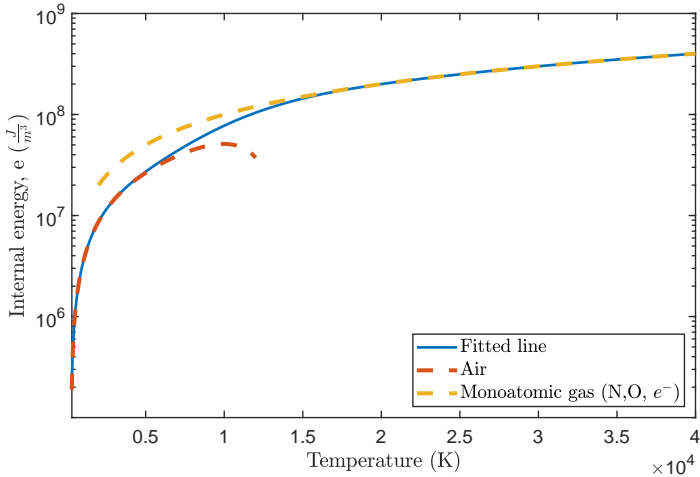


Figure 5.7: Internal energy of air-plasma as a function of temperature.

Assuming an internal energy increase at constant volume, at the beginning of the discharge, air is present in the weakly ionized plasma; the

heat capacity of air at constant volume (red line) correctly describes the internal energy. At very high temperatures, once all the air molecules are dissociated and ionized, the kinetic energy of the fully ionized gas better approximates the internal energy of the system (yellow line). Since the internal energy steadily increases and is known at the two extremes (air and fully ionized plasma), the fitted line is proposed where the internal energy is assumed to be equal to the one of air for temperatures below 3'000 K, and the fully ionized plasma internal energy is taken above 20'000 K. Between 3'000 and 20'000 K a polynomial interpolation of 4th degree is used.

Equation (5.7) shows the energy conservation equation that is used to calculate the temperature variation in the plasma.

$$p_{el} - \frac{dn_e}{dt} E_i = v_{pl} i_{pl} - \frac{dn_e}{dt} E_i = \frac{d}{dt} \left(\frac{3}{2} n_e k_B T_e V_{pl} \right) + \tilde{c}_v V_{pl} \frac{dT_g}{dt} \quad (5.7)$$

E_i is the average ionization energy taken as the molecular weighted average of the ionization energy of N_2 (15,6 eV) and O_2 (12,06 eV), equal to 14,86 eV, and \tilde{c}_v (reported in Equation (5.8)) is the modified heat capacity ratio derived from the internal energy (e) depicted in Figure 5.7.

$$\tilde{c}_v = \frac{de}{dT} \quad (5.8)$$

The excitation energy is negligible in comparison to the ionization energy and is, therefore, neglected [108].

Experimental Validation

The model is validated using the experimental discharge data presented in Section 4.2. The current and voltage during the NPD of 15 randomly selected experiments, having different pressures and gap distances, are compared against data originating from the model. Electrode gaps from 0.2 up to 0,8 mm and pressures from 2 up to 8 bar are selected. The stray capacitance is estimated from experiments where no breakdown is present and is set equal to 6 pF. In these experiments the measured

current is equal to the derivate of the applied voltage multiplied by the stray capacitance. An equivalent inductance of 120 mH is estimated from experiments where the spark gap is shorted. Therefore, the derivative of the measured current multiplied by the stray capacitance is equal to the measured voltage.

For the model validation, the measured incident pulse is an input to the model, while the reflected pulse is simulated and compared to measured experimental waveforms to calculate the model error. The gap voltage and current are uniquely determined by the reflected waveform Equation (3.2).

The unknown model parameters are the plasma radius (r_{pl}), the effective gap distance (d_{eff}), and the statistical time (t_s). The effective gap distance is introduced to consider the effect of the inhomogeneous electric field. In fact, in Section 4.2, the static breakdown voltage using a spark plug at a nominal gap size of 1 mm is 36% lower (due to the effect of the inhomogeneous electric field) than the breakdown voltage achieved with the same spark plug at a nominal gap size of 0,2 mm and similar products of pressures and gap distances. The statistical time is the instant at which the ionization process described by Equation (5.5) is switched on. It accounts for the seed electron's random appearance within an average time interval given by t_s . Simulations are performed to minimize the mean error (\hat{e}) of the reflection as a function of d_{eff} , t_s , and r_{pl} according to Equation (5.9).

$$\hat{e} = \frac{\sum |i_{r,exp} i_{r,sim}(r_{pl}, d_{eff}, t_s)|}{||i_{r,exp}||} \quad (5.9)$$

In some further experiments, the light emitted by the breakdown of a NPD is collected via the lens system and fed into the spectrograph to perform OES. The electron density (n_e) is estimated with the Stark broadening using the FWHM of the Lorentzian fit of the hydrogen neutral line at 656 nm (H_α). The pair of OI (neutral oxygen) spectral lines at 715 and 777 nm are used to estimate the electron temperature using the Boltzmann plot method and tabulated data from the NIST database [94, 97].

5.2.2 Results

Model Response Investigation

The model output across a large set of parameters is evaluated using a 50 ns long (FWHM) Gaussian pulse with a 10 ns rise time and a 20 ns fall time. Pulse amplitudes (U_0) ranging from 2 kV to 14 kV into a 75 Ohm matched load and plasma radii from 1 μm to 1 mm are simulated for a total of 4'758 simulations. The electrode gap is 0,4 mm, the pressure is 5 bar, and the temperature is 300 K. As described above, the stray inductance is estimated to be 120 nH, and the stray capacitance is 6 pF. In these simulations, the statistical time lag is neglected. A free electron is supposed to be always present in the gap by setting the lower boundary for the electron density to 1 in Equation (5.5). Therefore, the statistical time lag is neglected in these simulations.

The active electrical circuit limits the maximal current through the gap (see Equation (3.2)). Figure 5.8 shows the maximal normalized current as a function of incident pulse amplitude and plasma radius (on a logarithmic scale). The normalized current is calculated according to Equation (5.10). For a load without stray parameters, a value of one of the normalized currents represents a short, while a value of zero is present for an open load.

$$\hat{i} = \frac{Z_0 i_{pl}}{2U_0} \quad (5.10)$$

By neglecting the stray parameters, the normalized current value tends to 1 as the plasma resistance R_{pl} tends to 0 and goes to 0 as R_{pl} tends to infinity. The 0 level on the left part in Figure 5.8 depicts the region where the electric field is too low to ionize the gas and reduce the plasma resistance appreciably. The current does not reach the maximum for r_{pl} between 1 to approx. 10 μm , and for large r_{pl} .

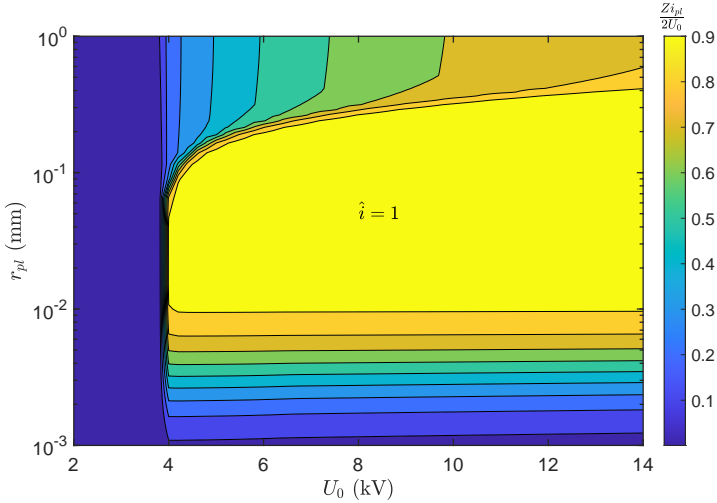


Figure 5.8: Normalized maximal current trough the plasma during the discharge as a function of incident pulse amplitude and plasma radius.

Figure 5.9 shows, on top, the current and voltage variation and, on the bottom, the gas temperature during the NPD for U_0 of 6 kV.

The peak voltage for all three plasma radii is the same at 11.7 kV. The voltage drops to practically zero after the breakdown only for the 40 μm radius. For the 5 and 500 μm radii, a plateau in voltage of respectively 3.5 and 5,8 kV is reached. A plateau in voltage is reached for the small radius despite the high electron density because the conducting area is too small to decrease R_{pl} to small values. For the large radius, the gas temperature increase is slower (due to the large plasma volume to heat), which results in the effective ionization frequency remaining below zero for low electric fields (see Figure 5.6).

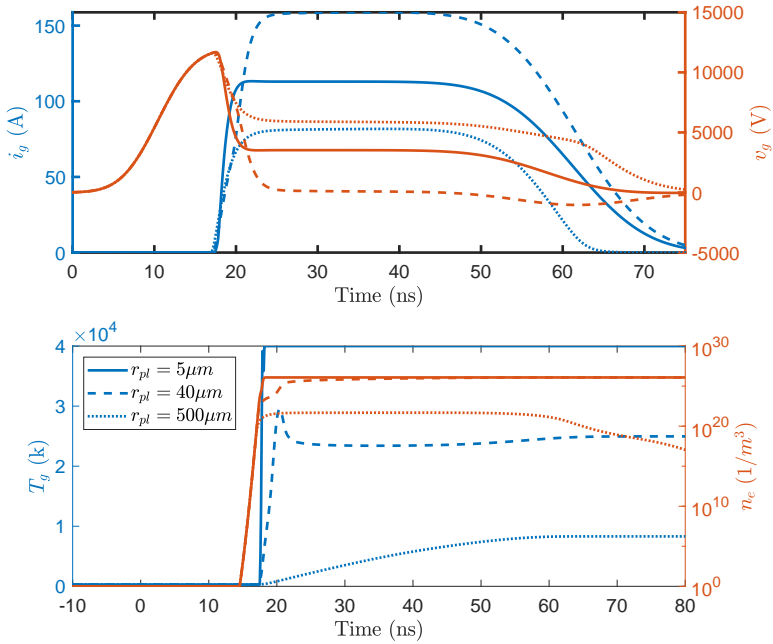


Figure 5.9: Plasma current and voltage (top) as well as gas temperature (bottom) for different plasma diameters at U_0 of 6 kV.

Figure 5.10 shows the maximal gas temperature during the NPD as a function of incident pulse amplitude and plasma radius. The gas temperature is arbitrarily limited to a physically plausible 40'000 K. This assumption is discussed in more detail in the following.

The higher the incident pulse voltage and the smaller the plasma radius, the higher the maximal plasma temperature due to the higher pulse energy and the lower plasma volume to heat.

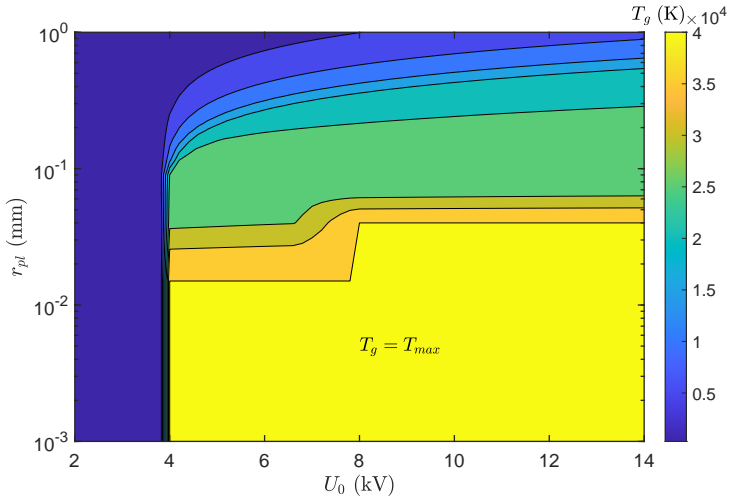


Figure 5.10: Maximal gas temperature as a function of incident pulse amplitude and plasma radius.

Figure 5.11 shows the maximal electron density as a function of incident pulse amplitude and plasma radius.

The particle number density limits the electron number. The maximal electron density (set due to the employed ionization mechanism at 1 electron per molecule) is reached only when high temperatures ($>25'000$ K) are present.

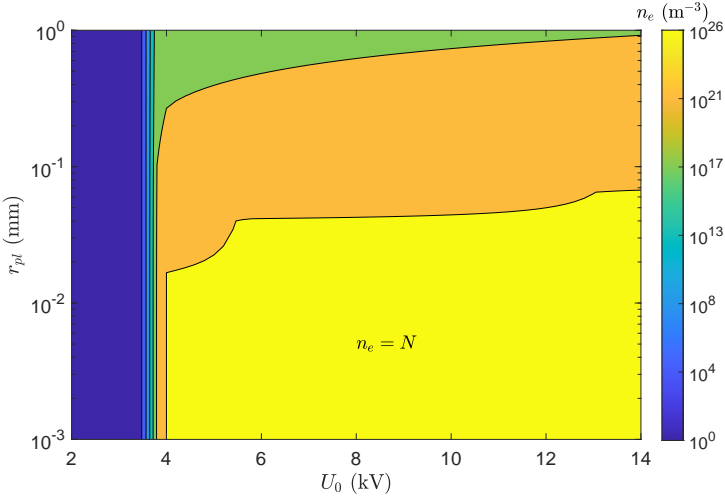


Figure 5.11: Maximal electron density as a function of incident pulse amplitude and plasma radius.

Experimental Comparison

The upper subplot in Figure 5.12 shows the total measured and simulated current and voltage over the load for an NPD in the air at 3 bar and 0,5 mm electrode gap distance. The lower subplot shows the simulated gas temperature and electron density on a semi-logarithmic scale. The plasma radius (r_{pl}), the statistical time lag, and the (effective) electrode gap distance are varied in the model until the error between simulated and experimental reflected current is minimized (Equation (5.9)).

The plasma radius that minimizes the error is 9,7 μm , the gap distance is 0,46 mm, and the statistical time lag is 12 ns. After the peak voltage, the gas temperature and electron density rapidly increase, and a fully ionized spark channel is formed. Due to the small plasma radius in the simulation, the voltage reaches a plateau after the breakdown at approx. 1 kV from the remaining discharge. In the experiments, higher gap voltages are present at the beginning of this plateau and lower towards the end, probably due to a radius smaller than simulated in

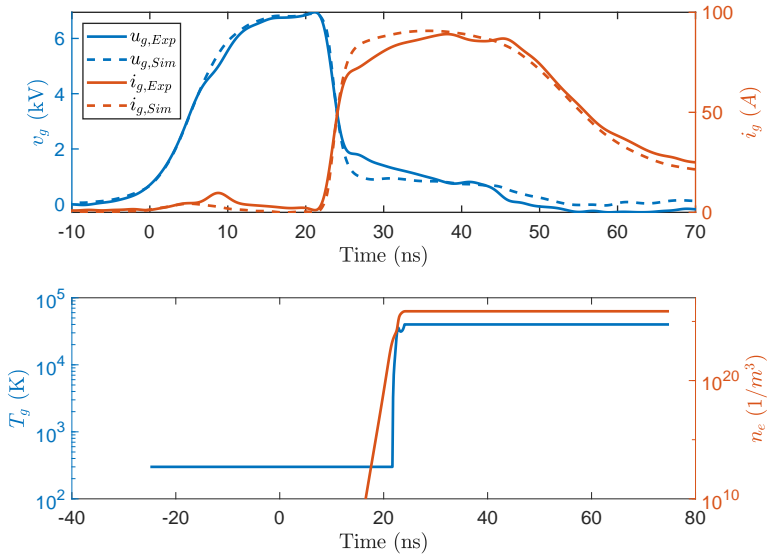


Figure 5.12: NPD experimental model validation, synthetic air, electrode gap distance of 0,5 mm, pressure 3 bar, and ambient gas temperature (pressure and temperature before the breakdown).

the beginning and larger toward the end.

Figure 5.13 shows the experimentally measured reflected current (mean of the absolute value) against the simulation's average error for the 15 investigated experiments.

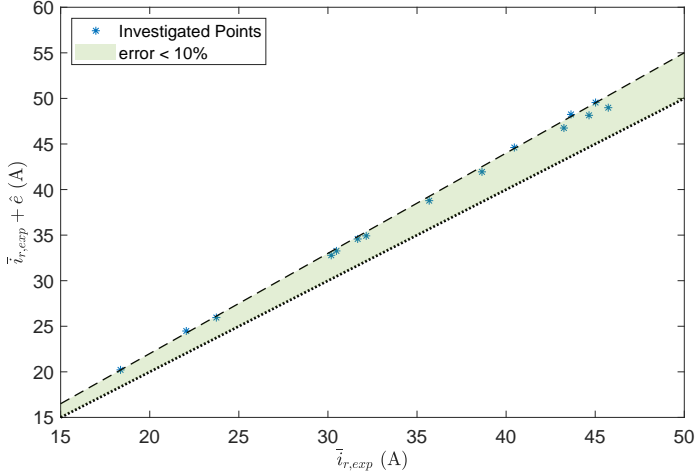


Figure 5.13: Model agreement, experimental reflected current vs. averaged error.

In most of the investigated points, the error remains below 10%. The plasma radius ranges from 6.4 up to 14,7 μm . Figure 5.14 shows the experimentally measured energy calculated as the difference between incident and reflected pulse energy and the simulated energy, calculated as the integration of the product of plasma voltage and current.

The difference between simulated and experimental energy is lower than 10%. Since during the discharge, the impedance is matched only for a brief moment, the share between energy deposited to the plasma and the supplied energy is low in the investigated cases, lying between 13% and 33%; those figures are in line with the results reported in Section 3.3.

The simulated gas temperature is arbitrarily limited to 40'000 K. This is not entirely correct since the plasma does not absorb the electrical power after this limit. One approach is, after reaching the maximal temperature, to redirect the power into a plasma volume increase ($V(t)$) according to Equation (5.11), where E_i is the ionization energy, and E_d is the dissociation energy [108].

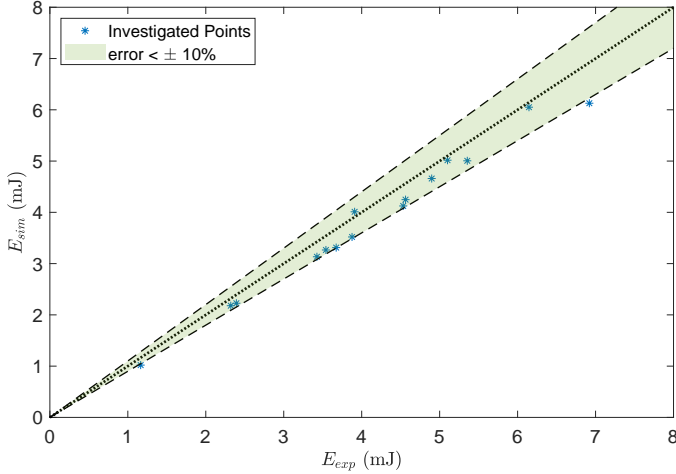


Figure 5.14: Model agreement simulated vs. experimental energy deposition to the plasma.

$$V(t) = \int_{V_0}^{V(t)} \frac{\eta \cdot v_{pl} i_{pl}}{E_i + E_d + \int_{T_0}^{T_{pl}} \tilde{c}_v dT} dt \quad (5.11)$$

In Equation (5.11) η is the power fraction used to enlarge the plasma radius. As soon as the maximal (arbitrary) temperature is reached, a value of $\eta = 1$ indicates that all the available power is used to ionize and dissociate additional air having the temperature and composition of the gas before breaking down, enlarging the plasma volume.

Figure 5.15 on top shows the total measured and simulated current and voltage over the load for an NPD in the air at 3 bar and 0,5 mm electrode gap distance. The bottom subplot shows the gas temperature and the plasma radius. This simulation minimizes the reflected current error as a function of the initial plasma radius and η while keeping the same statistical time lag and gap distance as shown in Figure 5.12.

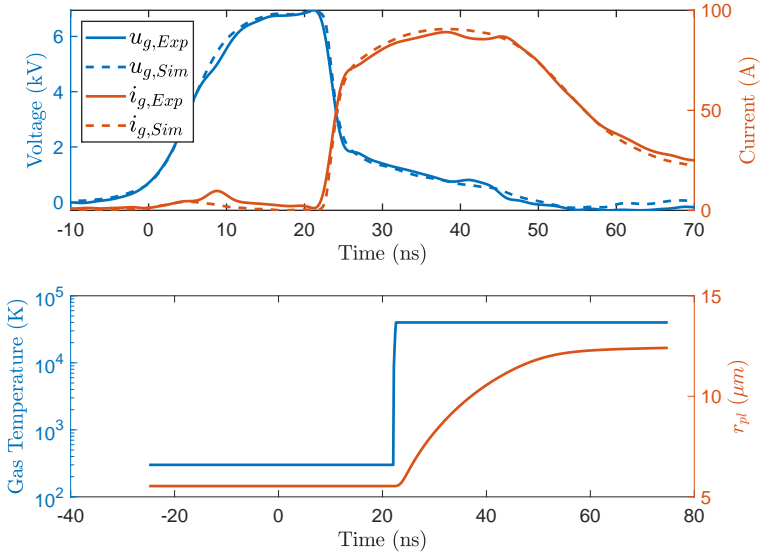


Figure 5.15: NPD experimental model validation with radius increase, synthetic air, pressure 3 bar, electrode gap distance of 0,5 mm, ambient temperature.

The voltage and current agreement is better than before. The simulated initial plasma radius is $5,6 \mu\text{m}$, and η is 6.5%. Figure 5.16 shows the model agreement, including the plasma expansion.

The overall agreement is better than before (mean error of 7% vs. 9%). The best agreement in reflected current is reached when a small fraction ($\eta = 5\text{-}10\%$) of the power increases the plasma radius.

To further evaluate the response of the model, OES analysis of the NPD is performed. For this purpose, the ignition cell is filled with air and hydrogen (5%) to 5 bar. Hydrogen is added to the air to experimentally estimate the electron density, using the stark broadening effect on the H_α spectral line as explained in Section 5.1. The impact of the hydrogen addition on the simulation is neglected. The simulated plasma radius is $3,5 \mu\text{m}$, the maximum electron density is $1.2 \cdot 10^{26} \text{ m}^{-3}$, and the

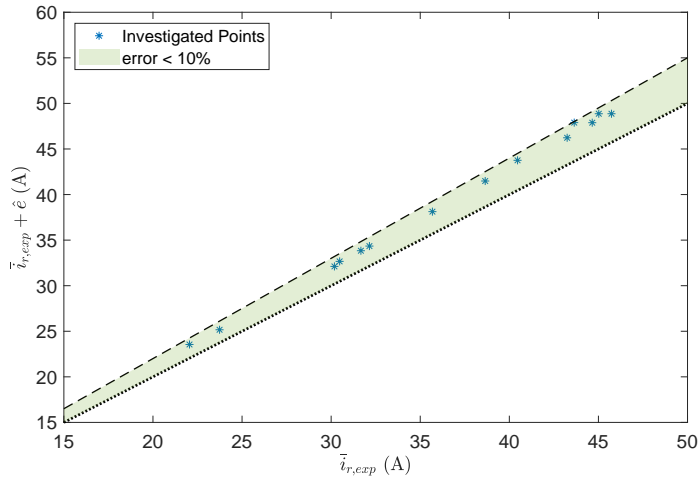


Figure 5.16: Model agreement with increase in plasma radius, experimental reflected current vs. averaged error.

temperature reaches 40'000 K.

Figure 5.17 shows the acquired OES spectrum of 50 experiments between 640 and 785 nm. The 50 images are summed and normalized. The image is taken at 340 ns after the NPD since it represents the first instance where clear atomic emissions are visible after the continuum emission, which is present after the breakdown. Atomic neutral lines of hydrogen, oxygen, and nitrogen are visible. Appendix B outlines how the spectral image is post-processed before analysis.

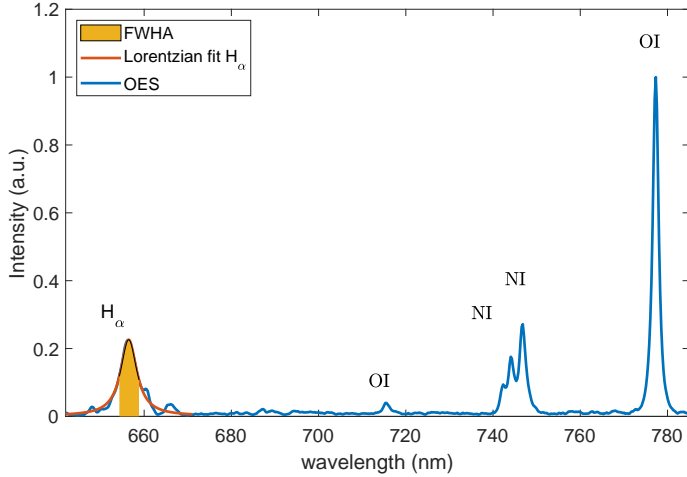


Figure 5.17: OES of NPD, 5 bar, Air and H₂.

The estimated electron density is $8 \cdot 10^{23} \text{ m}^{-3}$, and the electron temperature is estimated to 13'000 K using the Boltzmann plot method. Following the NPD in the first hundreds of ns, the plasma kernel is expected to expand at sonic speed isentropically [109]. Figure 5.18 shows the temperature and electron density evolution following the NPD starting at a temperature of 40'000 K and an electron density of $1.2 \cdot 10^{26} \text{ m}^{-3}$.

In spite of the low precision of the OES temperature and electron density measurements, the measured quantities are remarkably consistent with the expected isentropic sonic expansion that is expected to be present after the NPD. The reported temperature and electron density error is the minimal and maximal value calculated from the single experiment among the 50 acquired spectra.

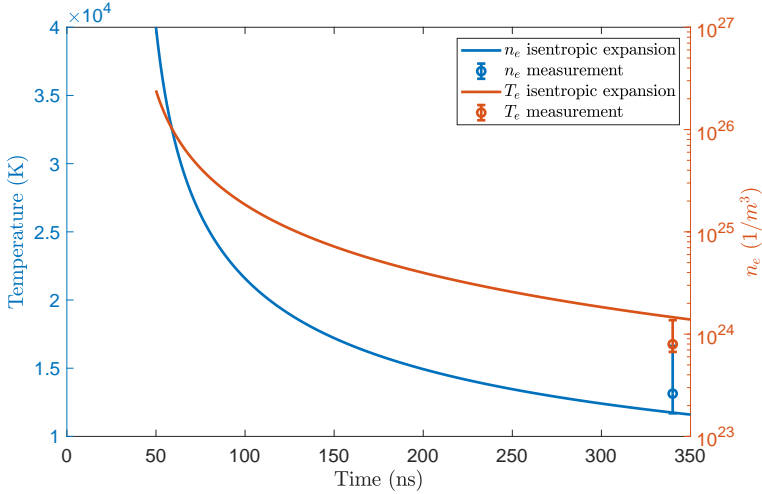


Figure 5.18: Temperature and radius evolution, sonic isentropic expansion.

5.2.3 Summary and Discussion

This section proposes a zero-dimensional NPD ignition model incorporating the electrical circuit that drives the plasma, a model for the energy exchange between the circuit and the plasma, and a simple ionization scheme. The model is first evaluated over a wide range of pulse amplitudes and plasma radii for discharges in air at initial temperatures and pressures of 300 K and 5 bar. Afterward, experimentally measured voltages and currents are compared against simulated ones to estimate possible conditions in the plasma (temperature, electron density, and plasma radius).

In the experiments, high currents at low voltages are measured. Gas temperatures above 20'000 K result in positive ionization frequency when no voltage is applied, which is needed to explain the measured high currents at low voltages. Molecular dissociation is expected to play a significant role at these high temperatures. The simple proposed ionization scheme only accounts for N_2 and O_2 ionization (only to the first degree). Figure 5.19 shows the concentration evolution of N_2 , O_2 ,

N, and O at 8'000 and 30'000 K using the reactions 1 to 19 reported in [13]. These reactions describe the thermal dissociation of N_2 and O_2 . Air (79% N_2 and 21% O_2) is present at the simulation start.

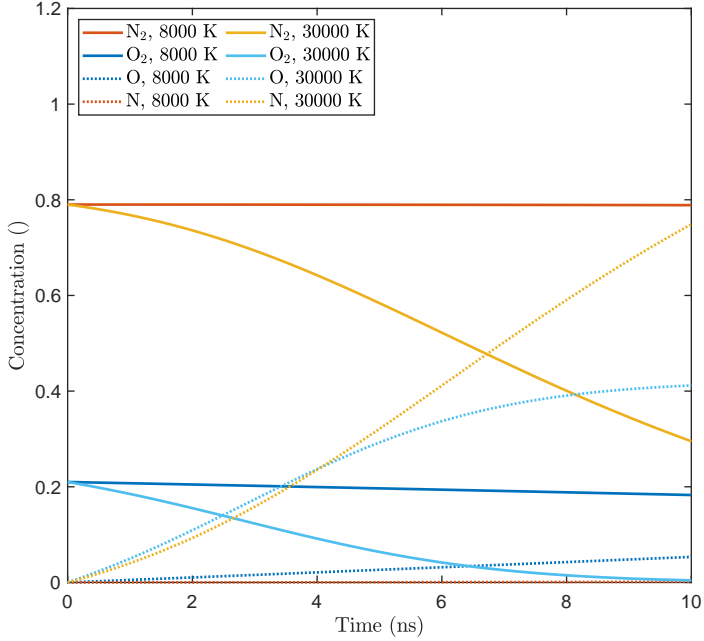


Figure 5.19: N_2 and O_2 dissociation

The air dissociation (Figure 5.19) is unimportant in the ns time scale at temperatures below 8'000 K. Nevertheless, it should be considered for temperatures over 10'000-20'000 K.

The fundamental investigation over a large set of parameters is used to estimate the impact on plasma temperature, current, and electron density for different applied voltages and plasma radii. At 6 kV amplitude of the incident pulse under NPD, the electron density and temperature quickly increase faster than the dissociation time scale for small radii (below approx. 50 μm). The gas temperature remains below the crit-

ical temperature for radii larger than $500 \mu\text{m}$, making the ionization scheme adequate in this range. For NPD, where high electric fields are present for several ns at high temperatures (above $8'000 \text{ K}$), the impact ionization of N and O atoms should be considered.

For the comparison against the experimental measurement, small discharge radii (6.4 up to $14,7 \mu\text{m}$) give the best agreement in reflected current for the analyzed experiments. For these plasma radii, the plasma kernel's temperature always increases faster than the timescale of dissociation. Nevertheless, after the fast voltage drop and the rapid temperature increase (first few ns), the molecules will dissociate and further ionize.

The plasma resistance formula (Equation (3.14)) is usually used for weakly ionized plasmas [59]. Weakly ionized plasma is present at the beginning of the discharge or in the fundamental analysis for large plasma radii. During the experimental validation, the plasma quickly reached the maximum possible ionization degree (all molecules ionized to the first degree). The formula for strongly ionized plasmas proposed in [59] does not yield plausible results since negative conductivity is calculated with the present electron density. Other formulas proposed are more phenomenological in nature [108, 110, 111] and therefore outside the scope of this investigation. Furthermore, the equation used here leads to very plausible results.

Often, NPDs are presented as low temperatures or transient plasma discharges [6, 101, 112]. In [113] an overview of the key processes important for the stabilization of non-equilibrium plasma is presented (i.e. preventing the transition to a thermal plasma). The authors highlight thermal instabilities as the most common instability resulting in a spark discharge. Even a small fluctuation in the electron density leads to a positive feedback loop consisting of an increase in Joule heating, followed by an increase in gas temperature, resulting in a reduction in the local gas density, which leads to an increase in the reduced electric field and, therefore, in a further increase in the ionization frequency. In filamentary discharges, these instabilities are also responsible for the transition from a streamer to a spark channel. In [113] nanosecond discharges are classified as non-equilibrium plasma discharges since the above-mentioned instability needs more time to develop than the pulse duration. In this investigation, due to the small gap size, the streamer

propagation time is negligible (approx. 1 ns for a 1 mm gap). After the streamer bridges the gap and forms a weakly ionized channel, the results show that if the electric field strength is large enough, the instabilities can develop even in the absence of a reduction of the local gas density. The reason is that joule heating, due to the small radius of the weakly ionized plasma and the large electric field strength, results in a thermal runaway that allows the gas temperature to increase to $\sim 20'000$ K and above, resulting in positive ionization frequencies even when the electric field strength drops to low values.

The proposed 0D model shows that large plasma radii are needed at above atmospheric pressures to sustain transient or non-thermal discharge, which is sometimes unrealistic. In fact, for all the investigated cases, the best agreement between the experimental and simulated voltage over the load is reached with small plasma radii where a fully ionized plasma in local thermal equilibrium is quickly established, as shown in [13]. The OES measurement seems to highlight the presence of a high-temperature plasma.

The model incorporates a simple load circuit. The effect of additional electrical components in the load could be investigated, for example, by adding a ballast resistor or inductance to reduce the current during the discharge.

The addition to the model that increases the plasma radius as a function of the electrical power delivered after the set peak temperature is reached gives very good agreement with the measured current. Nevertheless, the power used for the radius increase is lower than the power available (below 10%). Heat losses due to conduction via the electrodes or radiation shouldn't be relevant [3]. According to [3], after the breakdown, the process is concentrated into a narrow ($40\ \mu\text{m}$) high temperature ($60'000$ K) channel where all the heavy particles are dissociated and ionized to high degrees (presence of N^{4+} ions), where the potential energy is a factor of roughly 4 higher than the thermal energy. In the proposed model, the potential energy is only partially accounted for since in the initial phase (constant radius), only the energy necessary to ionize the O_2 and N_2 is accounted for, while during the expansion, only the dissociation energy and ionization to the first degree is accounted for. After the formation of the channel due to the extremely rapid temperature increase, the pressure inside the channel rises to hundreds of

bars, causing the emission of a shock wave that carries away a relevant energy fraction (an estimated 30%) [3]. The channel's expansion should not appreciably affect the plasma resistance because it will simultaneously increase the area (A) and decrease the electron density (n_e) in Equation (3.14). Future investigations could focus on accounting for the plasma's potential energy and the energy necessary to expand the channel. It is worth mentioning that the proposed model correctly accounts for the energy delivered to the plasma; the problem is only that it does not completely capture where the energy is stored. Furthermore, the proposed model returns plausible data in agreement with the literature [3, 13] both in terms of electron density (at least in the order of magnitude), plasma temperature, and channel dimension.

A 0D discharge model for nanosecond pulsed discharge that includes the active electrical circuit, the ionization in the plasma, and the temperature increase is proposed. The model is compared to NPD electrical measurement using an automotive spark plug at 2 to 8 bar synthetic air pressures and electrode gap distances from 0.2 to 0,8 mm. The main findings are reported below:

- ▶ Despite its simplicity, the model is capable of capturing relevant parameters such as electron density, electron and gas temperature, and the impact of the active electrical circuit.
- ▶ The comparison with the measurement data shows that the plasma electrical resistance rapidly drops to a low value after the breakdown. This steep drop can only be explained if a fully ionized micrometric-sized thermal spark is formed.
- ▶ For the investigated experiments, after the breakdown, the simulated gas temperature and electron density increase to the respective maximum values (which is limited to 40'000 K for the temperature and equal to the particle number density for the electron density) in less than a ns after the breakdown.
- ▶ Non-thermal or transient discharges with relatively low gas temperatures seem only possible if the plasma radius is large (hundreds of μm), which is not the case in the analyzed experiments.
- ▶ Due to the fast voltage and current transients present, the circuit's stray parameters are important and should be accounted

for, particularly during the fast voltage drop right after the gap voltage peak.

The model could be used to optimize NPD discharge. A few examples are reported below:

- ▶ Test the impact of different electrode geometry; one could imagine that a larger electrode's area offering a homogenous field over the area could form a larger plasma that, due to the energy deposition over a larger volume, would result in a slower plasma thermalization.
- ▶ Simulate the impact of variation in the line impedance or the effect of additional passive components. For example, inductance or resistances could be added to the circuit to limit the plasma current or the reflected energy. The model could be used to decide their ideal magnitude.
- ▶ Electrical engineers designing pulse generators could have an idea of the varying load under different applied voltages that dictate different requirements in the high voltage part of the pulse generators, allowing for a more effective design strategy.

In the future, the model could be adapted to account for a more detailed ionization mechanism, including the dissociation and ionization of atomic nitrogen and oxygen, ideally also to the second degree. The impact of the energy needed to expand the plasma channel should also be integrated. Furthermore, the model could be adapted to account for a more complex discharge circuit, including, for example, more stray components, time-varying impedance, and the measuring circuit [114].

Multiple pulses at high repetition frequencies are used in most applications dealing with NPD. Usually, after 2-3 pulses, a stationary voltage and current signature during the discharge is reached (Section 3.3). This model could be utilized to estimate the initial conditions present before subsequent pulses in NRPD, for example, by changing the initial electron density, gas composition, or temperature in as a function of the time delay between pulses or the pulse number.

The approach for CFD simulations of combustion in spark-ignited engines is to incorporate a model (of varying complexity) to simulate the energy transfer between the electrical discharge circuit, the thermal ex-

pansion after the spark discharge, the subsequent transition to a flame propagation, and the effects of local flow condition (affecting the kernel displacement and possible restrike). Once a critical radius is reached, a combustion model is then initialized [115]. In some of these models, the length of the channel is varied as a function of the cross-flow. Nevertheless, this is not necessary under NPD because, due to the very fast discharge times, the length cannot be affected by local (slower) flow dynamics. The proposed model could be used as (part of) the ignition model in/for CFD simulations. After an NPD, the modeled conditions (temperature density and composition) could be input as a source term for the CFD combustion model. If the temperatures are low enough, whether the species could be accounted for by the combustion model remains a factor to consider. Nevertheless, it will probably be necessary to account for the isentropic expansion and the recombination of ions and electrons into neutral particles in the ignition model. It is worth mentioning that with some modifications to the circuit, the proposed model could also be used to simulate classical ignition discharges as well.

6

Ignition and Combustion

Ignition of hard-to-ignite fuels is a very important requirement for future ICE, especially as renewable, stable fuels like methane of biogenic or synthetic origin and ammonia are adopted for energy security purposes or in hard-to-electrify sectors such as marine, heavy-duty, and co-generation [1]. Higher efficiency in SI engines is achievable with higher CR, increased specific heat ratio or reduced wall heat or quenching losses. These advantages can be exploited by applying Diesel-like process parameters like high CR, air excess, and EGR, as well as charge stratification. However, these strategies with SI concepts present drawbacks, such as slowing down premixed combustion, increasing cyclic variability, and increasing unburned fuel emissions [3, 116, 117]. These effects are linked to the low reactivity of the fuel-air mixture, having a high minimum ignition energy and a low laminar flame speed [118].

TJI shortens the combustion duration and reduces unburned fuel emissions [116]. TJI is applied by adding a small combustion chamber, the PC connected to the MC via small nozzle/s. The PC is filled from the MC during the compression stroke, and the contained charge is ignited near the TDC with a spark plug. Combustion inside the PC expels the hot, partially burned gases into the MC, providing high ignition energy and additional turbulence, increasing the combustion speed inside the MC and reducing the unburned fuel emission [116, 119, 120]. The PC can be either passive when the PC is directly filled during compression from the gas present in the MC or active if an auxiliary fuel is added to the PC, usually during the intake or compression stroke [121].

ICE usually burns the fuel in two distinct processes depending on the reactivity of the fuel used. Compression Ignition (CI) engines use a high reactivity fuel, such as diesel, which is directly injected at high pressures in the combustion chamber. In this case, the combustion progress is determined by the mixing of the fuel jets with the surrounding air. In SI engines, a low-reactivity fuel, such as gasoline or methane, is usually injected either on the intake port (called PFI) or directly into the combustion chamber (called Direct Injection (DI)). DI usually occurs during the late intake or early compression stroke to achieve good mixing. The low reactivity fuel is then ignited (usually using a spark plug) near TDC, and the flame front propagates through the premixed air/fuel charge. Due to flame quenching near the walls, and due to measures like reduced CR or non-ideal combustion phasing to avoid unwanted combustion phenomena (pre-ignition or knocking), the efficiency in SI engines is usually lower than their CI counterparts. An option to use renewable fuels like hydrogen, methane, or ammonia while profiting from the higher efficiencies of the Diesel cycle is the jet-guided SI combustion [122–124], where a high-pressure low reactivity gaseous fuel is injected near TDC, and ignited with some type of ignition promoter (spark plug, pilot fuel, ...). The fuel conversion occurs predominantly in stratified, jet-guided, diffusion-controlled modes. This concept allows for the suppression of unwanted combustion phenomena and could result in high efficiencies. Nevertheless, the significant momentum of the high-pressure jet leads to difficult conditions for reliable ignition.

Considering the above-sketched framework, the effect of NRPD ignition is investigated in various setups and conditions. Section 6.1 investigates the plasma to early flame transition under NRPD, and looks at the subsequent effect on TJI in the OPC. In Section 6.2, a technique to detect successful ignition is presented. In Section 6.3, a novel combustion process about H₂ jet-guided spark ignited combustion is analyzed in the RCEM, and the effects of ignition using NRPD are investigated and compared against inductive ignition. Finally, Section 6.4 presents the investigations performed on a 4-cylinder engine operated with natural gas; the engine is operated both in classical configuration (spark plug mounted directly in the combustion chamber), called OC, and in PC configuration.

6.1 Investigation of Ignition and Combustion in an Optically Accessible Pre-Chamber Setup

The OPC is used to analyze the plasma to early flame kernel transition using NRPD ignition in the PC thanks to the double Schlieren arrangement that allows for close-up visualization of the near electrodes region and for flame position and speed over the entire PC length. The effect of the combustion in the PC using different ignition strategies (number of pulses and ignition systems) at different AFR on combustion in the MC is analyzed discussed as well. The results originate from a conference contribution [31] and two publications, one dealing with the analysis of the combustion in the PC [27] and the other explaining its effect on MC combustion [28].

In the performed experimental campaign the temperature at intake and pressure before ignition (12.4 bar and 363 K) are selected to correspond to a density of $11,6 \text{ kg/m}^3$ (density condition of an engine having a CR of 10 and pressure 1 bar at the beginning of compression). Three different air-fuel equivalence ratios (λ) were considered, namely $\lambda = 1$, $\lambda = 1.4$, and $\lambda = 1.8$. Laminar and turbulent initial conditions in the PC were obtained by setting the dwell time to 0.5 and 0,005 s, respectively. In the OPC, NRPD ignition (5, 10, 20, and 50 pulses) using the pulse generator that provides the pulses with 50 ns duration at 10 kHz PRF is compared against ignition achieved with a commercially available ignition coil (BERU) providing up to 60 mJ of secondary energy with a maximum spark duration of 2,2 ms at 800 V Zener load. Each experimental condition is repeated twenty times.

Turbulent Jet Ignition in the Optical Pre-Chamber

One exemplary experiment at $\lambda = 1.4$ and NRPD ignition with 10 pulses is used to describe TJI in the OPC. Figure 6.1 shows four frames of the Schlieren imaging on the top. The bottom left subplot shows the measured pressure in the PC in blue and the measured pressure difference between PC and MC in red. In the bottom right plot, the HRR and the absolute value of the enthalpy flow in and out of the PC are marked in blue, and the cumulative HRR is in red. The points in both graphs highlight the times of the four depicted Schlieren frames. The

developed thermodynamic analysis of the PC combustion is reported in Appendix A.1, and is published in [26].

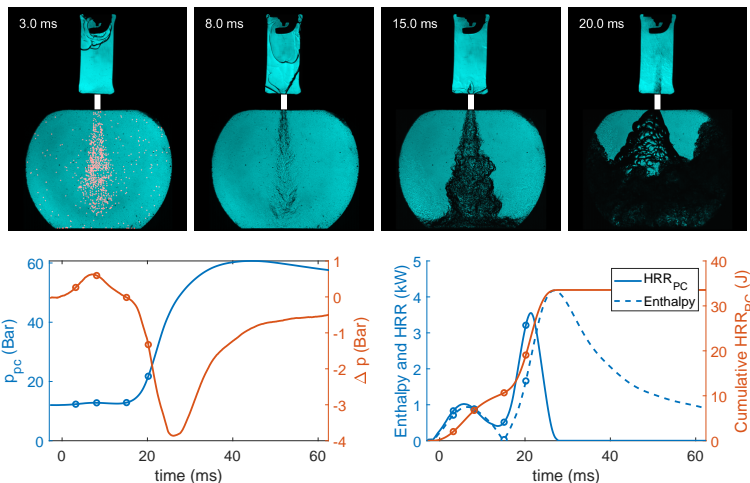


Figure 6.1: Schlieren frames and HRR in the PC, NRPD ignition, 10 pulses, $\lambda = 1.4$.

The Schlieren images show the areas where density gradients are present, thereby serving as a proxy for identifying the flame front and, therefore, regions with HRR. As shown in [118] and visible in Figure 6.1 the TJI ignition process can be divided into three phases:

1. Flame front propagation in the PC while unburned mixture (also called cold-jet) is pushed into the MC. The cold jet only carries turbulence that can enhance the combustion speed in the MC [120]. This is visible in frame 1 at 3 ms, where the difference in Schlieren activity against the background image in the MC is enhanced in post-processing and depicted in red to visualize small changes in density gradients.
2. PC burned gases pushed into the MC. Start at frame 2 (8 ms) end at frame 3 (15 ms). Starting at the peak in enthalpy flow from the PC and finishing at the 0 crossing (the absolute value of the enthalpy is depicted; therefore, the second bump represents the

backflow).

3. Inverse flow from the MC into the PC. At 20 ms, the pressure inside the MC is higher than in the PC, and the partially burned mixture inside the MC is pushed back to the PC, where it reacts, as can be seen from the second bump in the HRR and the large density gradients in the PC visible from the fourth Schlieren frame. During the inverse flow, there is a first phase where partially burned gas is pushed back, reacting in the PC, followed by a second phase, occurring after around 30 ms, where burned gas is pushed back. These two phases are recognizable by the HRR analysis (reported in Appendix A.1) and by the Schlieren activity, which is very small during the second phase despite the large pressure differences [26].

The apparent HRR and the cumulative HRR in the MC are calculated, neglecting the enthalpy flow from and in the PC according to Equation (6.1).

$$\begin{aligned}
 HRR_{MC}(t) &= \frac{c_V(T)}{R} V_{MC} \frac{dp_{MC}}{dt} \\
 iHRR_{MC}(t) &= \int_0^t HRR_{MC}(t) dt
 \end{aligned} \tag{6.1}$$

Figure 6.2 shows the apparent HRR and the cumulative HRR in the MC, the points highlight the times of the four depicted Schlieren frames in Figure 6.1.

After PC ignition and combustion the hot turbulent gas jet ignites the charge in the MC and a fast HRR is present.

Section 6.1.1 describes the effect of NRPD ignition in the PC, focusing on the flame propagation and his comparison against the inductive ignition system. Section 6.1.2 describe the effect that different propagation speed have on the TJI of the charge in the MC

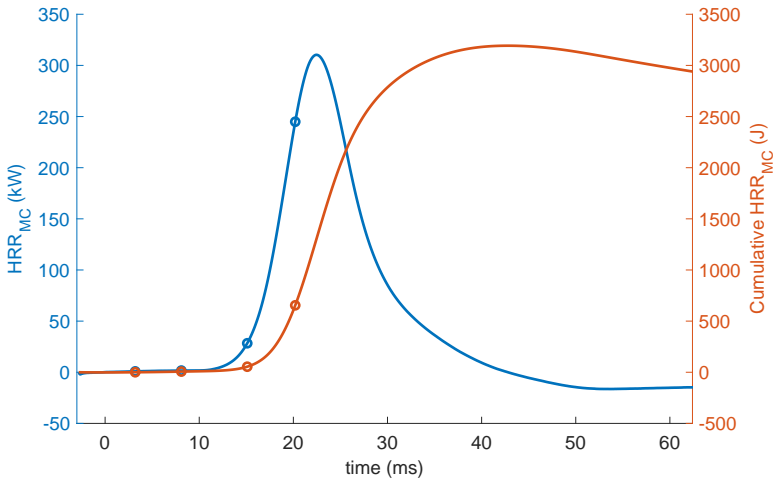


Figure 6.2: HRR in the MC, NRPD ignition, 10 pulses, $\lambda = 1.4$.

6.1.1 Plasma to Early Flame Kernel Transition in the Pre-Chamber

Flame Front Measurement in the Pre-Chamber

In the PC, a routine is used to detect the flame front position. The flame front is chosen as the point on the flame contour, which is furthest from the central electrode of the spark plug. Figure 6.3 shows the flame front detection at four different time instants (0.4, 0.6, 1.5, and 11 ms) of an experiment in lean condition ($\lambda = 1.8$) where ten pulses are applied at 12,4 bar and 90 °C in laminar condition.

The red surface in Figure 6.3 represents the flame contour detected by the algorithm. Two flame relative positions are used in this investigation. The first is the maximal radial distance on the detected contour from the central spark plug's electrode; the yellow lines represent this distance in the four subplots in Figure 6.3. The second is the furthest flame position in the horizontal direction and is represented as blue vertical lines in Figure 6.3. This two-position strategy was selected be-

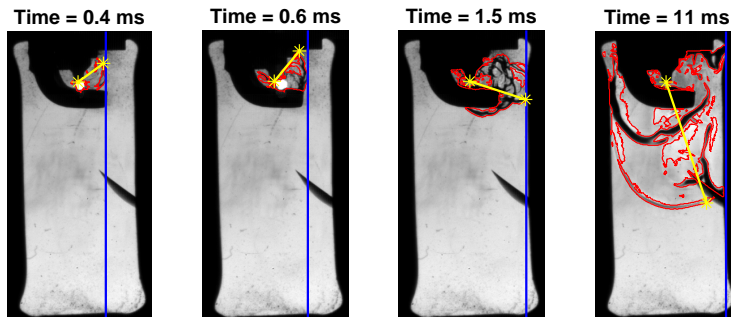


Figure 6.3: Flame front position measurement, NRPD ignition, 10 pulses, $\lambda = 1.8$.

cause following the flame in the vertical position resulted in incomplete tracking due to the spark plug's ground electrode presence hindering the view of the kernel development. The proposed post-processing routine allows for the accurate tracking of the plasma and flame position during the early ignition phases.

Ignition Success and Early Flame Development

Figure 6.4 shows Schlieren images of inductive and NRPD (50 pulses at 10 kHz) at laminar and turbulent conditions at four different times after the discharge (from 1 to 4 ms). The sequence shows the evolution of the plasma to the early flame kernel using the camera focusing near the electrodes for the very lean case ($\lambda = 1.8$) at 12,4 bar.

For the NRPD ignition, a bright spark is visible at all depicted time steps. Ten pulses each ms for the first 5 ms (for a total of 50 pulses at 50kHz) are applied, and the pulse position is synchronized within a few hundred ns with the camera frame rate. It can be seen that for NRPD, the flame quickly develops for both initial laminar and turbulent conditions, and at 4 ms after ignition, it exists the visible region (of the magnification). Instead, the inductive case is much slower, and after a few ms, it quenches before reaching the end of the PC.

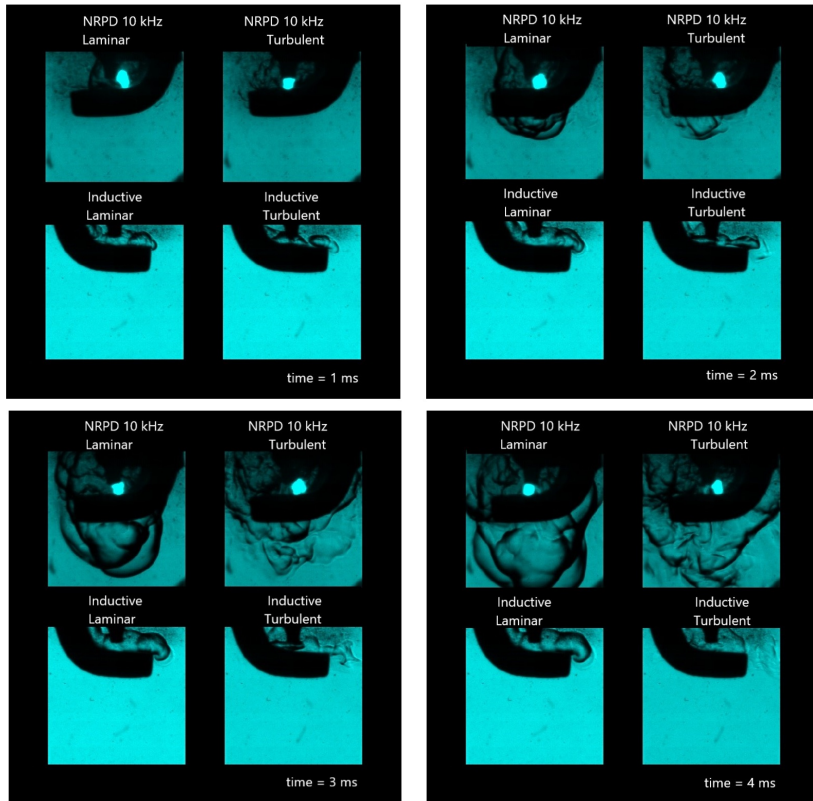


Figure 6.4: NRPD vs. inductive ignition in laminar and turbulent conditions, 1, 2, 3, and 4 ms after ignition, 50 pulses, $\lambda = 1.8$

Figure 6.5 shows the percentage of successful ignition for at $\lambda = 1.8$, 12,4 bar, and 90°C . The ignition is successful if the flame reaches the PC's end.

The percentage of successful ignition increases when NRPD is used. Five pulses are already enough for flame propagation along the entire PC's length for all the laminar cases, while ten pulses are needed to achieve 100% for the turbulent cases. For higher pulse number, ignition is always successful. The effect of different pulse numbers can be

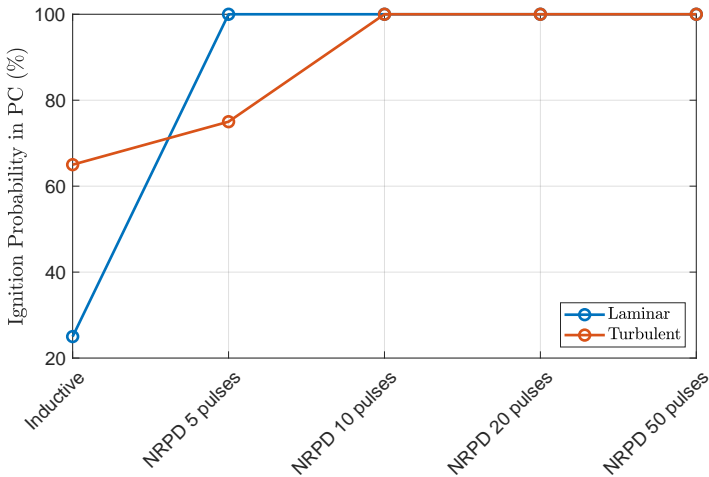


Figure 6.5: Percentage of successful ignition for inductive and NRPD at different pulse numbers and 10 kHz repetition rate, $\lambda = 1.8$.

investigated using the development of flame position over time.

Flame position analysis in the Pre-chamber

Figure 6.6 shows the average flame front distance from the central electrode over 20 repetitions against time. The laminar cases are depicted on the left-hand side, and the turbulent ones on the right. From top to bottom, the air dilution increases: on top, the stoichiometric cases are shown, in the middle $\lambda = 1.4$, and on the bottom $\lambda = 1.8$. In each plot, different colors are used for the different ignition strategies. The dotted line represents the inductive ignition system. The colored full lines (red to green) represent NRPD ignition with varying numbers of pulses (5, 10, 20, and 50). In the bottom subplots, the black dots on the NRPD curves represent the time corresponding to the last delivered nanosecond pulse.

In all the cases, NRPD ignition leads to faster propagation; the difference is larger for laminar cases and when the AFR is higher. The

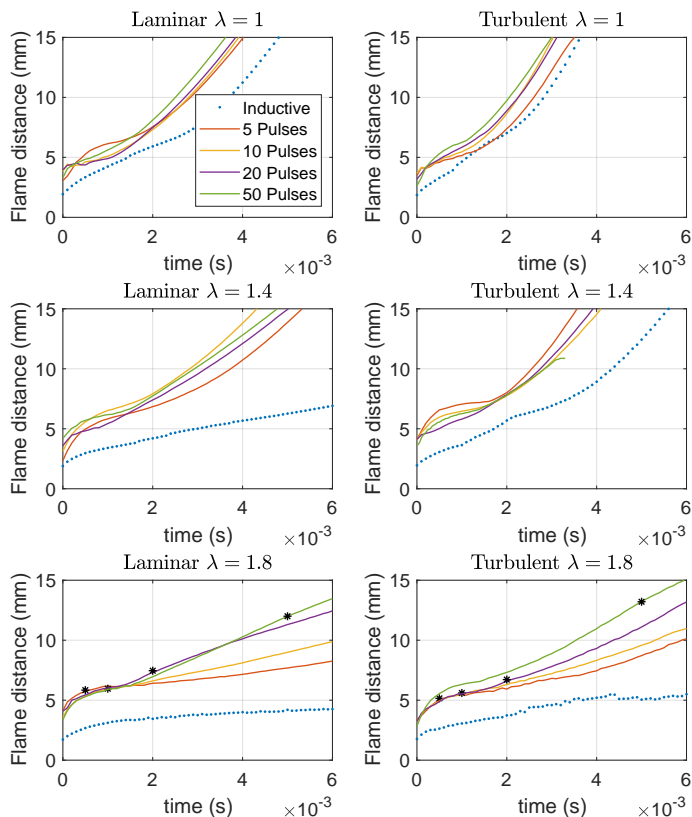


Figure 6.6: Flame front distance from the spark plug's central electrode.

difference between different pulse numbers is visible only at lean conditions and is more pronounced for higher AFRs. Two different flame propagation phases seem to be present. During the first 1.5 ms, the expansion for NRPD is not dependent on the gas composition nor the initial turbulence level. In this phase, NRPD exhibits a higher flame-plasma expansion rate when compared to inductive ignition; this higher

expansion rate is also maintained during the second phase. The second phase starts after 2 ms; for NRPD ignition, the effect of a high number of pulses is visible where the flame speeds are expected to be low (high AFR or low turbulence). Higher pulse numbers are advantageous for achieving a higher flame speed in this phase. The black dots in the bottom subplots show when the NRPD ignition ends. As expected, the flame position deviates from where the ignition is still active only after the black dots.

In order to overcome the limit of the ground electrode impeding the visualization of the kernel development in the vertical direction, it is interesting to examine the kernel development considering the velocity only in the "undisturbed" horizontal direction. Figure 6.7 shows the horizontal flame front distance for $\lambda = 1.4$ and $\lambda = 1.8$ and for laminar and turbulent initial conditions.

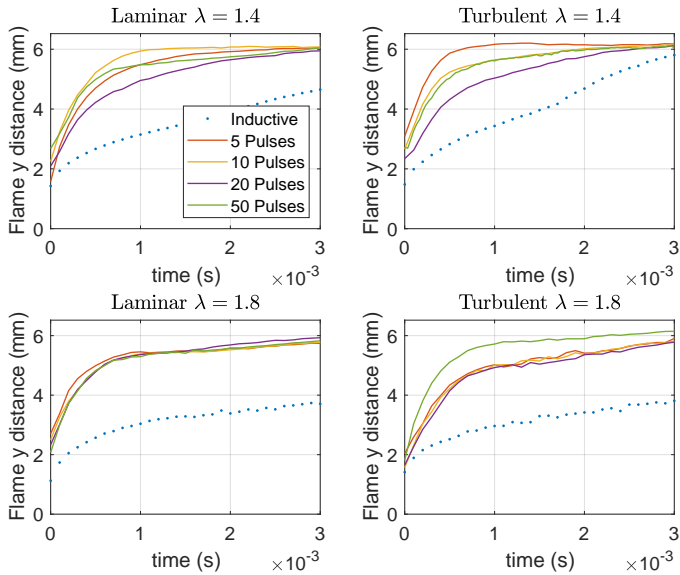


Figure 6.7: Lateral flame front distance from the spark plug's central electrode.

The maximal distance of the visible flame front in the lateral direction is

approx. 6 mm. Afterward, it reaches the limit of the window. The flame expansion for inductive is slower (blue points) while no constant trend is recognizable when a different number of pulses are applied, suggesting that different pulse sequences do not change the initial ignition phases.

In order to examine the flame kernel development, two benchmarks were selected, namely 5 mm radial distance and 10 mm radial distance. The distances are measured from the central electrode as illustrated in Figure 6.3. Figure 6.8 shows the time needed (and standard deviation) by the flame to reach a 5 mm distance from the central electrode (radial distance) for initial laminar conditions on the top and for initial turbulent conditions on the bottom, for the different ignition strategies investigated.

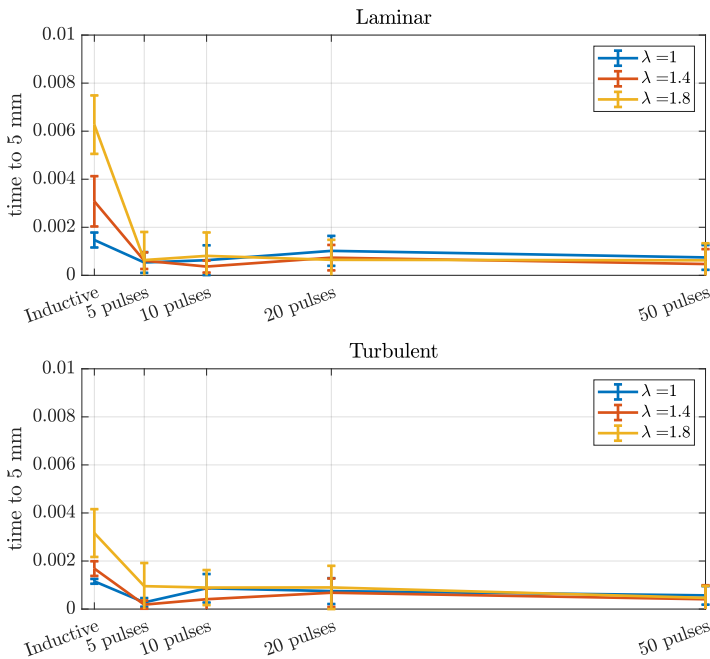


Figure 6.8: Time needed to reach 5 mm from the electrodes in the PC.

The time needed to reach the 5 mm distance for pulsed discharge is, on average, always less than 1 ms for all NRPD cases. Therefore, no appreciable difference is recorded between different NRPD pulse patterns at 10 kHz. The time to reach the 5 mm mark is affected by the AFR for the inductive case: the higher the air dilution, the longer the time. NRPD expansion to 5 mm is not affected by the AFR.

Figure 6.9 shows the mean time (and standard deviation) it takes for the flame to reach the 10 mm radial distance from the central electrode for the different ignition strategies in laminar (top) and turbulent (bottom) conditions.

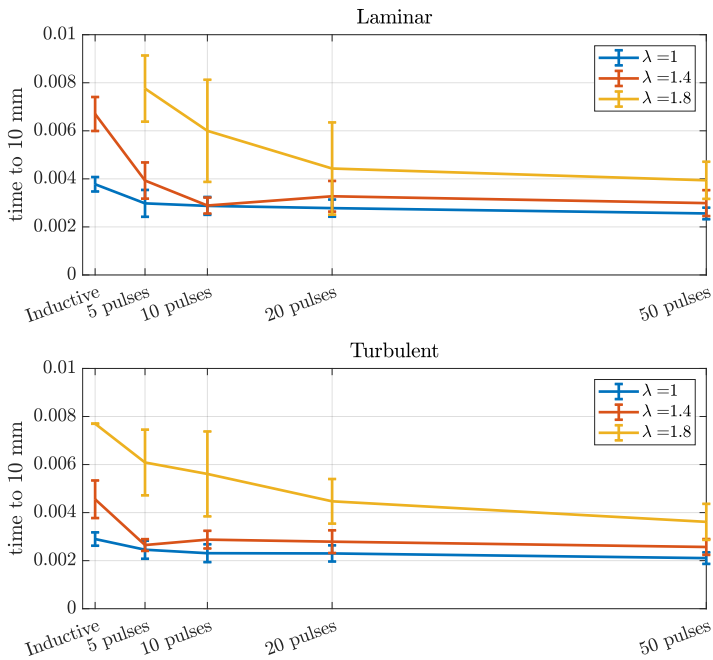


Figure 6.9: Time needed to reach 10 mm from the electrodes in the PC.

When a higher number of pulses is used, the flame reaches the 10 mm distance faster. The effect is more pronounced for the leaner condition.

Distances above 10 mm are reached faster the closer the AFR gets to stoichiometric.

Figure 6.10 shows the flame distance as a function of time for different λ values. The experiments are grouped for the different turbulence initial conditions (laminar and turbulent) and different ignition strategies.

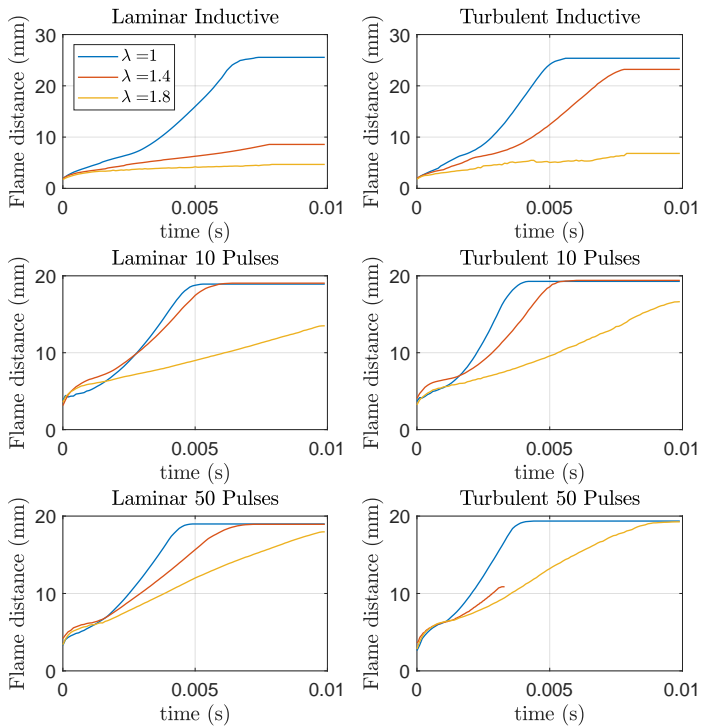


Figure 6.10: Flame front distance from central spark plug's electrode λ variation.

For the inductive case (laminar and turbulent conditions), the flame distance starts to vary in dependence of AFR already after 0,5 ms. For NRPD, the effect on λ appears later, at approx. 1,5 ms. Higher pulse numbers reduce the propagation speed loss due to dilution.

Figure 6.11 depicts the mean flame speed in the PC for the different ignition strategies at the different AFR and for turbulent and laminar conditions in the PC.

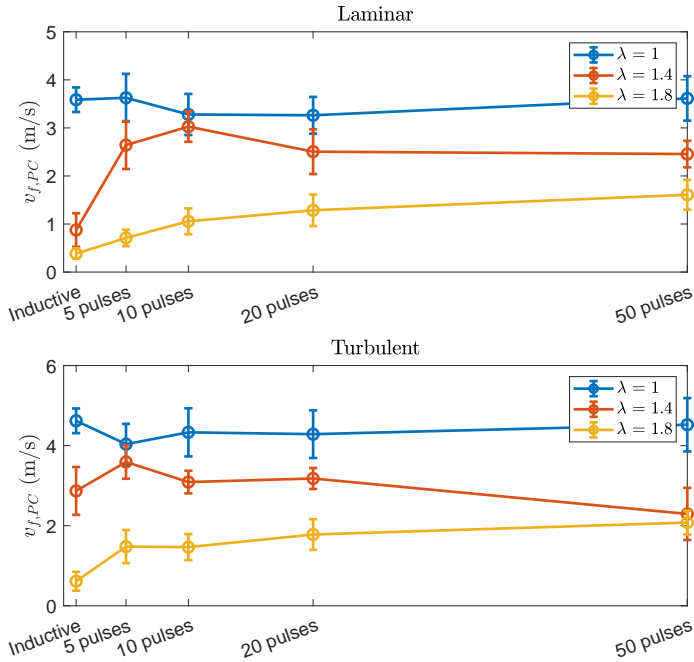


Figure 6.11: Mean flame speed in the PC.

The flame front propagation speed in the PC increases with increasing number of pulses at the leanest condition ($\lambda = 1.8$, Figure 6.11). This effect is more apparent for laminar initial conditions, but similar observations, albeit with a higher standard deviation, can be drawn from turbulent cases. The flame propagation is also faster using NRPD ignition for $\lambda = 1.4$ under laminar conditions. For the other cases, the trends fall within the standard deviation, and therefore, no reliable trends can be drawn.

The mean flame front propagation is used to analyze TJI in the MC.

6.1.2 Turbulent Jet Ignition and Combustion in the Main chamber

The simultaneous Schlieren setup in the PC, and in the MC enables the analysis of the interaction between the ignition and combustion in the PC and the ignition of the charge in the MC by the turbulent hot jet for the different investigated cases.

Figure 6.12 shows five frames of the TJI ignition process using inductive and NRPD ignition with 5, 10, and 50 pulses ($\lambda = 1.8$) for laminar initial conditions in the PC. This results in a total of 20 frames (5x4) where different instants, from left to right, and the different ignition strategies, from top to bottom, are depicted. The first four frames are taken for each experiment at 10, 15, 30, 45 ms after ignition. The last frame for each experiment is selected as the frame where the fast combustion in the MC is present (if ignition is successful), the instant at which it is evident that the flame is quenched in the PC, or the hot jet is not able to ignite the charge in the MC. For each ignition strategy, the experiment is selected in which the mean flame speed in the PC is closest to the mean over the 20 experiments.

Using inductive ignition (first row) the flame propagates slowly ($\sim 0,4\text{m/s}$) in the PC and usually does not even reach the end of the PC. When NRPD 5 pulses are delivered (second row), the flame front propagation is slow ($\sim 0,7\text{m/s}$), resulting in a hot jet entering the MC and mixing at a low rate with the colder gases. The result is a slow volume reaction with a low HRR and high combustion duration (approximately 90 ms). When 10 pulses are delivered (third row), the jet exiting the PC is faster ($\sim 1\text{m/s}$) and needs a shorter time to mix, leading to earlier ignition in the MC and faster flame propagation. In this case, the combustion duration in the MC is lower ($\sim 40\text{ms}$). Finally, when a 50 pulses case is examined (last row), an even higher flame propagation is reached ($\sim 1,6\text{m/s}$). The higher speeds result in a faster penetration of the hot jets in the MC. As a result, the hot jet mixes faster with the rather cold ambient gases, leading to a colder mixture (where the hot jet is mixed) that does not ignite. This observation is related to the overmixing phenomenon presented by Vera-Tudela et al. [35].



Figure 6.12: Ignition sequence in the PC and in the MC using the inductive and NRPD ignition system with 5, 10, and 50 pulses. 10 kHz, 12,4 bar, 90 °C, $\lambda = 1.8$. Laminar conditions in the PC.

Figure 6.13 shows five frames of the TJI ignition process using inductive and NRPD ignition with 5, 10, and 50 pulses ($\lambda = 1.8$) for turbulent initial conditions in the PC. This results in a total of 20 frames (5x4) where different instants (from left to right) and the different ignition strategies (from top to bottom) are depicted. The first four frames are taken for each experiment at 10, 15, 20, 40 ms after ignition. The

last frame for each experiment is selected as the frame where the fast combustion in the MC is present (if ignition is successful) or the instant at which it is evident that the hot jet is not able to ignite the charge in the MC. For each ignition strategy, the experiment with the maximal pressure in the MC is selected.

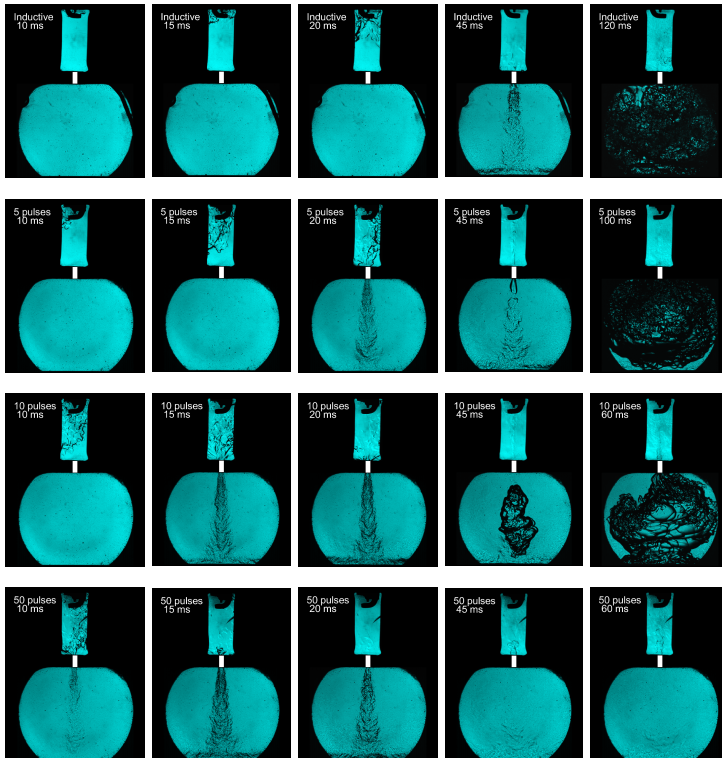


Figure 6.13: Ignition sequence in the PC and in the MC using the inductive and NRPD ignition system with 5, 10, and 50 pulses. 10 kHz, 12,4 bar, 90 °C, $\lambda = 1.8$. Turbulent conditions in the PC.

A similar pattern, as seen for the laminar case, is present when turbulent

conditions are present in the PC. NRPD ignition with 50 pulses has the fastest flame propagation in the PC, already at 10 ms. The turbulent jet mixes with the charge in the MC, but the mixing is too strong to ignite the charge. In the other three cases, the jet is able to ignite the MC charge. NRPD ignition using 10 pulses shows the best trade-off, in fact the charge in the MC is the first to ignite and allows for the shortest combustion duration (37 ms vs. 47 and 46 ms for the inductive and 5 pulses NRPD respectively).

The ignition probability in the MC is the occurrence of ignition in the MC due to the hot turbulent jet coming from the PC. For each test condition, 20 repetitions are performed, and the ignition probability is calculated as the ratio between successful ignition and total number of experiments performed.

Figure 6.14 depicts, on the top, the ignition probability as a function of the ignition strategy used. The bottom subplot depicts the ignition probability against the average flame speed in the PC.

The ignition probability in MC improves when NRPD is used instead of inductive ignition. For $\lambda = 1$, the ignition probability in the MC is 40% for inductive ignition and up to approximately 100% when NRPD ignition is used (at 5 pulses). For $\lambda = 1.4$, all tested cases ignited. For $\lambda = 1.8$, only 5% ignition success in the MC is present with inductive, and up to 90% with NRPD (best at 5 and 10 pulses).

The ignition probability in the MC is likely to be linked with mixing effectiveness: below a certain threshold, the jet entering the MC is too slow for effective mixing, and above another threshold, there is over-mixing. From the bottom subplot in Figure 6.14 it can be observed that there is an optimum flame front speed in PC (approximately between 1.4 and 4,0 m/s) for which the reliable ignition in the MC is achieved while for lower and higher values of flame speed in PC, the ignition in MC is less effective. This observation confirms the role of mixing. When the flame speed is too low, the hot jet exiting the PC mixes with small quantities of unburned MC's gas, resulting in quenching. Conversely, when the flame speed is too high, the hot jet is too diluted in the cold mixtures, resulting in a low reaction rate, or quenching.

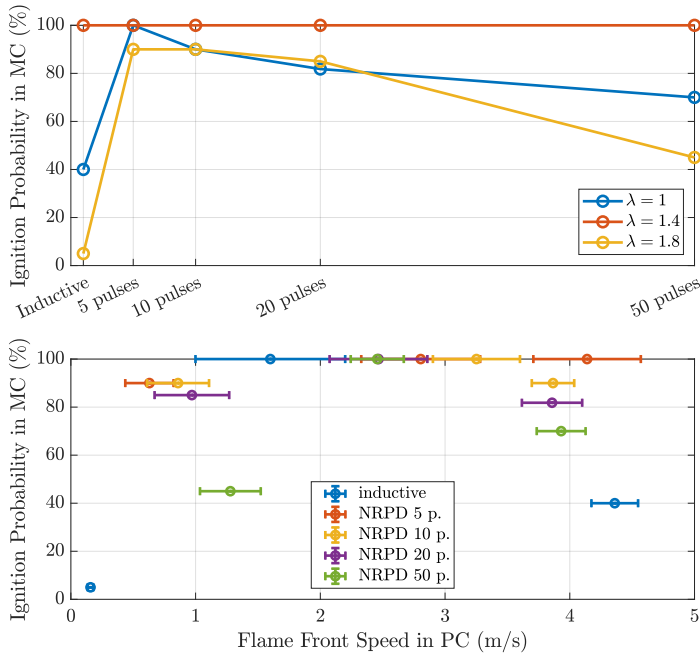


Figure 6.14: Ignition probability in the MC vs. number of pulses (top). Ignition probability in the MC vs. flame front propagation speed in PC (bottom). Laminar conditions in the PC.

Figure 6.15 depicts, on the top, the ignition probability as a function of the ignition strategy used and on the bottom the ignition probability against the average flame speed for turbulent initial conditions in the PC.

The same trend in the ignition probability in MC vs. flame front propagation in PC is observed when the turbulent cases are considered, with an optimum around 3 m/s in the PC, corresponding to 75% ignition probability in the MC. The ignition probability is overall lower when the turbulent cases are considered. This is likely due to the complex interactions occurring between turbulence in the PC, flame kernel

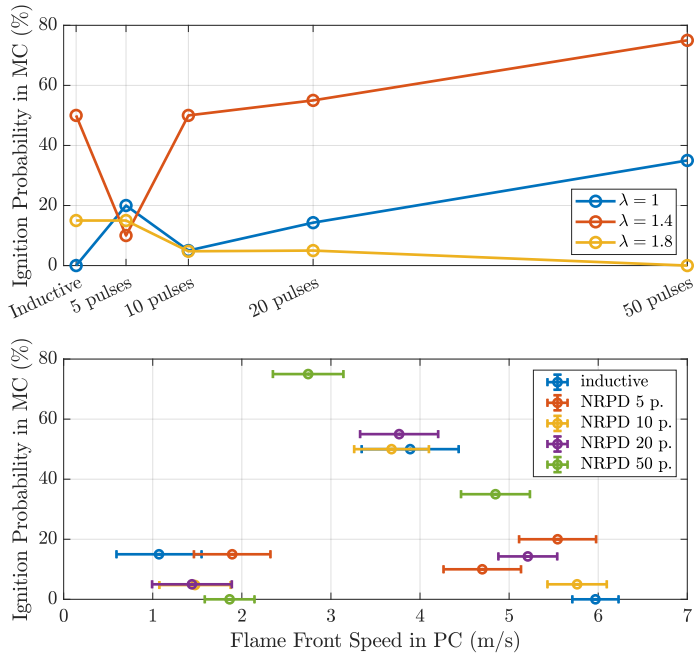


Figure 6.15: Ignition probability in the MC vs. number of pulses (top). Ignition probability in the MC vs. flame front propagation speed in PC (bottom). Turbulent conditions in the PC.

motion, and speed of jets entering the MC.

6.1.3 Summary and Discussion

In the OPC's PC, a more robust ignition is achieved with NRPD in comparison to classical inductive ignition system. The difference between different pulse numbers is visible only at lean conditions, and it is more pronounced for higher air to fuel ratios. This can be explained by the more energy required to ignite leaner conditions. Two regions of the ignition event are detected using NRPD, the first one lasting one to two ms, which is not affected by the OPC conditions (initial turbulence level and AFR) nor the number of pulses. The second region starts after 2 ms after the start of ignition and lasts till the end of the flame propagation. In this second phase, a higher number of pulses is advantageous to increase the flame propagation speed when the flame is usually slow (high AFR and low initial turbulence conditions). It is known that the heat addition of the ignition increases the flame speed during the early kernel expansion [125]. Pulsed discharge seems to enhance this effect significantly. In fact, the increases in ignition success rate at high AFR with NRPD could probably be explained by the increase in ignition radius using pulsed discharge [5]. The increase in flame speed when NRPD is applied after the flame has reached the critical radius is still partially unclear. A possible explanation could be the effect of the shockwave created by the NPD [126]. This effect could enhance the turbulence level and, hence, the flame speed.

In order to effectively ignite the charge in the MC, there is an optimum range of flame front propagation speed in PC for which the jets entering the MC ensure adequate mixing with the MC mixture that results in reliable ignition. Therefore, ignition probability in MC has a maximum in a certain range of flame front propagation in PC. Turbulent PC conditions lead to a reduced ignition probability in MC when compared to laminar PC conditions, for all the pulse number and repetition frequencies investigated. This confirms that, while the NRPD strategy improves the ignition in PC, the role of mixing is then the prevailing effect when TJI comes into play. Nevertheless, the possibility of varying the number of pulses offers a further degree of freedom to effectively ignite the MC charge. The combination of NRPD and PC concepts proved to be able to ignite extra-lean mixtures under different conditions reliably. However, just increasing the number of pulses is not the rule of thumb, as it proved to aid ignition in the PC but led to misfires in the MC.

It is worth noticing that in a running engine, the heat losses and turbulence conditions are different from those in the present setup. The presence of turbulence in the combustion chamber of an engine and the lower wall heat losses due to warmer walls result in a much higher ignition probability when compared to that obtained in the OPC setup. In fact, in [116], operations up to $\lambda = 1.8$ were possible in a running engine without misfires. Therefore, the OPC setup represents a “worst-case scenario” for the ignition in engine conditions. Even if the actual performance of a real engine is strictly dependent on the combustion concept of that specific engine (λ value, EGR, fuel, turbulence levels, size of the engine, pressure level, homogeneous or stratified mixture, etc.), it is reasonable to expect that an improvement in the ignition in the OPC translate in an improvement also in a full metal engine setup.

6.2 Ignition Detection

The material presented in this section originates from the article titled "Ignition detection with the breakdown voltage measurement during nanosecond repetitively pulsed discharges" [22].

In SI engines, classical inductive or capacitive ignition systems deliver one ignition event per engine cycle; the only actuating variable is the timing of the ignition. If the ignition is unsuccessful or the combustion process is non-optimal, the only possible adjustment is within the following engine cycle, where the fuel quantity or the ignition timing could be adjusted. In contrast, ignition detection during the early stage of combustion, in conjunction with a fast actuator, allows the engine to react to misfires within the same engine cycle. If the detection and actuation are sufficiently rapid, the slight advance of combustion phasing from the ideal location will have a minor impact. With an NRPD system, the number of pulses and the repetition frequency could be varied to stabilize the ignition process. This possibility of reacting on ignition detection is even more interesting for systems with direct fuel injection to the combustion chamber, where additional fuel could be applied within the same engine cycle.

Current measurement by applying a DC voltage after ignition over the spark plug electrodes in SI-Engines has been successfully used to detect abnormal combustion (misfire and knock) and the location of the peak

pressures [127, 128]. Several reactions in the combustion process include ions, which are detected by the current measurement and can be used for feedback control. Nevertheless, during early flame kernel formation, ions produced by the electrical discharge are likely still present between the electrodes making the reading inaccurate. Therefore, this technique is best suited for information between cycles, not during the ignition or early flame kernel event itself.

The discharge current and voltage are affected by the surrounding gases. For example, in [129], the authors have shown that the spark discharge duration correlates with the fluid velocity around the spark plug. Knowing the fluid velocity could help to gain information about the stochastic nature of the turbulence during the ignition event, which is known to impact the cycle-to-cycle variation [130]. Although the flow velocity could affect the later combustion stage and, in extreme cases, also result in flame quenching, knowing the fluid motion around the spark plug does not directly correlate to reliable ignition detection.

A fast flame detection technique based on the breakdown voltage measurement is introduced in [131], which presented an analysis of a second spark plug used as a detecting probe. The authors detect the flame front by applying a voltage slightly below the breakdown threshold across the gap, and once the flame arrives at the probe, the breakdown strength between the gap is reduced, triggering the breakdown event. The proposed active plasma probing method is much faster than ion current monitoring. It takes only 10 μs for the voltage to collapse, while it takes 800 μs for the ion current to rise to the maximal value. This investigation outlines the dependency of the breakdown voltage on the gas composition variation during combustion. However, due to the distance between the two spark plugs (also physically constrained), this approach is not suited to detect the establishment of the early flame kernel.

The goal of ignition is to start a self-sustained chemical reaction. The plasma expansion following a nanosecond discharge depends on the voltage supply but is not dependent on the mixture composition. Regardless of the plasma condition, there is always a zone where the ideal temperatures for the chemical reaction are present, leading to the establishment of an early flame kernel strongly affected by the gas composition [2, 3, 32]. The breakdown voltage under NRPD is investigated

in Chapter 4, where the peak voltage during a nanosecond discharge depends on the used electrode material and spacing, the density between the electrodes, and the pulse rise rate. After the discharge, the plasma recombination and cooling depend on the heat losses to the electrodes and the surrounding gas temperature. Therefore, it can be expected that if the delay between nanosecond pulses is long enough (on the order of milliseconds), the local density between the electrodes will be affected by the presence and strength of the early flame kernel. This could allow ignition detection by measuring the pulse breakdown voltage after early flame kernel formation, before any pressure increase due to combustion, and before significant flame front expansion. Such a methodology could allow for closed-loop ignition control with NRPD. In addition, detecting the early flame kernel could be valuable for other applications, such as energy-efficient flame stabilization or feedback control of thermoacoustic instabilities in secondstage combustors of gas turbines [132].

A consistent initialization of non-equilibrium plasma discharges for use in engine CFD codes is proposed in [133], where it is shown that the approach produces results that agree with experiments on the ignition of stoichiometric air-methane mixtures. Longer dwell times between pulses require more energy to establish flame propagation. Simulations show that using two 1,4 mJ pulses with a 300 μs dwell time is insufficient to establish a robust flame propagation, and 300 μs after the second discharge, the temperature between the electrodes falls below 800 K. In contrast, when the pulses have a dwell time of 100 μs , flame propagation is possible. The temperature between the electrodes after 300 μs exceed 1'500 K. Due to the minor heat release, the pressure is similar for the two cases, so the local density would be nearly half for the second case. Applying a third nanosecond pulse after 300 μs would result in different breakdown voltages for the two conditions and, therefore, detect the case where a flame front is present.

6.2.1 Theory Behind the Ignition Detection Technique

As shown in Chapter 4, the breakdown voltage under slowly increasing voltages scales approximately linearly with the density, while the breakdown voltage of NPDs depends on the static breakdown voltage and on the pulse rise rate. The scatter of this value depends on the appearance of the seed electron that starts the electron avalanche, called the stat-

istical time lag, which exponentially decreases at high electric fields. These two features outline that even though large voltage transients are present under NRPD, the breakdown voltage value is still highly dependent on the local density if the pulse rise rate and electrode spacing are kept constant.

In SI-Engines, combustion is initiated with an electrical discharge. During a nanosecond discharge during the first few tens of nanoseconds, the gas heats to approximately 20-50'000 K, and the pressure increases. The plasma is fully dissociated and ionized [109]. Following the discharge, a strong shockwave expands the plasma kernel, decreasing the pressure and temperature [3, 126]. During the expansion, the plasma recombines, and if the mixture is ignitable, its surface turns into the flame front, a thin reaction sheet where the chemical reactions occur. While the initial plasma kernel growth ($< 100 \mu\text{s}$) is not affected by the AFR, the following inflammation process is strongly affected by the gas composition, the flame curvature and stretch, and the flow velocity in the vicinity of the spark plug. Following inflammation, a turbulent flame develops [32].

The idea behind the ignition detection technique is that inflammation affects the local density following the nanosecond pulse after plasma kernel expansion. If the inflammation is successful, the heat losses from the gas present between the electrodes and the surrounding burned gas are lower than if the early flame is quenched. Lower heat losses will result in a lower local density. If a further nanosecond pulse is applied after the plasma kernel expansion, the breakdown voltage provides insight into the local density and, therefore, the inflammation process. Furthermore, different AFRs result in different burned gas temperatures and, therefore, different cooling rates and local densities.

The NRPD ignition pulse pattern for ignition detection purposes is, therefore, composed of the main pulse sequence at high PRF and an additional (control) pulse after a delay. Figure 6.16 shows the voltage at the gap for a representative experiment in the RCEM.

The main ignition sequence is composed of five pulses at 10 kHz, and the control pulse is placed 1.5 ms after the start of ignition, using the pulse generator A.

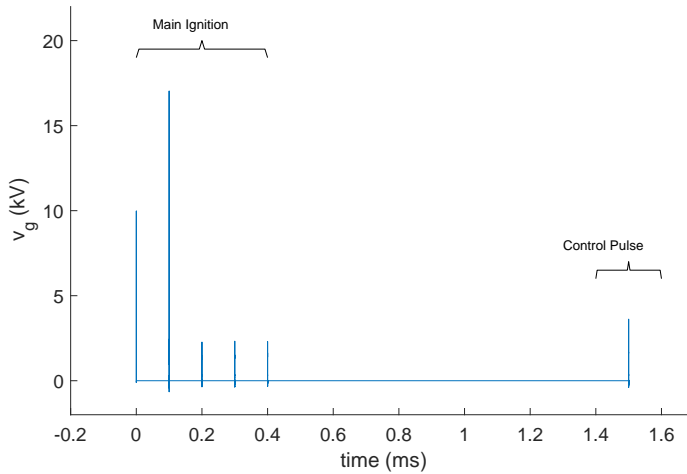


Figure 6.16: Pulse pattern used for ignition detection in the RCEM

6.2.2 Experiments in the Ignition Cell

Figure 6.17 shows the gap current and voltage for a 20-pulse ignition at 10 kHz with one control pulse 5 ms after the start of ignition using the J-gap spark plug.

The first pulse was not enough to achieve breakdown, visible from the low peak gap current. The measured 5 A peak current for the first pulse is in line with the expected capacitive current for the present voltage rise rate and the capacitance of the spark plug. The second pulse is the first one where the breakdown is possible due to the higher pulse amplitude at approximately 18 kV. For the following pulses at 10 kHz (0.2–1.9 ms), the maximal voltage between the electrodes is approximately 2.5 kV. The reduced local density between the electrodes due to the heating resulting from the previous pulse and the presence of active and charged species can explain this behavior. The pulse used to evaluate the ignition is the control pulse at 5 ms. The control pulse’s maximal gap voltage for the depicted case is 7.3 kV, and the energy it deposits to the plasma is 13 mJ.

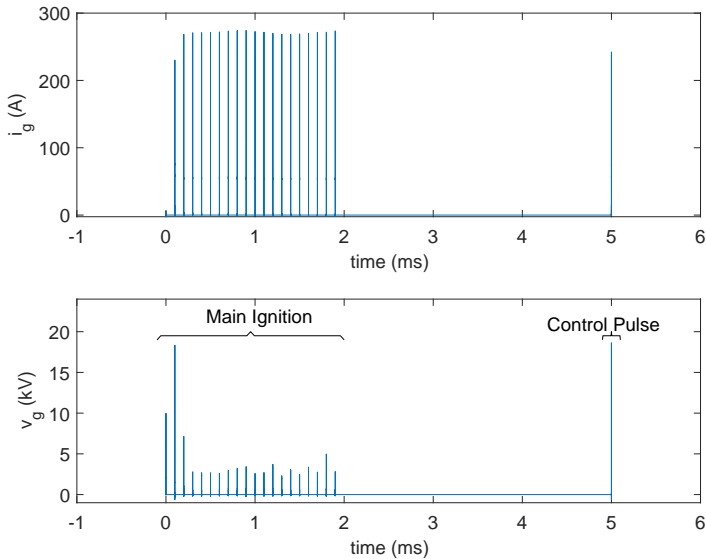


Figure 6.17: Pulse pattern for ignition detection, 5 bar $\lambda = 1.5$, J-gap spark plug.

Figure 6.18 summarizes the results of 50 repetitions at 5 bar, ambient temperature, and $\lambda = 1.5$ with the same pulse pattern as above, the effectiveness of the ignition detection method. An ignition is treated as successful if the pressure increases by more than one bar. On the top left corner, the boxplot is used to group the statistics of the breakdown voltage where ignition was successful and where quenching was present. The red vertical line depicts the median, while the blue rectangle outlines the region between the 25th and 75th percentiles, and the black marks extend to the most extreme data point. The red plus represents the outliers. In the top right corner, the waveforms of the recorded voltages during the control pulse for the extreme cases of quenching (highest breakdown voltage red line) and ignition (lowest breakdown voltage purple line) are depicted. The black lines on the same plot are used to show the voltage that would develop over the gap if there was no breakdown (prospective voltage). On the bottom, the pressure against

time is also reported for the two extreme cases.

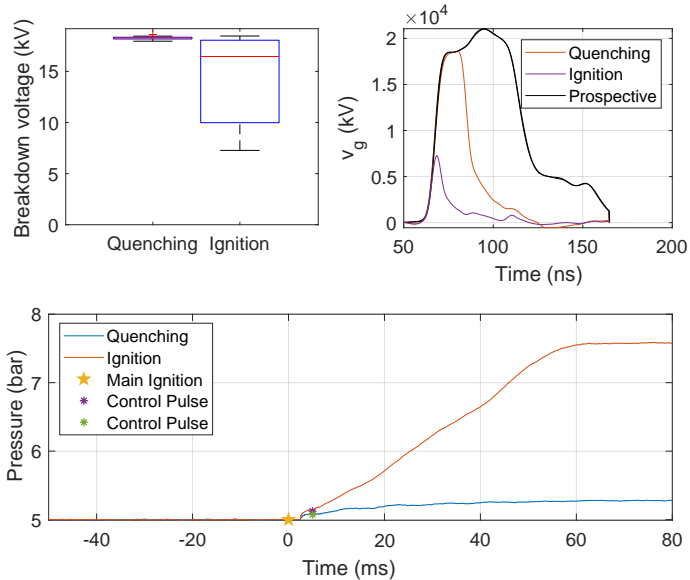


Figure 6.18: Ignition detection for the J-gap spark plug, 50 repetitions, 5 bar, and $\lambda = 1.5$. Statistics boxplot (up-left), voltage waveforms (up-right) and pressure evolution (bottom) of the extreme cases.

Breakdown voltages above 18 kV were measured for the nine cases where no ignition was detected, while voltages as low as 7,3 kV were measured when the pressure rise suggested successful ignition. The two black waveforms in Figure 6.18 top-right overlap, outlining that the difference in breakdown voltage is not due to different applied voltages. The pressure waveforms against time show that the control pulse is applied before significant pressure rises due to combustion are present.

Figure 6.19 depicts the statistics of the ignition detection for different delay times of the control pulse for the surface spark plug operated at $\lambda = 1.35$ and 10 bar. Each group comprises two boxplots, one for the cases where ignition was successful (right), and one for the cases where quenching occurred (left). The main ignition is performed with ten

pulses at 10 kHz.

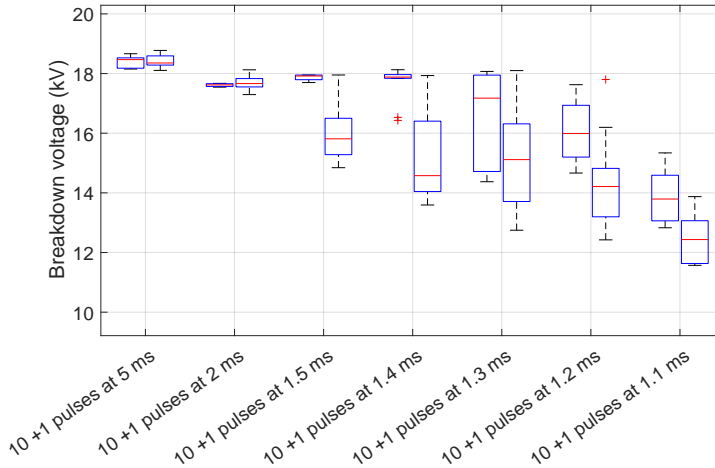


Figure 6.19: Statistical boxplot of the ignition detection with the surface gap spark plug for different delays of the control pulse, 20 repetitions each, 10 bar, $\lambda = 1.35$, and surface spark plug.

For delay times below 1.5 ms, the statistics indicate the possibility of distinguishing between ignition and quenching. Nevertheless, it is clear that some overlap is present. The control pulse is always placed before a notable pressure increase inside the constant volume cell and is thus feasible for a possible closed-loop reaction scheme.

6.2.3 Experiments in the Rapid Compression and Expansion Machine

The rapid compression before combustion in the RCEM replicates pressure and temperature conditions at ignition timing much closer to those of an engine than the ignition cell setup. The geometry and piston motion allow for flame propagations and HRR similar to those in engines. Furthermore, the optical accesses allow for analyzing the ignition event and early flame propagation with Schlieren imaging. The RCEM

is therefore used to analyze the ignition detection technique by performing six sets of experiments, each with ten repetitions. The same parameters are used in each experiment except for the injected methane mass. This results in the same pressure and temperature trajectory during compression but different expansion trajectories, depending on the combustion. Methane is injected during the slow throttled motion before the rapid compression (see Section 2.4). Due to the high injection pressures used (~ 100 bar) and the long time before the rapid compression starts (~ 2 s), the fuel has enough time and momentum to mix perfectly [134]. During the filling process, the air mass slightly scatters between different experiments, which results in a slight variation in λ (up to 7 %). The walls of the RCEM are heated to 60°C , and the compression process further increases the temperature before ignition. For these experiments, the J-gap spark plug is used. The main ignition is achieved with five pulses at 10 kHz, and the control pulse is at 1,5 ms.

Figure 6.20 (left) shows in double logarithmic scale the pressure–volume trace for three different experiments having three different λ values; the star represents the spark timing, while the dots represent the control pulses' location. In Figure 6.20 (right), the pressures and piston positions are depicted against time (in red and blue, respectively).

A straight line in the double logarithmic plot (Figure 6.20, left) shows that the compression process is very close to polytropic, because, for a polytropic change of state, pV^n is constant (with p being the pressure, V the volume, and n the polytropic exponent). The location of the control pulse is well before the deviation from the straight line outlining that the detection of successful ignition is achieved before notable heat release takes place.

From Figure 6.20 (right), it can be seen that the combustion process influences the piston motion in the RCEM. In fact, a faster pressure increase after TDC results in a higher piston acceleration. During compression, the pressure traces for the different experiments overlap before ignition. After ignition, there is a rather long time when the pressure curves still overlap because the HRR is slow. The pressure curves diverge only after the combustion process starts.

The spark timing in SI-Engines is usually adjusted to achieve (whenever possible) the best efficiency. This results in having the center of com-

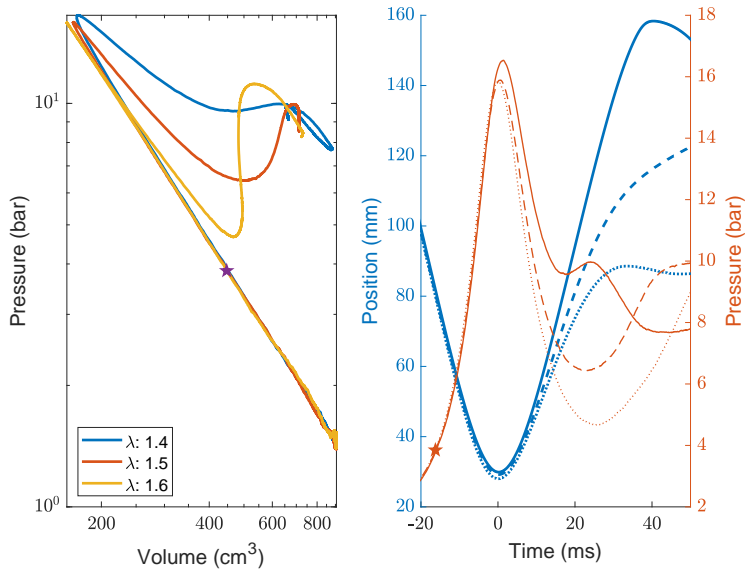


Figure 6.20: Pressure traces in the RCEM: pressure, volume (left); pressure and position vs. time (right).

bustion at a rather constant position, usually at 8°CA after TDC. Variation in spark timing results in different breakdown voltages due to increasing density during compression. For the current investigation, the spark timing is kept constant to test the ignition detection technique without additional variation and to have similar densities at ignition timing for the different operating points tested.

Figure 6.21 shows the statistics of the control pulses' breakdown voltage against λ (on the left). Figure 6.21 (on the right) shows the breakdown voltage against the burned gas temperature when 10 % of the fuel mass is burned, estimated with the two-zone thermodynamic model [41].

The median of the control pulses' breakdown voltage increases with increasing λ , except for the last group ($\lambda = 2.4$). The scatter of the data tends to increase as well. The inverse trend is recognized for an increasing temperature of the burned zone.

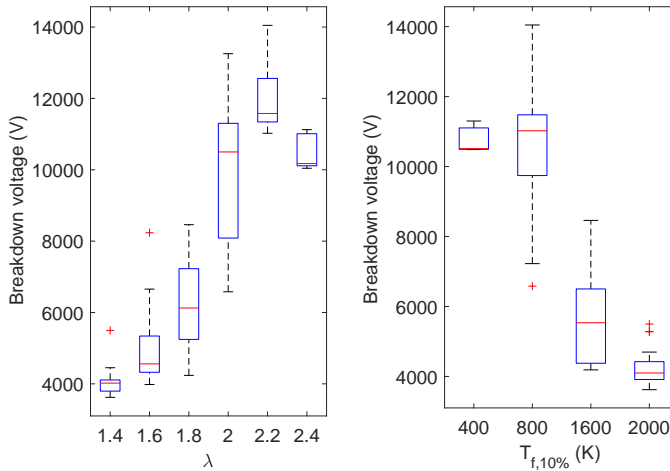


Figure 6.21: Boxplots of the control pulse breakdown voltage vs. λ (left) and vs. flame temperature (right).

Figure 6.22 shows four images at 1.5, 2.5, 5, and 10 ms taken from the Schlieren recording (through the side windows as explained in Section 2.4) for the experiments where the highest breakdown voltage of 14 kV was recorded.

In the experiment reported in Figure 6.22, it can be seen that the zone that reacts does not show a clear flame front when the control pulse is applied (1,5 ms) and that, at 10 ms, hardly any difference in density can be seen from the Schlieren video. This indicates that there was no successful initiation of a combustion process.

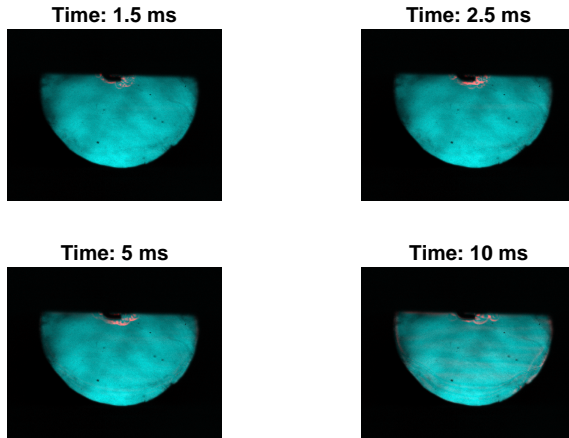


Figure 6.22: Four frames of the high-speed Schlieren video for the maximum recorded voltage of the control pulse (breakdown voltage of 14 kV, $\lambda = 2.2$).

Figure 6.23 shows four frames where the lowest breakdown voltage of 3,6 kV is recorded.

In this case ($\lambda = 1.4$, Figure 6.23), a clear flame front can be detected at the end of the ignition process (1,5 ms).

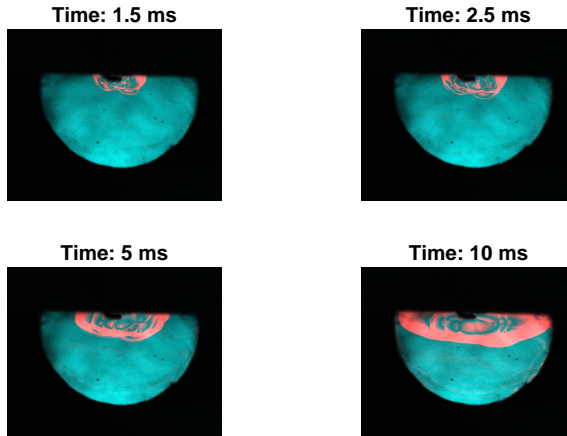


Figure 6.23: Four frames of the high-speed Schlieren video for the minimum recorded voltage of the control pulse (breakdown voltage of 3,6 kV, $\lambda = 1.4$).

Figure 6.24 shows, on the left, the voltage waveforms of the two extreme cases reported in Figure 6.22 (blue) and Figure 6.23 (red). On the right, the burned and unburned zone temperatures from the HRR analysis are depicted for the two cases.

From Figure 6.24, the breakdown voltage for the quenching experiment is four times higher than the one where the lowest breakdown voltage is recorded. The temperature during compression before combustion is approximately 500 K, while the burned temperatures exceed 2'000 K for the depicted case. Similar pressures are present during compression stroke for the leaner case, while the burned temperature is lower and peaks at around 1'650 K. The combustion process affects the pressure and the temperature in the unburned zone during the expansion stroke.

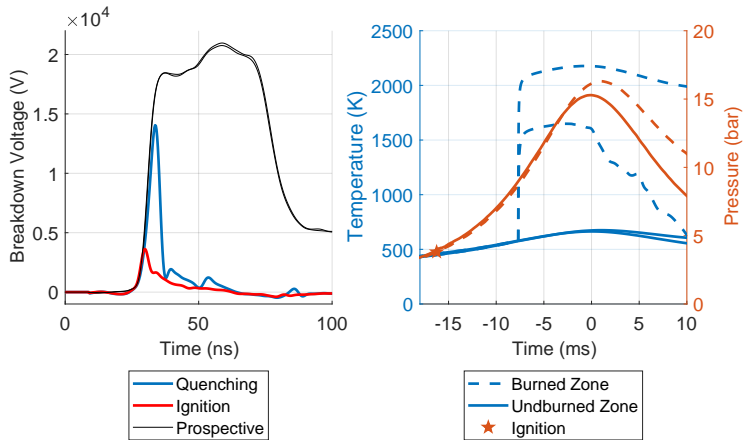


Figure 6.24: Voltage waveform of the extreme cases (left) and temperature evolution from two-zone thermodynamic analysis (right).

Figure 6.25 shows the HRR analysis for five experiments in the RCEM. The colors are used to identify the different experiments with different λ . The solid line depicts the HRR, while the dashed line shows its integration (i.e., the cumulative heat released).

Lower λ gives, as expected, a faster heat release. For the experiments at λ values of 1.4, 1.5, and 1.6, the measurement window was long enough to capture the complete combustion event. For $\lambda = 1.8$, only a portion of the combustion process is captured. In contrast, ignition was not possible for $\lambda = 2.1$, or the inflammation phase took so long that capturing the HRR during the first 100 ms was not possible.

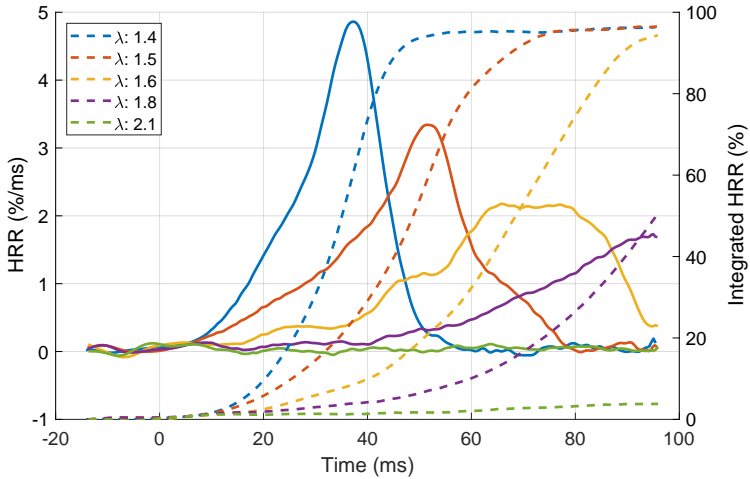


Figure 6.25: HRR of 5 experiments in the RCEM with varying AFR.

Figure 6.26 shows the measured breakdown voltage of the control pulse against the ignition delay time (Δt_{ign}), defined as the time between ignition and 10 % of mass fuel converted. Ten percent is used to avoid capturing very slow burning occurrences. All the experiments that could not reach 10 % fuel conversion are depicted on the furthest right of Figure 6.26 and labeled “Quenching”.

The graph (Figure 6.26) is divided into three regions. The red line is the one where all the breakdown voltage values are higher than the highest one where ignition was detected ($>8,5$ kV). We call this the quenching voltage threshold. The green region is the region where all the recorded breakdown voltages lie below the lowest voltage recorded where no HRR was present (6,6 kV). This line is referred to as the ignition voltage threshold. The yellow area lies between these two thresholds (6.6–8,5 kV).

When faster burning cycles are present (<38 ms), a breakdown voltage below the ignition voltage threshold is always measured. This means that these cycles can be divided from those where the flame quenches

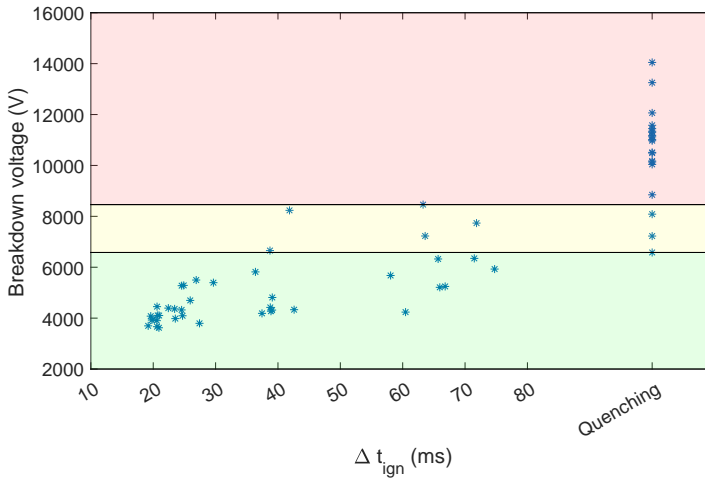


Figure 6.26: Breakdown voltage of the control pulse vs. ignition delay in the RCEM for all the experiments in the RCEM.

without superposition. The area between the two thresholds (yellow) outlines an area where combustion and quenching are hard to detect.

Figure 6.27 depicts four frames of the Schlieren videos at 1.5, 2.5, 10, and 40 ms after the start of ignition for the point that defines the ignition voltage threshold line. The first frame shows the instant where the control pulse is applied.

Despite the very high overall λ of 2.1, a flamekernel is clearly visible which expands over the entire visible area.

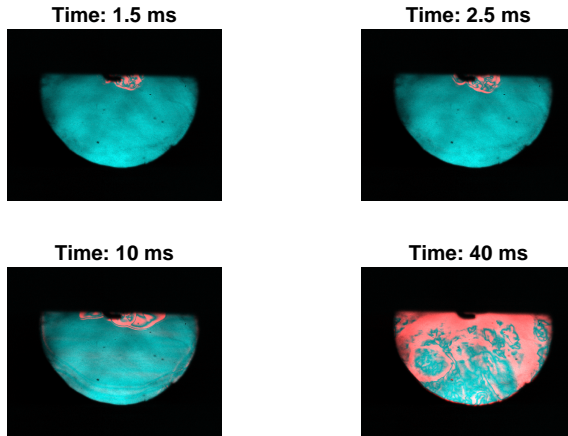


Figure 6.27: Four frames of the high-speed Schlieren video for the lowest breakdown voltage where no HRR is detected (breakdown voltage of 6,6 kV, $\lambda = 2.1$).

Figure 6.28 shows four Schlieren video frames (1.5, 2.5, 10, and 40 ms) for the point that defines the quenching voltage threshold.

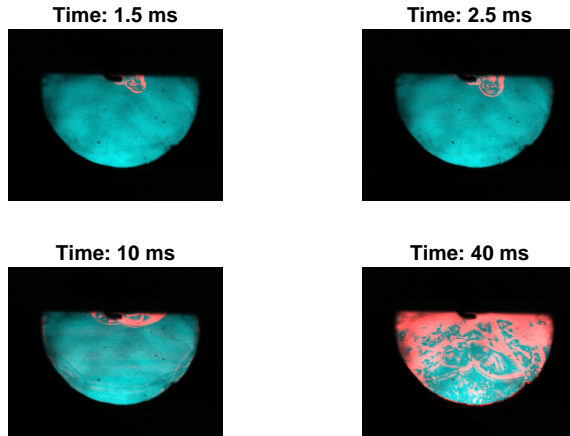


Figure 6.28: Four frames of the high-speed Schlieren video for the highest breakdown voltage where the HRR is detected (breakdown voltage of 8,5 kV, $\lambda = 1.8$).

The overall λ is 1.8, but similar images to the case of the ignition voltage threshold are present. Similar recordings are also visible for the other 6 cases in the yellow zone, two with no ignition and four with slow HRR.

Figure 6.29 shows the HRR analysis for the points that define the two thresholds.

The same HRR is measured between the two experiments until 20 ms after ignition. After 20 ms for the experiment with the higher λ exponential growth versus time is present, while for the lower λ a slow linear growth is found.

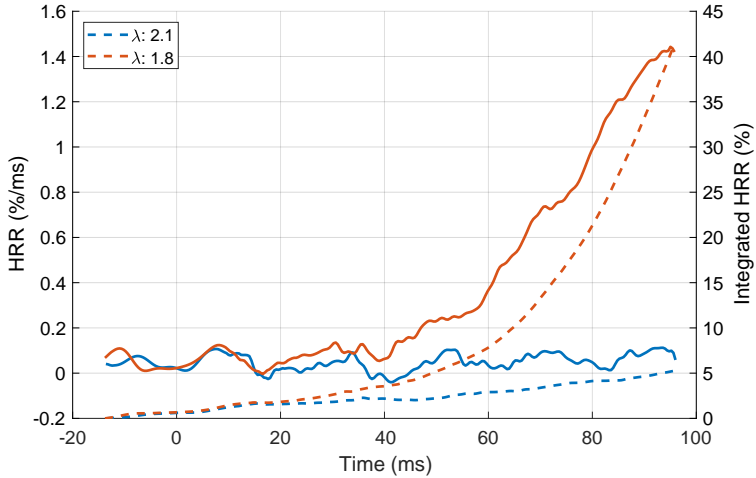


Figure 6.29: HRR of the two thresholds (quenching and ignition).

Figure 6.30 shows the apparent flame area (A_f) at 5 ms against the measured breakdown voltage of the control pulse. The apparent flame area is calculated with an arbitrary unit calculated as the number of all the pixels that are treated as flame (a.u.), as explained in Section 2.5. The red line represents a fit line between the data points, while the dashed pink lines represent the error ($\text{one-}\sigma$) around the fit.

The breakdown voltage of the control pulse decreases as the apparent flame area increases.

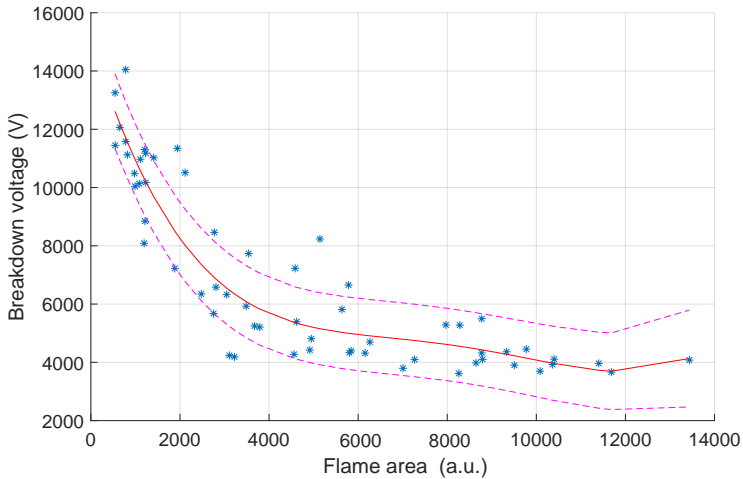


Figure 6.30: Apparent flame area measured at 5 ms after ignition vs. break down voltage.

Figure 6.31 groups all the experiments in two boxplots. On the left, the experiments with an apparent flame area at 5 ms below 800 a u ($A_f < 800$) are shown, while on the right, those above 800 a u ($A_f > 800$) are displayed.

The 800 a u apparent flame area (Figure 6.31) at 5 ms divides the two breakdown groups without superposition, where lower breakdown voltages are present for larger apparent flame areas. The two groups present some overlap if later times or larger threshold flames are chosen.

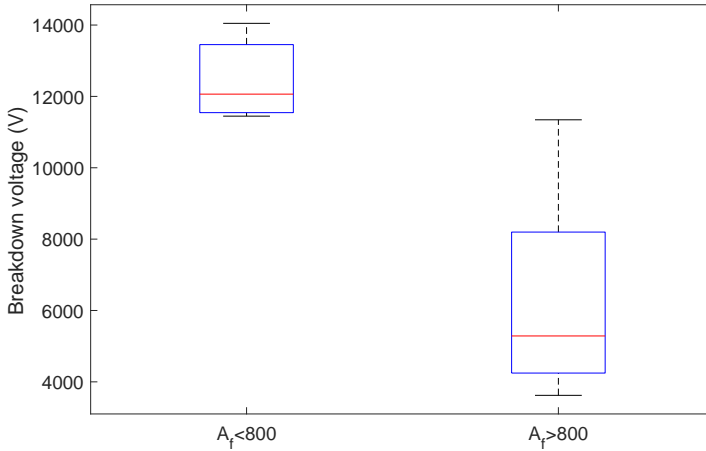


Figure 6.31: Breakdown voltage of the control pulse vs. apparent flame area at 5 ms after ignition.

Figure 6.32 shows the breakdown voltage of the control pulse as a function of the flame area at 5 ms and the overall λ .

Lower breakdown voltages of the control pulse are present when larger initial flame kernels and lower AFR are present.

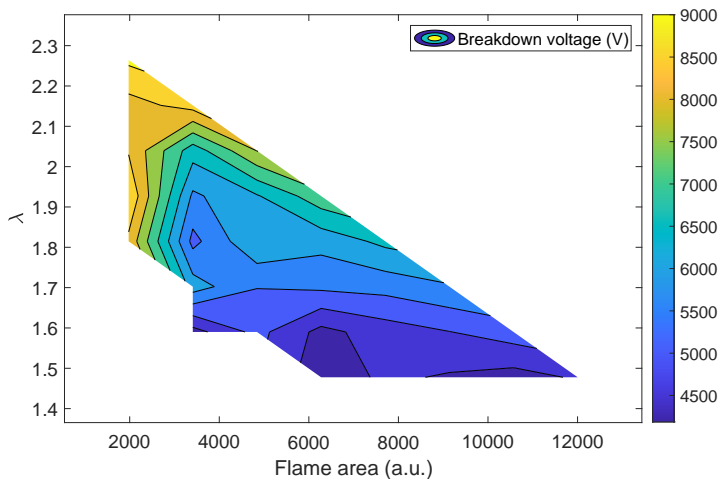


Figure 6.32: Breakdown voltage variation as a function of apparent flame area and λ .

6.2.4 Summary and Discussion

The initial plasma kernel growth (up to approx. 100 μs) is not affected by the AFR. Non-thermal plasma discharge simulations show a similar temperature profile for times below 100 μs for different fuels and dilutions [133]. After approx. 100 μs , the early flame kernel is influenced by the in-cylinder conditions. During this phase, the kernel's presence, and dimension affect the local temperature and therefore the density. The breakdown strength of the gas is consequently also affected. The breakdown voltage of an additional pulse (control pulse) placed in this phase returns lower values when a strong kernel is present.

The possibility of using the control pulse breakdown voltage for ignition detection purposes is investigated at the ignitability limit inside the CVC. A lower breakdown voltage is observed when the ignition is successful. The ideal time for ignition detection is different for the two investigated spark plugs, probably depending on the spark plug's heat range, the number of pulses used in the main ignition sequence, and the different gas densities and compositions. There is an ideal dwell

time for the delay between the end of the main ignition sequence and the control pulse between 0.5 and 5 ms. When the dwell time is too short, the breakdown voltage value is still affected by the previous discharge, while when the delay is too long, the local density between the electrodes decreases back to the value typical of quenching conditions.

The breakdown voltage for ignition and quenching experiments in the CVC shows some overlap. One reason is that the breakdown voltage value under nanosecond pulses naturally scatters due to the stochastic nature of the seed electron appearance. Furthermore, even if an early flame could be formed and correctly detected by the ignition detection technique, the flame could quench at a later stage without giving a measurable pressure rise. Conversely, when the control pulse detects no early flame, this pulse could be the one responsible for starting the combustion process. From the analysis in the RCEM, these extreme cases can be recognized thanks to Schlieren imaging and a detailed heat release analysis.

Inside the RCEM, experiments at different λ are performed. The dwell time between the last pulse of the main ignition sequence and the control pulse is 1 ms for all experiments. This time delay is insufficient in all the experiments for an appreciable pressure increase due to combustion. The only factors that can explain a decrease in gas breakdown strength are higher local temperature (density) and/or higher density of active and excited species, both reducible to the presence of a flame kernel.

The breakdown voltage of the control pulse increases with increasing λ . This is in line with the theory behind the ignition detection method. The heat losses between the burned gas present between the electrodes and the flame kernel are lower if λ is lower due to the higher flame temperatures. Similar effects are reported in [131], where higher voltage strengths are present in the flame front of reacting mixtures for higher AFRs. The minimum voltage necessary to have a breakdown when the flame arrived at the spark plug increased from 3,3 kV to 4 kV for a λ increase from 1.2 to 1.6 [131]. The voltage increase ratio is inversely proportional to the adiabatic flame temperature ratio (2'080 K vs. 1'730 K). The authors attribute the higher breakdown strength to the lower ion density and temperatures present in the flame front of diluted combustion, having lower reaction rates.

From the HRR analysis, it is clear that the fast-burning cycles and the

cycles where no initial flame kernel is visible are distinguishable from their breakdown voltage value. The cycles with ignition delay times below 38 ms have a breakdown voltage lower than 6 kV, which is less than the lowest recorded breakdown voltage of 6,6 kV present when no HRR is present.

Experiments with lower HRR sometimes overlap with experiments where no HRR is detected. Similar flame kernels are detected from the Schlieren video analysis for these experiments. The difference in HRR rises in a later stage of combustion, as is visible from the HRR analysis.

The breakdown voltage's control pulse decreases with lower AFRs and larger areas of the initial flame kernels. Both effects result in lower local density between the electrodes. On the one hand, lower λ results in higher local temperatures and, therefore, lower density. On the other hand, a larger flame area reduces the surface-to-volume ratio reducing the specific heat losses. This influence further explains the overlapping experiments where similar local density (i.e., breakdown voltage) can be found in experiments with a large flame area and a high λ or experiments having a small flame area and a lower λ value.

The prospective voltage of the control pulse remains constant for all the experiments, and the breakdown voltage for all the experiments in the RCEM occurs during the rising part of the nanosecond pulse (Figure 6.24). Therefore, as shown in Chapter 4, the breakdown voltage linearly depends on the gas density. The highest measured breakdown voltage in the RCEM is approximately four times higher than the lowest. This correlates well with the temperature ratio of the burned gas ($\sim 2'000$ K) estimated with the two-zone thermodynamic analysis calculated for the experiments with a fast HRR and temperatures before combustion of 500 K, which is the temperature present in the RCEM at ignition timing due to the polytropic compression. Since the difference between the unburned and burned zone decreases for increasing AFR, the maximal possible density ratio decreases. Nevertheless, with a compression temperature of 900 K (typical of engines) and a highly diluted combustion ($\lambda = 2$) the adiabatic flame temperature is above 1'900 K, which still gives theoretical density ratios between unburned and burned zone above 2.

The presented ignition detection technique provides the possibility of combustion monitoring based on the breakdown voltage value of an

additional pulse during inflammation after ignition. Several factors influence the breakdown voltage value: the spark plug geometry and its heat range, the initial pressure, and temperature, the rising rate of the applied voltage, the number of pulses of the main ignition sequence, etc. Nevertheless, if most factors are kept constant, the technique is a reliable ignition diagnostic technique. A further limitation of the proposed method is the ideal location of the control pulse. The sooner the failed ignition is detected, the more time is available to react to quenching. The disadvantage of short dwell times is that later flame quenching is impossible to capture, as has been seen in some RCEM experiments with a high air excess ratio.

This technique offers the advantage of being a very fast detection method. The breakdown voltage value is affected by the inflammation process only a few hundred microseconds after the ignition event, well before there is an increase in pressure due to the heat release. The control pulse is applied in the ignition cell before the pressure increases and in the RCEM before the pressure deviates from polytropic compression. Such a velocity of detection is usually reserved for optical detection methods. Nevertheless, the proposed technique only relies on measuring the breakdown voltage of one additional discharge after ignition in the same location. This gives the theoretical possibility of fast closed-loop control of ignition with NRPD, where additional pulses are delivered to better ignite the mixtures when a high breakdown voltage of the control pulse is present. Even a coupling of fast ignition detection with a direct fuel injection system could be possible, allowing the possibility of providing more fuel before a new ignition attempt.

For in-vehicle applications, one approach for monitoring the success of ignition is the shunt measurement in the middle of the HV cable, which gives the advantage of no need to place a voltage probe near the spark plug. Furthermore, if the supplied pulse is stable throughout the operations, ignition success can be characterized only by the reflected voltage's maximal value. Since a typical engine ECU does not have a sufficient sampling rate to represent the shunt measurement, a trigger circuit could be applied, for example, to stop the ignition process when the reflected voltage falls below a given threshold.

Since the breakdown voltage of the control pulse decreases with decreasing λ , the technique could also be used to detect λ at the spark

plug location in applications where this measurement is impossible, for example, in active PCs and stratified combustion. The precision of the technique is limited, but a deviation in λ of approx. 0.2 is feasible to detect with one-sigma confidence in the RCEM (Figure 6.21). If the λ estimation goal is the optimization of variables such as injection timing or duration inside an active PC, the repetition of the measurement could increase the precision of the estimation.

Because multi-spark inductive coils are currently state-of-the-art ignition systems in various vehicles, this technique could probably also be applied without an NRPD ignition system. Nevertheless, one problem is counterintuitively bounded by the fast-rising pulse nature of NRPD. One would assume that the breakdown voltage value scatter would decrease with decreasing voltage gradients. Nevertheless, the dependence of the seed electron generation rate on a reduced electric field could result in less scatter with NRPD, making this diagnostic technique not applicable or less precise with comparable slow increasing voltage systems. Therefore, the ignition diagnostic technique in future works should also be investigated with state-of-the-art multi-spark ignition systems.

The current investigation is performed in setups where the charge motion is nonexistent (ignition cell) or highly reduced (RCEM) when compared to ICEs. Turbulence could move the flame kernel away from the electrodes making the detection more difficult. In future research, the effect of turbulence on the ignition diagnostic technique should be evaluated in SI Engines. After assessment in engines, the technique could be applied, for example, to reduce cycle-to-cycle variability.

6.3 Jet-Guided Hydrogen Combustion

This section outlines an investigation of hydrogen jet-guided spark-ignited combustion. Particularly, this chapter focuses on the effect of using NRPD to ignite the underexpanded jet at its periphery and the comparison against inductive ignition. This section originates from the article titled "Optical and Thermodynamic Investigation of Jet-guided Spark Ignited Hydrogen Combustion" [23].

Since the 1930s, hydrogen has been a focal point in ICE research due to its potential as a clean and renewable fuel. Hydrogen exhibits distinct physical and chemical characteristics compared to traditional fuels. Hy-

drogen has a high (laminar) flame speed; even in the absence of turbulence, the flame speed is faster than the laminar one due to thermo-diffusive effects [135]. Hydrogen has a high auto-ignition temperature, making it a promising candidate for combustion in the Otto cycle. Nevertheless, the minimum ignition energy of hydrogen is an order of magnitude lower than typical hydrocarbon fuels, and its flammability limits are much broader, making hydrogen-air mixtures very susceptible to hotspots and leading to abnormal combustion events such as pre-ignition, knock, and back-fire [136]. Furthermore, hydrogen has a low quenching distance, increasing heat transfer, especially when a premixed charge is present [137]. Due to hydrogen's inherent trade-off between very low ignition energy and very high auto-ignition temperature, it is not a priori clear if it should be burned using the Otto or the Diesel cycle. This trade-off has led researchers to investigate hydrogen combustion in various combustion concepts [136, 138]. The following paragraphs highlight some relevant research and motive for the alternative combustion strategy proposed in this work.

Hydrogen-fueled ICE usually employ premixed spark-ignited concepts. Achieving a reliable Otto combustion process involves measures like cold spark plugs, optimized CRs (typically lower than gasoline engines), prevention of hot spots through cooled exhaust valves and reduced piston top land, and low-turbulence combustion chambers to reduce wall heat losses and minimize abnormal combustion events [139]. Most heavy-duty engines in use today employ compression-ignition concepts, using diesel as the high-reactivity fuel to enable self-ignition and diffusion-controlled combustion. In contrast, most alternative heavy-duty engines made for hydrogen employ a more straightforward approach: port-fuel injection or sometimes DI (during the intake or early compression stroke) of the fuel and spark ignited premixed combustion. These concepts often result in abnormal combustion limitations, resulting in low power densities due to the high AFR usually employed and/or low efficiencies due to lower CR or non-ideal combustion phasing than their Diesel counterparts [140]. Port fuel hydrogen injection encounters additional limitations compared to DI, including issues related to volumetric efficiency and compression losses [136]. High Pressure Direct Injection (HPDI) is applied in a single-cylinder automotive-sized engine. It has been shown that retarding the Start of Injection (SOI) leads to increased charge stratification and enhanced efficiency. The reason is associated with the low quenching distance of hydrogen, which contributes to el-

evated wall heat losses. Charge stratification is effective in reducing the combustion temperatures near the walls and, therefore the heat losses [137].

Another combustion approach to increase engine efficiency is HCCI [141]. Nevertheless, due to the high auto-ignition temperature of hydrogen-air mixtures, very high CRs are needed for the self-ignition of port fuel-injected premixed air hydrogen mixtures with the additional disadvantage of a highly narrow equivalence ratio region without misfire or preignition and knock [142].

Research on hydrogen jet combustion has primarily focused on auto-ignition studies conducted in constant volume combustion chambers [136]. Hydrogen has shown a notable temperature dependency according to the Arrhenius equation, with ignition delays reaching a satisfactory level for Diesel engine combustion at approximately 1'120 K [143]. Due to the elevated temperatures required for auto-ignition of the hydrogen jet it is evident that jet-guided mixing controlled hydrogen combustion is only practically feasible using some type of ignition promoter, be that a spark/glow plug PC or pilot ignition.

Thanks to the hydrogen's low ignition energy and the broad flammability limits, ignition of the hydrogen jet should be less difficult than the ignition of other gaseous jets like, for example, methane. Methane jet-guided combustion has gained significant research attention. A recent work from Vera-Tudela et al. ([122]) presents a study on the ignitability of a high-pressure direct-injected methane jet with a diesel pilot, a PC, and a glow plug in an optical test rig. The findings underline the PC's effectiveness in achieving superior ignition results for the methane jet. McTaggart-Cowan et.al.([123]) reports experimental and numerical results on a Westport 15L engine, where natural gas jet guided combustion is performed with injection pressures up to 600 bar. The approach involves injecting a small diesel pilot slightly before TDC, followed by the main natural gas injection. The delay between the diesel pilot and the gas injections mainly influences the premixed peak [144].

Coming back to hydrogen jet-guided combustion, the study conducted in [145] explores the application of hydrogen-diesel dual fuel HPDI in a constant volume combustion chamber. The hydrogen jet ignites after mixing with the burned gas from the diesel pilot injection and the subsequent HRR is primarily influenced by the hydrogen injection, ex-

hibiting characteristics reminiscent of autoigniting Diesel combustion. Following ignition, a peak inHRR is observed, which depends on the hydrogen mass injected before ignition, and subsequently, a constant diffusion flame is sustained until the End of Injection (EOI) of hydrogen. In [124, 146], an optical SI engine was utilized to explore jet-guided combustion via high-pressure (50 bar) DI of hydrogen. The investigations centered on stratified charge operation, where SI occurs immediately after and during the injection. The researchers noted a rise in cycle variability for jet-guided combustion. Despite the availability of optical images capturing combustion and AFR measurements at the ignition site, a thorough investigation into the HRR and a detailed description of the evolution of in-cylinder pressure is lacking.

This section investigates hydrogen jet-guided spark-ignited ignition and combustion in a RCEM where varying thermodynamic conditions similar to ICE are present. A high-pressure hydrogen jet is injected near TDC during the compression stroke, and spark ignited at the jet periphery, with subsequent fuel conversion occurring predominantly in jet-guided, stratified, diffusion-controlled mode. This combustion concept could achieve high power density while allowing the shaping of the combustion process as a function of the hydrogen injection. Furthermore, the heat release controlled by the fuel injection rate should ensure the suppression of knocking phenomena, thus allowing combustion phasing and engine geometries to achieve high thermodynamic efficiency.

Building upon the foundation laid out in [147] this study thoroughly investigates hydrogen DI using a Gasoline Direct Injection (GDI) injector. In the previous research ([147]), a systematical investigation was carried out by varying levels of charge stratification, advancing from premixed operation to stratified combustion and ultimately achieving jet-guided spark-ignited combustion. The results obtained in [147] confirm the feasibility of this combustion concept and underline the crucial interplay between the incoming jet and the spark. However, a comprehensive examination of the factors influencing ignition and combustion and the associated physical processes is still lacking, thus motivating the present investigation.

The high-pressure jet carries significant momentum and exhibits high velocities. Considerable turbulence is produced in the shear layer, posing challenging conditions for ignition. Such drawbacks can be mitigated

ated by using NRPD ignition. The sharp increase of voltage in such a nanosecond-ignition system results in efficient deposition of the energy necessary for ignition in short times. With NRPD, the breakdown time, conductive plasma formation, and energy deposition unfold within the timespan of nanoseconds. Conversely, the turbulence timescale is expected to be several orders of magnitude longer. This difference highlights the significantly faster processes associated with breakdown and plasma formation using NRPD compared to the comparatively slower timescale of turbulence in the system.

The rest of this section presents and discusses the experimental conditions in the RCEM (Section 6.3.1), some basics about gaseous HPDI and the gas visualization with non-reactive tests (Section 6.3.2), and the jet-guided ignition (using NRPD and inductive discharge) and combustion (Section 6.3.3). The pulse generator A is used for the NRPD ignition.

6.3.1 Experimental Conditions in the Rapid Compression Expansion Machine

Two operating points are investigated in this analysis. The first operating point has a CR of approx. 6.2, a displacement of 790 cm³, and a filling pressure of 1.1 bar. The second point has a CR of 9.3, the same displacement, and a pressure of 1.3 bar before compression. The CR in the RCEM is not to be interpreted exactly in the same way as in an ICE. The machine doesn't allow for sub-atmospheric initial pressures, therefore low load (throttled) conditions with low end-of-compression pressures are achieved using low CR. Due to the energy limitation in the two operating points, the same amount of fuel is injected. High variations of in-cylinder pressure during the high CR point are achieved by phasing the combustion to relatively early times. An early combustion phasing gives the advantage of achieving high-pressure variations thanks to the increasing pressures due to compression without the need to release a large amount of energy, which could otherwise damage the machine.

6.3.2 Evaluation of Injection Conditions and Non-Reacting Tests

In order to have a predictable and constant HRR during jet-guided combustion, the injection pressure should be high enough to maintain

sonic conditions against increasing combustion pressures so that the flow is choked at the injector's nozzle exit, and the injector's geometry and injection pressure solely affect the mass flow.

The pressure of the hydrogen line that feeds the GDI injector is at 110 bar. Equation (6.2) describes the fuel's mass flow rate as a function of the discharge coefficient (c_d), the injection pressure (p_0), the injector's nozzle area (A), and the isentropic coefficient (γ) by assuming no friction in the flow, no inertial effects, and zero-dimensional flow [148].

$$\dot{m} = c_d A \sqrt{\gamma \rho_0 p_0 \left(\frac{2}{\gamma + 1} \right)^{\frac{\gamma+1}{\gamma-1}}} \quad (6.2)$$

Real gas effects are considered in the isentropic coefficient and in the density of hydrogen (ρ_0), which are retrieved from the NIST database [94].

All the experiments are performed using a 16 ms injection duration, defined as the duration at which the injector's coil is energized. Since the flow is assumed to be choked in all conditions, the pressure in the cylinder won't affect the mass flow rate.

The injected mass is measured in the RCEM employing the principle of ideal gas law by injecting fuel at the BDC before the fast compression and recording the pressure increase. The measured injected mass with a 16 ms injection duration is 11.54 mg, and negligible scatter between experiments is present. This results in an overall λ of 2.9 for the low CR experiments and a λ of 3.6 for the high CR experiments. Assuming a steady injection mass flow rate for the entire duration when the coil is energized, the mass flow rate through the injector is 0,72 g/s. Figure 6.33 shows combinations of discharge coefficients and injection pressures (p_0) that result in the estimated mass flow rate (blue line) calculated according to Equation (6.2). The maximal cylinder pressure to have choked conditions ($p_{\text{cyl,max}}$) is reported in red and is calculated according to Equation (6.3).

$$p_{\text{cyl,max}} = \left(\frac{1}{\gamma + 1} \right)^{\frac{\gamma}{\gamma-1}} p_0 \quad (6.3)$$

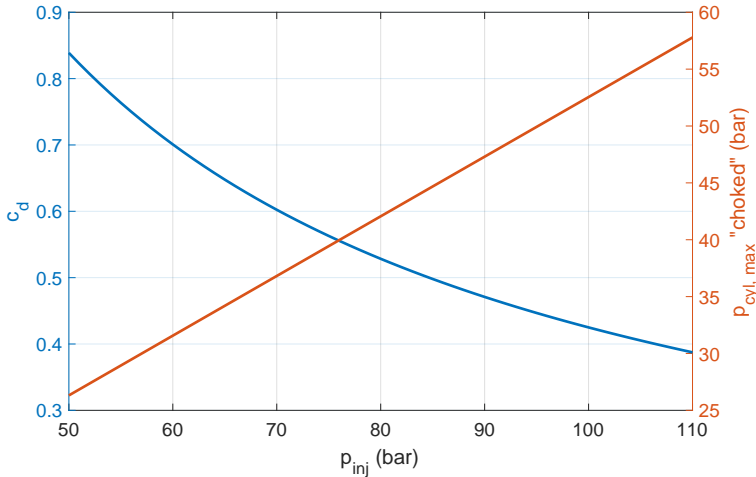


Figure 6.33: Discharge coefficient and injection pressure for the measured mass flow.

From this estimation, for example, an actual injection pressure at the injector's nozzle of 85 bar and a discharge coefficient of 0.5 (effective diameter of 0,4 mm) could explain the measured mass flows.

Figure 6.34 shows four post-processed frames at 0.4, 0.8, 1.5, and 4 ms after SOI for the non-reactive optical experiments recorded with the Schlieren technique through the piston view. The piston view offers a larger visualization area when compared to the tangential view, but since the spark plug is removed to allocate the window, only non-reactive experiments are possible in this configuration. The spark plug location in the reactive experiments would correspond to the middle of the circle. Due to the low density of hydrogen, post-processing of the Schlieren images is needed to visualize the jet morphology. A routine that enhances the difference between an image before injection (background) and the actual image is developed. The background image is depicted on a blue scale while the intensity of the difference is increased and depicted with shades of red.

For one frame at 400 μ s, two circular sections are visible. The shutter

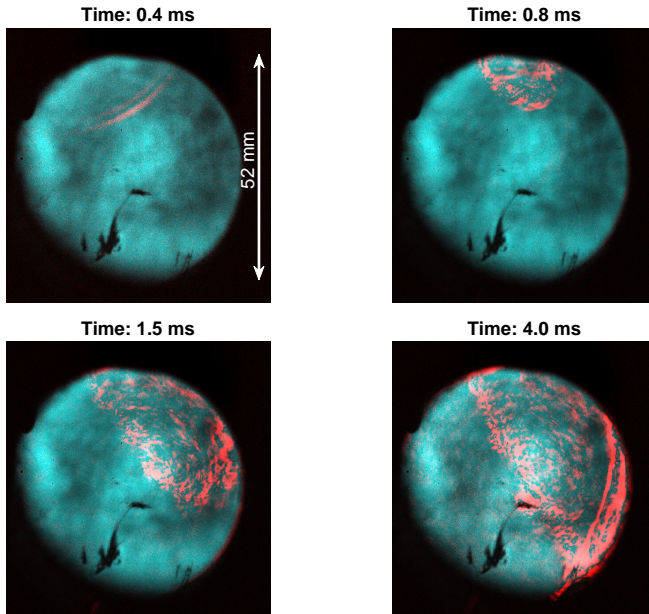


Figure 6.34: Schlieren visualization for non-reacting tests. Backpressure 8-13 bar.

speed is $2,5 \mu\text{s}$, and the lines are only visible for a single frame. The two circles are the shock wave that originates from the injector's tip due to the establishment of the underexpanded jet. The shockwave propagates through the air in the cylinder and moves at the speed of sound; therefore, it is only visible for one frame. The hydrogen jet appears at around 0.6 ms in the top left corner. Since the injector hole has an inclination of about 20° with respect to the axis that passes in the middle of the window (spark plug location), ignition happens at the periphery of the jet, as can be seen in the frame at 1.5 and 4 ms.

The jet remains consistently conical over time, with its head touching the wall and subsequently deflecting downward. Figure 6.35 shows the in-cylinder pressure (red) and the piston position (in blue) during the non-reacting experiment reported in Figure 6.34. The dashed red line highlights the region (near TDC) where the injection is active.

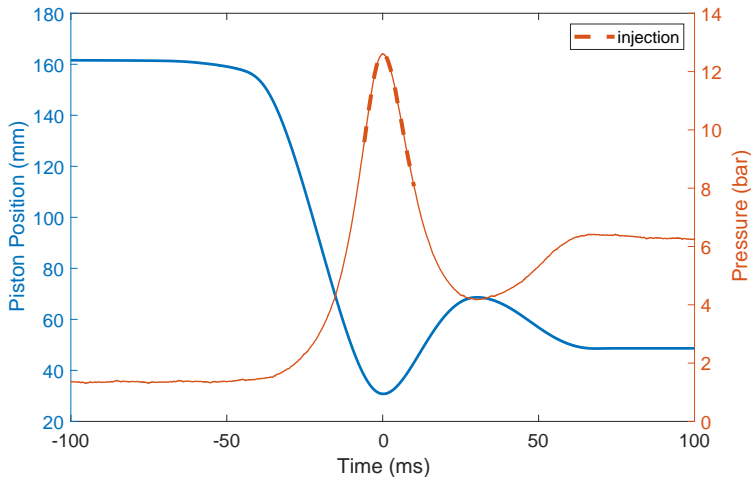


Figure 6.35: Non-reacting experiment, in-cylinder pressure and piston position, high CR.

In non-reactive experiments, the pressure varies only due to the piston's ballistic motion; therefore the in-cylinder pressure during injection ranges between 8 and 13 bar.

6.3.3 Jet-Guided Ignition and Combustion

The experiments dealing with jet-guided ignition and combustion are organized as follows: first, one experiment performed at low CR using the inductive ignition system is discussed in detail, followed by a description of the effects of variation between SOI and ignition. Next, a comparison of inductive ignition against NRPD is performed. Afterward, the effect of SOI on ignition delay for low and high CR using the NRPD ignition is described. Finally, the SIBS measurements are

presented for the low CR experiments and NRPD ignition.

Jet-Guided Hydrogen Ignition and Combustion (Inductive Ignition)

Figure 6.36 shows the OH* chemiluminescence recording on top and, in the middle, the Schlieren images during the ignition and inflammation process. The red circle in the OH* chemiluminescence represents the outer circumference of the visible part of the piston window. At the bottom, the graph illustrates the pressure evolution (in blue) and the HRR (in red). The black line depicts the fuel power input (p_{fuel}), which is defined according to Equation (6.4), where Δt_{inj} is the time when the coil of the injector is energized t_{SOI} is the SOI time, t_{EOI} is the EOI time, m_{fuel} is the total injected fuel mass, and u is the unit step function.

$$p_{\text{fuel}}(t) = \frac{m_{\text{fuel}}}{\Delta t_{\text{inj}}} LHV [u(t - t_{\text{SOI}}) - u(t - t_{\text{EOI}})] \quad (6.4)$$

The points in the bottom subplots depict the instances at which the frames are captured. The OH* images are post-processed to visualize better the regions where the reaction occurs. The difference against the background (image before ignition) is depicted on a green scale. A similar routine is used for the Schlieren images. The background is depicted on a green scale before inflammation and using a blue one afterward.

At 1,3 ms, the spark is visible from the OH* image. In fact, due to ionization and dissociation, the breakdown process (the spark formation) emits light over a broad spectral range, including the one around 310 nm [34]. At 1,3 ms, the hydrogen jet is visible from the Schlieren image on a green background. According to the Schlieren images, starting from 2,1 ms, a flame kernel develops between the electrodes, and at 2,5 ms, it already encompasses the entire visible region. After this instance no helpful information can be gained from the Schlieren imaging. From the OH* images taken perpendicularly to the Schlieren ones, it can be appreciated that the flame kernel does not develop near the electrodes. The kernel moves simultaneously in the direction and to the core of the gas jet.

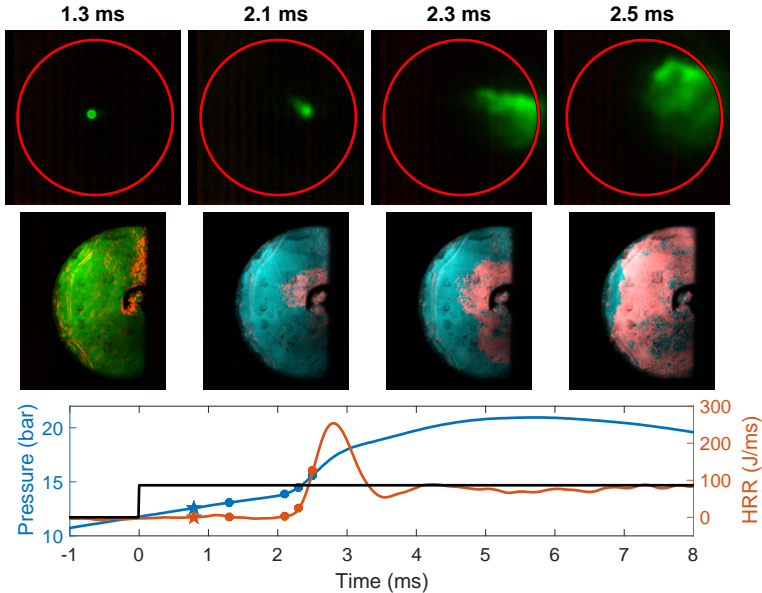


Figure 6.36: Hydrogen jet ignition and inflammation, inductive ignition, low CR

Figure 6.37 shows four frames of the OH^* chemiluminescence recording during jet-guided combustion (after the ignition sequence, between 2.8 and 16.8 ms), on the top, and the pressure and HRR trace against time, on the bottom, with points signaling the locations of the depicted frames.

After the HRR peak, which is visible from a large area where OH^* intensity is present (4.8 ms), the OH^* chemiluminescence intensity is pretty stable in location, and it is cone-shaped, exiting the injector's tip. After EOI, a tail of HRR is present with the OH^* chemiluminescence active near the right corner (at the wall opposite to the injector axis).

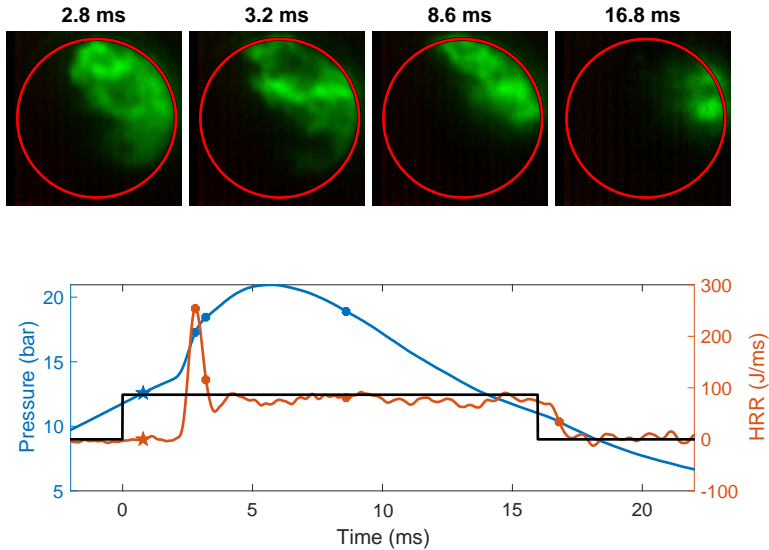


Figure 6.37: hydrogen jet-guided combustion and extinction, inductive ignition, low CR

Delay Between Start of Injection and Ignition Inductive Ignition System

Two variables substantially affect the combustion in the jet-guided mode in the current configuration: the injection and ignition timing. Since the spark timing is the input that most affect the combustion start time, its location has been held constant slightly before TDC. At the same time, the SOI is varied by keeping its duration and, therefore, the injected mass constant.

Figure 6.38 shows the results of 60 experiments where three different injection start times are used, resulting in a delay between SOI and spark of 1, 4, and 7 ms, respectively. The figure shows a representative experiment with combustion for each delay, where the location of the HRR peak was the closest to the mean of all the experiments having the same injection and ignition location. Figure 6.38 depicts, on the left, in

double logarithmic scale, the pressure-volume trace in blue, the ignition locations with blue stars, and the time when hydrogen is injected is highlighted in green. On the right, the pressure against time is plotted in blue, and the HRR in red. The different line styles (full, dashed, pointed) are used in both plots for the same delays between injection and ignition. The time scale of the plot on the right has been shifted so that time zero is always the start of the injection.

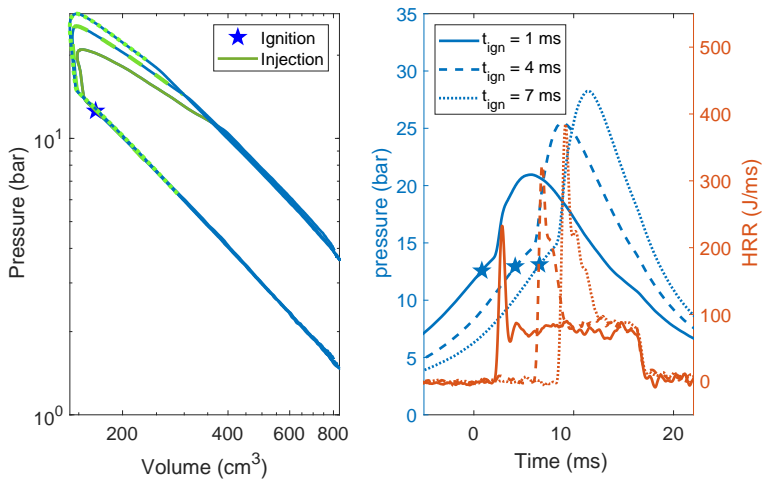


Figure 6.38: Delay between SOI and ignition: effect on pressure-volume trace (left) and HRR (right). Inductive ignition, low CR

The ignition timing is held constant at the time when the piston is at 29 mm from the cylinder head. The pressure at ignition time is practically the same between the three experiments. Ignition is always at the same location, but for longer SOI to ignition delay, the ignition delays are longer, and more energy is converted during the initial HRR peak, resulting in a higher peak pressure. The delay between SOI and ignition affects the HRR shape, combustion duration, and the resulting pressure-volume trajectory. Different pressure volume trajectories are present during combustion by varying the delay, but their values are similar before and after combustion.

Figure 6.39 shows the HRR in blue and the cumulative energy released in red for the same experiments reported in Figure 6.38. The black line represents the fuel power input as defined in Equation (6.4), and the red dashed horizontal line represents the total fuel energy input.

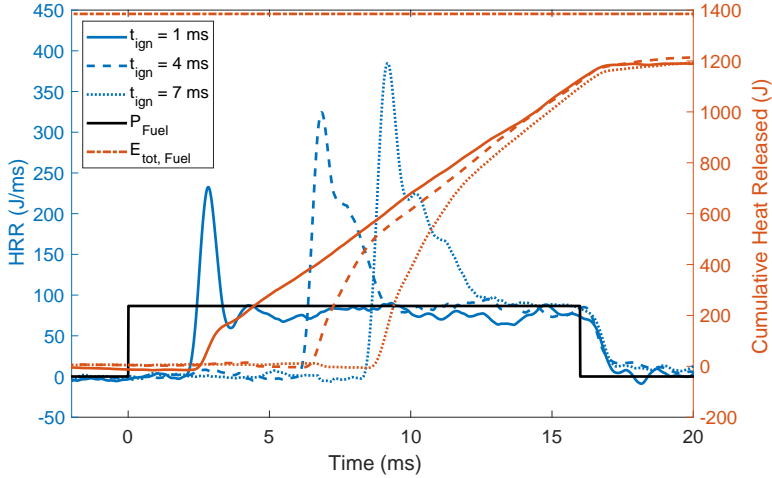


Figure 6.39: Delay between SOI and ignition: effect on the HRR and energy released

The longer the delay, the more time the fuel has to mix with the air, resulting in a higher and longer premixed peak. Since the ignition timing and the injection duration are held constant, advancing the SOI results in a shorter diffusion part of the HRR. For delays between SOI and ignition of 1 and 4 ms, the HRR reaches a quasi-constant value of 70-90 J/ms after the premixed peak, which is similar to the fuel power input, which is 86 J/ms. The total cumulative HRR reaches approximately 90% for all the cases.

Table 6.1 reports the data of the experiments shown before (mean of the 20 repetitions). The delay between SOI and ignition should be equal across all experiments, but since ignition and injection are controlled based on the piston position and the RCEM is a free-floating device, slightly different pressure in the working or the driving volume results in slightly different trajectories and therefore also delays. The premixed

peak duration is defined as when the HRR is 20% above the fuel power input, while the energy is the cumulative HRR until the HRR drops below this 20% threshold. The standard deviations of the data are reported in brackets. The ignition success rates for the experiments in the table are respectively 80, 80, and 100% for increasing delay.

Table 6.1: SOI to ignition delay data and premixed peak data for the tests reported.

SOI to ignition Δt	Ign. to premix peak	Premix peak intensity	Premix peak $\Delta t, E$
$t_{\text{ign}} = 0.83$ (0.04) ms	$\Delta t_{\text{ign,HRR}} =$ 1.95(0.41) ms	$HRR_{\text{max}} =$ 275.3(36.4) $\frac{\text{J}}{\text{ms}}$	$\Delta t_{\text{pk}} = 0.7(0.1)$ ms $E_{\text{pk}} = 147(29)$ J
$t_{\text{ign}} = 4.14$ (0.04) ms	$\Delta t_{\text{ign,HRR}} =$ 2.70(0.53) ms	$HRR_{\text{max}} =$ 374.8(30.5) $\frac{\text{J}}{\text{ms}}$	$\Delta t_{\text{pk}} = 2.5(0.3)$ ms $E_{\text{pk}} = 528(65)$ J
$t_{\text{ign}} = 6.59$ (0.04) ms	$\Delta t_{\text{ign,HRR}} =$ 2.59(0.51) ms	$HRR_{\text{max}} =$ 421.9(40.5) $\frac{\text{J}}{\text{ms}}$	$\Delta t_{\text{pk}} = 3.2(0.3)$ ms $E_{\text{pk}} = 715(60)$ J

The longer the delay between SOI and ignition, the larger the maximum HRR, the higher the premixed energy release, and the longer the ignition delays are. The maximum in-cylinder pressure rise rate increases with increasing delay: its value is 12 bar/ms for the shortest delay, 15 for the 4 ms delay, and 17 bar/ms for the longest delay. Two factors are required to achieve a precise and reproducible HRR in jet-guided mode: a constant injected mass flow, which can be achieved with a stable injection pressure and a constantly choked condition through the injector's nozzle, and reproducible spark to inflammation delay. The delay between the spark and the time at which the HRR is above 25 J/ms is 1,5 ms for the shortest delay, 2,2 ms for the 4 ms, and 2 ms for the longest investigated delay. The shortest inflammation is reached with the shortest delay, even though the charge is less premixed.

Comparison Ignition Systems

A longer delay between the SOI and ignition results in a longer ignition delay and more variability between the experiments (Table 6.1). Ignition using the conventional inductive ignition system is compared against the NRPD ignition in Figure 6.40. The NRPD discharge is com-

posed of ten pulses at 10 kHz PRF. Figure 6.40 shows the HRR analysis for a representative experiment with combustion, where the location of the HRR peak was the closest to the mean of all the experiments. The dashed line is used to show the inductive system, while the full line is used for the NRPD.

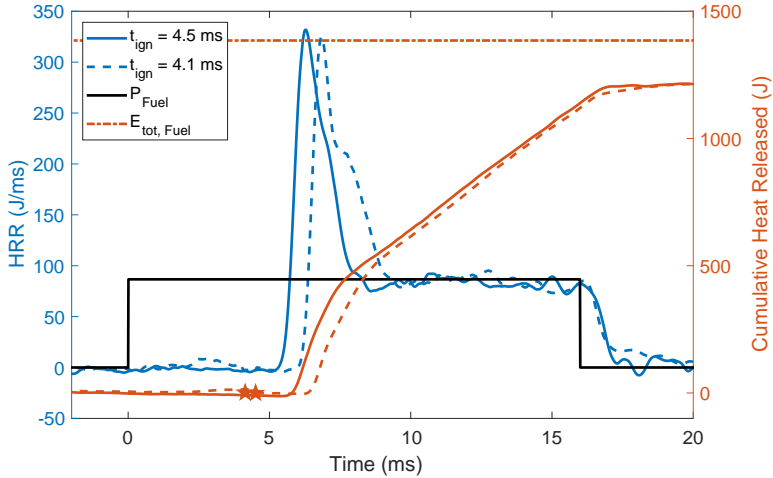


Figure 6.40: Inductive (dashed line) vs. NRPD (full line) comparison: HRR, low CR.

Table 6.2 reports some data (mean value and standard deviation in parentheses) from the experiments' 20 repetitions for the inductive and NRPD experiments having similar delay between SOI and ignition.

The experiments using NRPD show a higher success of ignition (95 vs 90%). Even though the spark occurs slightly before for the inductive experiments, the peak of the HRR occurs later. For similar conditions, the later the HRR peak is with respect to the SOI, the higher its intensity. The opposite occurs when inductive ignition is compared to NRPD, meaning that a higher share of the fuel injected before ignition reacts during the premixed part of the combustion when NRPD ignition is used. This higher conversion is kept till the End of Combustion (EOC), as shown by the 1% higher maximum cumulative HRR.

Table 6.2: Injection to ignition delay and premixed peak: inductive vs. NRPD comparison.

SOI to ignition Δt	Ign. to premix peak	Premix peak intensity	Maximum iHRR
NRPD			
$t_{\text{ign}} =$ 4.52(0.06) ms	$\Delta t_{\text{HRR}} =$ 1.90(0.16) ms	$HRR_{\text{max}} =$ 420(35) $\frac{\text{J}}{\text{ms}}$	$iHRR_{\text{max}} =$ 89(0.5)%
Inductive			
$t_{\text{ign}} =$ 4.14(0.04) ms	$\Delta t_{\text{HRR}} =$ 2.70(0.53) ms	$HRR_{\text{max}} =$ 375(30) $\frac{\text{J}}{\text{ms}}$	$iHRR_{\text{max}} =$ 88(0.9)%

Delay Between SOI and Ignition NRPD Ignition System

As done using the inductive ignition system, the delay between the SOI and ignition is also varied using NRPD ignition (10 pulses at 10 kHz). Figure 6.41 shows, for each delay, a representative experiment with combustion, where the location of the HRR peak was the closest to the mean of all the experiments having the same injection and ignition location. The spark timing is slightly later (compared to the inductive experiments) and held constant when the piston is at 26 mm from the cylinder head.

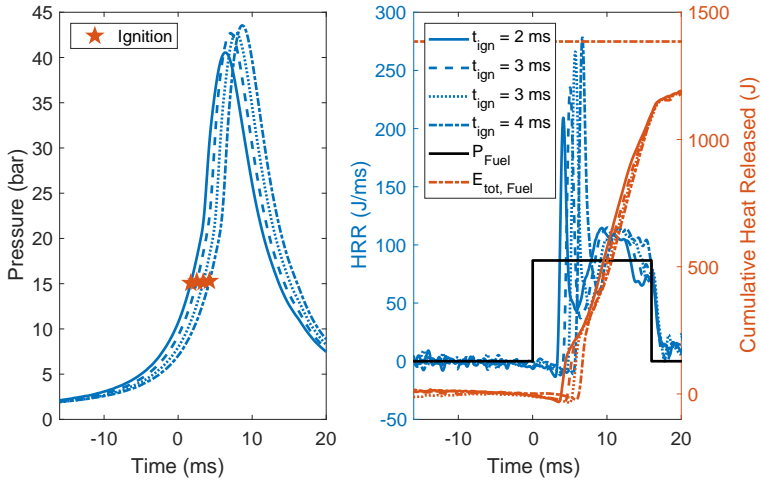


Figure 6.41: Delay between SOI and ignition: effect on pressure-time trace (left) and HRR (right). NRPD ignition, low CR.

As for the inductive case, an increased delay between SOI and ignition results in a higher premixed peak, and during the diffusion portion of the combustion, the HRR closely follows the fuel power input. Figure 6.42 shows the pressure-volume trace in a double logarithmic scale for the experiment where the delay between injection and ignition is 3 ms.

Since the ignition timing is closer to TDC and the ignition delay is short when NRPD ignition is applied, the compression and expansion follow four processes close to polytropic. A straight line in the double logarithmic plot shows a process that is close to polytropic because for a polytropic change of state pV^n is constant (where p is the pressure, V is the volume, and n is the polytropic exponent). For n equal to 0, the process is isobaric. When n is equal to 1, the process is isothermal, while if it tends to infinity, it is isochoric, and for air, when n is equal to approx. 1.4, the process is isentropic.

The compression in the left subplots (Figure 6.42) is close to isentropic. The fast (premixed) heat addition results in a process close to isochoric

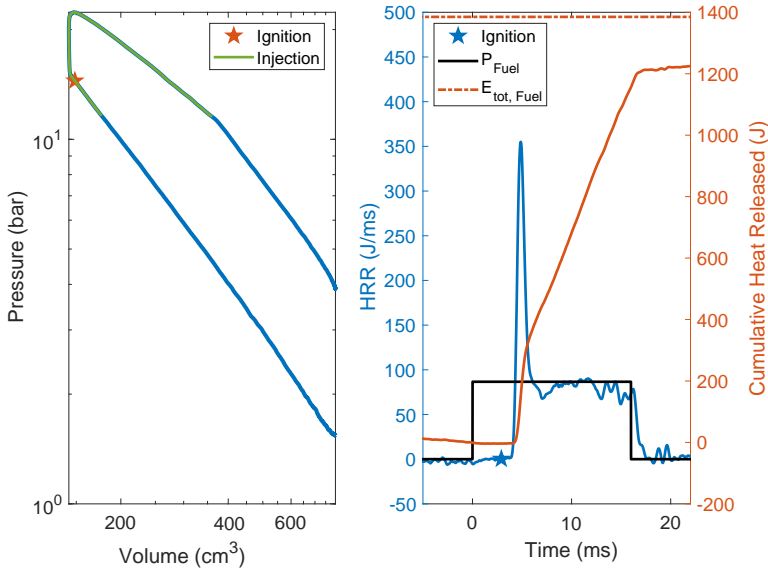


Figure 6.42: Pressure-volume trace for a test with a 3 ms delay between SOI and ignition. NRPD ignition, low CR.

(constant volume heat addition). During the expansion, two processes close to polytropic are present. After EOI, the expansion polytropic exponent is slightly higher than during compression due to the higher wall heat losses, while the polytropic exponent is lower when heat is added to the system.

For an ideal gas in a closed system, the polytropic index can be calculated according to Equation (6.5). By neglecting the wall heat losses, the added heat (dq) depends only on the HRR.

$$n = (1 - \gamma) \frac{dq}{dw} + \gamma \quad (6.5)$$

Figure 6.43 shows the change in the polytropic coefficient (in blue) and the HRR and work, (in red) during the jet-guided combustion process.

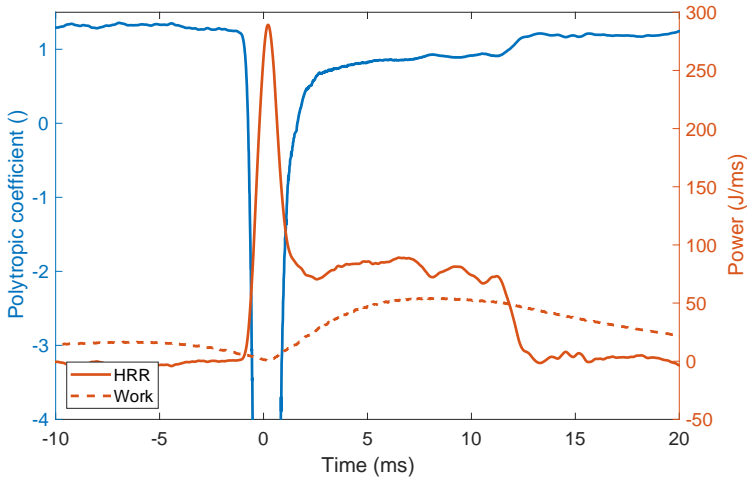


Figure 6.43: Polytropic coefficient during combustion, NRPD ignition, low CR.

Since the added heat (dq) is very high during the premixed portion and practically no work (dw) is done due to the negligible change in volume, the isentropic exponent is much higher than unity, resulting in a quasi-isochoric process. Interestingly, during the diffusion-controlled combustion, the process is again close to polytropic with an exponent of approx. 0.9. The reason is that the HRR is very constant, and since the variation in work is minor when compared to the added heat, the process is close to polytropic.

Table 6.3 reports the relevant data (mean value and standard deviation in parentheses) from the experiments' 20 repetitions for the five investigated delays (as shown in Figure 6.41). The premixed peak duration is when the computed HRR is above 20% of the fuel power input. The energy is the total converted energy until the HRR has dropped below this threshold.

The delay and its scatter between the spark and the premixed peak is shorter when NRPD ignition is used. The lower scatter and the later ignition result in the premixed part of the combustion being closer to

Table 6.3: SOI to ignition delay variation, NRPD ignition low CR.

SOI to ignition Δt	Ign. to premix peak	Premix peak intensity	$\max(dp/dt)$ bar/ms
$t_{\text{ign}} = 2.9$ ms	$\Delta t_{\text{max}} = 1.9(0.3)$ ms $HRR_{\text{max}} = 415(34) \frac{\text{J}}{\text{ms}}$	$\Delta t_{\text{pk}} = 1.4(0.3)$ ms $E_{\text{pk}} = 334(49)$ J	13.8(1.8)
$t_{\text{ign}} = 3.5$ ms	$\Delta t_{\text{max}} = 1.9(0.3)$ ms $HRR_{\text{max}} = 395(40) \frac{\text{J}}{\text{ms}}$	$\Delta t_{\text{pk}} = 1.7(0.3)$ ms $E_{\text{pk}} = 392(52)$ J	14.1(1.4)
$t_{\text{ign}} = 4.5$ ms	$\Delta t_{\text{max}} = 1.9(0.2)$ ms $HRR_{\text{max}} = 420(35) \frac{\text{J}}{\text{ms}}$	$\Delta t_{\text{pk}} = 2.2(0.2)$ ms $E_{\text{pk}} = 490(31)$ J	14.7(1.5)
$t_{\text{ign}} = 6.5$ ms	$\Delta t_{\text{max}} = 2.0(0.5)$ ms $HRR_{\text{max}} = 464(25) \frac{\text{J}}{\text{ms}}$	$\Delta t_{\text{pk}} = 3.0(0.2)$ ms $E_{\text{pk}} = 713(57)$ J	14.9(1.8)
$t_{\text{ign}} = 8.9$ ms	$\Delta t_{\text{max}} = 2.0(0.3)$ ms $HRR_{\text{max}} = 519(38) \frac{\text{J}}{\text{ms}}$	$\Delta t_{\text{pk}} = 3.7(0.5)$ ms $E_{\text{pk}} = 919(57)$ J	15.5(1.1)

isochoric. Due to the lower scatter and the later spark timing, the average pressure gradient for similar delay remains lower for the NRPD experiments when compared to coil ignition tests.

The goal of jet-guided combustion is to achieve high efficiency without knock occurrence. Higher CRs and pressures are, therefore, investigated. The RCEM driving and filling pressures are varied to achieve higher peak cylinder pressures during combustion. The resulting operating point represents a point with a higher CR (9.3) when compared to the previous experiments (6.2). The filling pressure is also higher for these experiments (1.3 vs 1.1 bar). Figure 6.44 shows the results of 80 experiments where four SOI are used, resulting in a delay between ignition and spark of 1.7, 2.5, 3., and 4.2 ms. NRPD ignition with 20 pulses at 10 kHz is used. The figure shows a representative experiment with combustion for each delay, where the location of the HRR peak was the closest to the mean of all the experiments having the same injection and ignition location. Figure 6.44 shows the pressure against time (blue) on the left, while on the right, the HRR and the cumulative HRR are plotted in blue and red, respectively. The different line styles are used in both subplots for the same delays.

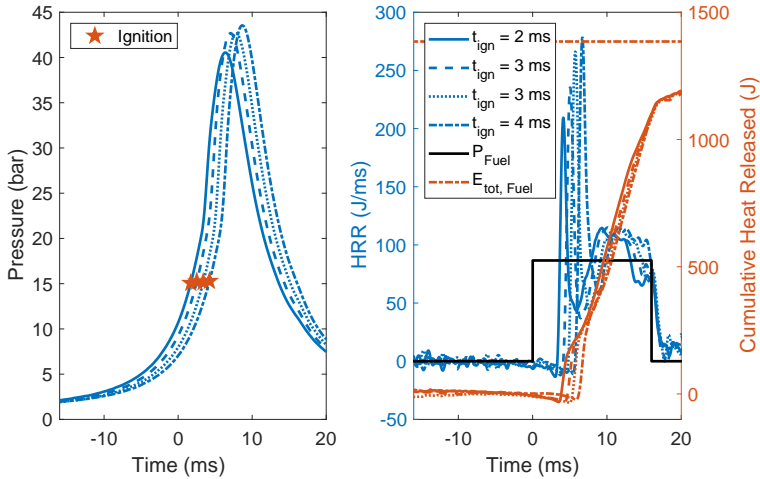


Figure 6.44: Delay between SOI and ignition: effect on pressure-time trace (left) and HRR (right). NRPD ignition, high CR.

As for the previously reported experiments, the injection duration is 16 ms. The injected mass is the same if choked conditions are present in all experiments. Due to the higher driving pressure used in these experiments, higher peak pressures are reached (approx. 40 vs. approx. 25 bar). As seen for the lower CR experiments (Figure 6.39 and Figure 6.41), the premixed peak increases the longer the delay between SOI and ignition. Nevertheless, at these higher pressures, the diffusion part of the combustion is not as constant as for the low-pressure experiments. The HRR after the premixed peak falls lower than the fuel power input (black line in Figure 6.44 right). Afterward, it re-increases above the black line. This pulsation is also visible from the OH^* chemiluminescence recording. The peak pressure for these experiments is as high as 47 bar. The minimum of the HRR values are reached when the in-cylinder pressures are close to the peak pressure.

Figure 6.45 shows respectively three frames of the recording of the OH^* chemiluminescence during ignition (2.2, 3.3, and 3.6 ms) on top, during combustion (4.2, 5.7, and 11.8 ms) on the bottom, and, in the middle,

the pressure and HRR trace against time. The points indicate the times when the frames are taken for the experiment reported in Figure 6.44 with a 2,5 ms delay between SOI and ignition.

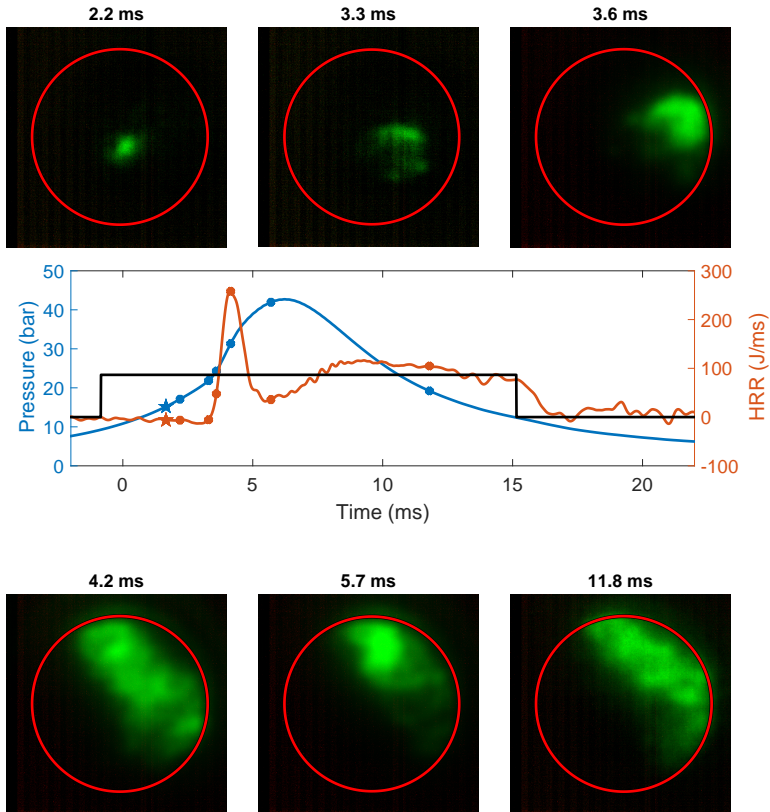


Figure 6.45: OH* chemiluminescence (top), pressure, and HRR traces (bottom) for a 2,5 ms delay between SOI and ignition case. NRPD ignition, high CR.

At 2,2 ms after the SOI, the luminous emission indicates the presence of the spark. Subsequently, the ignition kernel migrates both towards the

core of the jet and in the direction of the wall. During the HRR peak (4,2 ms), a large area shows OH* activity, indicating a large zone where the fuel is reacting. Up to now, the thermodynamic and optical analysis show similar effects as shown for the low CR experiments (Figure 6.36, Figure 6.37).

After the peak, the HRR drops, and the OH* chemiluminescence moves closer to the injector tips as the pressures increase to the maximal pressure. As the pressure decreases, the OH* signal moves away from the injector, and the OH* active area increases as the HRR does. The brightest spot in OH* chemiluminescence moves towards the injector as the pressure increases and back towards the wall as it decreases. This effect is not present for the low CR experiments where, during combustion, a conical reaction zone that is approximately constant in position is present.

Figure 6.46 shows the maximum absolute distance from the injector where OH* activity is detected (in blue) and the HRR (in red) for the 2,5 ms delay. The depicted distance and HRR are the average among the 20 repetitions.

The 48 mm distance detected at the spark timing is the distance between the spark plug and the injector (the breakdown emits lights in the range of the OH* chemiluminescence). Afterward, the maximum distance increases following the premixed peak. The distance right after the premixed peak decreases and increases inversely to the pressure in the cylinder. At 10 ms, the premixed peak arrives at the cylinder wall, but the maximum distance increases further toward the bottom, as shown in the 11,8 ms OH* frame depicted in Figure 6.45.

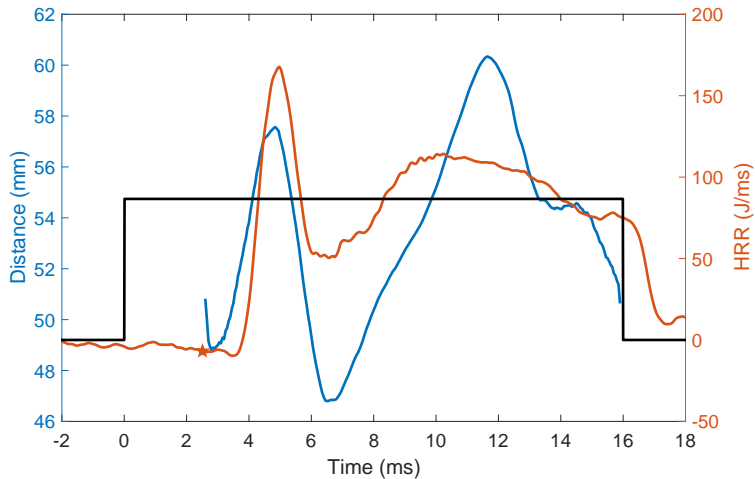


Figure 6.46: OH^* chemiluminescence maximum distance for a 2.5 ms delay between SOI and ignition, NRPD ignition, high CR.

Table 6.4 reports the data (mean value and standard deviation in parentheses) from the experiments' 20 repetitions. The ignition success of all the experiments is 100%, with the exception of one experiment for the 1,7 ms delay where one misfire is present.

Slightly higher completeness of combustions are reached in the high CR cases compared to the low ones (Table 6.4 and Table 6.3). Also, the premixed peak intensities are lower for similar delays between SOI and ignition.

Table 6.4: SOI to ignition delay variation data (tests in Figure 6.44), high CR tests NRPD ignition.

SOI to ign. Δt	Ignition to premix peak Δt	Premix peak Δt and E	$\max(iHRR)$
$t_{\text{ign}} = 1.7 \text{ ms}$	$\Delta t_{\text{max}} = 2.5(1.0) \text{ ms}$	$\Delta t_{\text{pk}} = 1.0(0.2) \text{ ms}$ $E_{\text{pk}} = 167(41) \text{ J}$	$HRR_{\text{max}} = 246(25) \frac{\text{J}}{\text{ms}}$ $iHRR_{\text{max}} = 91.7\%$
$t_{\text{ign}} = 2.5 \text{ ms}$	$\Delta t_{\text{max}} = 2.5(0.8) \text{ ms}$	$\Delta t_{\text{pk}} = 1.1(0.1) \text{ ms}$ $E_{\text{pk}} = 204(35) \text{ J}$	$HRR_{\text{max}} = 275(33) \frac{\text{J}}{\text{ms}}$ $iHRR_{\text{max}} = 92.3\%$
$t_{\text{ign}} = 3.3 \text{ ms}$	$\Delta t_{\text{max}} = 2.4(0.4) \text{ ms}$	$\Delta t_{\text{pk}} = 1.2(0.2) \text{ ms}$ $E_{\text{pk}} = 227(20) \text{ J}$	$HRR_{\text{max}} = 288(21) \frac{\text{J}}{\text{ms}}$ $iHRR_{\text{max}} = 92.2\%$
$t_{\text{ign}} = 4.2 \text{ ms}$	$\Delta t_{\text{max}} = 2.6(0.9) \text{ ms}$	$\Delta t_{\text{pk}} = 1.5(0.2) \text{ ms}$ $E_{\text{pk}} = 291(36) \text{ J}$	$HRR_{\text{max}} = 304(26) \frac{\text{J}}{\text{ms}}$ $iHRR_{\text{max}} = 91.6\%$

Local Air to Fuel Ratio Measurements Using Spark Induced Breakdown Spectroscopy

The SIBS technique estimates the local AFR during reactive experiments at the ignition location and time. Figure 6.47 and Table 6.5 report the results from the SIBS investigation performed during the reactive experiments using NRPD ignition at low CR. Figure 6.47 shows the sum of all the post-processed spectra having the same delay between SOI and ignition, starting from 3 ms up to 9 ms. The spectra are normalized by dividing the spectra by the respective OI (777 nm) intensity. The different atomic emissions are reported on top of the relative peak.

The oxygen and nitrogen peaks have practically the same relative intensity between the experiments. This outlines that the spectral technique is capable of returning relative concentration since the nitrogen-to-oxygen ratio is not expected to vary for different locations and AFR. The normalized hydrogen intensity increases for increasing delay between SOI and ignition, which outlines a decrease in local λ . Table 6.4 reports quantitative results from the SIBS technique for the different delays between SOI and ignition. The λ single experiments and λ sum spectra report the average λ measured over the 20 repetitions. To calculate the " λ single experiments" for each experiment out of 20 repetitions, the intensity of H_{α} over O_{777} is calculated, and the re-

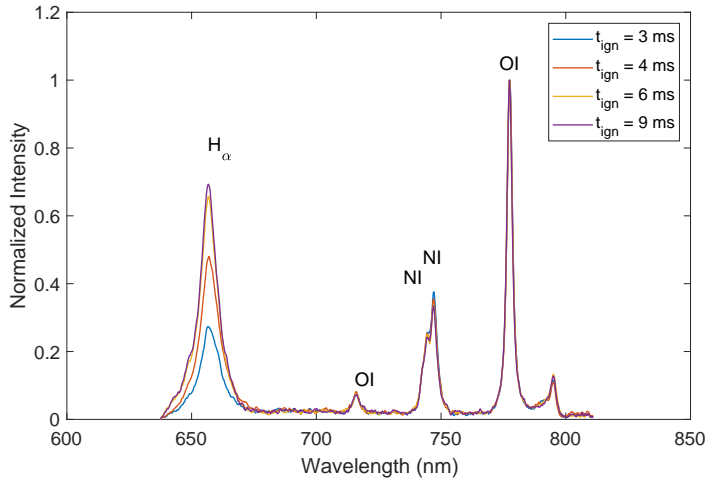


Figure 6.47: SOI to ignition delay effect on SIBS features: NRPD ignition low CR.

spective λ interpolating from the polynomial calibration (Section 5.1.2) is calculated. The mean value is reported with its standard deviation. To calculate the " λ sum spectra" all 20 spectra are summed, and one λ is calculated from the polynomial calibration. The deviation of the value is dependent on the calibration precision. From an investigation of the calibration, it is unclear which of these two values is more precise. The λ minimum and maximum values over the 20 experiments are also reported. Table 6.5 also reports the ignition success rate in percentage.

Large variations in λ among the 20 repetitions having similar SOI to ignition delays are obtained as visible from the λ_{\max} λ_{\min} difference. The SIBS technique measures an instantaneous mixture composition between the electrodes at ignition timing. Due to the turbulence induced by the injection and since the ignition happens at the periphery of the jet, high variability in the AFR for the repetition of the same experiment is expected. Overall it can be seen that for increasing delays, the λ decreases, as expected by the higher time for the hydrogen to mix. Furthermore, it can be noted that the local λ is relatively low. The next chapter provides a detailed discussion of the results, where

Table 6.5: SOI to ignition delay effect on SIBS measurements: NRPD ignition low CR.

SOI to ign. Δt	λ single	λ sum	λ_{\max} single	λ_{\min} single	Ignition success
$t_{\text{ign}} = 2.9$ ms	8.8(1.5)	$8.7_{7.7}^{9.7}$	Air	4.4	70%
$t_{\text{ign}} = 3.5$ ms	7.9(2.0)	$7.2_{6.4}^{8.2}$	Air	4.6	100%
$t_{\text{ign}} = 6.5$ ms	6.2(1.4)	$6.2_{5.5}^{7.0}$	8.6	2.8	100%
$t_{\text{ign}} = 8.9$ ms	6.3(1.4)	$6.0_{5.3}^{6.7}$	8.9	2.8	100%

the effect of the measured local AFRs are interpreted with the other results.

6.3.4 Summary and Discussion

Throughout the investigation, an injection duration of 16 ms was used with a pressure upstream of the injector of 110 bar. The cumulative HRR displayed a notable constancy across all experiments, indicating the likely presence of choked conditions, even when the in-cylinder pressure rose to 45 bar. This implies an effective injection pressure of at least 85 bar and a corresponding discharge coefficient of approximately 0.5. The internal geometry of the injector is unknown, and the injector was developed for gasoline injection; therefore, notable pressure loss inside the injector could be present. Since the sharpness of the hole is also unknown, and the hole is not axial, the 0.4 mm effective diameter ($c_d = 0.5$) also seems plausible. The observation of a consistent HRR during diffusion combustion for the low CR, closely mirroring the fuel power input (Figure 6.39), indicates that the injection mass flow rate is remarkably stable throughout the injection process. This constancy suggests the absence of significant pressure oscillations in the fuel line.

Discrepancies of up to 45% between the flow measurement and the theoretical maximum value are reported in [149] using a Bosch HDEV5 GDI injector. The researcher attributed the lower value to a combination of a discharge coefficient (c_d) of less than unity, due to the sharp edge nozzle, and an internal pressure loss across the injector, which leads to a pressure difference between the reservoir (in our case, the hydrogen

line) and the pressure directly upstream the nozzle. Using Schlieren imaging and the near nozzle jet behavior, the researcher estimate an injection pressure of 84 bar with a reservoir pressure of 100 bar and a discharge coefficient of 0.77. The estimation is performed by capturing the transition to a highly underexpanded jet as described in [150], which happens at a pressure ratio of 3.85. Our measurements yield comparable outcomes, with an even lower discharge coefficient and a greater pressure drop inside the injector. This could be attributed to the smaller injector diameter, likely reducing the discharge coefficient, and the use of an older injector, which may contribute to a higher pressure drop in the used setup.

Turner's model [151] holds broad acceptance in the study of underexpanded gas jets. According to this model, a jet originating from a round nozzle is expected to take on an axisymmetric conical shape, characterized by three regions: a fuel-rich core containing fuel, a steady-state area where air is entrained, and a transient vortex region [136]. Scaling laws can be applied to estimate the penetration length, with dependencies on chamber density, momentum flow, and nozzle diameter [152]. The circular sections detected during the non-reactive experiments at 0.5 ms after SOI are the shockwaves characteristic of the formation of an underexpanded hydrogen jet (Figure 6.33). The barrel structure length (h_B) typical of highly underexpanded jets follows Equation (6.6), where Π is the pressure ratio and d is the nozzle diameter [150].

$$h_B = 0.67d\sqrt{\Pi} \quad (6.6)$$

The pressure ratio during the non-reactive jets ranges from 6 to 10; therefore, the expected barrel shape is not visible in the current configuration. The piston covers the first 18 mm from the injector tip, and the barrel structure is likely to extend for only approximately 1 mm. The images at later times depict the steady state conical region where air is entrained and the transient vortex region as described in [150]. The recorded jet morphology during non-reactive experiments only represents the reacting experiments before ignition and combustion. Afterward, the increase in pressure and the combustion process will affect the jet morphology. The formation of the barrel structure at a pressure ratio above 3.85 is expected to impact the overall air-fuel mixing significantly [136]. With the estimated injection pressure of 85 bar, the jet is expected

ted to be highly underexpanded for in-cylinder pressures below 23 bar, which is the case during ignition and inflammation but is not always the case during reactive experiments. The points above regarding the jet morphology and the non-reactive experiments serve for the analysis of the reactive results discussed in the following paragraphs.

In the presented reactive experiments, the HRR of jet-guided hydrogen combustion shows stages of combustion similar to those present in compression ignition Diesel combustion [32]. The ignition delay period in jet-guided combustion is not influenced by the fuel evaporation, mixing, and chemical delay, as is the case when diesel fuel is used, but is primarily affected by the delay between SOI and ignition. In the investigated configuration, the spark happens at the periphery of the gas jet at relatively lean conditions (SIBS measurements). From the OH^* images, it can be seen that the plasma kernel is transported toward the fuel-rich core of the jet, following the expected air entrainment direction [151]. Once the plasma-flame kernel reaches the fuel-richer region, most of the fuel injected before inflammation reacts quickly, resulting in the premixed combustion phase. In spite of the very fast combustion of the already premixed fuel, an evident flame propagation is visible. The longer the delay between SOI and ignition, the higher and longer the premixed peak. The in-cylinder pressure also affects the duration and energy released during the premixed peak. In fact, the experiments with higher in-cylinder pressures during ignition and combustion show a reduced premixed peak intensity and a shorter duration for similar delays between SOI and ignition, highlighting the importance of the jet morphology (known to be dependent on the pressure ratio[136]).

Following the inflammation and the premixed combustion, the burning rate is limited by the rate at which ideal mixtures for combustion become available. The fuel-air mixing process controls the HRR, also called diffusion combustion. For the low CR cases, the HRR during the diffusion combustion phase is very flat and closely follows the fuel power input. The fuel-air mixing process and combustion are matched to the injected fuel mass. The OH^* chemiluminescence takes the shape of a cone with a relatively constant position and area. For the low CR cases during the majority of the combustion process, the pressure ratio remains above 3.85, indicating that the hydrogen jets are probably highly underexpanded for the entire combustion duration.

For the high CR experiments, the inflammation and premixed combustion are qualitatively similar to the already discussed experiments, while the diffusion-controlled portion of the combustion differs. The mixing and combustion process does not match the injected fuel mass. The HRR is lower than the fuel power input when the in-cylinder pressures are high and is higher once the in-cylinder pressures have dropped. After the inflammation, the pressure ratio falls to around two, which is the limit for choked conditions. Therefore, the jets are probably not highly underexpanded and mix less effectively with the air. The OH^* chemiluminescence doesn't take the constant conical shape as it does for the low CR experiments (Figure 6.37); instead, it decreases and increases again following the HRR (Figure 6.45). The reactive area moves toward the injector tip as the pressure increases and away from it as it decreases. Interestingly, the recorded maximum distance from the injector where chemiluminescence is present during the re-increase inversely scales (till the wall is approached) with the density to the power of $1/4$. This relation is expected to happen for the tip penetration length, according to [152].

The variation of the HRR present in the high CR experiments during the diffusion-controlled combustion is explained (by considering the optical and thermodynamic measurements) by the transition from a high to a moderate underexpanded jet. This transition is present due to the higher combustion and compression pressures. Two further, less likely factors could explain this effect. First, the higher CR results in the piston reaching a position closer to the cylinder head (16 and 25 mm) and, therefore, to the injector nozzle (5 mm from the head), which can result in an interaction between the piston and the incoming jet, temporarily reducing the combustion rate. Second, since the pressure at the injector nozzle is only estimated, it is unsure if choked conditions are present when the combustion pressures are high, which would lead to a lower mass flow rate. The pressure of the hydrogen line is at 110 bar, but the actual injection pressure could be much lower (Figure 6.33). Sub-critical conditions at the injector's nozzle could be present if the injection pressure drops below 80 bar. Since the calculated cumulative HRR reaches approximately the same level for all the experiments, and since this value depends on the actual injected mass, non-choked injection conditions should not be present or only for a short time without substantially affecting the total injected mass and, therefore, total fuel energy.

The completeness of combustion calculated with the 2-zone thermodynamic approach returns a rather low completeness of combustion, around 90%, with minor differences between the different experiments. Two factors can explain the low conversion rate. First, the wall heat losses are simulated following the Woschni approximation, which gives good agreement before and after the combustion process, as can be seen from the flat line before 0 and after 16 ms of the cumulative HRR in all the figures where the HRR is reported. Still, they could largely be underestimated during the combustion process due to the jet-wall interactions. An increase of 50% in the wall heat losses during combustion could increase the cumulative HRR up to $\sim 100\%$. Second, due to the high jet-momentum flow typical of underexpanded jets, a large portion of hydrogen could "escape" the flame front without contributing to the HRR. Since it is not clear if the wall heat losses are higher than computed or if the completeness of combustion is higher, the HRR calculation is not modified. Results from reactive CFD are needed to estimate either the wall heat losses or the incomplete combustion magnitude.

As in for Diesel combustion, [32] jet-guided hydrogen combustion depicts a late combustion phase where, after injection, the remaining hydrogen share reacts. OH* images show that this late combustion phase happens opposite to the injector tip (Figure 6.37).

An increased delay between SOI and ignition decreases the average local AFR near the spark plug. One would think that a decrease in local λ would result in a decrease in ignition delay. Instead, no reduction in ignition delays is present; it actually slightly increases. The independence between local AFR and ignition delay gives further foundations to the theory that the inflammation is mainly affected by the transport of the kernel in the fuel-rich region rather than an actual flame propagation starting from the spark plug.

NRPD ignition is advantageous in igniting the incoming hydrogen jet. First, the ignition delay is shorter and scatters less, which results in a more reproducible HRR peak intensity and delay. In spite of a similar delay between SOI and ignition, the premixed peak is higher using NRPD ignition, highlighting a higher share of the fuel injected before inflammation reacts. This advantage is kept for the entire combustion process, resulting in a higher completeness of combustion (higher cu-

mulative HRR).

The high-pressure loop cycle of an ideal engine is usually composed of an isentropic compression till TDC, an instantaneous isochoric heat addition, and again an isentropic expansion till BDC. Additional constraints are often posed to the heat addition, for example, a maximal pressure for mechanical protection or a maximal pressure gradient constraint to limit the noise [153, 154]. The fast HRR measured in the RCEM outlines the possibility of shaping the HRR of jet-guided hydrogen combustion similarly to what is done for Diesel engines [155]. Processes very close to polytropic ones are present for the low CR cases (Figure 6.42 and 6.45). If high-pressure ratios are present, the mixing and combustion characteristic time seems shorter than hydrogen's characteristic injection time, resulting in a constant HRR. An ideal engine cycle where the premixed portion of the combustion increases the pressure up to the maximal rated pressure followed by a constant pressure heat addition during the diffusion combustion portion seems feasible if the correct mass flow rate and SOI to ignition delay are chosen.

This investigation outlines a detailed optical and thermodynamic investigation into jet-guided hydrogen combustion in a rapid compression and expansion machine. For this purpose, hydrogen is injected at high pressures and spark-ignited at its periphery, with fuel conversion taking place predominantly in diffusion-controlled mode. The main findings are reported below:

- ▶ Reliable SI of highly underexpanded hydrogen jets is possible. This type of combustion could result in very high efficiency since hydrogen can be combusted using Diesel-like process parameters without knock limitations. This combustion process is similar to Diesel combustion; the premixed, diffusion, and late combustion phases are recognizable.
- ▶ The OH* chemiluminescence and Schlieren images show that the air entrainment carries the flame-plasma kernel to the fuel-richer core of the jet, rapidly combusting the already (partially) mixed fuel, leading to the premixed combustion phase. Afterward, the combustion is dominated by the mixing process.
- ▶ During the diffusion-controlled combustion phase, a constant mixing and combustion of hydrogen equal to the injected mass flow

rate is present for low in-cylinder pressures. When the in-cylinder pressures are higher, the mixing and combustion rate slows down and is lower than the injected hydrogen mass. This difference happens when the gas jet changes from a highly to a moderately underexpanded jet.

- ▶ SOI to ignition delay mainly affects the premixed peak, but the in-cylinder density and ignition source also impact.
- ▶ SIBS reveals low AFR at ignition time and location, ranging from 2.8 up to pure air, depending on the condition. Furthermore, significant λ variations among repetitions of the same experiment are present due to the ignition at the periphery and the high injection-induced turbulence. The average λ at ignition time and location decreases from 8.7 to 6 for increasing delay between SOI and ignition. Despite these variations, the local AFR does not affect the ignition delay. The transportation of the kernel toward the fuel-richer core seems to be the relevant ignition mechanism.
- ▶ Two ignition systems are used to ignite the incoming jet: a classical inductive ignition system and NRPD ignition, the latter showing a higher ignition success rate and a faster inflammation.

Several open points remain to be addressed in future research. CFD modeling of the performed experiment is currently being developed. CFD results will shed some further light on the presented experimental results, for example, by highlighting the mechanism responsible for inflammation or by explaining the reason behind the relatively low completeness of combustion. On the experimental side, investigations by varying the injection pressure or different locations of the spark plug could highlight interesting results. The overall λ in the current experiments is relatively high (above 3). Using synthetic EGR, lower λ values could be investigated in the RCEM without having problems with the energy limitations of the RCEM. As stoichiometric conditions are approached, the combustion rate will probably be reduced due to local oxygen scarcity. This combustion concept is currently being transferred to a single-cylinder 0.5L displacement volume research engine operated with a hollow cone outward opening injector. In spite of the very different experimental test rigs, similar combustion features are measured, thus confirming the feasibility of the concept.

6.4 Full Engine Experiments

As mentioned before, Diesel-like process parameters, such as higher CR, air excess, EGR, and high combustion peak pressures, are advantageous for increasing efficiency levels of SI engines. This section, therefore, aims to experimentally analyze the effects of NRPD ignition in an engine that has the possibility to set compression-ignition-like process parameters. Five different combustion concepts are analyzed on the same engine platform, allowing for a direct comparison of NRPD to inductive discharge ignition. The investigated combustion strategies are: passive PC with air and EGR dilution, active PC with air dilution, and OC with air and EGR dilution. This section is derived from the article titled "Effect of using Nanosecond Repetitively Pulsed Discharge and Turbulent Jet Ignition on ICE Performance", where the impact of NRPD ignition inside a PC is presented, to the author's best knowledge, for the first time.

This section is organized as follows: Section 6.4.1 presents the experimental campaign, the selected operating points, and the methods used to analyze ignition and combustion. The engine results are presented in Section 6.4.2: which covers: the comparison of NRPD and inductive discharge ignition in the OC under various AFRs, the experiments performed in active and passive PC for various AFRs, and the EGR results. Toward the end of Section 6.4.2, all the combustion strategies and ignition concepts are compared at their respective peak efficiency.

6.4.1 Materials and Methods

Experimental Campaign

Two real-world-operation-relevant points for the engine under investigation are selected from an investigation reported in [44]. The first point (Point A) has a brake torque of 100 Nm (6,4 bar Brake Mean Effective Pressure (BMEP)) and an engine speed of 1'500 rpm, which is a relevant point in terms of fuel consumption. The second point (Point B) has a brake torque of 30 Nm (1,9 bar BMEP) and an engine speed of 1'200 rpm, representing a relevant point with the lowest power. Figure 6.48 depicts the analyzed variations over the two selected points.

Five variations are investigated, all using the NRPD and inductive dis-

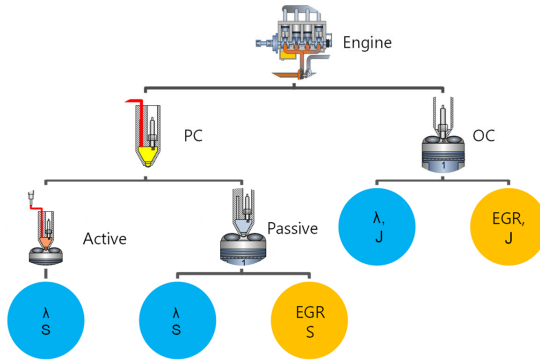


Figure 6.48: Experimental campaign graphical representation of the different configurations using air dilution (λ), EGR, J- or surface-type (S) spark plugs.

charge ignition systems. The EGR investigations are performed with PFI delivering a $\lambda = 1$ mixture to the engine, i.e., active PC operation is impossible in this case as it would lower λ below stoichiometric conditions. Air dilution is analyzed for all configurations. Preliminary investigations in OC configuration using NRPD ignition have shown negligible differences for PRF above 50 kHz and the use of different spark plug geometries. The OC experiments are therefore performed at 50 kHz PRF using the j-gap spark plug. The preliminary investigation in OC showed some advantages in using 100 kHz PRF and surface gap spark plugs; the PC experiments were consequently performed at 100 kHz PRF using the surface gap spark plug.

Loss Analysis

Quite often, better combustion strategies do not lead to expected increased brake thermal efficiencies as, for example, wall heat losses increase, unburned fuel increases, or the like. Therefore, a loss analysis is a powerful tool for understanding ignition strategies' on the various effects on efficiency. An algorithm-based loss analysis is developed, the description of the algorithm is reported in Appendix A.2.

Heat Release Rate Analysis in the Main Chamber

The apparent HRR is discretely calculated based on the first thermodynamic law and the pressure measurement (p_{cyl}) at the current crank angle (subscript i) and the previous angle (subscript $i-1$) according to Equation (6.7) [156].

$$\begin{aligned} HRR_i = & \frac{\gamma_i(T_{\text{cyl},i})}{\gamma_{i,1}(T_{\text{cyl},i-1})} p_{\text{cyl},i} \frac{V_i - V_{i-1}}{\Delta\rho} + \dots \\ & \dots \frac{V_i}{\gamma_i(T_{\text{cyl},i} - 1)} \frac{p_{\text{cyl},i} - p_{\text{cyl},i-1}}{\Delta\rho} + \Delta Q_w \end{aligned} \quad (6.7)$$

Where γ is the heat capacity ratio calculated using NASA polynomials depending on the average temperature and the combustion progress, V is the cylinder volume, and Q_w are the wall heat losses calculated using Woschni's approach [40]. The enthalpy exchange with the PC is considered negligible when compared to the HRR of the MC.

A more precise combustion HRR of some operating points is analyzed with a two-zone thermodynamic approach that divides the gas into two zones (fresh and burned gas) with equal pressure but different temperatures [32]. This allows for more precise caloric properties estimation assuming the chemical equilibrium of 18 species. The wall heat losses are modeled using Woschni's approach [39], the wall temperatures are calculated using Bargende's approach [40], and the blowby is accounted for using a labyrinth-seal approach [39].

Heat Release Rate Analysis in the Pre-Chamber

The double pressure indication (PC and MC) of cylinder 1 is used for the calculation of the apparent HRR inside the PC following the novel approach presented in Appendix A.1 and published in [26]. The method utilizes the precise simultaneous pressure measurement inside the PC and MC to calculate the average mass and temperature inside the PC, the apparent HRR, and the enthalpy flow between the two volumes.

6.4.2 Results

λ Variation Open chamber

Figure 6.49 depicts the measured brake thermal efficiency as a function of λ for the operating point A for inductive discharge (in blue) and NRPD ignition (in red). The last point at a λ of 1.8 for the inductive discharge system is the extreme point without misfires, while for the NRPD ignition system, the extreme point at a λ of 1.95 is the maximum point achievable due to boosting limitations. For the NRPD ignition system, the PRF is 50 kHz, and the number of pulses is increased from 10 to 100 to stabilize combustion at high AFR. The black stars in Figure 6.49 depict the number of pulses used.

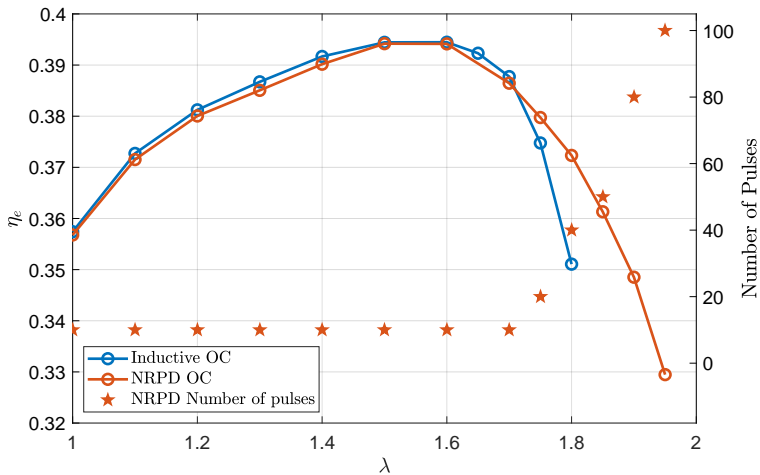


Figure 6.49: Brake thermal efficiency as a function of λ , inductive discharge vs NRPD ignition, OC, Point A (1'500 rpm/100 Nm).

Similar efficiencies are present till peak efficiency for both ignition systems. For higher AFRs, the efficiency drop is slower using NRPD ignition, resulting in notable higher efficiencies for λ s above 1.7.

Figure 6.50 shows the Coefficient of Variation (COV) of the Indicated

Mean Effective Pressure (IMEP).

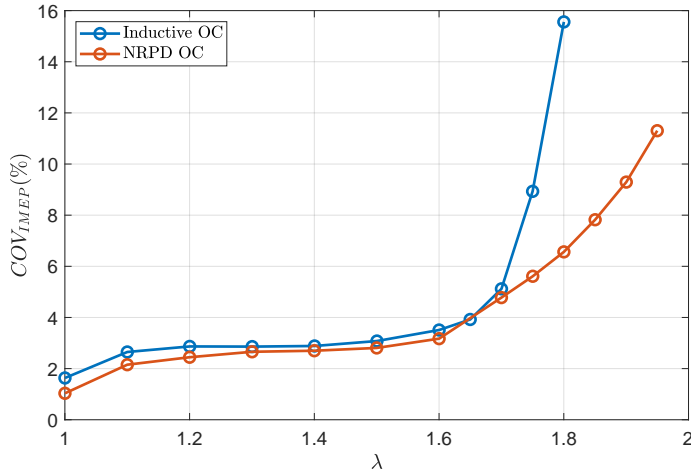


Figure 6.50: COV of IMEP as a function of λ , inductive discharge vs NRPD ignition, OC, Point A.

The COV of IMEP is a value to assess combustion stability. Values below approx. 5% are typically considered to guarantee smooth engine operation. The rapid increase of COV for the inductive ignition system over 5% rapidly results in unstable operation and misfire. This threshold is surpassed at a similar λ for the NRPD ignition system. Nevertheless, the increase happens much slower and doesn't result in misfires.

Figure 6.51 shows the ignition delay between spark timing and 5% of Mass Fraction Burned (MFB) and the combustion duration from MFB5 to MFB95 for inductive discharge (in blue) and NRPD (in red) ignition system.

The ignition delay is faster for the NRPD ignition system over the entire range, and the curves diverge significantly starting at $\lambda = 1.5$. After $\lambda = 1.6$, the ignition delay for the inductive discharge system rapidly increases, while the NRPD increases at a much slower pace. The combustion duration is similar for NRPD and inductive discharge

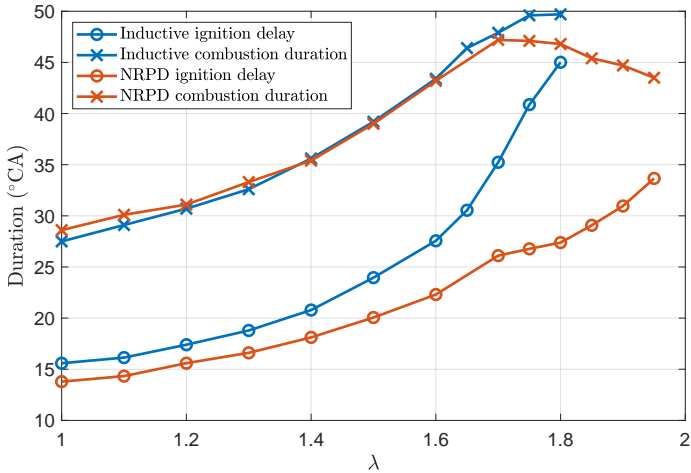


Figure 6.51: Ignition delay and combustion duration, inductive discharge vs. NRPD ignition, OC Point A.

ignition systems till $\lambda = 1.6$; afterward, the combustion duration for NRPD is shorter than for the inductive ignition system.

Figure 6.52 depicts the results of the loss analysis. The dotted lines are used for the inductive discharge ignition system, while the solid lines are used for the NRPD ignition system. Figure 6.52 reports the loss due to the real combustion, the loss due to incomplete combustion, the wall heat losses, and the pumping losses. The black line is used to depict the ideal efficiency increase compared to the stoichiometric case.

The loss analysis returns similar results between inductive discharge and NRPD ignition for the open chamber experiments up to $\lambda = 1.6$. Above λ of 1.6, the incomplete combustion losses rapidly increase, decreasing the overall efficiency. Using NRPD, the incomplete combustion losses rise slower for high λ s. For NRPD ignition above λ of 1.7, the combustion inefficiency becomes lower despite the higher AFR due to the faster combustion, as shown in Figure 6.51.

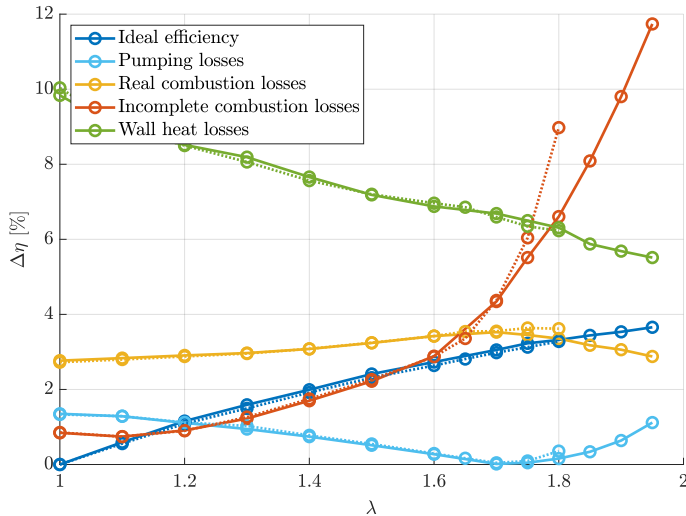


Figure 6.52: Loss analysis results, inductive discharge vs. NRPD ignition, passive OC Point A.

Figure 6.53 on top shows the HRR (in blue) and the combustion progress (in red) as percent, calculated using the two-zone thermodynamic approach using the averaged pressure over 300 cycles and all the cylinders. The black dotted lines show the combustion efficiency (higher value for the NRPD experiment). The red triangle and star are used to highlight the ignition timing for the inductive discharge and NRPD ignition system. The bottom subplot in Figure 6.53 shows the pressure-volume diagram in a double logarithmic scale. In both subplots, solid and dashed lines are respectively used for the NRPD and inductive discharge experiments.

The combustion with the NRPD ignition system is slightly shorter and has a higher HRR peak (15%), the inflammation is faster, and the completeness of combustion is higher. Due to the same operating condition, the two pressure curves are similar. Nevertheless, the pressure for the inductive discharge case is slightly higher during compression due to the higher necessary intake pressure to maintain the torque level.

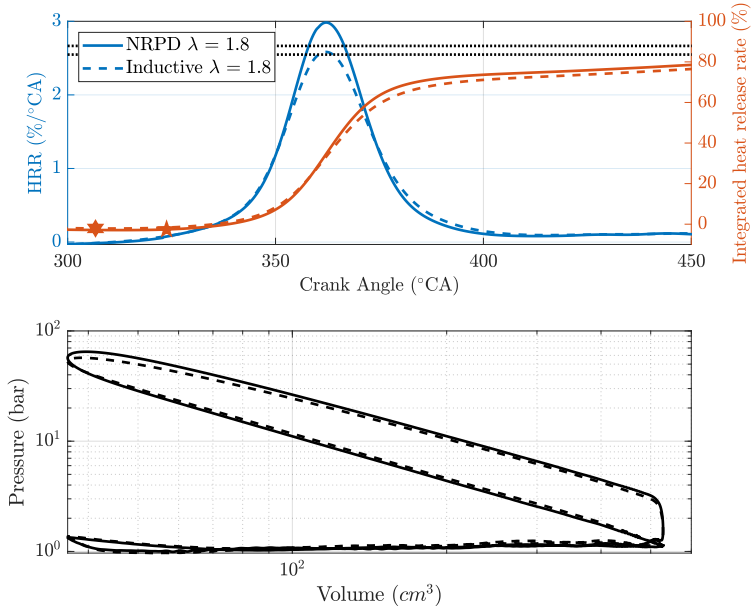


Figure 6.53: HRR and pressure-volume diagram, inductive discharge vs. NRPD ignition, OC Point A λ of 1.8.

λ Variation Passive Pre-Chamber

Figure 6.54 depicts the brake thermal efficiency variation as a function of λ at Point A for inductive discharge (in blue) and NRPD (in red) ignition. The PC is operated passively (no additional PC fueling). The stars depict the NRPD number of pulses. The NRPD ignition PRF is 100 kHz. The leanest shown points are at the border of misfires. If the HRR in the PC is so weak that the pressure increase inside the PC is similar to the pressure increase due to compression, misfires occur. This happens when the pressure between the PC and MC remains below zero during the entire compression. Controlling the COC to later angles mitigates the problem at the expense of efficiency. The stochastic occurrence of these cycles results in relatively efficient combustion and acceptable emissions when compared to OC operations.

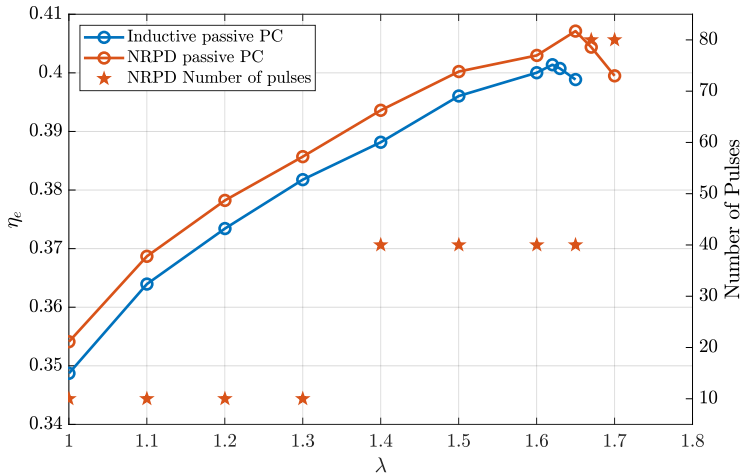


Figure 6.54: Mechanical efficiency as a function of λ , inductive discharge vs NRPD ignition, passive PC, Point A (1'500 rpm/100 Nm).

The brake thermal efficiency is consistently higher using the NRPD ignition system over the entire range. The λ where the efficiency peaks is higher for the NRPD ignition compared to the inductive discharge ignition system from a λ of 1.6 to 1.65. Fuel consumption reductions of 1.4% are achieved at their respective efficiency peak using the NRPD ignition.

Figure 6.55 shows the HRR analysis computed with the two-zone thermodynamic analysis on top and the pressure-volume diagram in double logarithmic scale on the bottom at a λ of 1.65 for inductive discharge and NRPD ignition. The star is used to highlight the ignition timing with the NRPD ignition system while the triangle is used for the inductive ignition.

At the ignition limit for inductive ignition, short, stable combustion is still achievable with the NRPD ignition system, resulting in an increased peak efficiency. Figure 6.56 shows the COV of IMEP for the same experiments reported in Figure 6.54.

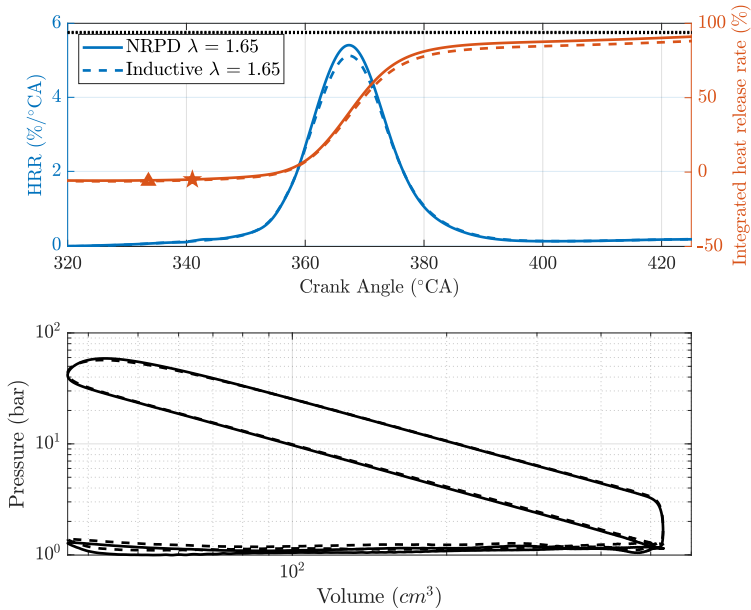


Figure 6.55: HRR and pressure-volume diagram, inductive discharge vs. NRPD ignition, passive PC. Point A, λ of 1.65.

The COV (Figure 6.56) is constant and similar for the investigated ignition systems until λ of 1.6. For the inductive ignition system, the COV increases rapidly at a λ of 1.65, making stable operation impossible (misfires). For NRPD ignition, the COV rises slower, and the limit for operation without misfires is reached at λ of 1.7.

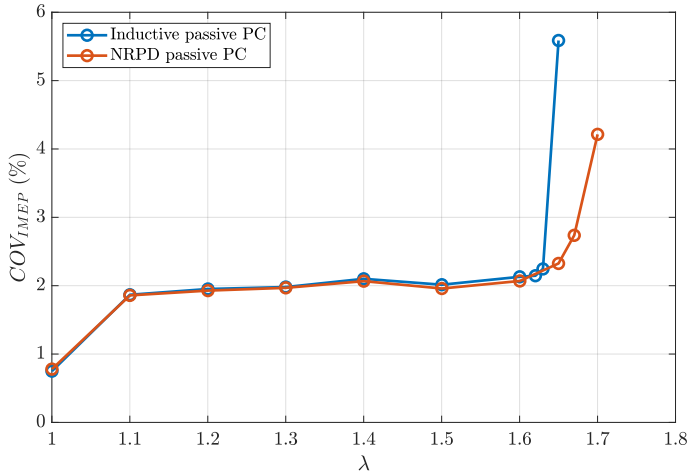


Figure 6.56: COV of IMEP as a function of λ , inductive discharge vs. NRPD ignition, passive PC, Point A

Figure 6.57 shows the results of the loss analysis. The dotted lines represent the results using the inductive discharge ignition system. The NRPD results are summarized using the solid lines.

As figure 6.54 shows, the peak efficiency is reached close to the λ limit of operations. Stable operations is impossible right after peak efficiency for the three investigated combinations. The limit of stable operations is visible in the loss analysis from the increase in incomplete combustion and real combustion losses in the three leanest points. The efficiency peaks due to reductions in wall heat losses, pumping losses, and an increase in the ideal efficiency. The real combustion losses are relatively constant until the peak efficiency point, while the incomplete combustion losses increase with further air dilution. Higher overall efficiencies using NRPD ignition are present thanks to reduced real combustion losses.

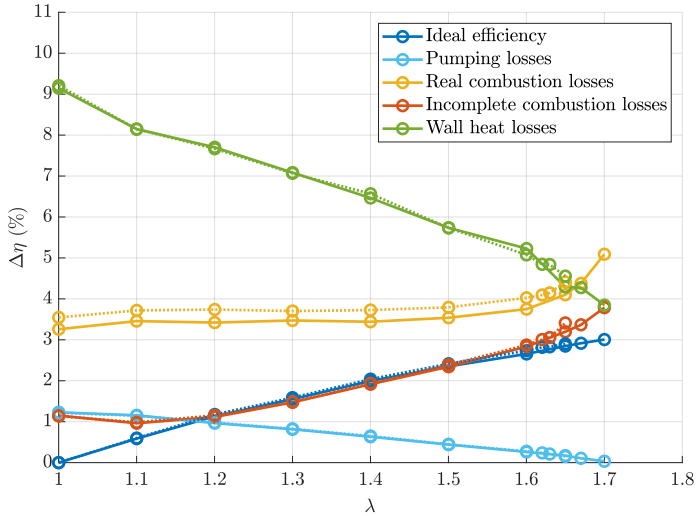


Figure 6.57: Loss analysis results as a function of λ , inductive discharge (dotted lines) vs. NRPD ignition (solid lines), passive PC, Point A.

Figure 6.58 shows the combustion duration (5-95% MFB) and ignition delay (ignition timing to 5% MFB) for the same experiments reported in Figure 6.54 computed with the 1-zone thermodynamic analysis as used in the loss analysis.

Similar combustion durations can be observed for the inductive and NRPD ignition. Shorter ignition delays from a λ above 1.4 are present using NRPD ignition. Interestingly, the loss analysis (Figure 6.57) returns a higher combustion efficiency for the NRPD ignition despite a similar (or even slower) combustion duration, highlighting the impact of different HRR shapes and the first and last 5% of MFB.

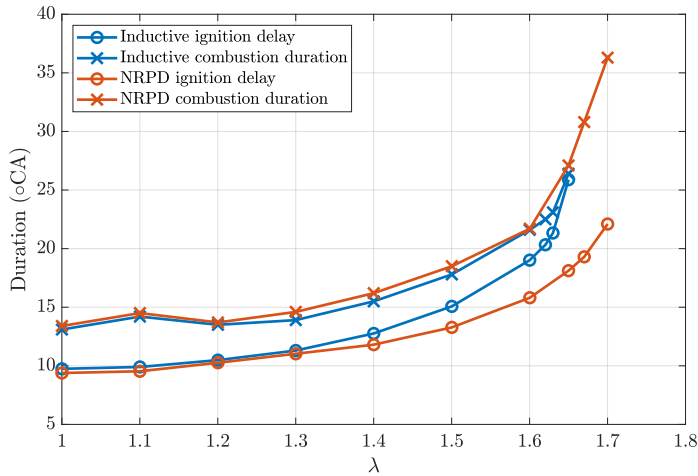


Figure 6.58: Combustion duration (5-95 MFB) and ignition delay (0-5 MFB), inductive discharge vs NRPD ignition, passive PC, Point A.

Figure 6.59 depicts the HRR analysis computed with a two-zone thermodynamic analysis on top and the pressure-volume diagram on the bottom at a λ of 1.5 for inductive discharge and NRPD ignition. The star and the triangle are used for the NRPD and inductive ignition timings respectively.

Similar HRRs are present at $\lambda = 1.5$ with the two ignition systems; the NRPD results in a slightly higher HRR peak. The pressure-volume diagram (Figure 6.59 bottom) shows that the pressure during the pumping loop is higher for the inductive system (lower efficiency, more mass in the cylinder to achieve the same load at the same AFR). The two-zone thermodynamic analysis is much more capable of capturing small differences in HRR, especially for the end phase of combustion phenomena [32]. The 10 to 90% MFB using the two-zone analysis is much longer using the inductive ignition system (32 vs. 16 °CA) due to the slow rise of the combustion process towards the end. The two black points in the upper subplot in Figure 6.59 show the 90% MFB.

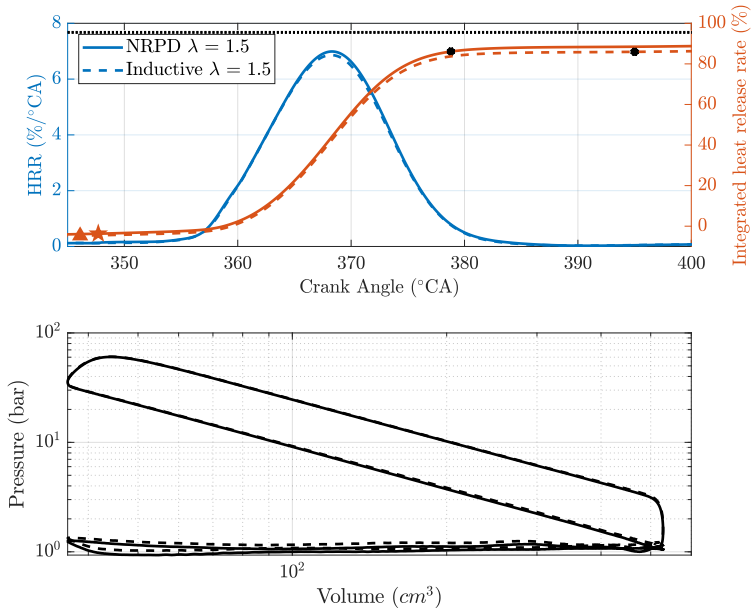


Figure 6.59: HRR and pressure-volume diagram for the inductive discharge vs. NRPD ignition, passive PC. Point A, λ of 1.5.

Figure 6.60 shows the Total HydroCarbon (THC) emissions using inductive and NRPD ignition systems.

The inductive ignition system produces slightly higher THC emissions, highlighting the possibility of different end-of-combustion phenomena when using the NRPD ignition system.

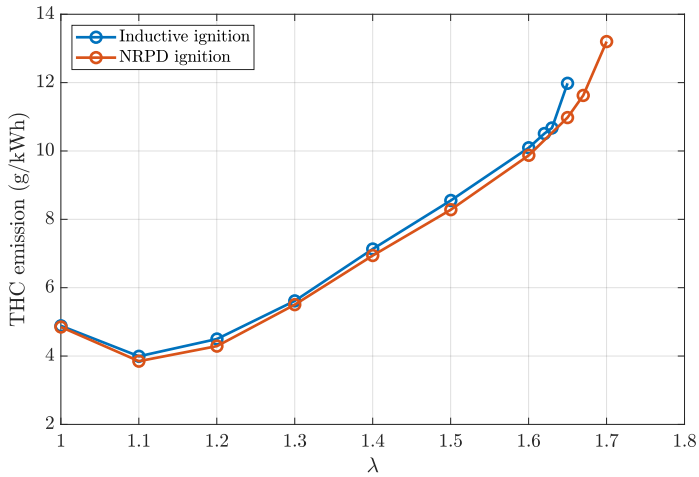


Figure 6.60: Total Hydrocarbon Emissions, inductive discharge vs. NRPD ignition, passive PC. Point A, $\lambda = 1.5$

Figure 6.61 shows, the HRR's details for the same point as shown in Figure 6.59. To clarify the analysis further, the two-zone thermodynamic analysis is done individually for each cylinder.

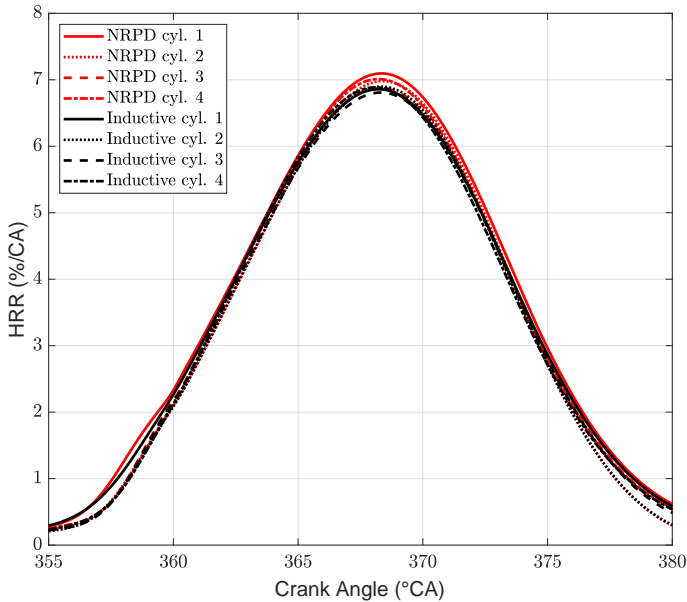


Figure 6.61: Cylinder individual detail of the HRR and pressure-volume diagram, inductive discharge vs. NRPD ignition, passive PC Point A λ of 1.5.

For all the cylinders, the HRR is higher using NRPD ignition and reaches a higher peak. Figure 6.62 shows the results of the thermodynamic analysis inside the PC (Appendix A) for point A and a λ of 1.5. The top subplot shows the pressure difference between PC and MC (in red) and the HRR in the MC for the average over 300 cycles in cylinder 1 (only one where a pressure sensor is present in the PC). The bottom subplot shows the enthalpy flow from the PC into the MC (in blue) and the cumulative HRR (in red).

The pressure increase in the PC is faster and reaches a higher peak using the NRPD ignition system, which results in a higher enthalpy flow during TJI. A double peak in pressure is present with the NRPD ignition system; it is not clear if this is due to some interference between

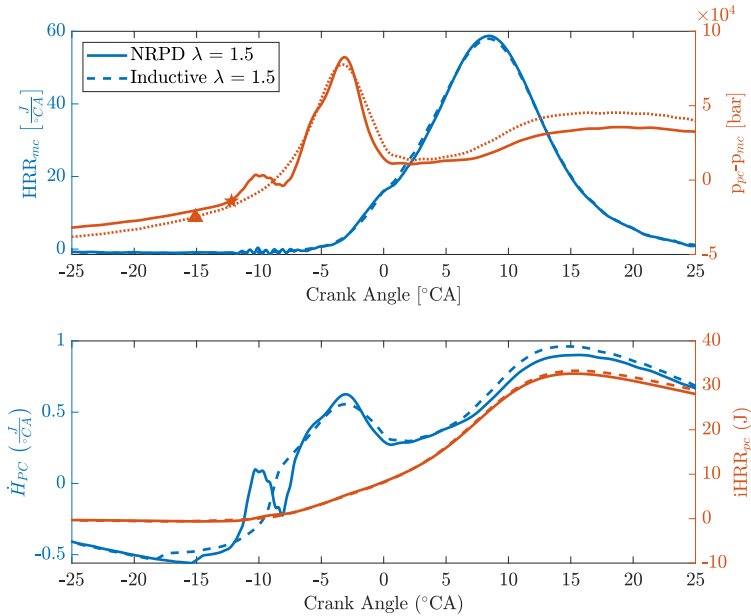


Figure 6.62: PC thermodynamic analysis, inductive vs NRPD ignition, passive PC, Point A, λ of 1.5.

the pressure measurement and the ignition system, or if there is a real difference.

λ Variation Active Pre-Chamber

Figure 6.63 depicts the brake thermal efficiency as a function of λ at Point A for inductive discharge (in blue) and NRPD (in red) ignition; the star represents the number of pulses. In these experiments, the PC is actively fueled during the intake stroke. A similar fuel mass flow rate is used for both ignition systems for the PC scavenging process. The algorithm presented in [121] controls the AFR in the PC at the moment of ignition to an estimated λ of approx. 0.9.

The brake thermal efficiency using NRPD ignition is consistently higher

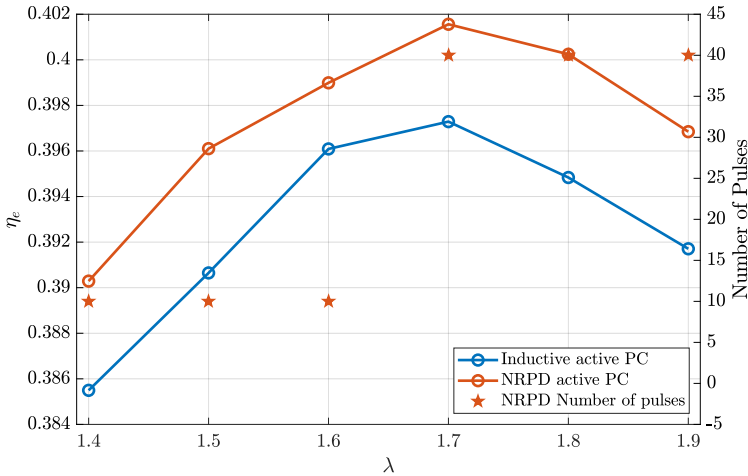


Figure 6.63: Brake thermal efficiency as a function of λ , inductive discharge vs NRPD ignition, active PC, Point A (1'500 rpm/100Nm).

than that achieved with the inductive discharge ignition system over the investigated AFR range. For both ignition systems, the efficiency peaks at a λ of 1.7, where the NRPD efficiency is higher by 0.4% point, resulting in a fuel consumption reduction of 1%.

Figure 6.64 shows the loss analysis results for the experiments presented in Figure 6.63. The dotted lines indicate inductive discharge ignition, while the full lines indicate the NRPD ignition system.

The peak efficiency is reached at a λ of 1.7 for both ignition systems, where the trade-off between increased incomplete combustion losses against ideal efficiency increase and reduction of pumping losses peaks. The increase in efficiency using the NRPD ignition is visible as a mix in reduction between wall heat losses and real combustion losses. It is worth mentioning that, with the used loss analysis, not well-captured HRR effects using the 1-zone thermodynamic analysis will be reflected in variations in wall heat losses (as explained in Appendix A.2).

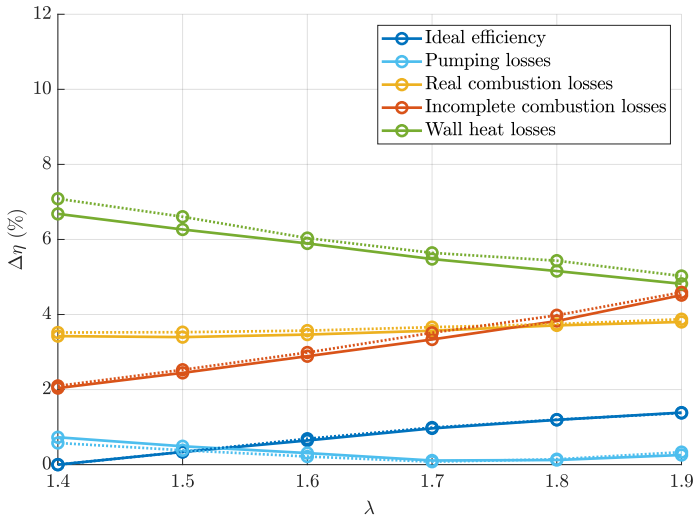


Figure 6.64: Loss analysis results as a function of λ , inductive (dotted) discharge vs NRPD (solid) ignition, active PC, Point A.

Figure 6.65 depicts the combustion duration 5-95% of MFB and the ignition delay for the NRPD and the inductive discharge ignition system.

Using the NRPD ignition, slightly shorter ignition delays and slightly longer combustion durations are present. The loss analysis (Figure 6.64) returns a higher combustion efficiency for the NRPD ignition despite a similar (or even slightly longer) combustion duration, highlighting the impact of different HRR shapes and the first and last 5% of MFB (a similar effect as in the passive PC case).

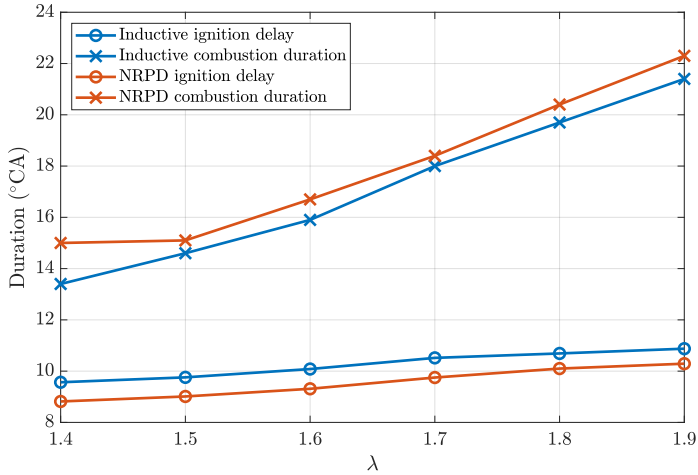


Figure 6.65: Combustion duration (5-95 MFB) and ignition delay (0-5 MFB), inductive discharge vs NRPD ignition, active PC, Point A.

Figure 6.66 shows the HRR (in blue) and the MFB (in red) in percent calculated using the two-zone thermodynamic approach using the averaged pressure over 300 cycles and for all cylinders. The bottom subplot in Figure 6.66 shows the pressure-volume diagram in a double logarithmic scale. In both subplots, solid and dashed lines are used for the NRPD and inductive discharge experiments. The triangle and star are used to highlight the average ignition time for the inductive discharge and NRPD ignition systems.

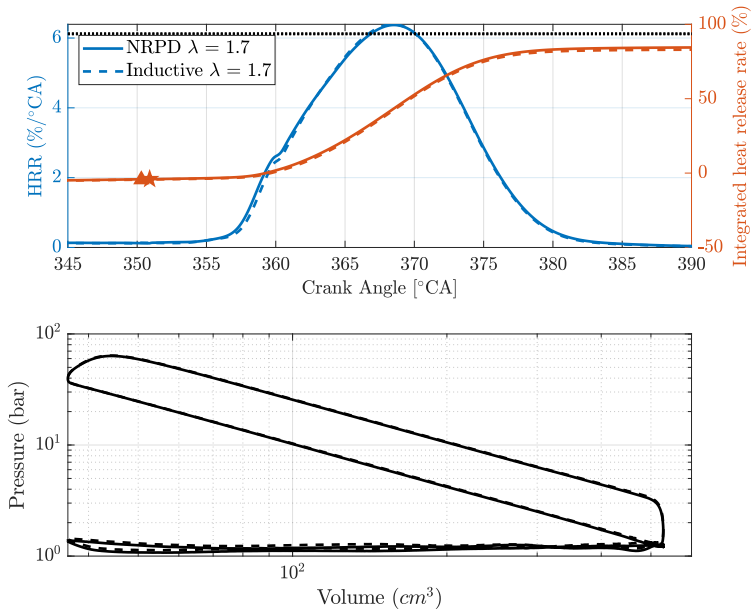


Figure 6.66: HRR and pressure-volume diagram, inductive discharge vs. NRPD ignition, active PC Point A λ of 1.7

Higher completeness of combustion is achieved using NRPD ignition. This is again reflected in a slight but consistently lower THC emission level, as shown in Figure 6.67.

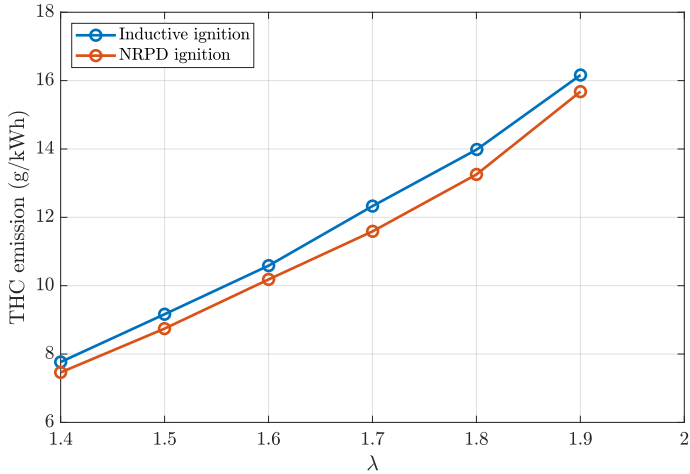


Figure 6.67: Total Hydrocarbon Emissions, inductive discharge vs. NRPD ignition, active PC, Point A.

Two clearly different positive slopes are recognizable for the HRR reported in Figure 6.66, a first one with a higher gradient lasting till approx. 360°CA and a second till approx. 370°CA . The first one, with a higher gradient, is attributed in the literature to the strong ignition energy present once the turbulent jets (still active) ignite the charge in the MC, also called PC discharge [157]. Once TJI finishes and the MC combustion progresses, the second (lower gradient) increase is present. A flex-point highlights the transition between these two phases [158]. The rise rate in the first phase is faster and reaches a higher HRR using the NRPD ignition system. Figure 6.68 shows for the same point as shown in Figure 6.66 the detail of this non-symmetric first half of HRR. To make the analysis clearer, the two-zone thermodynamic analysis is done individually for each cylinder.

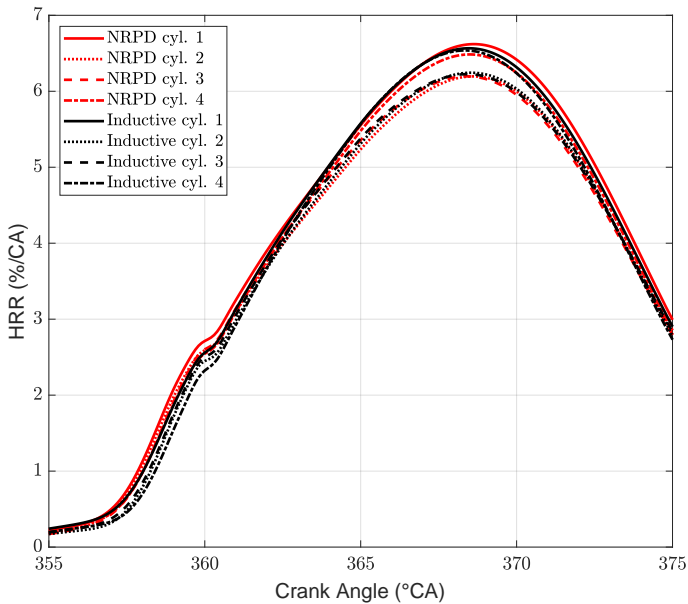


Figure 6.68: Cylinder individual detail HRR, inductive discharge vs. NRPD ignition, active PC, Point A λ of 1.7.

Despite similar overall conditions for all the cylinders, the flex point and gradient are higher using NRPD ignition. Figure 6.69 shows the results of the thermodynamic analysis inside the PC for the actively fueled PC, point A, and a λ of 1.7. The top subplot shows the pressure difference between PC and MC (in red) and the HRR in the MC for the average over 300 cycles in cylinder 1. The bottom subplot shows the enthalpy flow from the PC into the MC (in blue) and the cumulative HRR (in red).

Using NRPD, the pressure difference peak between PC and MC is narrower, and the resulting enthalpy flow from the PC to the MC is higher. The small plateau before the quick increase in pressure is present because the average over 300 cycles is evaluated. In some cycles, the pressure increases sooner, which explains the small increases observed.

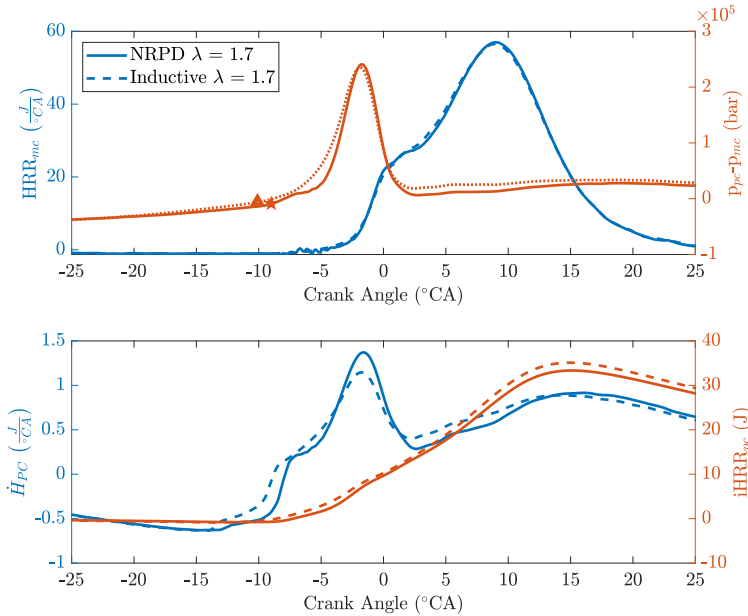


Figure 6.69: PC thermodynamic analysis, inductive vs. NRPD ignition, passive PC, Point A, λ of 1.7.

Exhaust Gas Recirculation Variation Open Chamber and Passive Pre-chamber

Figure 6.70 depicts the brake thermal efficiency as a function of the EGR rate for the four investigated combinations at $\lambda = 1$ operation. The dashed lines are used for the passive PC experiments, and the solid lines are used for the OC experiments. Red and blue colors are used for the NRPD and inductive discharge ignition systems experiments, respectively. The NRPD ignition PRF is 50 kHz for the OC experiments and 100 kHz for the PC experiments, 10 pulses are used in all the PC experiments, while in OC. 10 pulses are used till an EGR rate of 25%, the number of pulses is 40 at 30% and 100 afterward.

In OC configuration using NRPD ignition, the efficiency peaks at a higher EGR rate than the inductive discharge ignition system. The ef-

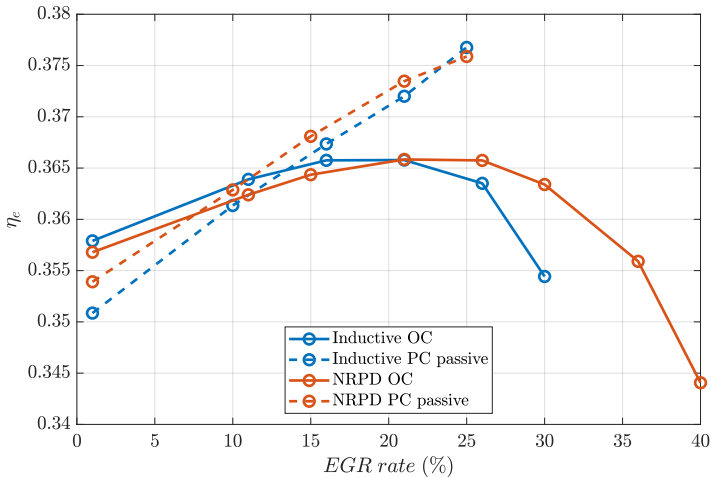


Figure 6.70: Mechanical efficiency as a function of EGR rate, inductive discharge vs. NRPD ignition, OC and passive PC, Point A (1'500 rpm/100 Nm)

efficiency at low EGR rates is higher in OC configurations than for PC experiments. Nevertheless, the efficiency of PC experiments steadily increases until the ignition limit. The efficiency peak for the PC experiments is reached right before the limit of stable ignition at 25% of the EGR rate for both ignition systems, where similar efficiencies are measured using the NRPD and the inductive ignition systems. It is worth mentioning that at the limit of ignition, the EGR rate oscillates during the measurement; it is, therefore, possible that the actual value for the NRPD could be slightly higher. In the other points, slightly higher efficiencies are present when using NRPD ignition.

Figure 6.71 shows the loss analysis for the experiments reported in Figure 6.70. Figure 6.71 reports the OC experiments on the left subplot and the PC experiments on the right. The dotted and full lines are, respectively, used for the NRPD and inductive discharge ignition systems.

Similar losses are present in the OC till an EGR rate of approx. 20%;

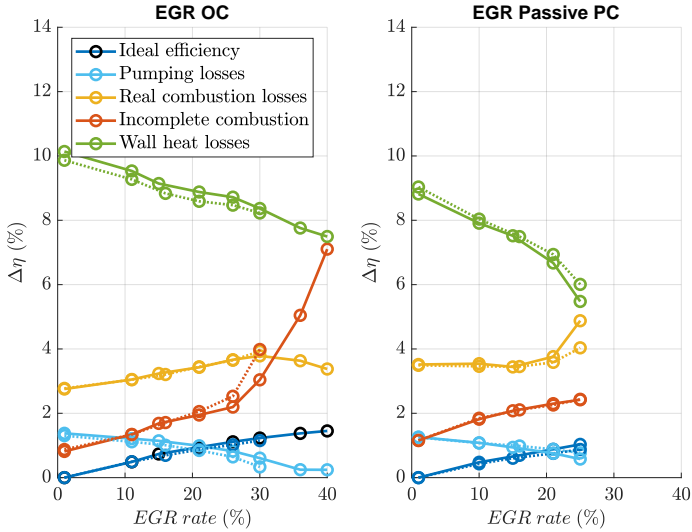


Figure 6.71: Loss analysis results as a function of EGR rate, inductive discharge vs. NRPD ignition, OC (left), passive PC (right), Point A.

afterward, the incomplete combustion losses using the inductive discharge ignition system increase faster. For the passive PC experiments, similar losses are present for the two ignition systems. The small increase in efficiency for the NRPD ignition is present due to lower wall heat losses, while at 25% EGR, the incomplete combustion losses are higher using the NRPD ignition system.

Overall Comparison

Figure 6.72 shows the loss analysis investigation as bar graphs for the investigated ignition concepts. The white blocks represent the brake thermal efficiency (η_E) while all the colored blocks represent the various efficiency losses, from bottom to top: the mechanical efficiency losses ($\Delta\eta_M$), the pumping losses ($\Delta\eta_{LP}$), the expansion losses ($\Delta\eta_{EX}$), the wall heat losses ($\Delta\eta_W$), the real combustion losses ($\Delta\eta_{RC}$), the losses due to incomplete combustion ($\Delta\eta_{IE,ic}$), and the real charge

losses ($\Delta\eta_{IE,r1}$). The first six bars depict the best efficiency achievable using air dilution, and the last four using EGR dilution at overall stoichiometric operations. The different ignition concepts are for AFR variation passive PC, active PC, and OC, all with NRPD and inductive discharge ignition. The 6 AFR variations and the 4 EGR variations are sorted from the highest to the lowest efficiency. The OC point with NRPD ignition and a λ of 1.7 is also reported in the seventh position for direct comparison against the PC data. Due to stoichiometric operation, the PC is operated only without additional scavenging for the EGR cases, the resulting ignition concepts are therefore passive PC and OC.

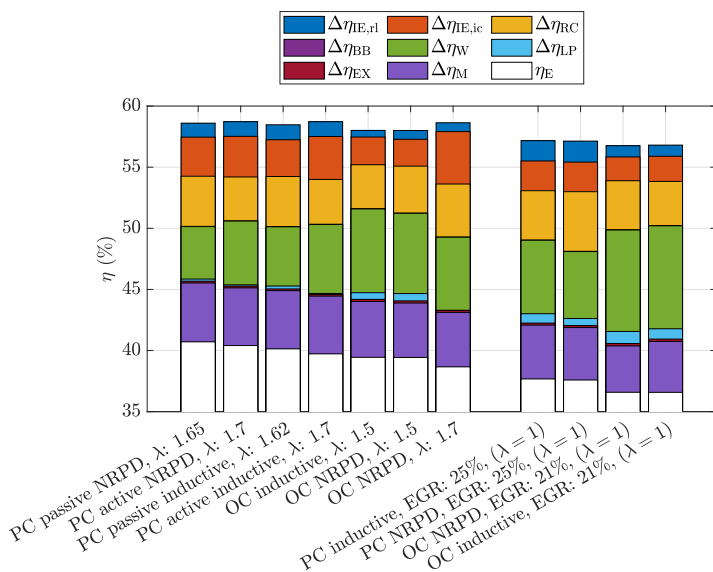


Figure 6.72: Loss analysis, comparison of the investigated ignition concepts at peak efficiency, point A.

Figure 6.73 depicts, for the same points as in Figure 6.72, the THC, the Carbon Monoxide (CO) and NO_x emissions, and the exhaust temperature. The passive PC point using NRPD at λ of 1.6 is also added (third position) for direct comparison against the inductive ignition system.

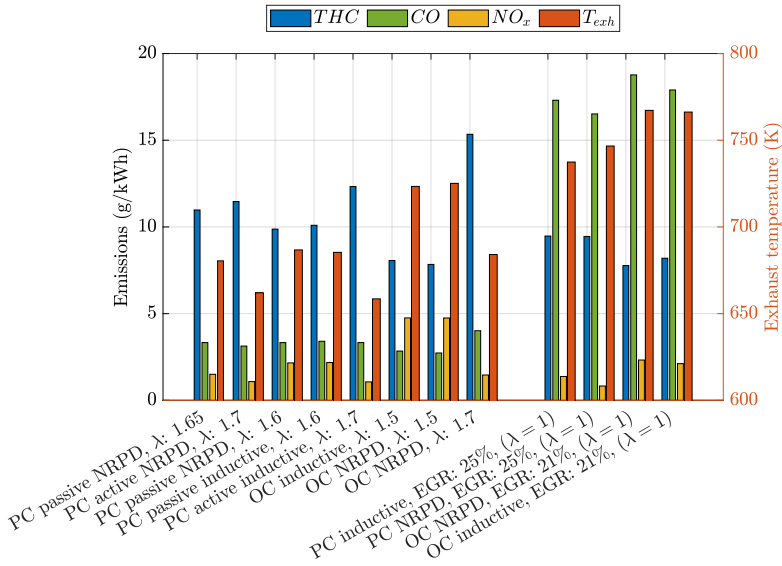


Figure 6.73: Emissions, comparison of the investigated ignition concepts at peak efficiency, point A.

The highest η_e is reached using the passive PC and NRPD ignition at a λ of 1.65. Similar efficiency is reached for the active PC and NRPD ignition (40.7% vs. 40.4%). Using the inductive ignition system, peak efficiencies of 40.1 and 39.7 are reached for passive and active PC, respectively. Changing from passive to active PC while remaining at peak efficiency (NRPD ignition) results in an increase of 4% in THC and a reduction of 33% in NO_x. No notable differences at peak efficiency (λ of 1.5) are present in efficiency or emissions between the inductive discharge and NRPD ignition systems; only a slight reduction in THC emission is present (3%). The CO emissions are less critical since they are much simpler to oxidize (in an oxidation catalyst) than the THC emissions, mainly composed of unburned methane.

For EGR dilution at $\lambda = 1$ operation, which would enable using a three-way-catalyst, similar peak efficiencies are reached using NRPD and inductive ignition in PC and OC configuration.

Figure 6.74 shows the variation in fuel consumption and emissions (THC and NO_x) compared to the inductive discharge ignition system in OC for the six different ignition strategies for point A at a λ of 1.6.

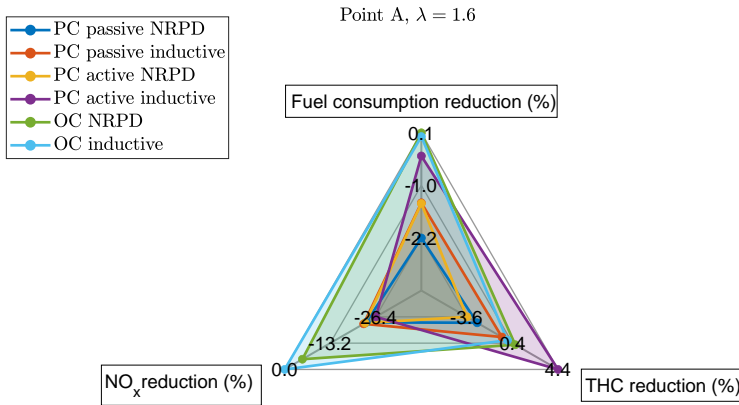


Figure 6.74: Spider chart of efficiency and emissions, Point A, λ of 1.6.

The smallest triangle in Figure 6.74 may be used to indicate the best ignition strategy. At Point A, λ of 1.6, the NRPD ignition with passive PC shows the best results, decreasing fuel consumption, THC, and NO_x emissions.

We have so far discussed only operating point A ((1'500 rpm/100 Nm)). Figure 6.75 shows the loss analysis as bar graphs for the different investigated ignition concepts at peak efficiency for the low-load operating point B (1500 rpm / 30 Nm), again sorted from highest to lowest efficiency.

Similar trends are visible at the lower load point for all the investigated ignition strategies and for AFR and EGR dilution. The efficiency is the highest for the passive PC and NRPD ignition; similar efficiencies are present for the active PC operated with NRPD. The passive PC efficiency increases by 0.5% using NRPD ignition (2% fuel consumption

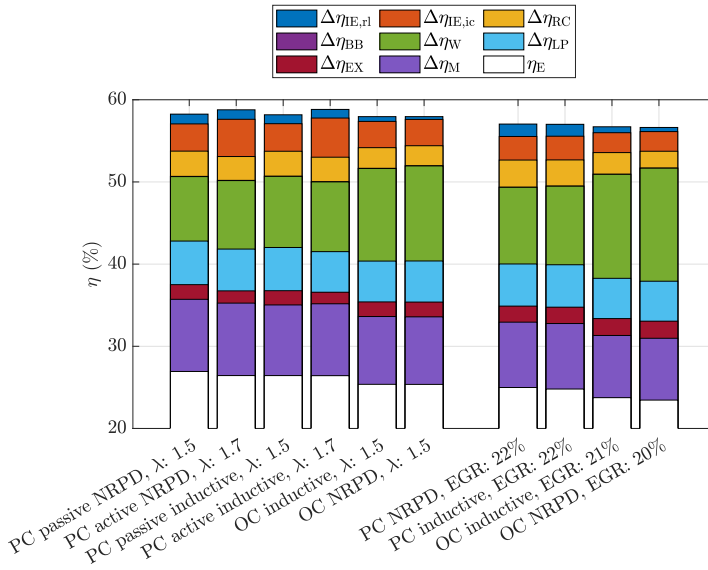


Figure 6.75: Loss analysis, comparison of the investigated ignition concepts at peak efficiency, point B.

reduction) at a λ of 1.5. For the EGR experiments at peak efficiency, a slight increase in efficiency of 0.2% (0.8% fuel consumption reduction) at 22% of EGR and λ of 1 is present using the NRPD ignition.

Figure 6.76, depicts, for the same points as in Figure 6.75, the THC, the CO and NO_x emissions and the exhaust temperature.

The emissions trends are similar for point B compared to point A. There are no notable emissions differences between NRPD and inductive discharge ignition in OC experiments, while lower THC and NO_x emissions are present for the PC experiments.

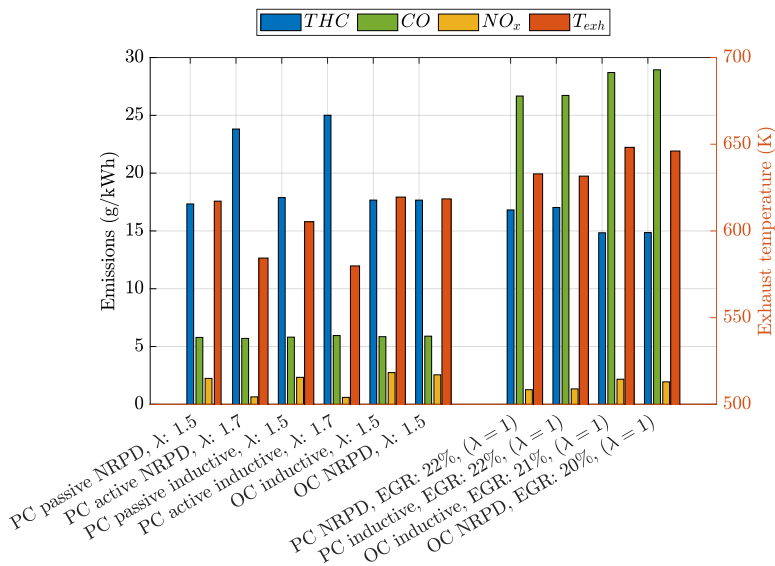


Figure 6.76: Emissions, comparison of the investigated ignition concepts at peak efficiency, point B.

6.4.3 Summary and Discussion

In OC experiments, the brake thermal efficiency of NRPD is similar to that of inductive discharge ignition systems for λ values up to 1.6 and EGR rate up to 20%. Afterward, the losses due to longer combustion durations and incomplete combustion increase faster than the increase in ideal efficiency present for higher dilutions, leading to lower efficiencies. NRPD ignition, especially with a high number of pulses at high PRF, reduce the real combustion and incomplete combustion losses. In fact, the inflammation and the initial combustion phase are faster, and unburned hydrocarbon emissions are lower. The efficiency peaks for both ignition systems at λ of 1.6 at the same value. Despite effective flame stabilization using NRPD, the unburned hydrocarbon emissions rapidly increase after peak efficiency, probably due to large quenching distances near the walls, which does not allow for higher efficiency values. In fact, from the loss analysis, the efficiency would still increase

substantially by neglecting the increase in unburned hydrocarbon emission (methane slip). A lower quenching distance (i.e., a lower methane slip) could be achieved, for example, by adding hydrogen to methane. On the same engine used in this investigation, 30-40% of THC emission reduction was achieved by adding only 3.5% (by mass) of hydrogen [44]. In the OC experiments, the ignition delay is always shorter when using the NRPD ignition system. For the OC configuration and point A at peak efficiency, the delay between ignition and 5% of MFB is 5 °CA longer for the inductive discharge ignition system. Some studies investigate the effect of variation in the ignition system or spark plug design while keeping the ignition angle constant [16, 17, 19, 159]. In those cases, a faster inflammation phase could result in higher efficiency due to variation in the COC phasing, which is not the case in this investigation due to the feedback-controlled COC which always guarantees maximum efficiency ignition settings.

For the passive PC experiments, increasing the dilution (either by λ increase or increasing the EGR rate) results in increased efficiency until approx. a λ of 1.6 or an EGR rate of 20%. Right after peak efficiency, the combustion becomes unstable, and misfires are detected. Actively fueling the PC decreases the efficiency but results in a much more stable combustion. The active PC efficiency peaks at an overall λ of 1.7 and combustion without misfire till the boosting limits are achieved. For the PC experiments, NRPD ignition results in higher efficiency, particularly when air dilution is used. The loss analysis shows that the efficiency increase is mainly due to decreased real combustion and wall heat losses. A more detailed investigation using a two-zone thermodynamic analysis in the MC and a pressure-based analysis of the combustion in the PC outlines that a higher enthalpy flow from the PC during TJI is present using NRPD ignition resulting in a higher HRR during the PC-discharge [157]. Furthermore, the EOC (only visible using the two-zone thermodynamic analysis) is reached sooner using NRPD ignition, which is also visible from the slightly but consistently higher THC emissions present using the inductive ignition system. This EOC effects are interpreted by the loss analysis as wall heat losses.

PC ignition results in higher peak efficiency when compared to OC. From the loss analysis, this increase in efficiency results from a reduction in wall heat losses, which could be due to different flame propagation. Additionally, the end of the combustion phase can explain this differ-

ence. In fact, in the loss analysis, the EOC losses could be interpreted, particularly for slow combustion speeds, as wall heat losses.

A higher number of pulses is beneficial for both OC and PC, the higher the λ . For the OC experiments, the advantage is directly visible on the test bench by a decrease in the spark advance necessary for keeping the COC at 8°CA , while for the PC experiments (especially for the passive PC), due to the rapid variations, this is more difficult to visualize directly. For this reason, the number of pulses was increased linearly for the OC experiments and more in step increments for the PC experiments.

Due to the differences in combustion shape between NRPD and inductive discharge ignition, different ideal COC could be present.

COC variation experiments show that the efficiency around 8°CA after TDC is rather constant due to a constant trade-off between decreasing wall heat losses and increasing combustion inefficiency. Figure 6.77 shows the efficiency variation for COC (feedback-controlled) variation from 4 to 14°CA after TDC for the inductive ignition system (dashed line) and for NRPD ignition (full line) for the passive PC at Point A and stoichiometric operation.

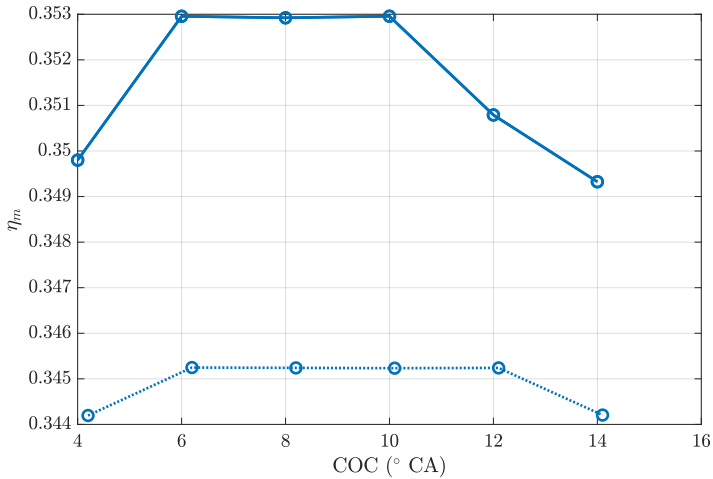


Figure 6.77: Efficiency against COC, stoichiometric condition, Point A.

The mechanical efficiency is practically constant for COC from 6 to 12 $^{\circ}$ CA after TDC for the inductive ignition system and from 6 to 19 $^{\circ}$ CA after TDC for NRPD ignition. Figure 6.78 shows the results of the loss analysis for the COC variation.

For earlier COC, the real combustion losses decrease, and the wall heat losses increase. There is an equal decrease in wall heat losses and an increase in real combustion losses.

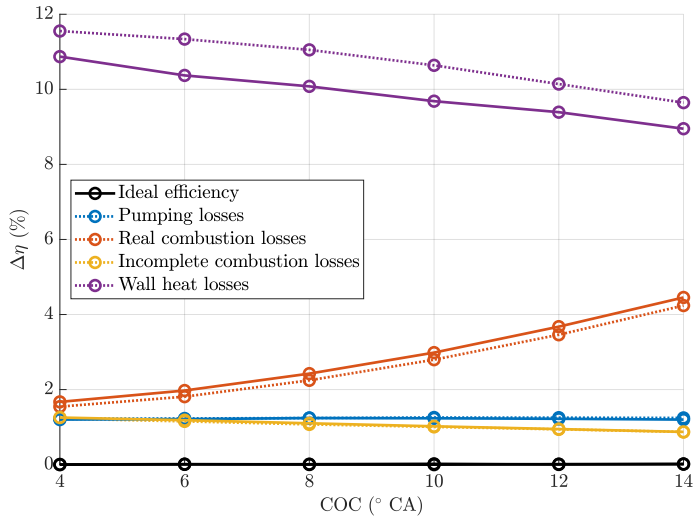


Figure 6.78: Loss analysis against COC, stoichiometric condition, Point A, inductive ignition.

Figure 6.79 shows a photo of the first cylinder mounted on the engine with the cylinder head removed after the experimental campaign. Ten nozzles connect the PC and MC, seven of those tangentially, and three points straight to the piston hemispherical recession.

In Figure 6.79, the marks of the impinging jets are visible. Furthermore, from optical analysis [120] and Section 6.1, it is clear that, unlike classical spark plug setups where the flame starts developing at the spark plug location in the MC, the jets exiting the PC hit the piston and that the flame front in the MC travels from the piston toward the PC. From the thermodynamic analysis performed, it is evident that the flame propagates differently using NRPD compared to inductive discharge ignition systems. The HRR inside the PC is faster and stronger, resulting in a higher and shorter positive pressure difference between the PC and MC during ignition (Figure 6.62 and Figure 6.69).

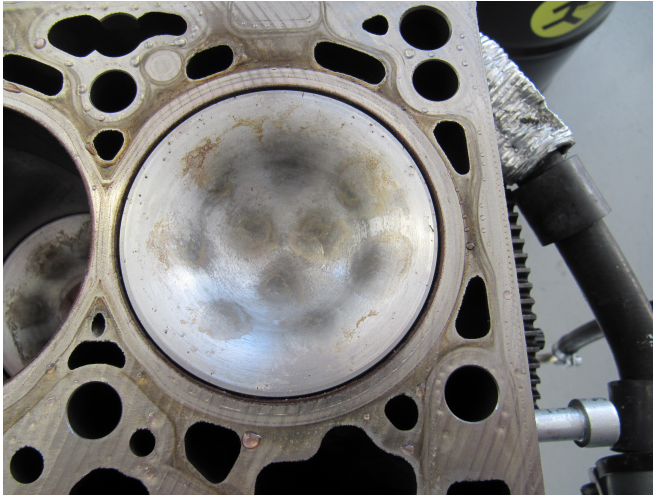


Figure 6.79: Photo of the piston one in the short block with marks of the ten impinging jets.

The spider plot in Figure 6.80 shows the variation in brake thermal efficiency against the OC inductive discharge experiments, the incomplete combustion losses ($\Delta\eta_{E,ic}$), the wall heat losses ($\Delta\eta_W$), and the real combustion losses ($\Delta\eta_{RC}$) for the six investigated combustion processes for Point A at a λ of 1.6.

The green and light blue areas are superposed, highlighting the similarity between the NRPD and inductive discharge ignition systems in the OC configuration. Turbulent jet ignition speeds up combustion, which is visible from the reduction in real combustion losses. The incomplete combustion losses are lower using turbulent jet ignition, probably thanks to lower quenching distances due to faster and jet-enhanced combustion. The active PC with inductive discharge ignition has incomplete combustion losses similar to OC configurations, possibly due to the incomplete combustion inside the PC. For the passive PC, NRPD ignition is better thanks to lower real combustion losses, particularly due to the first and last 5% of cumulative HRR.

Six ignition strategies, OC, PC active, and PC passive, all achieved with inductive discharge and NRPD ignition, are investigated in a 4-cylinder

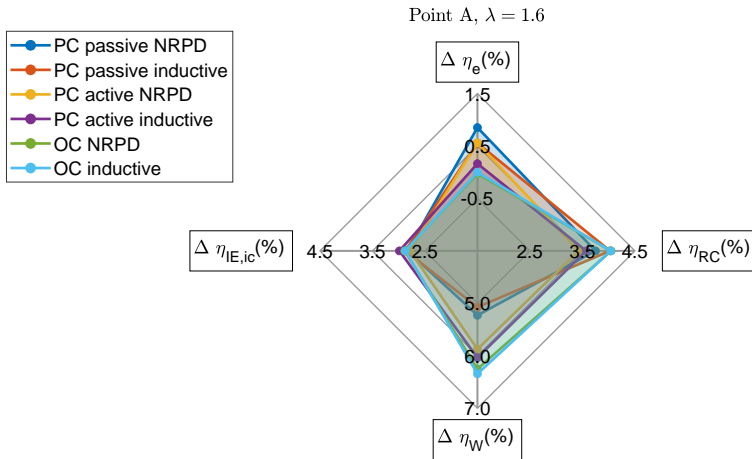


Figure 6.80: Spider chart loss analysis, Point A, λ of 1.6.

engine operated with the relatively hard-to-ignite fuel methane (natural gas). The effect of ignition strategies on efficiency and emissions is investigated on two operating points at different AFR and EGR rates at overall stoichiometric conditions. For the EGR investigation, only passive PC experiments are performed. The following conclusion can be drawn:

- ▶ The same peak efficiency is reached in OC configuration using inductive discharge and NRPD ignition systems by varying AFR and EGR rates at a λ of 1.6 and an EGR rate of 20%. After peak efficiency, the efficiency using NRPD ignition, especially using a high number of pulses, decreases at a slower pace thanks to the reduced amount of unburned hydrocarbon emission and overall shorter combustion.
- ▶ The emissions levels (THC and NO_x) in OC configuration are similar for the two ignition systems till peak efficiency, highlighting that the enhanced plasma ignition does not contribute to additional emissions.

- ▶ For the PC experiments using NRPD ignition, an efficiency increase resulting in about 2% fuel savings (especially in air-diluted conditions) compared to inductive discharge ignition is present over the investigated dilution range and for both points. This is due to a stronger turbulent jet that ignites the charge in the MC, which also impacts the EOC phase (being shorter using NRPD ignition).
- ▶ The active PC offers the advantage of more stable combustion and a broader range of combustion without misfires at the expense of fuel consumption.

In this investigation, the combination of NRPD ignition and passive PC is the best ignition concept. The overall efficiency is the highest, and the emissions are lower than using inductive discharge ignition. 3D information about the differences present using NRPD in PC could shed light on the ongoing processes and possible further optimizations. These investigations could be done experimentally in optically accessible engines or using CFD simulations and the data presented in this investigation. Furthermore, the PC volume and number of holes have been optimized for the inductive ignition system; due to the different combustion inside the PC, it is possible that a different PC volume would represent the ideal for NRPD ignition. It is possible that a smaller PC volume and NRPD still give enough ignition energy, resulting in lower PC-related losses. Due to the detected advantage of NRPD ignition in passive PC, a simpler PC spark plug could be used for future investigations, possibly using PC spark plugs with electrodes designed for NRPD ignition. Also, it would be beneficial to study the effects we have reported here for methane using other fuels, as for example for ammonia or methanol. One interesting future research question could be whether using NRPD ignition in a passive PC configuration could substitute pilot injection concepts for hard-to-ignite fuels.

7

Summary and Outlook

7.1 Summary and Conclusions

This thesis investigates a novel ignition system based on NRPD for SI ICE. Four main research areas are identified and discussed: electrical characterization of the NPD, breakdown mechanism under nanosecond overvoltage transients, multiphysics modeling of NPD, and effect of NRPD on ignition and combustion. The main findings are reported below:

A measurement technique based on shunt measurement is developed. This technique allows for simultaneous voltage and current measurement over the load by measuring the current (or voltage) in the middle of the coaxial cable that connects the pulse generator to the spark plug. This "remote configuration", where the measurement is not performed near the HV electrode, allows for monitoring the discharge in practical applications. Under engine-relevant conditions, each time that the energies necessary for ignition (\sim mJ) are delivered, a breakdown followed by the formation of a well-developed spark is always present. In these conditions, after the breakdown, the voltage rapidly drops to low values, and the current rises to values only limited by the active electrical circuit. The electrical measurements outline the importance of the electrode geometry: in spite of the similar breakdown voltage of the first pulse using a J-gap and surface gap spark plugs, the energy deposited to the plasma is consistently higher when surface spark plugs are used; this is thanks to a slower voltage drop rate after the breakdown and a

high breakdown voltage for subsequent pulses.

Due to the fast voltage and current transients present during NPD, even small stray inductances and capacitance of the load have an important impact on the voltage and current that forms and sustains the plasma. A simple equivalent circuit for the load composed of a capacitance of ca. 6 pF in parallel with a 120 nH inductance and a time-varying resistance effectively describes the measured voltages and currents. The ohmic resistance describes the plasma conductivity as a function of the plasma cross-section area, the electron mobility, and the electron number density.

The investigation of the effect of pulse rise rate and pulse duration shows that under pulsed discharge, the breakdown voltage is always above the static breakdown voltage. The probability of pulsed discharge breakdown increases as both the pulse amplitude and duration increase. Furthermore, the breakdown voltage value increases with increasing pulse rise rate. The delay time between reaching the static breakdown voltage and the actual breakdown voltage decreases with increasing overvoltage. The delay time is constituted by statistical and formative times. Both the statistical and formative times decrease with increasing overvoltage. For ignition purposes, the pulse rise rate should be as high as possible to deliver a larger energy input in the breakdown phase.

The electrical breakdown of synthetic air is also experimentally studied in a well-defined quasi-uniform electrode configuration (sphere–plane). The influence of the electrode material and the presence of UV illumination are investigated for both DC and pulsed voltages. The results highlight the important role of seed electron provision for breakdown under short transient voltages. Evidence for a field-assisted emission of seed electrons with a pressure-dependent onset field is found from time lag measurements. An empirical expression is derived based on the Fowler-Nordheim formula to quantify the seed electron generation rate. The expected dependence of the breakdown threshold on the cathode material (work function) was confirmed for breakdown under slowly increasing voltages (Townsend mechanism). Interestingly, a dependence of the breakdown voltage on the cathode material was also found for nanosecond pulsed voltages (dominated by the streamer mechanism). This suggests that the field emission of electrons from the cathode is the dominant source of seed electrons in large cathode electric fields.

The developed multiphysics discharge model incorporates the high-frequency transmission line, a lumped equivalent circuit for the load, a two-temperature model for heavy particles and electrons, and an ionization scheme. The temperature variation is based on the energy conservation equation using the electrical power as a source. The ionization mechanism includes the impact ionization of N_2 and O_2 and two- and three-body attachments on O_2 , and it depends on the applied electric field and gas temperature. The comparison of the simulation results with the experimental data shows that the plasma electrical resistance rapidly drops to low values within approximately 1-2 ns after the breakdown. The drop is explained by the formation of a fully ionized micrometric-sized thermal spark at temperatures above $\sim 30\,000\text{K}$. OES measurements support this conclusion.

The spark kernel and flame expansion are experimentally investigated for different AFR ratios and different initial turbulence levels in the optical PC. The evolution of the flame position in the PC using NRPD shows two different phases. The first one is where the expansion is not affected by the cell condition (AFR, turbulence level and number of pulses), which lasts approximately 1,5 ms. In this first phase, the expansion rate with NRPD is much higher when compared to the inductive ignition system. The second phase is the region where the AFR and turbulence impact the propagation speed. In this region, the influence of NRPD ignition and increased number of pulses is only apparent when the flame speed is low (low AFR and low turbulence) and has the effect of increasing the flame velocity. Higher flame speed in the PC is not always the desired input to ignite the charge in the MC. In fact, for reliable ignition and fast combustion of the charge in the MC, there is an optimum range of flame front propagation speed in the PC for which ideal mixing between the hot jet and the charge in the MC is present.

Knowing whether an ignition event initiated by a series of nanosecond electrical discharges was successful or not gives the possibility of using this information for closed-loop ignition control. A methodology for detecting successful ignition under NRPD ignition is presented. After a nanosecond discharge, the heat loss from the particles (plasma-gas) between the electrodes and the surrounding gas is different if a robust flame kernel is established. If a flame kernel is present, the heat losses are lower, resulting in a lower local density of the gas between the electrodes. The breakdown voltage value of a nanosecond pulse is

proportional to the local density. A control pulse is applied after the main ignition sequence to detect successful ignition. Lower breakdown voltages of the control pulse are present if a robust early flame kernel is present. The control pulse is applied before the pressure rises due to the presence of fast combustion, allowing ignition to be detected during the inflammation phase, thus allowing the possibility to place additional ignition events, if necessary.

Hydrogen combustion in engines usually relies on the Otto cycle. This combustion concept usually results in poor power density and non-ideal efficiencies due to the lean premixed operation and low compression ratio required to avoid preignition and knocking. Alternatively, hydrogen can be directly injected at high pressures into the combustion chamber, and spark ignited at the periphery of the jet, with fuel conversion taking place predominantly in jet-guided (diffusion) mode while injection remains active. The high-pressure jet carries significant momentum and exhibits high velocities that results in challenging conditions for ignition. Jet-guided combustion mode shows similarities with the Diesel combustion process, with a premixed phase of combustion mainly affected by the delay between SOI and ignition and a premixed phase affected by the hydrogen mass flow. Using NRPD ignition, the delay between the spark and ignition is shorter, and the completeness of combustion is higher, highlighting the positive impact of a fast ignition when high turbulence is present. NRPD ignition also results in a lower scatter of the premixed phase (intensity and location) that is expected to be the main driver of cycle-to-cycle variations for this combustion concept.

The spectral analysis of the electromagnetic emission produced by the ignition is correlated to the local AFR for the hydrogen jet-guided experiments. The optical emission produced under NRPD ignition results in much higher spectral intensities when compared to standard automotive ignition systems. Accurate AFR measurement is, in this investigation, only possible using NRPD ignition.

The combination of NRPD ignition and TJI is investigated on a full-engine setup. The aim is to use a technology for a robust early flame phase (NRPD) in combination with a technology for a fast combustion of the bulk charge (TJI). For this purpose, a flexible turbocharged light-duty four-cylinder engine operated with natural gas is used. The used engine can be fitted with a classical OC spark plug or with PCs (active

or passive). In addition, the AFR can be freely controlled, and EGR can be used. Five different combustion strategies are investigated on this setup with NRPD ignition and compared against a state-of-the-art inductive discharge ignition system. The combustion strategies are passive PC with air and EGR dilution, active PC with air dilution, and OC with air and EGR dilution. Despite the faster inflammation present with NRPD ignition, similar peak efficiencies and emissions are reached in OC configuration using the inductive discharge and NRPD ignition systems, which are achieved by varying AFR and EGR rates. Above dilution levels for peak efficiency, the efficiency using NRPD ignition decreases at a slower pace and tolerates higher AFR and EGR rates, thanks to a more complete and shorter combustion. For the PC experiments using NRPD ignition, an efficiency increase and a reduction of emissions compared to inductive discharge ignition are present for the investigated AFR and EGR rates for both active and passive PC operations. The efficiency increase is present due to a stronger PC discharge visible from the HRR and thanks to a faster end phase of combustion. When compared to passive PC, active PC operations offer the advantage of higher dilution tolerance. Active PC operations result in faster and more complete combustion that is overcompensated by the increased wall heat losses, reducing the overall efficiency. The results show that passive PC with NRPD ignition may be an ideal ignition concept that maximizes engine efficiency and minimizes emissions.

Overall NRPD ignition shows benefits for ignition in engines. Under engine-relevant conditions, NPD forms a thermal spark that, thanks to the high-delivered powers and multiple pulses, results in a large flame-plasma kernel that results, when compared to state-of-the-art ignition systems, in a faster and more reproducible plasma to early flame kernel transition. This becomes particularly interesting as novel combustion concepts or novel renewable fuels are applied, as has been shown for the cases of TJI and jet-guided combustion.

7.2 Outlook

In this section, some ideas and inputs for further research and investigations on NRPD are proposed.

- ▶ With NRPD ignition, severe spark plugs erosion is present. The

erosion is probably caused by the high temperatures and the high currents present after the breakdown. There are several possibilities to reduce the current once a highly conductive plasma is formed. One effective way to reduce the discharge currents is to add a resistor on the coaxial cable's shield in the neighborhood of the spark plug. The effect is similar to the one that would be present if a cable with a higher impedance is used. This would result in a limitation of the maximal current. Another more interesting possibility is adding an inductance before the spark plug. If the impedance magnitude is correctly selected, the rise rate of the current will be lower than the pulse duration, reducing the peak current without the disadvantage of dissipating the energy in the resistance. Preliminary experiments and simulations using the OD model are performed that outline that both strategies are feasible. Due to the rather small inductances necessary for the desired outcome (500-1'000 mH), this is probably the simpler strategy since a few loops of the HV wire (air core coil) already give the desired inductance. Appendix C presents some results of the preliminary investigations of the erosion problem.

- ▶ Under NRPD ignition, a high impact of the electrode geometry is present, both in terms of energy deposition as well as ignition and combustion performance. In this investigation, out-of-the-shelf spark plugs are used and only slightly modified. The best performance is reached using cold surface-type spark plugs. In the future, custom-built spark plugs for NRPD ignition could be developed, concentrating on the ideal electrode geometries and maybe the inclusion of some passive components (coil) to reduce the peak current. Since the best ignition concept in the engine experiments is NRPD ignition and passive PC, a PC-spark plugs with electrodes optimized for NRPD could represent an interesting research. Preliminary experiments have outlined that the surface-type spark plugs and J-gap spark plugs with larger gaps degrade at a slower pace when compared to the standard gap size, J-gap spark plugs. The development of custom-build spark plugs could simultaneously improve the NRPD ignition performance and the igniter lifetime.

- ▶ The pulse formed at the generator also has a significant impact on the discharge. However, since most of the nanosecond pulse gen-

erators currently commercially available have rather limited capabilities in pulse shaping, the investigations on NRPD ignition are limited to one pulse shape, and only minor variations are tested, mostly the effect of PRF and sometimes maximal amplitude. An interesting investigation could be on the effect of variation in pulse duration, maximal amplitude, and pulse rise rate.

- ▶ NRPD ignition gives the best results (relative to standard ignition system) in difficult conditions, for example, in OC configuration at very high AFRs NRPD ignition could represent a valuable ignition source for fuels that are even harder to ignite than methane, as for example for ammonia, which is a fuel that is gaining a lot of interest to decarbonize the maritime sector [160].
- ▶ An efficient way to provide multi-point plasma-assisted ignition could also be the nanosecond surface dielectric barrier discharge [161]. For this, a similar setup as the one presented in this thesis can be used. The difference is that the electrodes should be coated with some type of dielectric that hinders the transition from a streamer to a well-developed spark and, therefore, keeps the plasma resistance and, therefore, the applied voltage too high values. With dielectric barrier discharge, all the electrode's cells (fulfilling the breakdown criterion) will break down, and a more diffuse, weakly ionized plasma could be formed. Such a setup could also be interesting for a plasma reactor based on NRPD.
- ▶ Finally, it could be interesting also to evaluate if some of the findings presented for NRPD ignition are transferable to other applications, such as, for example, if the 0D modeling approach could be used to describe the plasma present in a coaxial pulsed spark reactor as the one shown in [99], which is used for methane pyrolysis.

A

Appendix A

This appendix outlines two thermodynamic-based approaches for analyzing combustion in ICE.

Section A.1 outlines a method for pressure trace based thermodynamic analysis of PC combustion. The analysis is published in [26], and is titled "Method for Pressure Trace Based Thermodynamic Analysis of PC Combustion".

Quite often, changes in combustion strategies do not lead to increased brake thermal efficiencies as, for example, wall heat losses increase, unburned fuel increases, or the like. Therefore, an engineer sitting at the test bench is often faced with the problem that an anticipated effect is not visible, but it is hard to understand why. The loss analysis (outlined in Section A.2) is a very powerful tool to understand where the losses occur in engines.

A.1 Pressure Trace Based Thermodynamic Analysis of Pre-Chamber Combustion

Figure A.1 shows the four steps of the pressure-based methodology to analyze ignition and combustion inside the PC.

As a first step, fast and accurate crank angle-based pressure measurements inside the PC and MC are needed to perform the analysis. Usually, high-precision and very dynamic piezoelectric pressure sensors,

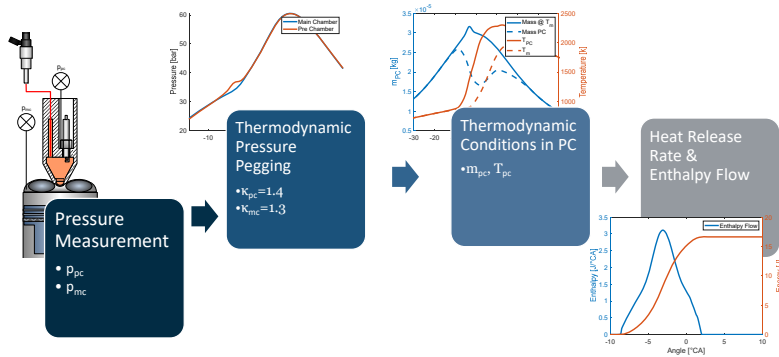


Figure A.1: Scheme of PC combustion process thermodynamic analysis.

which are designed to withstand in-cylinder conditions, are used to monitor the pressures inside the engine's cylinders. Because of the nature of piezoelectric crystals, which deliver electrical charge when the mechanical stress changes, such sensors can measure only pressure changes, and pressure signals must be derived using charge integration devices, so-called charge amplifiers. As is common with integration devices, they have an initial value problem, which leads to the situation that the measured values must be precisely shifted by a correct offset value to represent a precise absolute pressure curve [162]. This process is often called "pegging". Precise pegging is particularly important in the situation reported here, where pressure differences between the PC and the MC are to be determined, which results in subtracting two comparably large numbers.

As a second step, the mass in the PC is determined for the entire process, including the combustion phase where temperatures differ significantly between PC and MC.

As a third step, a reliable and fast methodology to estimate the mass and temperature in the PC is performed. The last step is calculating the interesting PC-related thermodynamic variables, particularly the enthalpy flow between PC and MC and the inside the PC.

A.1.1 Thermodynamic Pegging

A thermodynamic method shifts the pressure measured in the MC and PC. Equation (A.1) shifts the pressures signals by using the pressure and volume measured at two instances during the compression stroke. In this study 100°CA bTDC (index 1) and 65°CA bTDC (index 2) is chosen. The Equation (A.1) assumes that the compression process is a constant polytropic process with exponent κ [162].

$$\Delta p_{\text{pegging}} = \frac{p_{2,\text{unpegged}} - p_{1,\text{unpegged}}}{\left(\frac{V_1}{V_2}\right)^\kappa - 1} - p_{1,\text{unpegged}} \quad (\text{A.1})$$

It is likely that the polytropic coefficients are not equal in the PC and MC since the surface-to-volume ratios, the wall temperatures, and the gas composition (due to residuals and actively fueled PCs) are different. Therefore, different polytropic coefficients must be applied to peg the PC and the MC pressure sensor. These coefficients can be estimated in operation without injection and combustion (motoring operations). Figure A.2 shows the pressure difference between PC and MC, during the compression and expansion stroke in motoring operation at 2'000 rpm and open throttle body. The blue line depicts the pressure difference if the same polytropic coefficient of 1.33 is used for PC and MC pegging. The red line shows the pressure differences when different coefficients (1.33 for the MC and 1.37 for the PC) are used. The polytropic coefficient of 1.37 is chosen because it results in the same mean pressure difference during compression and during expansion.

The pressure difference between MC and PC should be positive during compression (PC filling) and negative during the expansion (PC emptying) with similar magnitudes, as is the case for the red line in Figure A.2. The polytropic coefficients will be different for different engines and can be effectively estimated in motoring operations.

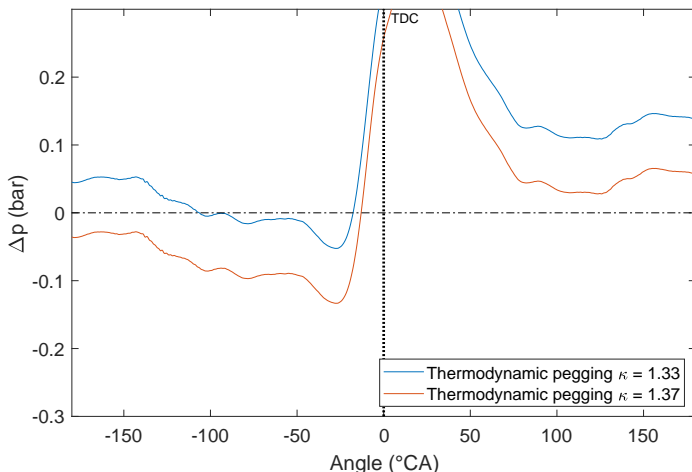


Figure A.2: Pressure difference between PC and MC, motoring curve.

A.1.2 Determining Pre-Chamber Thermodynamic Conditions

Equation (A.2) describes how the initial mass, after fuel injection, inside the PC ($m_{PC,0}$) is computed, under the assumption of equal gas temperatures in the MC and PC. While the volume of the PC (V_{PC}) is constant, the MC volume (V_{MC}) changes as a function of time due to the piston kinematics.

$$m_{PC,0} = m_{tot} \cdot \frac{V_{PC}}{V_{MC}(t)} \cdot \frac{p_{PC}}{p_{MC}} \quad (\text{A.2})$$

Due to the high gas flow of fresh charge flowing from the MC into the PC during compression before ignition and the burned gas flow flowing from the PC into the MC after the EOC, the assumption of equal temperature between the MC and PC should be approximately valid before and after combustion. Due to the flame propagating from the PC in the MC and the reverse flow typically present during combustion inside

the MC, Equation (A.2) is not valid during ignition (flame propagation inside the PC) and MC combustion.

Due to the typical small pressure difference (relative to the pressure magnitude) between the PC and the MC, the mass flow from one chamber to the other can be calculated under the assumption of a subsonic compressible flow through an isenthalpic (frictionless and isentropic) orifice using Equation (A.3) [163].

$$\begin{aligned} \dot{m}(t) = c_d A \sqrt{\frac{p_{in}}{R_{in} T_{in}}} \left(\frac{p_{out}}{p_{in}} \right)^{\frac{1}{\gamma}} \dots \\ \dots \sqrt{2\gamma \left(\frac{\gamma - 1}{\gamma} \right) \left(1 - \left(\frac{p_{out}}{p_{in}} \right)^{\frac{\gamma - 1}{\gamma}} \right)} \end{aligned} \quad (\text{A.3})$$

In Equation (A.3), the subscripts *in* and *out* are consistent with the flow direction; *in* is used for the higher pressure, and *out* is used for the lower pressure. The pressure difference between PC and MC is, in all the investigations, small relative to the pressure magnitude, the subsonic assumption is therefore valid. In Equation (A.3), γ is the isentropic coefficient, which is calculated as the ratio of constant heat capacities as a function of the temperature in the higher-pressure reservoir (Equation (A.4)). The specific heat capacities at constant pressure are calculated using NASA polynomials [107] depending on the gas composition and distinguishing between fresh and burned gas.

$$\gamma = \frac{c_p(T)}{c_v(T)} \quad (\text{A.4})$$

The total area *A* of all the PC nozzles is used in Equation (A.3), and two different discharge coefficients c_d for in- and outflow are iteratively determined. An algorithm based on Equation (A.3) is developed to estimate the time-varying mass in the PC during ignition and combustion. Figure A.3 depicts the flowchart describing the iteration process.

For the proposed method, the inflow and outflow discharge coefficients are iterated until the PC mass calculated using Equation (A.3) before

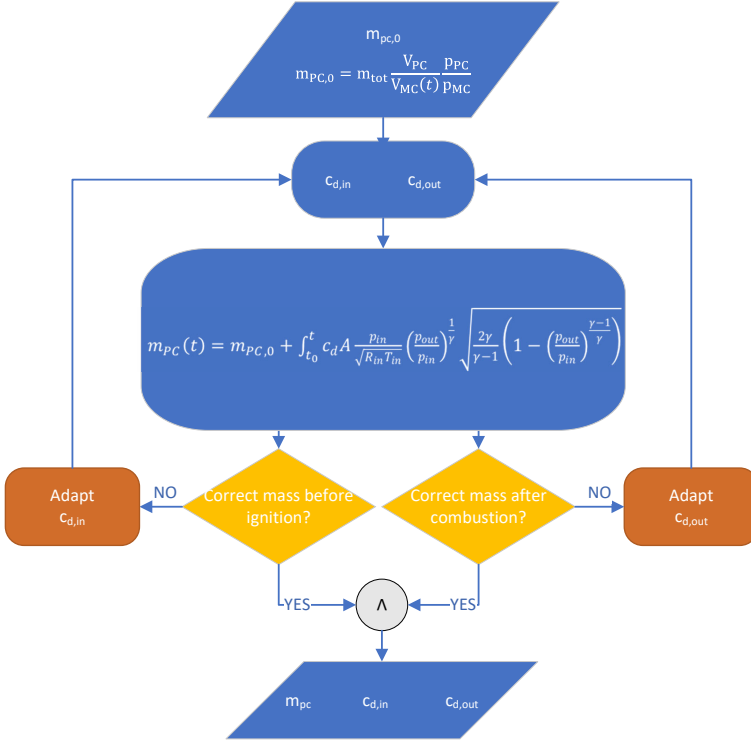


Figure A.3: Pressure difference between PC and MC, motoring curve.

ignition and after EOC closely matches the mass computed using Equation (A.2). The discharge coefficient for the flow entering the PC ($c_{d,in}$) is respectively increased or decreased if the PC mass before ignition is smaller or bigger than $m_{PC,0}$. The discharge coefficient for the flow exiting the PC ($c_{d,out}$) is respectively increased or decreased if the PC mass after EOC is bigger or smaller than $m_{PC,0}$. This algorithm is repeated for each measurement, resulting in different discharge coefficients for different conditions.

Figure A.4 shows on the upper subplot the pressure and the pressure

difference and on the bottom $m_{PC,0}$ and m_{PC} as a function of crank angle during compression and expansion for one exemplary measurement. The different colors highlight the assumption and the algorithm's actions.

- ▶ The green area is where equal temperatures in the PC and MC are assumed, resulting in m_{PC} equal to $m_{PC,0}$.
- ▶ The yellow and the red areas are where the m_{PC} is calculated with Equation (A.3). $m_{PC,0}$ is different then m_{PC} resulting in different temperatures in PC and MC.
- ▶ The yellow area is where the $c_{d,in}$, and $c_{d,out}$ are fitted with the algorithm reported in Figure A.3. $c_{d,in}$ is varied until m_{PC} is practically equal to $m_{PC,0}$ in the first yellow area, between 20 °CA before ignition (SA-20) and ignition (SA). $c_{d,out}$ is varied until m_{PC} is practically equal to $m_{PC,0}$ in the second yellow area, between 20 °CA after the EOC (EOC+20) and 40 °CA after the EOC (EOC+40). After the algorithm minimizes the error in the yellow region $c_{d,in}$, and $c_{d,out}$ are kept constant for the mass calculation in the yellow and red areas. In the yellow areas, since the algorithm minimizes the difference between m_{PC} and $m_{PC,0}$, the gas temperature in the PC is very similar to that in the MC.

Two different discharge coefficients are used to take into account possible geometry difference (different edges), and to make the algorithm stable. The temperature in the PC is calculated using the ideal gas law and the iteratively calculated PC mass.

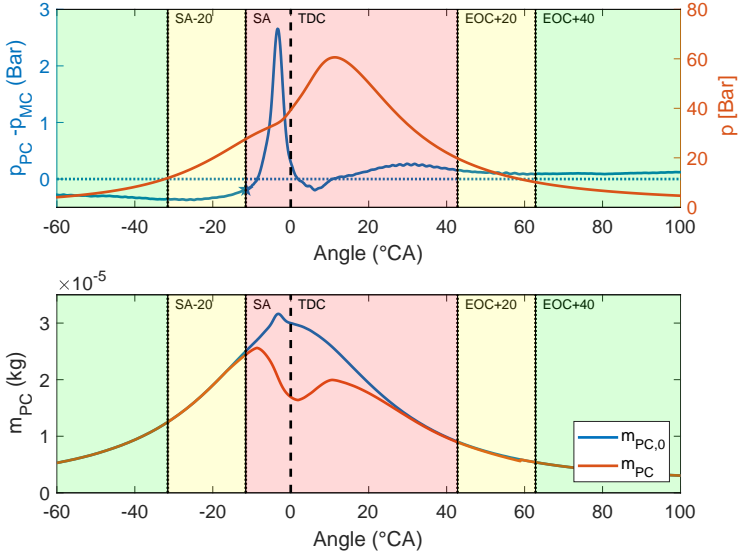


Figure A.4: mass calculation algorithm assumption regions.

A.1.3 Computing Combustion Progresses in Pre-Chamber and Main Chamber

According to the energy conservation, by neglecting the wall heat losses and the kinetic energy flow, the HRR due to combustion inside the PC is calculated according to Equation (A.5) [120].

$$HRR_{PC} = \frac{c_v(T_{PC})}{R} V_{PC} \frac{dp_{PC}}{dt} + c_p(T) \dot{m} T_{PC} \quad (\text{A.5})$$

Where c_v and c_p denote the heat capacities for constant pressure and temperature, R is the gas constant, and the heat capacities are calculated using NASA polynomials depending on the PC temperature and assuming burned gas flowing out and in. The enthalpy flux is calculated according to Equation (A.6).

$$\dot{H}_{PC} = \dot{m}_{noz} c_p(T) T \quad (\text{A.6})$$

The combustion progress inside the MC is discretely calculated according to the Equation (A.7) [156]. c_p depends on the MC temperature and on the progress of combustion.

$$\Delta HRR_{MC|i} = \frac{c_v(T)}{R} V_{MC} \left(p_i - p_{i-1} \cdot \left(\frac{V_{i-1}}{V_i} \right)^{\gamma(T)} \right) \quad (\text{A.7})$$

The HRR calculations in the PC and MC are discretely calculated using the measurement at the current crank angle (subscript i) and the previous angle (subscript i-1) at a 0,1 °CA resolution. A discrete calculation (between i and i-1) is used to compute the pressure derivative of Equation (A.5), also at a 0,1 °CA resolution, assuming a constant engine speed over the entire engine cycle.

A.2 Loss Analysis

According to Pischinger et al., the losses in an ICE can be divided into the following separate parts [153].

- ▶ $\Delta\eta_{IE,rl}$ efficiency decrease due to real charge (i.e. the influence of changing properties of the working fluid; measurement input needed: cylinder pressure, valve timing)
- ▶ $\Delta\eta_{IE,ic}$ efficiency decrease due to incomplete combustion (measurement input needed: unburned hydrocarbons, carbon monoxide)
- ▶ $\Delta\eta_{RC}$ efficiency decrease due to real combustion process (i.e. the effect that combustion is not isochoric as the isochoric process is the ideal process with the highest efficiency, this loss is also strongly influenced by MFB50 phasing)
- ▶ $\Delta\eta_{BB}$ efficiency decrease due to leakages or blowby (measurement input needed: cylinder pressure or blowby massflow)

- ▶ $\Delta\eta_W$ efficiency decrease due to wall heat losses (comparably simple process simulation needed to quantify the work of the high-pressure process without wall heat- and leakage losses – measurement input needed: cylinder pressure)
- ▶ $\Delta\eta_{EX}$ efficiency decrease due to expansion losses (input: valve timings)
- ▶ $\Delta\eta_{LP}$ efficiency decrease due to pumping losses, which could also be an efficiency gain in case of turbocharging with a positive pumping loop (measurement input needed: cylinder pressure)
- ▶ $\Delta\eta_M$ efficiency due to friction losses (measurement input needed: cylinder pressure and brake torque)

The proposed algorithms follow the same process with the only exception of how the inefficiencies of combustion wall heat losses and blow-by are calculated. In fact, Pischinger et al. state that "Wegen der Komplexität der Zusammenhänge ist es nicht möglich, alle Einflüsse getrennt messtechnisch oder rechnerisch exakt zu erfassen. Da sich die einzelnen Verluste gegenseitig beeinflussen, ist neben der Art der Berechnung auch deren Reihenfolge von Bedeutung. Die Erstellung der Verlustanalyse erfolgt mittels wiederholter Prozessrechnung, ..." [153].

The proposed algorithm aims to calculate all the losses in one iteration, but the procedure will not be as precise as an iterative process based on a simulation environment. Nevertheless, the procedure has been tested against an iterative process based on a Simulink model that fits simulated pressure curves against the measured one using the Wiebe function to fit the HRR, the Woschni formula for the wall heat losses, and the orifice equation for the blowby losses. The simulation-based approach often resulted in difficulty in returning plausible data (for example, wall temperatures below 0K, disagreement in the pressure curve at the end of the expansion stroke, or inconsistent losses variation for parameter variation). Therefore, the proposed approach seems to yield much more robust results.

The algorithm uses the HRR calculated on the measured in-cylinder pressure curve (for example, according to Rassweiler and Withrow) to decouple the effect of real combustion from the inefficiency due to wall heat losses. Since the blowby losses are relatively small (usually below

1%), they will be calculated based on the calculated pressure without wall heat losses. This will not reflect the truth completely, but the effect will be minor since the blowby losses are rather small.

The algorithm is presented on an OC point with an air-fuel equivalence ratio (λ) of 1.8 at an engine speed of 1'500 rpm and 100 Nm of torque.

The next section presents the theory and equation needed for the loss analysis. The equations and assumptions are shown in the same order that should be (and are) applied for the loss analysis.

A.2.1 Ideal Engine, Ideal Load

The maximum possible efficiency of the engine is the maximal work theoretically possible by filling the cylinder volume in BDC, performing an isochoric combustion process, and not having any effort for gas exchange. The filling is assumed to occur at the density present in the intake manifold (pressure and temperature) and the desired AFR if port fuel is injected and with pure air if directly injected. The heat addition is calculated with the ideal fuel energy present. Figure A.5 shows the measured pressure-volume diagram for the point under analysis in double logarithmic scale in blue.

The ideal engine cycle depicted with the four red circles in Figure A.5 consists of an isentropic compression, a constant volume heat addition, an isentropic expansion, and a constant volume heat rejection.

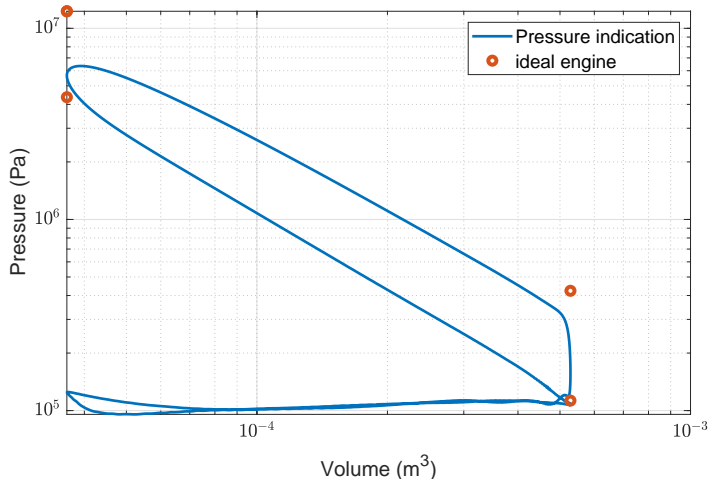


Figure A.5: Ideal engine, ideal load

A.2.2 Ideal Engine Real Load

The only difference with A.2.1 is that the compression starts at Intake Valve Closing (IVC) timing with the real filling. The real filling is calculated as the sum of the fresh gas mass flow (air and fuel) and an estimation of the residual gas present in the cylinder at IVC calculated according to Equation (A.8) [148]. The heat addition is calculated with the real added fuel energy (mass flow measurement).

$$x_{fc} = \frac{V_c + V_d}{V_d} - \left(\frac{p_{em}}{p_{im}} \right)^{1/\gamma_{eg}} \frac{V_c}{V_d} \quad (\text{A.8})$$

A.2.3 Ideal Engine Incomplete Combustion

Same cycle as in A.2.2 the only difference is that incomplete combustion is taken into account. The emissions to consider are different depending on the application. For this investigation, only the methane emissions are considered because they represent the relevant share of losses present due to incomplete combustion in gas engines, mainly when high AFRs

are used.

The incomplete combustion should be considered only for one cylinder and one cycle according to Equation (A.9) where Z is the number of strokes, n_e the engine speed, N_{cyl} is the number of cylinders in the engine, and \dot{m}_i is the considered emission mass flow.

$$Q_{\text{un}} = \frac{1}{N_{\text{cyl}} n_e \frac{2}{Z}} \sum \dot{m}_i LHV_i \quad (\text{A.9})$$

Figure A.6 shows the added fuel energy that is used in sections A.2.1, A.2.2 and A.2.3, namely the ideal added heat ($Q_{\text{F,id}}$), the measured added heat (Q_{F}), and the added heat accounting for incomplete combustion ($Q_{\text{F,un}}$).

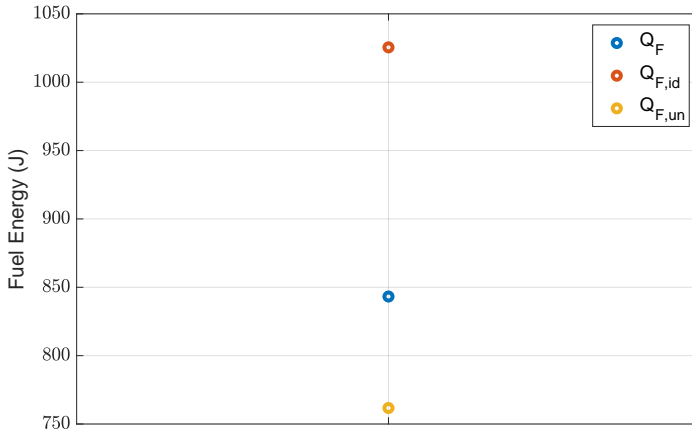


Figure A.6: Added fuel heat.

The ideal engine (W_{ie}) work and efficiency (η) are calculated according to Equation (A.10).

$$\begin{aligned}
 W_{ie} &= m \cdot (q_{in} - q_{out}) \\
 \eta_{IE} &= \frac{W_{IE}}{Q_F}
 \end{aligned}
 \tag{A.10}$$

A.2.4 Real Combustion

The loss due to real combustion is calculated by taking into account the calculated HRR shape. Multiple constant volume heat addition and isentropic compressions are calculated from the Start of Combustion (SOC) to the EOC. Table A.1 reports the algorithm to calculate the real combustion pressure without the effect of wall heat losses and blowby ($p_{r,c}$).

Table A.1: Algorithm: real combustion pressure calculation.

Process	Equation
Heat capacity ratio:	$\gamma_i = \frac{c_p(T_i)}{c_v(T_i)}$
Isentropic compression:	$p_{s,i+1} = p_{c,i} \left(\frac{V_i}{V_{i+1}} \right)^\gamma$ $T_{s,i+1} = T_i \left(\frac{V_i}{V_{i+1}} \right)^{\gamma-1}$
Share of fuel converted:	$x_i = \frac{HRR_i}{\int_{SOC}^{EOC} HRR_i}$
Isochoric heat addition:	$T_{c,i+1} = \frac{x_i Q_B}{c_v(T_i)} + T_{s,i+1} = T_{i+1}$
Combustion pressure:	$p_{c,i+1} = p_{s,i+1} \cdot \frac{T_{c,i+1}}{T_{s,i+1}}$

Figure A.7 shows the pressure-volume diagram in double logarithmic scale of the real combustion effect. The ideal cycle with the effective fuel burned is depicted in yellow, the measured pressure trace is depicted in blue, while the pressure with real combustion but without the effect of blowby and wall-heat losses is depicted in red.

The real combustion work and inefficiency are calculated according to Equation (A.11).

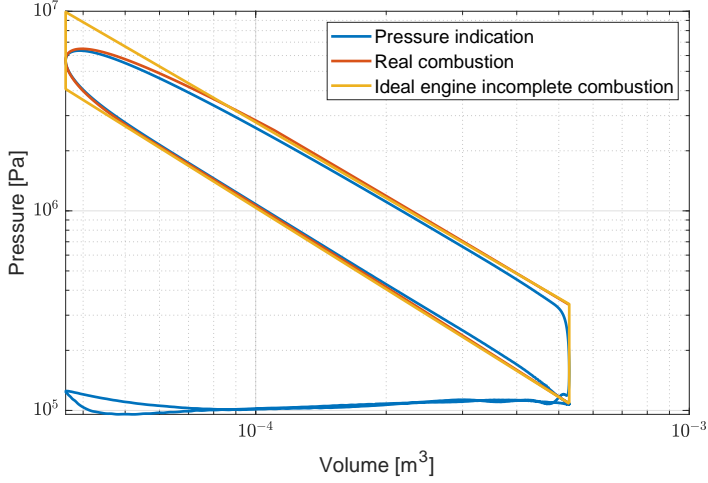


Figure A.7: Real combustion effects.

$$\begin{aligned}
 W_{\text{RC}} &= \int_{\text{BDC}}^{\text{BDC}} p_c dV \\
 \Delta\eta_{\text{RC}} &= \frac{W_{\text{IE,ic}} - W_{\text{RC}}}{Q_{\text{F}}}
 \end{aligned} \tag{A.11}$$

A.2.5 Blowby Losses

The losses due to blowby are calculated based on the real combustion pressure (p_c) red curve in Figure A.7. The mass flow losses (\dot{m}_{BB}) are computed using the orifice equation, and the in-cylinder pressure accounting for the blowby losses is calculated using the ideal gas law (Equation (A.12)).

$$\begin{aligned}
\dot{m}_{BB} &= \mu A \sqrt{\frac{p_c^2 - p_{cc}^2}{p_c v_c}} \\
m_{BB} &= m_{IVC} - \int_{BDC}^{TDC} \dot{m}_{BB} \\
p_{BB} &= p_c = \frac{m_{BB}}{m_{IVC}} \\
W_{BB} &= \int_{BDC}^{BDC} p_{BB} dV \\
\Delta\eta_{BB} &= \frac{W_{rc} - W_{BB}}{Q_f}
\end{aligned} \tag{A.12}$$

Where A is the orifice area, p_{cc} is the pressure in the crankcase, μ is the contraction coefficient, and v_c is the specific cylinder volume.

A.2.6 High and Low-Pressure Loop

Since the proposed approach is non-iterative, to correctly characterize the wall heat losses, the high-pressure and low-pressure loops need to be detected. Figure A.8 shows the measured high-pressure (HP) and low-pressure (LP) areas in a double logarithmic pressure-volume diagram in red and blue, respectively.

After EVO, the pressure at a given cylinder volume drops below the pressure during compression for the same volume (green circle in Figure A.8). This point (idx_{lp}) divides between the HP and LP loop. The work can be calculated according to Equation (A.13).

$$\begin{aligned}
W_{LP} &= \int_{idx_{lp}}^{idx_{lp}+360^\circ CA} p dV \\
W_{HP} &= \int_{idx_{lp}+360^\circ CA}^{idx_{lp}} p dV \\
W_i &= \int p dV
\end{aligned} \tag{A.13}$$

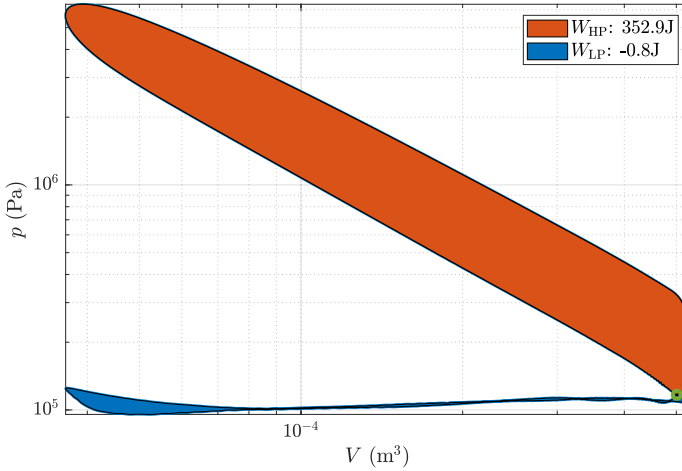


Figure A.8: High and low-pressure loop.

A.2.7 Expansion Losses

The losses due to expansion are usually small but can be relevant in some applications and, if not accounted for, with this approach, will be included in the wall heat losses. Figure A.9 shows the exhaust work losses in blue.

These losses are calculated between EVO and idx_{lp} as the difference between the pressure that would be present if no gas exchange were present (isentropic expansion from EVO to BDC and measured compression pressure) and the measured pressure during the exhaust stroke according to Equation (A.14).

$$W_{\text{ex},l} = \int_{\text{EVO}}^{idx_{lp}} p_{\text{ideal}} - p_{\text{meas}} dV \quad (\text{A.14})$$

$$\Delta\eta_{\text{EX}} = \frac{W_{\text{ex},l}}{Q_{\text{F}}}$$

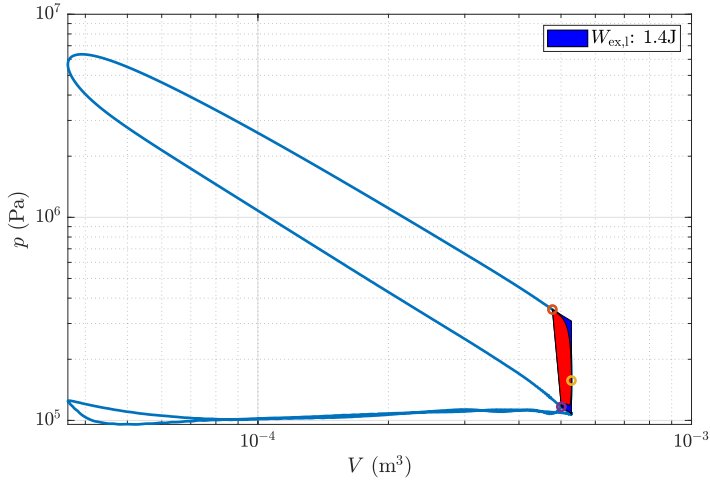


Figure A.9: Expansion losses.

A.2.8 Wall Heat Losses (the Rest)

The last relevant losses (based on the pressure indication) are the wall heat losses (W_w). They are therefore calculated as the difference between the work performed under the effect of the blowby the expansion losses and the measured HP work according to Equation (A.15).

$$\begin{aligned}
 W_W &= W_{BB} - W_{ex,l} - W_{HP} \\
 \Delta\eta_W &= \frac{W_W}{Q_F}
 \end{aligned}
 \tag{A.15}$$

A.2.9 Friction Losses

The mechanical losses are calculated according to Equation (A.16), where τ is the engine's torque and n the engine's speed.

$$\Delta\eta_M = \frac{W_i - W_M}{Q_F} \quad (\text{A.16})$$

$$W_M = n\tau$$

A.2.10 Exemplary Result

Figure A.10 shows the overall loss analysis results for the investigated point.

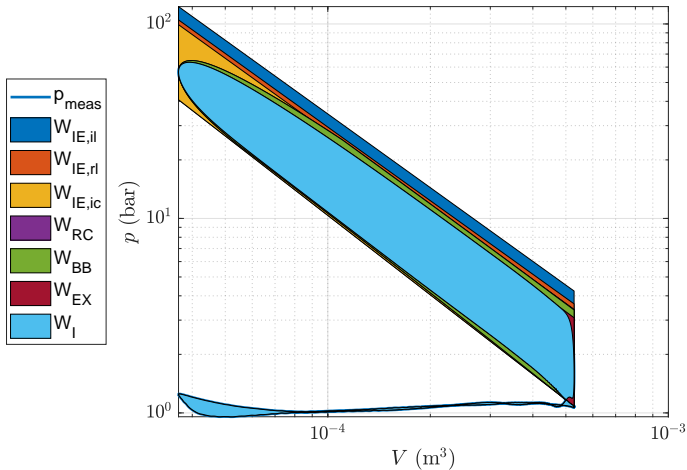


Figure A.10: Loss analysis visualization (pressure-volume diagram).

In Figure A.10, the pressure-volume traces for the works are depicted. The parallelogram shape of the larger areas outlines the ideal engine cycle that is performed with the ideal (blue) and real (red) load and the effect of incomplete combustion (yellow). Since the Blowby losses are small, the real combustion pressure trace and blowby seem superimposed (violet). At the start of the exhaust stroke, the expansion losses are visible in burgundy.

B

Appendix B

B.1 Optical Emission Spectroscopy

Figure B.1 shows the post-processing routine adopted for the SIBS analysis. The example reported is the same one as the one discussed in Section 5.2.2 for the discharge model validation.

The first subplot in Figure B.1 shows the acquired spectral image from the CCD camera. The lens setup allows for acquiring one-dimensional spectra across the electrode gap in the first subplot; the region between the electrodes where light is emitted is, therefore, recognizable. The second subplot shows the second step of the analysis that consists of the vertical average of the spectral image (full blue line), a baseline subtraction (dashed blue line), and the Optical Transfer Function (OTF) (red line) to account for how efficiently the different wavelengths are captured. The third subplot shows the post-processed spectrum where the baseline is subtracted; the spectrum is multiplied with the OTF, and normalized with the maximal intensity.

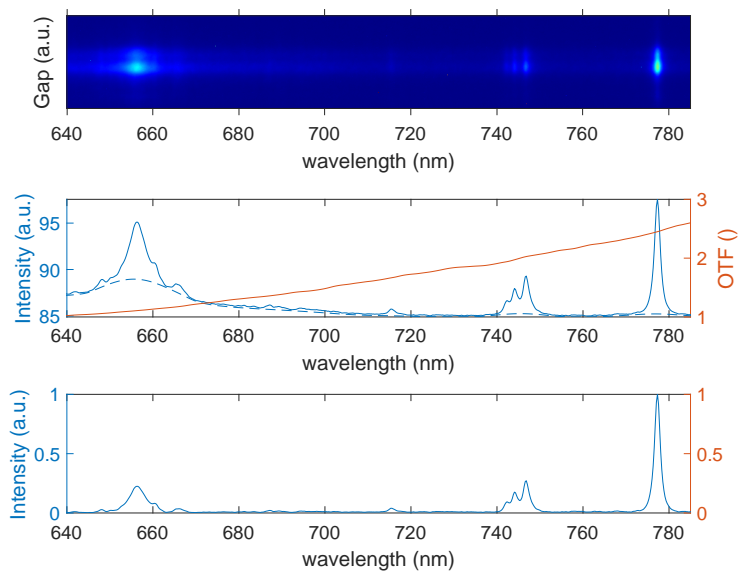
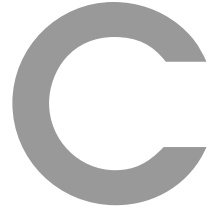


Figure B.1: OES processing, raw image, baseline and OTF, corrected spectrum



Appendix C

This appendix outlines the preliminary investigation into the problem of the erosion of the spark plugs' electrodes under NRPD ignition.

In the ignition cell, the wear in air at engine-relevant pressures with four different spark plugs are tested. The ignition is performed with a burst of 50 pulses at 50 kHz PRF. The time between bursts is 100 ms, which corresponds to a 4-stroke engine running at 1'200 rpm. The wear is addressed using measurements performed with a microscope before and after the experiments. The used spark plugs are a J-gap spark plug (NGK c9E) with two different initial gap sizes of 0.7 (referred to as SP1) and 1 mm (referred to as SP2), and the surface discharge spark plug used for the engine experiments (Champion G54V, referred to as SP3).

Figure C.1 shows SP1 before the experiments

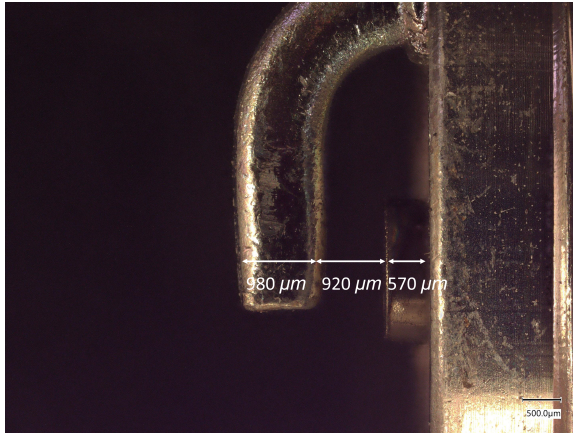


Figure C.1: SP1 before the wear experiment.

The diameter of the center electrode is $\approx 1'900 \mu\text{m}$ and its height is $\approx 570 \mu\text{m}$. The gap is $\approx 920 \mu\text{m}$ and the thickness of the ground electrode is $\approx 980 \mu\text{m}$.

Figure C.2 shows SP1 after the wear test (2 hours at ≈ 10 bar and 1'200 rpm in air).



Figure C.2: SP1 after the wear experiment.

The diameter of the center electrode is $\approx 1'870 \mu\text{m}$ and its height is $\approx 470 \mu\text{m}$. The gap is $\approx 1'100 \mu\text{m}$, and the thickness of the ground electrode is $\approx 930 \mu\text{m}$. After the test, both the center electrode and the ground electrode diminished in size, with the gap growing the most by about $300 \mu\text{m}$.

Figure C.3 shows SP1 after the same wear experiment; in this experiment, a passive coil limiting the peak current is added before the spark plug, the coil has an inductance of 470 nH .



Figure C.3: SP1 with a passive coil after the wear experiment

The diameter of the center electrode is $\approx 1'900 \mu\text{m}$ and its height is $\approx 360 \mu\text{m}$. The gap is $\approx 1'000 \mu\text{m}$, and the thickness of the ground electrode is $\approx 1'000 \mu\text{m}$. After the test, both electrodes diminish in size, but here, the center electrode diameter does not change. The gap for the spark plug with the passive coil increased by about a third less than the gap without the passive coil.

Figure C.4 shows SP2 before the wear experiment.

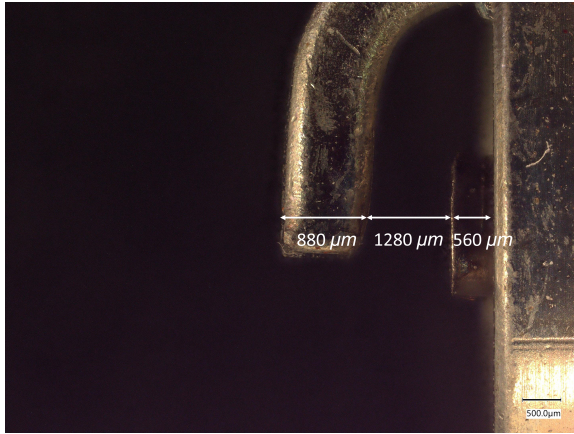


Figure C.4: SP2 before the wear experiment

The diameter of the center electrode is $\approx 1'900 \mu\text{m}$ and it's height is $\approx 560 \mu\text{m}$. The gap is $\approx 1'280 \mu\text{m}$, and the thickness of the ground electrode is $\approx 880 \mu\text{m}$. Figure C.5 shows SP2 after the wear test.



Figure C.5: SP2 after the wear experiment

After 2 hours at $\approx 10 \text{ bar}$ and $1'200 \text{ rpm}$ in air, the diameter of the

center electrode is $\approx 1'900 \mu\text{m}$, and its height $\approx 450 \mu\text{m}$. The gap is $\approx 1'320 \mu\text{m}$ and the thickness of the ground electrode is $\approx 980 \mu\text{m}$

Figure C.6 shows SP3 before the war test.

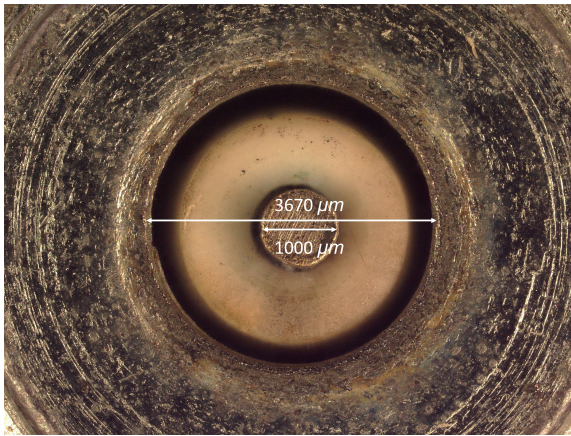


Figure C.6: SP3 before the wear experiment.

The center electrode diameter is $\approx 1'000 \mu\text{m}$, and the inside diameter of the ground electrode is $\approx 3'670 \mu\text{m}$.

Figure C.7 shows SP3 after the wear test.

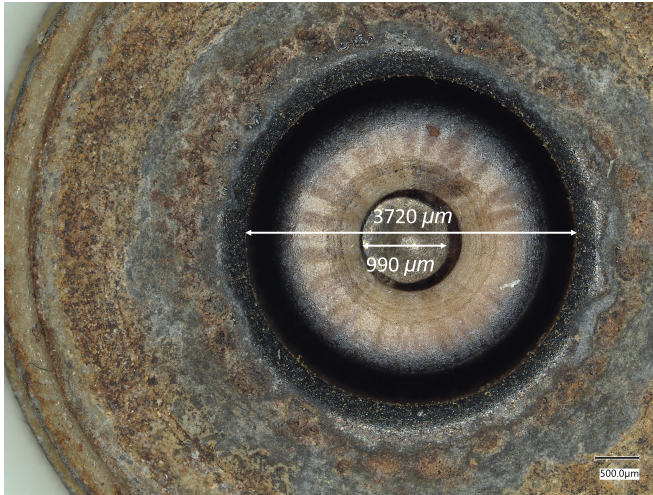


Figure C.7: SP3 after the wear experiment.

After 2 hours at ≈ 10 bar and 1'200 rpm in the air, the diameter of the center electrode is $\approx 990 \mu\text{m}$, and the inside diameter of the ground electrode is $\approx 3'720 \mu\text{m}$. The center electrode does not change in size, but the inner diameter of the ground electrode slightly increases in size.

Overall, the surface gap spark plug shows the least amount of wear. This might be due to the fact that it erodes away material more efficiently as it always arcs to the closest part of the ground electrode and thus has more material available. It is also the coldest spark plug that was tested, which means it can conduct more heat out of the spark plug tip. It also has a center electrode with a copper core, which is also a better conductor than sole nickel. Both factors can contribute to SP3 experiencing less wear. If we compare the different scenarios that were tested with the NGK C9E spark plug, we can observe that both the passive coil and the wider gap reduce the wear during the two-hour the gap size increases by ca. $180 \mu\text{m}$ with the smallest gap which is reduced to $100 \mu\text{m}$ using the passive coil and to $40 \mu\text{m}$ for the wider gap.

Bibliography

- [1] R. D. Reitz, H. Ogawa, R. Payri, T. Fansler, S. Kokjohn, Y. Moriyoshi, A. Agarwal, D. Arcoumanis, D. Assanis, C. Bae, K. Boulouchos, M. Canakci, S. Curran, I. Denbratt, M. Gavaises, M. Guenther, C. Hasse, Z. Huang, T. Ishiyama, B. Johansson, T. Johnson, G. Kalghatgi, M. Koike, S. Kong, A. Leipertz, P. Miles, R. Novella, A. Onorati, M. Richter, S. Shuai, D. Siebers, W. Su, M. Trujillo, N. Uchida, B. M. Vaglieco, R. Wagner, and H. Zhao, "IJER editorial: The future of the internal combustion engine," *International Journal of Engine Research*, vol. 21, no. 1, pp. 3–10, Jan. 2020.
- [2] T. Kammermann, G. Giannakopoulos, J. Koch, P. Soltic, and K. Boulouchos, "Early flame propagation of hydrogen enriched methane-air mixtures at quasi laminar conditions in a rapid compression expansion machine," *International Journal of Hydrogen Energy*, vol. 44, no. 49, pp. 27 107–27 122, Oct. 2019.
- [3] J. C. Hilliard and G. S. Springer, Eds., *Fuel Economy*. Boston, MA: Springer US, 1984.
- [4] F. Soldera, F. Mucklich, K. Hrastnik, and T. Kaiser, "Description of the Discharge Process in Spark Plugs and its Correlation With the Electrode Erosion Patterns," *IEEE Transactions on Vehicular Technology*, vol. 53, no. 4, pp. 1257–1265, Jul. 2004.
- [5] R. Maly, "Ignition model for spark discharges and the early phase of flame front growth," *Symposium (International) on Combustion*, vol. 18, no. 1, pp. 1747–1754, 1981.
- [6] S. Pancheshnyi, D. Lacoste, A. Bourdon, and C. Laux, "Ignition of Propane-Air Mixtures by a Sequence of Nanosecond Pulses," in *37th AIAA Plasmadynamics and Lasers Conference*. San Francisco, California: American Institute of Aeronautics and Astronautics, Jun. 2006.
- [7] G. Xu, C. Hanauer, Y. M. Wright, and K. Boulouchos, "CFD-Simulation of Ignition and Combustion in Lean Burn Gas Engines," *SAE Technical Paper Series*, vol. 1, no. Li, 2016.

- [8] J. Zhai, S.-Y. Lee, Z. Zhao, and D. Singleton, "Study of Flame Kernel Development at High EGR and High Flow Speed Using Conventional Spark Igniter and Non-Thermal Plasma Under Gasoline Engine Relevant Conditions," *Combustion Science and Technology*, pp. 1–21, Oct. 2022.
- [9] M. Scapinello, L. M. Martini, G. Dilecce, and P. Tosi, "Conversion of CH_4/CO_2 by a nanosecond repetitively pulsed discharge," *Journal of Physics D: Applied Physics*, vol. 49, no. 7, p. 075602, Jan 2016.
- [10] E. Delikonstantis, M. Scapinello, and G. Stefanidis, "Low energy cost conversion of methane to ethylene in a hybrid plasma-catalytic reactor system," *FUEL PROCESSING TECHNOLOGY*, vol. 176, pp. 33–42, 2018.
- [11] S. V. Korotkov, Y. V. Aristov, A. K. Kozlov, D. A. Korotkov, A. G. Lyublinsky, and G. L. Spichkin, "Installation for air cleaning from organic impurities by plasma formed by barrier discharge of nanosecond duration," *Instruments and Experimental Techniques*, vol. 55, no. 5, pp. 605–607, Sep. 2012.
- [12] D. Z. Pai, D. A. Lacoste, and C. O. Laux, "Transitions between corona, glow, and spark regimes of nanosecond repetitively pulsed discharges in air at atmospheric pressure," *Journal of Applied Physics*, vol. 107, no. 9, p. 093303, May 2010.
- [13] N. Minesi, P. Mariotto, E. Pannier, A. Vincent-Randonnier, G. D. Stancu, and C. O. Laux, "Kinetic mechanism and sub-ns measurements of the thermal spark in air," *Plasma Sources Science and Technology*, vol. 32, no. 4, p. 044005, Apr. 2023.
- [14] D. L. Rusterholtz, D. A. Lacoste, G. D. Stancu, D. Z. Pai, and C. O. Laux, "Ultrafast heating and oxygen dissociation in atmospheric pressure air by nanosecond repetitively pulsed discharges," *Journal of Physics D: Applied Physics*, vol. 46, no. 46, p. 464010, Nov. 2013.
- [15] S. A. Shcherbaney, T. Krzymuski, Y. Xiong, and N. Noiray, "Jetting axial flow induced by nanosecond repetitively pulsed discharges in quiescent ambient air," *Journal of Physics D: Applied Physics*, vol. 55, no. 38, p. 385202, Sep. 2022.

-
- [16] C. D. Cathey, T. Tang, T. Shiraishi, T. Urushihara, A. Kuthi, and M. A. Gundersen, "Nanosecond Plasma Ignition for Improved Performance of an Internal Combustion Engine," *IEEE Transactions on Plasma Science*, vol. 35, no. 6, pp. 1664–1668, Dec. 2007.
- [17] A. Tropina, L. Lenarduzzi, S. Marasov, and A. Kuzmenko, "Comparative Analysis of Engine Ignition Systems," *IEEE Transactions on Plasma Science*, vol. 37, no. 12, pp. 2286–2292, Dec. 2009.
- [18] S. A. Shcherbanev, Q. Malé, B. Dharmaputra, R. Solana-Pérez, and N. Noiray, "Effect of plasma-flow coupling on the ignition enhancement with non-equilibrium plasma in a sequential combustor," *Journal of Physics D: Applied Physics*, vol. 55, no. 42, p. 425202, Oct. 2022.
- [19] A. A. Tropina, A. P. Kuzmenko, S. V. Marasov, and D. V. Vilchinsky, "Ignition System Based on the Nanosecond Pulsed Discharge," *IEEE Transactions on Plasma Science*, vol. 42, no. 12, pp. 3881–3885, Dec. 2014.
- [20] M. Balmelli, R. Farber, L. Merotto, P. Soltic, D. Bleiner, C. M. Franck, and J. Biela, "Experimental Analysis of Breakdown With Nanosecond Pulses for Spark-Ignition Engines," *IEEE Access*, vol. 9, pp. 100 050–100 062, 2021.
- [21] M. Balmelli, Y. Lu, R. Farber, L. Merotto, P. Soltic, D. Bleiner, J. Biela, and C. M. Franck, "Breakdown of Synthetic Air Under Nanosecond Pulsed Voltages in Quasi-Uniform Electric Fields," *IEEE Access*, vol. 10, pp. 53 454–53 467, 2022.
- [22] M. Balmelli, L. Merotto, P. Soltic, and J. Biela, "Ignition detection with the breakdown voltage measurement during nanosecond repetitively pulsed discharges," *Energy Conversion and Management*, vol. 292, p. 117382, Sep. 2023.
- [23] M. Balmelli, L. Merotto, Y. Wright, D. Bleiner, J. Biela, and P. Soltic, "Optical and thermodynamic investigation of jet-guided spark ignited hydrogen combustion," *International Journal of Hydrogen Energy*, vol. 78, pp. 1316–1331, 2024.
- [24] M. Balmelli, R. Farber, P. Soltic, D. Bleiner, C. M. Franck, and

- J. Biela, “Zero-dimensional modeling of a nanosecond pulsed discharge,” *In final preparation for submission*.
- [25] M. Balmelli, T. Hilfiker, J. Biela, and P. Soltic, “Effects of using Nanosecond Repetitively Pulsed Discharge and Turbulent Jet Ignition on Internal Combustion Engine Performance,” *Energy Conversion and Management*, 2024.
- [26] M. Balmelli, D. Rogers, T. Hilfiker, Y. Wright, and P. Soltic, “Method for pressure trace based thermodynamic analysis of pre-chamber combustion,” *Energy Conversion and Management*, vol. 312, p. 118561, 2024.
- [27] L. Merotto, M. Balmelli, W. Vera-Tudela, and P. Soltic, “Comparison of ignition and early flame propagation in methane/air mixtures using nanosecond repetitively pulsed discharge and inductive ignition in a pre-chamber setup under engine relevant conditions,” *Combustion and Flame*, vol. 237, p. 111851, Mar. 2022.
- [28] W. Vera-Tudela, L. Merotto, M. Balmelli, and P. Soltic, “Experimental study of the ignition of lean methane/air mixtures using inductive and NRPD ignition systems in the pre-chamber and turbulent jet ignition in the main chamber,” *Energy Conversion and Management*, p. 115012, Dec. 2021.
- [29] R. Färber, Y. Lu, M. Balmelli, O. Seffl, and C. M. Franck, “Static breakdown threshold modeling of quasi-uniform gas gaps with a focus on the PDIV of contacting enameled wire pairs,” *Journal of Physics D: Applied Physics*, vol. 56, no. 43, p. 435204, Oct. 2023.
- [30] R. Färber, Y. Lu, M. Balmelli, O. Seffl, and C. M. Franck, “Dynamic electric breakdown modeling of quasi-uniform, dielectric-bounded gas gaps,” ETHZ, Tech. Rep., 2024.
- [31] *International Conference on Ignition Systems for Gasoline Engines – International Conference on Knocking in Gasoline Engines*. expert verlag, 2022.
- [32] J. B. Heywood, *Internal combustion engine fundamentals*, ser. McGraw-Hill series in mechanical engineering. New York: McGraw-Hill, 1988.

- [33] A. Küchler, *High Voltage Engineering*. Berlin, Heidelberg: Springer Berlin Heidelberg, 2018.
- [34] T. Kammermann, W. Kreutner, M. Trottmann, L. Merotto, P. Soltic, and D. Bleiner, “Spark-induced breakdown spectroscopy of methane/air and hydrogen-enriched methane/air mixtures at engine relevant conditions,” *Spectrochimica Acta Part B: Atomic Spectroscopy*, vol. 148, pp. 152–164, Oct. 2018.
- [35] W. Vera-Tudela, C. Barro, and K. Boulouchos, “Investigations on spark pre-chamber ignition and subsequent turbulent jet main chamber ignition in a novel optically accessible test rig,” *International Journal of Engine Research*, vol. 23, no. 9, p. 146808742110198, May 2021.
- [36] U. Gerke, “Numerical analysis of mixture formation and combustion in a hydrogen direct-injection internal combustion engine,” Ph.D. dissertation, ETH Zurich, 2007, artwork Size: 1 Band Medium: application/pdf Pages: 1 Band.
- [37] S. Schlatter, B. Schneider, Y. M. Wright, and K. Boulouchos, “Comparative study of ignition systems for lean burn gas engines in an optically accessible rapid compression expansion machine,” *SAE International*, pp. 2013–24–0112, Sep. 2013.
- [38] D. A. Mitakos, “Experimental Investigations for Phenomenological Modelling of Two-Stage Auto-Ignition under HCCI Conditions,” Ph.D. dissertation, ETH Zurich, 2014, artwork Size: 1 Band Medium: application/pdf Pages: 1 Band.
- [39] G. Woschni, “A universally applicable equation for the instantaneous heat transfer coefficient in the internal combustion engine,” *SAE Technical Paper 670931*, p. 19, Feb. 1967.
- [40] M. Bargende, “Equations for calculating the non-steady state wall heat losses in the high pressure part of petrol engines; ein gleichungsansatz zur berechnung der instationaeren wandwaermeverluste im hochdruckteil von ottomotoren,” May 1991.
- [41] O. P, “WEG, Rechenprogramm zur Berechnung des Wärmeentwicklungs-gesetzes aus gemessenen Brennraum-druckverläufen von Diesel- und Ottomotoren, Benutzerhandbuch

- und Programmdokumentation,” ETHZ IET-LAV, Zürich, Tech. Rep., Sep. 2005.
- [42] T. Kammermann, L. Merotto, D. Bleiner, and P. Soltic, “Spark-induced breakdown spectroscopy for fuel-air equivalence ratio measurements at internal combustion engine-relevant conditions,” *Spectrochimica Acta Part B: Atomic Spectroscopy*, vol. 155, pp. 79–89, May 2019.
- [43] P. Soltic, T. Hilfiker, R. Hutter, and S. Hänggi, “Experimental comparison of efficiency and emission levels of four-cylinder lean-burn passenger car-sized CNG engines with different ignition concepts,” *Combustion Engines*, vol. 176, no. 1, pp. 27–35, Feb. 2019.
- [44] P. Soltic and T. Hilfiker, “Efficiency and raw emission benefits from hydrogen addition to methane in a Prechamber-Equipped engine,” *International Journal of Hydrogen Energy*, vol. 45, no. 43, pp. 23 638–23 652, Sep. 2020.
- [45] A. G. Lyublinsky, A. F. Kardo-Sysoev, M. N. Cherenev, and M. I. Vexler, “Influence of DSRD Operation Cycle on the Output Pulse Parameters,” *IEEE Transactions on Power Electronics*, vol. 37, no. 6, pp. 6271–6274, Jun. 2022.
- [46] A. G. Lyublinsky, S. V. Korotkov, Y. V. Aristov, and D. A. Korotkov, “Pulse Power Nanosecond-Range DSRD-Based Generators for Electric Discharge Technologies,” *IEEE Transactions on Plasma Science*, vol. 41, no. 10, pp. 2625–2629, Oct. 2013.
- [47] I. Grekhov, A. Kardo-Sysoev, L. Kostina, and S. Shenderey, “High power subnanosecond switch,” in *1980 International Electron Devices Meeting*. IRE, 1980, pp. 662–663.
- [48] T. Juntasorn, P. Chancharoensook, and N. Pattanadech, “Partial Discharge Pulse Propagation in Coaxial Cable,” in *2022 8th International Conference on Engineering, Applied Sciences, and Technology (ICEAST)*. Chiang Mai, Thailand: IEEE, Jun. 2022, pp. 1–5.
- [49] F. Tholin, D. A. Lacoste, and A. Bourdon, “Influence of fast-heating processes and O atom production by a nanosecond spark

- discharge on the ignition of a lean –air premixed flame,” *Combustion and Flame*, vol. 161, no. 5, pp. 1235–1246, May 2014.
- [50] A. A. Dougal and L. Goldstein, “Energy Exchange between Electron and Ion Gases through Coulomb Collisions in Plasmas,” *Physical Review*, vol. 109, no. 3, pp. 615–624, Feb. 1958.
- [51] G. J. M. Hagelaar and L. C. Pitchford, “Solving the Boltzmann equation to obtain electron transport coefficients and rate coefficients for fluid models,” *Plasma Sources Science and Technology*, vol. 14, no. 4, pp. 722–733, Nov. 2005.
- [52] “SIGLO database, <http://www.lxcat.laplace.univ-tlse.fr>, retrieved June 4, 2013.”
- [53] “PHELPS database, <http://www.lxcat.laplace.univ-tlse.fr>, retrieved June 4, 2013.”
- [54] “MORGAN database, <http://www.lxcat.laplace.univ-tlse.fr>, retrieved June 4, 2013.”
- [55] M. Cernak, E. M. v. Veldhuizen, I. Morva, and W. R. Rutgers, “Effect of cathode surface properties on glow-to-arc transition in a short positive corona gap in ambient air,” *Journal of Physics D: Applied Physics*, vol. 28, no. 6, pp. 1126–1132, Jun. 1995.
- [56] R. Maly and M. Vogel, “Initiation and propagation of flame fronts in lean CH₄-air mixtures by the three modes of the ignition spark,” *Symposium (International) on Combustion*, vol. 17, no. 1, pp. 821–831, Jan. 1979.
- [57] M. Istenic, I. Smith, and B. Novac, “Dynamic Resistance Calculation of Nanosecond Spark-Gaps,” in *2005 IEEE Pulsed Power Conference*. Monterey, CA, USA: IEEE, Jun. 2005, pp. 608–611.
- [58] T. P. Sorensen and V. M. Ristic, “Rise time and time-dependent spark-gap resistance in nitrogen and helium,” *Journal of Applied Physics*, vol. 48, no. 1, pp. 114–117, Jan. 1977.
- [59] Y. P. Raizer, *Gas discharge physics*, 1st ed. Berlin: Springer Berlin, Heidelberg, 1997.
- [60] D. Lee, “Hydrogen production via the Kværner process and

- plasma reforming,” in *Compendium of Hydrogen Energy*. Elsevier, 2015, pp. 349–391.
- [61] W. Eckstein, “Sputtering Yields,” in *Sputtering by Particle Bombardment*. Berlin, Heidelberg: Springer Berlin Heidelberg, 2007, vol. 110, pp. 33–187, series Title: Topics in Applied Physics.
- [62] R. Färber, T. Guillod, F. Krismer, J. Kolar, and C. Franck, “Endurance of Polymeric Insulation Foil Exposed to DC-Biased Medium-Frequency Rectangular Pulse Voltage Stress,” *Energies*, vol. 13, no. 1, p. 13, Dec. 2019.
- [63] S. Kobayashi, Z. Bonaventura, F. Tholin, N. A. Popov, and A. Bourdon, “Study of nanosecond discharges in H₂–air mixtures at atmospheric pressure for plasma assisted combustion applications,” *Plasma Sources Science and Technology*, vol. 26, no. 7, p. 075004, Jun. 2017.
- [64] N. Hayakawa, F. Shimizu, and H. Okubo, “Estimation of partial discharge inception voltage of magnet wires under inverter surge voltage by volume-time theory,” *IEEE Transactions on Dielectrics and Electrical Insulation*, vol. 19, no. 2, pp. 550–557, Apr. 2012.
- [65] X. Xu, S. Jayaram, and S. A. Boggs, “Prediction of breakdown in SF₆/sub 6/ under impulse conditions,” *IEEE Transactions on Dielectrics and Electrical Insulation*, vol. 3, no. 6, pp. 836–842, Dec. 1996.
- [66] W. Legler, “Zur Statistik der Elektronenlawinen,” *Zeitschrift für Physik*, vol. 140, no. 2, pp. 221–240, Mar. 1955.
- [67] H. Raether, *Electron Avalanches and Breakdown in Gases*, ser. Butterworths advanced physics series. Butterworths, 1964, place: Washington Publisher: Butterworths.
- [68] R. Färber and C. M. Franck, “Streamer inception thresholds derived from a statistical electron transport model,” *Journal of Physics D: Applied Physics*, vol. 54, no. 43, p. 435202, Oct. 2021.
- [69] J. I. Levatter and S.-C. Lin, “Necessary conditions for the homogeneous formation of pulsed avalanche discharges at high gas

- pressures,” *Journal of Applied Physics*, vol. 51, no. 1, pp. 210–222, Jan. 1980.
- [70] G. A. Mesyats, “Similarity laws for pulsed gas discharges,” *Uspekhi Fizicheskikh Nauk*, vol. 176, no. 10, p. 1069, 2006.
- [71] —, *Pulsed power*. New York: Kluwer Academic/Plenum Publishers, 2005, oCLC: ocm55616619.
- [72] N. Kapcov, *Elektrische Vorgänge in Gasen und im Vakuum*, ser. Hochschulbücher für Physik. Deutscher Verlag der Wissenschaften, 1955.
- [73] M. Beyer, W. Boeck, K. Möller, and W. Zaengl, *Hochspannungstechnik*. Berlin, Heidelberg: Springer Berlin Heidelberg, 1986.
- [74] Y. Fu, P. Zhang, J. P. Verboncoeur, and X. Wang, “Electrical breakdown from macro to micro/nano scales: a tutorial and a review of the state of the art,” *Plasma Research Express*, vol. 2, no. 1, p. 013001, Feb. 2020.
- [75] G. L. Pilla, D. A. Lacoste, D. Veynante, and C. O. Laux, “Stabilization of a Swirled Propane–Air Flame Using a Nanosecond Repetitively Pulsed Plasma,” *IEEE Transactions on Plasma Science*, vol. 36, no. 4, pp. 940–941, Aug. 2008.
- [76] D. I. Pineda, B. Wolk, T. Sennott, J.-Y. Chen, R. W. Dibble, and D. Singleton, “The role of hydrodynamic enhancement on ignition of lean methane–air mixtures by pulsed nanosecond discharges for automotive engine applications,” *Combustion Science and Technology*, vol. 189, no. 11, pp. 2023–2037, 2017.
- [77] S. Pancheshnyi, “Photoionization produced by low-current discharges in O₂, air, N₂ and CO₂,” *Plasma Sources Science and Technology*, vol. 24, no. 1, p. 015023, Dec. 2014.
- [78] G. W. Penney and G. T. Hummert, “Photoionization Measurements in Air, Oxygen, and Nitrogen,” *Journal of Applied Physics*, vol. 41, no. 2, pp. 572–577, 02 1970.
- [79] “Viehland database, www.lxcat.net, retrieved on February 15, 2021.”

- [80] A. Fridman, A. Chirokov, and A. Gutsol, “Non-thermal atmospheric pressure discharges,” *Journal of Physics D: Applied Physics*, vol. 38, no. 2, pp. R1–R24, Jan. 2005.
- [81] D. Levko, “Mechanism of sub-nanosecond pulsed breakdown of pressurized nitrogen,” *Journal of Applied Physics*, vol. 126, no. 8, p. 083303, Aug. 2019.
- [82] P. A. Anderson, “The Work Function of Copper,” *Physical Review*, vol. 76, no. 3, pp. 388–390, Aug. 1949.
- [83] N. Barrett, O. Renault, H. Lemaître, P. Bonnaillie, F. Barcelo, F. Miserque, M. Wang, and C. Corbel, “Microscopic work function anisotropy and surface chemistry of 316L stainless steel using photoelectron emission microscopy,” *Journal of Electron Spectroscopy and Related Phenomena*, vol. 195, pp. 117–124, Aug. 2014.
- [84] H. B. Mann and D. R. Whitney, “On a Test of Whether one of Two Random Variables is Stochastically Larger than the Other,” *The Annals of Mathematical Statistics*, vol. 18, no. 1, pp. 50–60, Mar. 1947.
- [85] R. H. Fowler and L. Nordheim, “Electron Emission in Intense Electric Fields,” *Proceedings of the Royal Society of London. Series A, Containing Papers of a Mathematical and Physical Character*, vol. 119, no. 781, pp. 173–181, 1928.
- [86] L. Warne, R. Jorgenson, and S. Nicolaysen, “Ionization coefficient approach to modeling breakdown in nonuniform geometries.” Sandia National Laboratories (SNL), Tech. Rep. SAND2003-4078, 918222, Nov. 2003.
- [87] F. Llewellyn-Jones and F. Llewellyn-Jones, *Ionization and breakdown in gases*, ser. Science paperbacks 33. London: Methuen, 1966.
- [88] D. B. Go, *Ionization and Ion Transport*, ser. 2053-2571. Morgan & Claypool Publishers, 2018.
- [89] J. G. Trump, R. W. Cloud, J. G. Mann, and E. P. Hanson, “Influence of electrodes on D-C breakdown in gases at high pressure,” *Electrical Engineering*, vol. 69, no. 11, pp. 961–964, Nov. 1950.

- [90] S. Pancheshnyi, “Role of electronegative gas admixtures in streamer start, propagation and branching phenomena,” *Plasma Sources Science and Technology*, vol. 14, no. 4, pp. 645–653, Nov. 2005.
- [91] B. Baker, B. Johnson, and G. Maire, “Photoelectric work function measurements on nickel crystals and films,” *Surface Science*, vol. 24, no. 2, pp. 572–586, Feb. 1971.
- [92] G. J. Tallents, *An Introduction to the Atomic and Radiation Physics of Plasmas*. Cambridge University Press, 2018.
- [93] F. F. Chen, *Introduction to Plasma Physics and Controlled Fusion*. Cham: Springer International Publishing, 2016.
- [94] V. K. Shen, D. W. Siderius, W. P. Krekelberg, H. W. Hatch *et al.*, “Nist standard reference simulation website,” 2017.
- [95] S. Thakur and J. Singh, “Fundamentals of Laser Induced Breakdown Spectroscopy,” in *Laser-Induced Breakdown Spectroscopy*. Elsevier, 2007, pp. 3–21.
- [96] J. J. Camacho, M. Santos, L. Díaz, and J. M. L. Poyato, “Optical emission spectroscopy of oxygen plasma induced by IR CO₂ pulsed laser,” *Journal of Physics D: Applied Physics*, vol. 41, no. 21, p. 215206, Nov. 2008.
- [97] N. Kieu, F. J. Gordillo-Vázquez, M. Passas, J. Sánchez, and F. J. Pérez-Invernón, “High-Speed Spectroscopy of Lightning-Like Discharges: Evidence of Molecular Optical Emissions,” *Journal of Geophysical Research: Atmospheres*, vol. 126, no. 11, p. e2021JD035016, Jun. 2021.
- [98] M. A. Gigosos, M. A. González, and V. C. noso, “Computer simulated balmer-alpha, -beta and -gamma stark line profiles for non-equilibrium plasmas diagnostics,” *Spectrochimica Acta Part B: Atomic Spectroscopy*, vol. 58, no. 8, pp. 1489–1504, 2003, 5th European Furnace Symposium and 10th International Solid Sampling Colloquium with Atomic Spectroscopy.
- [99] M. Wnukowski, “Methane Pyrolysis with the Use of Plasma: Re-

- view of Plasma Reactors and Process Products,” *Energies*, vol. 16, no. 18, p. 6441, Sep. 2023.
- [100] M. Černák, T. Hoder, and Z. Bonaventura, “Streamer breakdown: cathode spot formation, Trichel pulses and cathode-sheath instabilities,” *Plasma Sources Science and Technology*, vol. 29, no. 1, p. 013001, Dec. 2019, publisher: IOP Publishing.
- [101] V. Gururajan and R. Scarcelli, “A nanosecond pulsed discharge circuit model for engine applications,” *Journal of Physics D: Applied Physics*, vol. 55, no. 15, p. 155205, Apr. 2022.
- [102] D. Z. Pai, D. A. Lacoste, and C. O. Laux, “Nanosecond repetitively pulsed discharges in air at atmospheric pressure—the spark regime,” *Plasma Sources Science and Technology*, vol. 19, no. 6, p. 065015, Dec. 2010.
- [103] D. Z. Pai, G. D. Stancu, D. A. Lacoste, and C. O. Laux, “Nanosecond repetitively pulsed discharges in air at atmospheric pressure—the glow regime,” *Plasma Sources Science and Technology*, vol. 18, no. 4, p. 045030, Nov. 2009.
- [104] A. Lo, A. Cessou, C. Lacour, B. Lecordier, P. Boubert, D. A. Xu, C. O. Laux, and P. Vervisch, “Streamer-to-spark transition initiated by a nanosecond overvoltage pulsed discharge in air,” *Plasma Sources Science and Technology*, vol. 26, no. 4, p. 045012, Mar. 2017.
- [105] A. Chachereau and S. Pancheshnyi, “Calculation of the Effective Ionization Rate in Air by Considering Electron Detachment From Negative Ions,” *IEEE Transactions on Plasma Science*, vol. 42, no. 10, pp. 3328–3338, Oct. 2014.
- [106] N. Minesi, “Thermal spark formation and plasma-assisted combustion by nanosecond repetitive discharges,” Theses, Université Paris-Saclay, Dec. 2020.
- [107] B. McBride, *NASA Glenn Coefficients for Calculating Thermodynamic Properties of Individual Species*, ser. NASA Technical Paper. National Aeronautics and Space Administration, John H. Glenn Research Center at Lewis Field, 2002.

- [108] H. Hess and R. Radtke, "On the calculation of low-inductance spark discharges," *Journal of Physics D: Applied Physics*, vol. 8, no. 6, p. 681, apr 1975.
- [109] N. Minesi, S. Stepanyan, P. Mariotto, G. D. Stancu, and C. O. Laux, "Fully ionized nanosecond discharges in air: the thermal spark," *Plasma Sources Science and Technology*, vol. 29, no. 8, p. 085003, Aug. 2020.
- [110] W. Weizel, "Berechnung des Ablaufs von Funken mit Widerstand und Selbstinduktion im Stromkreis," *Zeitschrift für Physik*, vol. 135, no. 5, pp. 639–657, Oct. 1953.
- [111] E. Rose, "Spannungszusammenbruch an schnellen Funken," *Annalen der Physik*, vol. 459, no. 1-5, pp. 15–35, Jan. 1959.
- [112] S. Shcherbaney, T. Morinière, R. Solana-Pérez, M. Weilenmann, Y. Xiong, U. Doll, and N. Noiray, "Anchoring of premixed jet flames in vitiated crossflow with pulsed nanosecond spark discharge," *Applications in Energy and Combustion Science*, vol. 1-4, p. 100010, Dec. 2020.
- [113] P. J. Bruggeman, F. Iza, and R. Brandenburg, "Foundations of atmospheric pressure non-equilibrium plasmas," *Plasma Sources Science and Technology*, vol. 26, no. 12, p. 123002, Nov. 2017.
- [114] D. Xiao, *Gas Discharge and Gas Insulation*, ser. Energy and Environment Research in China. Berlin, Heidelberg: Springer Berlin Heidelberg, 2016, vol. 6.
- [115] A. Onorati and G. Montenegro, *1D and Multi-D Modeling Techniques for IC Engine Simulation*. SAE International, Apr. 2020.
- [116] P. Soltic, T. Hilfiker, and S. Hänggi, "Efficient light-duty engine using turbulent jet ignition of lean methane mixtures," *International Journal of Engine Research*, p. 146808741988983, Nov. 2019.
- [117] H. M. Cho and B.-Q. He, "Spark ignition natural gas engines—A review," *Energy Conversion and Management*, vol. 48, no. 2, pp. 608–618, Feb. 2007.
- [118] S. Benekos, "A Direct Numerical Simulation Study on the Physi-

- cochemical Aspects of Turbulent Jet Ignition,” PhD Theses, diss no. 27111, ETH, Zurich, 2020.
- [119] L. Sforza, T. Lucchini, G. Gianetti, G. D’Errico, G. Onofrio, C. Beatrice, and P. Tunestal, “A 3D-CFD Methodology for Combustion Modeling in Active Prechamber SI Engines Operating with Natural Gas,” in *SAE Technical Paper No. 2022-01-0470*, Mar. 2022, pp. 2022–01–0470.
- [120] G. Xu, M. Kotzagianni, P. Kyrtatos, Y. M. Wright, and K. Boulouchos, “Experimental and numerical investigations of the unscavenged prechamber combustion in a rapid compression and expansion machine under engine-like conditions,” *Combustion and Flame*, vol. 204, pp. 68–84, Jun. 2019.
- [121] S. Hänggi, T. Hilfiker, P. Soltic, R. Hutter, and C. Onder, “Control-oriented analysis of a lean-burn light-duty natural gas research engine with scavenged pre-chamber ignition,” *Combustion Engines*, vol. 176, no. 1, pp. 42–53, Feb. 2019.
- [122] W. Vera-Tudela, B. Schneider, S. Wüthrich, and K. Herrmann, “Study on the ignitability of a high-pressure direct-injected methane jet using a diesel pilot, a glow-plug, and a pre-chamber,” *International Journal of Engine Research*, vol. 24, no. 2, pp. 360–372, Feb. 2023.
- [123] G. McTaggart-Cowan, K. Mann, J. Huang, A. Singh, B. Pachtchuk, Z. X. Zheng, and S. Munshi, “Direct Injection of Natural Gas at up to 600 Bar in a Pilot-Ignited Heavy-Duty Engine,” *SAE International Journal of Engines*, vol. 8, no. 3, pp. 981–996, Apr. 2015.
- [124] M. K. Roy, N. Kawahara, E. Tomita, and T. Fujitani, “Jet-guided combustion characteristics and local fuel concentration measurements in a hydrogen direct-injection spark-ignition engine,” *Proceedings of the Combustion Institute*, vol. 34, no. 2, pp. 2977–2984, 2013.
- [125] K. Boulouchos, T. Steiner, and P. Dimopoulos, “Investigation of flame speed models for the flame growth period during premixed engine combustion,” *SAE Technical Paper 940476*, p. 940476, Mar. 1994.

- [126] D. A. Xu, D. A. Lacoste, and C. O. Laux, "Schlieren Imaging of Shock-Wave Formation Induced by Ultrafast Heating of a Nanosecond Repetitively Pulsed Discharge in Air," *IEEE Transactions on Plasma Science*, vol. 42, no. 10, pp. 2350–2351, Oct. 2014.
- [127] L. Eriksson and L. Nielsen, "Ionization current interpretation for ignition control in internal combustion engines," *Control Engineering Practice*, vol. 5, no. 8, pp. 1107–1113, 1997.
- [128] J. Auzins, H. Johansson, and J. Nytomt, "Ion-Gap Sense in Misfire Detection, Knock and Engine Control," *SAE Technical Paper 950004*, p. 950004, Feb. 1995.
- [129] A. Irimescu, S. S. Merola, and B. Maria Vaglieco, "Spark anemometry applied through secondary current measurements in an optical spark ignition engine," *Energy Conversion and Management*, vol. 269, p. 116088, Oct. 2022.
- [130] G. Kosmadakis, D. Rakopoulos, J. Arroyo, F. Moreno, M. Muñoz, and C. Rakopoulos, "CFD-based method with an improved ignition model for estimating cyclic variability in a spark-ignition engine fueled with methane," *Energy Conversion and Management*, vol. 174, pp. 769–778, Oct. 2018.
- [131] L. Wang, X. Yu, B. Cong, L. Li, G. Chen, and M. Zheng, "Active Plasma Probing for Lean Burn Flame Detection," *SAE Technical Paper 2023-01-0293*, pp. 2023–01–0293, Apr. 2023.
- [132] S. Shcherbanev, B. A. Dharmaputra, and N. Noiray, "Flame stabilization with nanosecond repetitively pulsed discharge in the sequential combustor," in *AIAA SCITECH 2022 Forum*. San Diego, CA & Virtual: American Institute of Aeronautics and Astronautics, Jan. 2022.
- [133] V. Gururajan, R. Scarcelli, S. Biswas, and I. Ekoto, "CFD Modeling of Low Temperature Ignition Processes From a Nanosecond Pulsed Discharge at Quiescent Conditions," in *ASME 2021 Internal Combustion Engine Division Fall Technical Conference*. Virtual, Online: American Society of Mechanical Engineers, Oct. 2021, p. V001T06A010, v001T06A010.
- [134] A. Srna, M. Bolla, Y. M. Wright, K. Herrmann, R. Bombach, S. S.

- Pandurangi, K. Boulouchos, and G. Bruneaux, "Effect of methane on pilot-fuel auto-ignition in dual-fuel engines," *Proceedings of the Combustion Institute*, vol. 37, no. 4, pp. 4741–4749, 2019.
- [135] C. E. Frouzakis, N. Fogla, A. G. Tomboulides, C. Altantzis, and M. Matalon, "Numerical study of unstable hydrogen/air flames: Shape and propagation speed," *Proceedings of the Combustion Institute*, vol. 35, no. 1, pp. 1087–1095, 2015.
- [136] H. L. Yip, A. Srna, A. C. Y. Yuen, S. Kook, R. A. Taylor, G. H. Yeoh, P. R. Medwell, and Q. N. Chan, "A Review of Hydrogen Direct Injection for Internal Combustion Engines: Towards Carbon-Free Combustion," *Applied Sciences*, vol. 9, no. 22, p. 4842, Nov. 2019.
- [137] A. Wimmer, T. Wallner, J. Ringler, and F. Gerbig, "H₂-Direct Injection – A Highly Promising Combustion Concept," *SAE Technical Paper 2005-01-0108*, pp. 2005–01–0108, Apr. 2005.
- [138] J. Hwang, K. Maharjan, and H. Cho, "A review of hydrogen utilization in power generation and transportation sectors: Achievements and future challenges," *International Journal of Hydrogen Energy*, vol. 48, no. 74, pp. 28 629–28 648, Aug. 2023.
- [139] S. Verhelst, R. Sierens, and S. Verstraeten, "A critical review of experimental research on hydrogen fueled si engines," *SAE Technical Paper 2006-01-0430*, pp. 2006–01–0430, Apr. 2006.
- [140] D. Koch, T. Ebert, and A. Sousa, "Engine Adaptation from Diesel to H₂ HP-EGR Lean Combustion Concept," *MTZ worldwide*, vol. 81, no. 5, pp. 30–37, May 2020.
- [141] S. Verhelst, "Recent progress in the use of hydrogen as a fuel for internal combustion engines," *International Journal of Hydrogen Energy*, vol. 39, no. 2, pp. 1071–1085, Jan. 2014.
- [142] K. Lee, Y. Kim, C. Byun, and J. Lee, "Feasibility of compression ignition for hydrogen fueled engine with neat hydrogen-air pre-mixture by using high compression," *International Journal of Hydrogen Energy*, vol. 38, no. 1, pp. 255–264, Jan. 2013.
- [143] J. Naber, "Hydrogen combustion under diesel engine conditions,"

- International Journal of Hydrogen Energy*, vol. 23, no. 5, pp. 363–371, May 1998.
- [144] G. Fink, M. Jud, and T. Sattelmayer, “Fundamental Study of Diesel-Piloted Natural Gas Direct Injection Under Different Operating Conditions,” *Journal of Engineering for Gas Turbines and Power*, vol. 141, no. 9, p. 091006, Sep. 2019.
- [145] P. Rorimpandey, H. L. Yip, A. Srna, G. Zhai, A. Wehrfritz, S. Kook, E. R. Hawkes, and Q. N. Chan, “Hydrogen-diesel dual-fuel direct-injection (H2DDI) combustion under compression-ignition engine conditions,” *International Journal of Hydrogen Energy*, vol. 48, no. 2, pp. 766–783, Jan. 2023.
- [146] M. K. Roy, N. Kawahara, E. Tomita, and T. Fujitani, “High-Pressure Hydrogen Jet and Combustion Characteristics in a Direct-Injection Hydrogen Engine,” *SAE International Journal of Fuels and Lubricants*, vol. 5, no. 3, pp. 1414–1425, Aug. 2011.
- [147] L. Merotto, M. Balmelli, and P. Soltic, “Hydrogen direct injection: Optical investigation of premixed and jet-guided combustion modes,” *International Journal of Hydrogen Energy*, vol. 61, pp. 284–295, Apr. 2024.
- [148] L. Guzzella and C. H. Onder, *Introduction to Modeling and Control of Internal Combustion Engine Systems*. Berlin, Heidelberg: Springer Berlin Heidelberg, 2010.
- [149] H. L. Yip, A. Srna, X. Liu, S. Kook, E. R. Hawkes, and Q. N. Chan, “Visualization of hydrogen jet evolution and combustion under simulated direct-injection compression-ignition engine conditions,” *International Journal of Hydrogen Energy*, vol. 45, no. 56, pp. 32 562–32 578, Nov. 2020.
- [150] F. Duronio, C. Villante, and A. De Vita, “Under-Expanded Jets in Advanced Propulsion Systems—A Review of Latest Theoretical and Experimental Research Activities,” *Energies*, vol. 16, no. 18, p. 6471, Sep. 2023.
- [151] J. S. Turner, “The ‘starting plume’ in neutral surroundings,” *Journal of Fluid Mechanics*, vol. 13, no. 3, pp. 356–368, Jul. 1962.

- [152] V. D. Sakellarakis, “Mixing and Autoignition of Underexpanded Methane Jets at High Pressure Conditions,” Ph.D. dissertation, ETH Zurich, 2020, artwork Size: 146 p. Medium: application/pdf Pages: 146 p.
- [153] R. Pischinger, M. Klell, and T. Sams, *Thermodynamik der Verbrennungskraftmaschine*, 3rd ed., ser. Der Fahrzeugantrieb. Bonn: Springer, 2009.
- [154] G. Moretto, S. Hänggi, T. Albin, and C. H. Onder, “Combustion Rate Shaping for Cycle-to-cycle Control,” ETHZ, Tech. Rep., 2019.
- [155] G. Moretto, S. Hänggi, and C. Onder, “Optimal combustion calibration for direct-injection compression-ignition engines using multiple injections,” *International Journal of Engine Research*, vol. 24, no. 4, pp. 1414–1431, Apr. 2023.
- [156] M. F. Brunt, H. Rai, and A. L. Emtage, “The Calculation of Heat Release Energy from Engine Cylinder Pressure Data,” in *SAE Technical Paper No. 981052*, Feb. 1998, p. 981052.
- [157] C. E. C. Alvarez, G. E. Couto, V. R. Roso, A. B. Thiriet, and R. M. Valle, “A review of prechamber ignition systems as lean combustion technology for SI engines,” *Applied Thermal Engineering*, vol. 128, pp. 107–120, Jan. 2018.
- [158] A. García, J. De La Morena, J. Monsalve-Serrano, R. Lago Sari, and P. Tunestal, “Combining in-cylinder pressure and 1D simulation tools to understand the combustion characteristics of natural gas in pre-chamber ignition systems for energy generation,” *Energy Conversion and Management*, vol. 240, p. 114262, Jul. 2021.
- [159] T. Badawy, J. W. Turner, and H. Xu, “Evaluation of engine performance and emissions in an optical DISI engine with various spark plug designs and gaps,” *Fuel*, vol. 357, p. 129900, Feb. 2024.
- [160] S. Wüthrich, P. Cartier, P. Süess, B. Schneider, P. Obrecht, and K. Herrmann, “Optical investigation and thermodynamic analysis of premixed ammonia dual-fuel combustion initiated by dodecane pilot fuel,” *Fuel Communications*, vol. 12, p. 100074, 2022.

- [161] S. A. Shcherbanev, S. A. Stepanyan, N. A. Popov, and S. M. Starikovskaia, “Dielectric barrier discharge for multi-point plasma-assisted ignition at high pressures,” *Philosophical Transactions of the Royal Society A: Mathematical, Physical and Engineering Sciences*, vol. 373, no. 2048, p. 20140342, Aug. 2015.
- [162] D. R. Rogers, *Engine Combustion: Pressure Measurement and Analysis*. Warrendale, PA: SAE International, Aug. 2010.
- [163] K. Bardis, G. Xu, P. Kyrtatos, Y. M. Wright, and K. Boulouchos, “A Zero Dimensional Turbulence and Heat Transfer Phenomenological Model for Pre-Chamber Gas Engines,” in *SAE Technical Paper No. 2018-01-1453*, Apr. 2018, pp. 2018–01–1453.

Curriculum Vitae

Personal Details

Name Michelangelo Balmelli
Date of birth 30 April 1992
Place of birth Sorengo, Switzerland
Nationality Swiss

Education

2020 – 2024 Doctorate, ETH Zürich
Topic: Investigation into NRPD ignition for ICE
2017 – 2019 Master of Science in Mechanical Engineering
ETH Zürich
2012 – 2017 Bachelor of Science in Mechanical Engineering
ETH Zürich

Practical Experience

2020 – 2024 Empa, Dübendorf CH
PhD candidate in the Chemical Energy Carriers
and Vehicle Systems Laboratory
2019 – 2020 Empa, Dübendorf CH
Engineer in the Chemical Energy Carriers
and Vehicle Systems Laboratory
2018 BMW, München DE
Internship in the homologation testing department

